Dissertation

submitted to the

Combined Faculties of the Natural Sciences and Mathematics

of the Ruperto-Carola-University of Heidelberg, Germany

for the degree of

Doctor of Natural Sciences

Put forward by

Mathis Kolb

born in Heidelberg

Oral examination: November 21, 2018

Search for new physics with top quark pairs in the fully hadronic final state at the ATLAS experiment

Referees: Prof. Dr. André Schöning

Prof. Dr. Tilman Plehn

Search for new physics with top quark pairs in the fully hadronic final state at the ATLAS experiment

Fully hadronic final states containing top quark pairs ($t\bar{t}$) are investigated using proton-proton collision data at a center of mass energy of 13 TeV recorded in 2015 and 2016 by the ATLAS experiment at the Large Hadron Collider at CERN. The bucket algorithm suppresses the large combinatorial background and is used to identify and reconstruct the $t\bar{t}$ system. It is applied in three analyses.
A model independent search for new heavy particles decaying to $t\bar{t}$ using 36 fb^{-1} of data is presented. The analysis concentrates on an optimization of sensitivity at $t\bar{t}$ masses below 1.3 TeV. No excess from the Standard Model prediction is observed. Thus, upper limits at 95% C.L. are set on the production cross section times branching ratio of benchmark signal models excluding e.g. a topcolor assisted technicolor Z'_{TC2} in the mass range from 0.59 TeV to 1.25 TeV.
The prospects of a search for the production of the Higgs boson in association with $t\bar{t}$ using 33 fb^{-1} of data recorded solely in 2016 are studied. The expected sensitivity based on statistical uncertainties implies that at least 950 fb^{-1} of data would be required for an observation.
From the additionally conducted trigger study it is concluded that developments at trigger level are required to use the analysis strategy presented in future searches for new physics.

Suche nach neuer Physik mit Top Quark Paaren im vollhadronischen Endzustand am ATLAS Experiment

Vollhadronische Endzustände mit Top Quark Paaren ($t\bar{t}$) werden mit Proton-Proton Kollisionsdaten, die 2015 und 2016 bei einer Schwerpunktenergie von 13 TeV am ATLAS Experiment am Large Hadron Collider am CERN aufgenommen wurden, untersucht. Der Bucket Algorithmus unterdrückt den großen kombinatorischen Untergrund und identifiziert und rekonstruiert das $t\bar{t}$ System. Er wird in drei Analysen angewendet.
Eine modellunabhängige Suche nach schweren Teilchen, die in $t\bar{t}$ zerfallen, wird unter Verwendung von 36 fb^{-1} an Daten präsentiert. Die Analyse konzentriert sich auf eine Verbesserung der Sensitivität bei niedrigen Ditop Massen unterhalb von 1.3 TeV. Es lassen sich keine Abweichungen von der Standardmodellvorhersage beobachten. Daher werden Grenzwerte mit 95% C.L. auf das Produkt aus Wirkungsquerschnitt und Verzweigungsverhältnis für Referenzsignalmodelle bestimmt, die z.B. erlauben das "topcolor assisted technicolor" Z'_{TC2} zwischen 0.59 TeV und 1.25 TeV auszuschließen.
Die Perspektiven der Suche nach der assoziierten Produktion eines Higgs Bosons mit $t\bar{t}$ werden anhand von 33 fb^{-1} ausschließlich 2016 genommener Daten ermittelt. Die erwartete Sensitivität, basierend auf statistischen Unsicherheiten, würde mindestens 950 fb^{-1} an Daten für eine Beobachtung erforderlich machen.
Aus der zusätzlich durchgeführten Triggerstudie wird geschlussfolgert, dass Entwicklungen im Triggerbereich benötigt werden, um die präsentierte Analysestrategie in zukünftigen Suchen nach neuer Physik verwenden zu können.

Contents

1. Motivation and outline

The Standard Model of particle physics (SM) [1–7] describes the known elementary particles and their non-gravitational interactions. During the last decades, no disagreements with SM predictions have been found in measurements from numerous experiments. In particular, SM predictions are testable at the Large Hadron Collider (LHC) at CERN where the Higgs boson was discovered in 2012 [8, 9].

While the SM has been very successful, limitations and open questions within the framework of the SM remain. These include, amongst others, the existence of dark matter and dark energy as well as the fine-tuning of the Higgs mass. The shortcomings of the SM motivate the construction of theories extending or superseding the SM.

The LHC accelerates protons and collides them at the so far highest experimentally achieved energies. Thus, the LHC provides an excellent testing ground for phenomena Beyond The Standard Model (BSM) which are often associated with high energy scales.

The top quark is the heaviest elementary particle with a mass at the electroweak scale and a short life time that allows the top quark to decay before hadronization. Top quark pairs ($t\bar{t}$) are produced abundantly at the LHC due to the high center of mass energy of the proton-proton collisions. The large number of $t\bar{t}$ events produced facilitates the detailed study of this elementary particle and its production and decay mechanisms. Due to its high mass, the top quark is expected to play an important role in the SM and in models of phenomena Beyond the Standard Model. The Yukawa coupling between the Higgs boson and the top quark is close to unity in the SM. Thereby, the top quark is strongly linked to the process of electroweak symmetry breaking and can help to investigate it. Models of phenomena beyond the Standard Model often predict heavy new particles interacting with top quark pairs. Therefore, the search for signatures in the invariant mass of top quark pairs provides a promising tool to test extensions of the SM.

Such analyses require a good understanding of the top quark decay and techniques to identify and reconstruct the $t\bar{t}$ system. Resolved top quark reconstruction techniques are designed to achieve a matching between the partons from the $t\bar{t}$ decay and the reconstructed jets [10]. An unsuccessful matching would reduce the efficiency. Especially at high transverse momentum of the top quarks $p_T > 400$ GeV the decay products measured as jets start to merge. In the high transverse momentum regime of the top quark substructure based methods [11–15] are available to address the corresponding topologies. The substructure analyses generally require large radius jets referred to as large-R jets which completely contain the top quark decay as input. That requirement introduces a threshold on the transverse momentum of

the top quark at approximately 200 GeV. The bucket algorithm as introduced in Reference [16] is designed to provide a high efficiency top tagging algorithm based on small radius jets. It explicitly targets the fully hadronic $t\bar{t}$ decay mode. This decay mode has the largest branching ratio of around 46% but also requires dealing with the overwhelming background from multijet production at the LHC.

The bucket algorithm is applied in a search for heavy particles decaying to top quark pairs. The analysis concentrates on the optimization of sensitivity for small $t\bar{t}$ masses below 1.3 TeV. Sidebands in data are used to estimate and validate the highest background components consisting of SM $t\bar{t}$ and QCD multijets. Finally, the data is analyzed and results regarding expected and observed upper limits at 95% confidence level on the production cross section times branching ratio of new particles are presented.

A direct measurement of the top Yukawa coupling can be realized in the associated production of a Higgs boson with a top quark pair. The subsequent decay of the Higgs boson into a bottom quark pair and the fully hadronic decay mode of the top quarks provide one of the largest branching ratios. However, the high jet multiplicities and b-tagged jet multiplicities impose severe challenges due to the combinatorial backgrounds. In the channel with at least four b-tagged jets the bucket algorithm assigns jets to the $t\bar{t}$ system and thereby identifies a Higgs candidate from the remaining b-tagged jets. In a proof of principal analysis the reconstruction and the classification performance are evaluated in data and simulation, taking the trigger and the background modeling into account.

Both analyses depend on the performance of the ATLAS trigger system. The multijet trigger rates are likely to increase with higher luminosities which are expected at future data taking periods [17–20]. The peak instantaneous luminosity was $1.4 \times 10^{34}\text{cm}^{-2}\text{s}^{-1}$ in 2016, increased up to $2.1 \times 10^{34}\text{cm}^{-2}\text{s}^{-1}$ in 2018 [21] and can ultimately reach up to $7.5 \times 10^{34}\text{cm}^{-2}\text{s}^{-1}$ for the High Luminosity LHC (HL-LHC) [20]. The trigger rate of e.g. a typical six jet trigger increased by a factor of 1.5 for a luminosity change from $0.5 \times 10^{34}\text{cm}^{-2}\text{s}^{-1}$ in 2015 to $1.2 \times 10^{34}\text{cm}^{-2}\text{s}^{-1}$ in 2016 [17, 18]. A trigger optimization study investigates variables constructed from jets at the trigger level in data and simulation. In particular, trigger quantities motivated by the bucket algorithm are investigated. They can be used to improve or complement existing trigger strategies for the above mentioned analyses.

The thesis is structured as follows: The theoretical foundations and concepts are summarized in Chapter 2. The analyses are based on data and simulation produced in the ATLAS experiment at the LHC. An overview of the experimental setup is presented in Chapter 3. The bucket algorithm reconstructs top quark pairs in the fully hadronic decay mode. The algorithm is described in Chapter 4, followed by a performance evaluation of the bucket algorithm based on simulated events and data in Chapter 5. A search for heavy particles decaying to a top quark pair in the fully hadronic decay mode is presented in Chapter 6. In this search, the bucket algorithm is applied for the reconstruction of the top quark pair system. In addition, a feasibility study investigates the potential of the bucket algorithm in a measurement of the production of the Higgs boson in association with a top

quark pair in Chapter 7. The increasing luminosities at the LHC impose severe challenges on the trigger rates. Optimizations of the trigger strategy relying on bucket algorithm inspired variables are investigated in Chapter 8. Finally, the thesis concludes with a summary and outlook in Chapter 9.

2. Theory

The main theoretical concepts relevant for the analyses performed in this thesis are introduced in the following. The Standard Model of particle physics is reviewed in Chapter 2.1 with an emphasis on electroweak symmetry breaking and Quantum chromodynamics (QCD). QCD is an important ingredient for any physics study at a hadron collider. The corresponding concepts are summarized in Chapter 2.2. The role and properties of the top quark in the SM are explained in Chapter 2.3. The knowledge of the top quark together with the concepts of jet physics can be used to search for phenomena beyond the standard model. Some of the relevant models for top quark pair resonance searches are introduced in Chapter 2.4. The basic statistical tools necessary for the search are presented in Chapter 2.5. This chapter contains mainly introductory information which can be found in review articles and textbooks. The essential aspects of the physics and techniques are highlighted based on more detailed descriptions in the given references, which are used as a guideline here.

2.1. Standard Model of particle physics

The Standard Model (SM) of particle physics [1–4] is the currently most successful theory to describe elementary particles and their interactions, except for gravity. The SM is a quantum field theory characterized by the gauge group

$$SU(3)_C \times SU(2)_L \times U(1)_Y \quad . \tag{2.1.1}$$

The $SU(2)_L \times U(1)_Y$ part describes the electroweak interactions where the $SU(2)_L$ and $U(1)_Y$ are associated to the weak isospin and the hypercharge respectively. The non-abelian gauge group $SU(3)_C$ defines the strong interaction. The Lorentz group characterizes the underlying space time symmetry. The ground state is only invariant under $SU(2)_L$ and $U(1)_{\mathrm{QED}}$.

The particle content of the SM comprises elementary bosons and fermions. The fermions are further classified in quarks and leptons depending on their quantum numbers or group representations as summarized in Table 2.1. Each fermion comes in three generations, called flavors, of left-handed and where indicated right-handed chiral quarks and leptons. Only the quarks which are described by color triplets participate in the strong interactions. The leptons are singlets under $SU(3)_C$ and interact only electroweak. In addition, the other class of fundamental particles are bosons which are introduced in the context of the SM Lagrangian. The SM

field	$SU(3)_{\mathrm{C}}$	$SU(2)_{\mathrm{L}}$	$U(1)_{\mathrm{Y}}$
$q_L = \begin{pmatrix} u_L \\ d_L \end{pmatrix}$	**3**	**2**	$1/3$
u_R	**3**	**1**	$4/3$
d_R	**3**	**1**	$-2/3$
$l_L = \begin{pmatrix} \nu_L \\ k_L \end{pmatrix}$	**1**	**2**	-1
l_R	**1**	**1**	-2
ϕ	**1**	**2**	1

Table 2.1.: Representations and quantum numbers of the Higgs field (ϕ) and of the SM fermions consisting of quarks (q_L, u_R, d_R) and leptons (l_L, l_R). The hypercharge definition uses the convention $\mathrm{Y} = 2(Q - I_3)$ where Q is the electromagnetic quantum number and I_3 is the third isospin component. Furthermore, left (L) and right (R) handed fields are distinguished.

Lagrangian is composed of four parts.

$$\mathcal{L}_{\mathrm{SM}} = \mathcal{L}_{\mathrm{Gauge}} + \mathcal{L}_{\mathrm{Fermions}} + \mathcal{L}_{\mathrm{Yukawa}} + \mathcal{L}_{\mathrm{Scalar}} \tag{2.1.2}$$

It contains all terms which are allowed by renormalizability, gauge invariance and the quantum numbers listed in Table 2.1. The gauge sector $\mathcal{L}_{\mathrm{Gauge}}$ contains the gauge fields G^a_μ, W^b_μ and B_μ of the full $SU(3)_{\mathrm{C}} \times SU(2)_{\mathrm{L}} \times U(1)_{\mathrm{Y}}$ gauge group. Where a stands for the generators of $SU(3)_C$ and b for the generators of $SU(2)_L$. The gauge fields correspond to the spin one bosons mediating the forces. A typical representation of the $SU(2)$ is given by the Pauli matrices. An illustrative representation of the strong interaction $SU(3)$ and the G^a_μ interpreted as the eight gluon fields is given in Chapter 2.1.2.

The covariant derivative of the Standard Model acts on the matter fields ψ such as quarks in the following way

$$D_\mu \psi = \left(\partial_\mu - i\frac{g_1}{2} Y B_\mu - i\frac{g_2}{2} t_j W^j_\mu - i\frac{g_3}{2} \lambda_\alpha G^\alpha_\mu \right) \psi \tag{2.1.3}$$

where t_j and λ_α are appropriate representations of the symmetry groups. Based on the covariant derivative one can construct the Field strength tensor defined as

$$F_{\mu\nu} = [D_\mu, D_\nu] \tag{2.1.4}$$

The corresponding field strength tensors $G^a_{\mu\nu}$, $W^b_{\mu\nu}$ and $B_{\mu\nu}$ of the SM symmetry groups are used to parametrize the gauge field dynamics and interactions. Self interactions between the gauge fields arise from the non-abelian structure of $SU(3)_C$

and $SU(2)_L$ The gauge Lagrangian is given by

$$\mathcal{L}_{\text{Gauge}} = -\frac{1}{4}G^a_{\mu\nu}G^{\mu\nu}_a - \frac{1}{4}W^b_{\mu\nu}W^{\mu\nu}_b - \frac{1}{4}B_{\mu\nu}B^{\mu\nu} \tag{2.1.5}$$

Using the covariant derivative the fermion Lagrangian is given by the following expression

$$\mathcal{L}_{\text{Fermions}} = i\overline{\psi}\gamma^\mu D_\mu \psi \tag{2.1.6}$$

describing the kinematics of the matter fields and their interaction rules. So far all fermions are kept massless. The gluons of the strong force are massless in the SM. In the electroweak sector the gauge bosons are known to be massive. The generation of masses including the fermions in the Standard Model is described in Chapter 2.1.1

The massive quarks can interact between different generations. Such a process is referred to as mixing and described by the CKM matrix V_{CKM} which is a matrix close to unity. The matrix originates from the transformation of the Yukawa coupling matrices in the weak-eigenstate basis to the physical basis. The entries of the CKM matrix influence the strength of the charged current interactions between the quarks mediated by the $W^\pm$ bosons. The V_{CKM} is a 3×3 unitary matrix with three real parameters referred to as mixing angles and one phase associated to the CP violation in the quark sector. The charged current interaction for up-type quarks q^u_i with flavor i and down-type quarks q^d_i with flavor j in the physical states

$$\frac{-g}{\sqrt{2}}\overline{q}^u_i W^+_\mu V_{\text{CKM}} q^d_i \tag{2.1.7}$$

defines the entries of the CKM matrix

$$V_{\text{CKM}} \equiv \begin{pmatrix} V_{ud} & V_{us} & V_{ub} \\ V_{cd} & V_{cs} & V_{cb} \\ V_{td} & V_{ts} & V_{tb} \end{pmatrix} \simeq \begin{pmatrix} 1 & \epsilon & _\epsilon \\ \epsilon & 1 & \epsilon \\ _\epsilon & \epsilon & 1 \end{pmatrix} \ . \tag{2.1.8}$$

Here the last relation illustrates the hierarchy of the values of the V_{CKM} entries by the size of the small number ϵ.

2.1.1. Electroweak symmetry breaking

The construction of the Standard Model based on the gauge symmetries and the chiral symmetry does not necessarily require the presence of the isospin doublet of complex scalar fields ϕ. Experimental measurements have proven that most of the fermions and the electroweak gauge bosons are massive. Mass terms for the fermions can be explicitly introduced using the field ϕ and other mass terms can be added through the process of *spontaneous symmetry breaking*. In this process the Lagrangian is symmetric under transformations of a certain symmetry group

whereas the ground state is not. The introduction of the Higgs field and its interaction with the other SM particles can describe the observed masses. At first the isospin doublet ϕ of complex scalar fields adds four degrees of freedom to the model. Eventually they are identified with the so called Goldstone fields and the Higgs field.

The relevant term of the Higgs Lagrangian preserving renormalizibility and the symmetries is given by the following equation

$$\mathcal{L}_{\text{scalar}} = (D_\mu \phi D)(D^\mu \phi)^\dagger - V(\phi) \tag{2.1.9}$$

$$\text{with} \quad V(\phi) = \mu^2 \phi^\dagger \phi + \lambda (\phi^\dagger \phi)^2 \ . \tag{2.1.10}$$

Here the covariant derivative D_μ can be expressed by

$$D_\mu = \left(\partial_\mu - i \frac{g_1}{2} Y B_\mu - i \frac{g_2}{2} t_j W_\mu^j \right) \ . \tag{2.1.11}$$

The parameter μ appearing in the potential $V(\phi)$ quantifies the mass term and the positive parameter λ the quartic coupling. With $\mu^2 > 0$ only the trivial vacuum would exist. For $\mu^2 < 0$ a rotational symmetric minimum is defined by the minimum condition in the complex plane

$$|\phi| = \sqrt{\frac{-\mu^2}{2\lambda}} \equiv \frac{v}{\sqrt{2}} \tag{2.1.12}$$

The value of the ground state is quantified by the so-called *vacuum expectation value* v. The ground state which can be expressed by

$$\phi_0 = \frac{v}{2} e^{i\Theta} \tag{2.1.13}$$

is now only invariant under $U(1)_{\text{QED}}$ in contrast to the initial $SU(2)_L \times U(1)_Y$ symmetry. Setting the ground state to e.g. $\Theta = 0$ the other states cane be approximated as

$$\phi = \begin{pmatrix} 0 \\ v + \phi_1 + i\phi_2 \end{pmatrix} \tag{2.1.14}$$

Using this parametrization the mass matrix of the fields ϕ_i can be calculated from the second derivatives of the potential.

$$(M^2)_{kl} = \left. \frac{\partial^2 V}{\partial^2 \{\phi_k \phi_l\}} \right|_{\text{minimum}} \tag{2.1.15}$$

The result is a symmetric diagonal matrix with one mass-less field ϕ_2 and one

massive field ϕ_1.

$$M = \begin{pmatrix} 2\lambda v^2 & 0 \\ 0 & 0 \end{pmatrix} \tag{2.1.16}$$

Here the massive field corresponds to the Higgs field whereas the mass-less field corresponds to a Goldstone mode. The result also illustrates the Goldstone theorem which is at the center of the *spontaneous symmetry breaking*. If the ground state is only invariant under a sub-group G_S of the original symmetry group G there exists a massless spin-0 boson for each generator in G which is not part of G_S.

Through a suitable reparametrization of the fields and using the gauge freedom the doublet can be written in the simplified form

$$\phi = \frac{1}{\sqrt{2}} \begin{pmatrix} 0 \\ v + H(x) \end{pmatrix} \ . \tag{2.1.17}$$

Inserting this parametrization in the covariant derivative results in the Higgs interactions with the gauge bosons and in explicit gauge boson mass terms. The masses of the $W^{\pm}$ and the Z boson are given by

$$M_{W^{\pm}} = \frac{1}{2} v g_2 \tag{2.1.18}$$

$$M_Z = \frac{1}{2} \frac{v g_2}{\cos \Theta_W} = \frac{1}{2} v \sqrt{g_1^2 + g_2^2} \tag{2.1.19}$$

with the Weinberg angle Θ_W. After the symmetry breaking the three initial degrees of freedom of the scalar field are absorbed by the gauge bosons and constitute their longitudinal degrees of freedom. Furthermore, fermion masses can be created by explicit interaction terms with the Higgs field. These so-called Yukawa couplings are quantified by the Yukawa coupling constant y_f and appear in the Lagrangian in the mass basis as

$$\mathcal{L}_Y = \frac{1}{\sqrt{2}} (v + H) y_f f \overline{f} \tag{2.1.20}$$

From this term the fermion masses can be quantified as $m_f = v y_f / \sqrt{2}$. It also illustrates that the Higgs coupling to fermions is proportional to its mass. In addition to the Higgs mass the scalar potential also gives rise to the Higgs self couplings. Inserting the parametrization of Equation 2.1.17 in the potential $V(\phi)$ results in the component of the Lagrangian describing these trilinear and quadrilinear self couplings

$$\mathcal{L}_\lambda = -\lambda v H^3 - \frac{\lambda}{4} H^4 \ . \tag{2.1.21}$$

As the SM is a renormalizable quantum field theory (QFT) the scale depen-

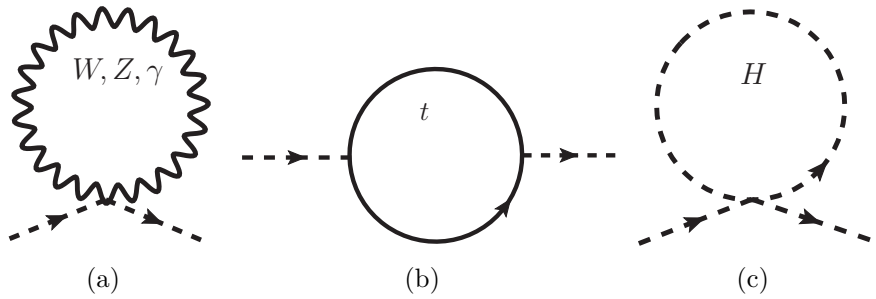

Figure 2.1.: Feynman diagrams of relevant quadratically divergent contributions to the SM Higgs mass.

dence of the Higgs self coupling λ is described by the renormalization group (RG) evolution at one loop [22] by

$$\frac{d\lambda}{\log Q^2} \approx \frac{1}{16\pi^2}(12\lambda^2 + 6\lambda y_t^2 - 3y_t^2 - \frac{3}{2}\lambda(3g^2 + g'^2) + \frac{3}{16}(2g^4 + (g^2 + g'^2)^2) \tag{2.1.22}$$

Here $y_t = \sqrt{2}m_t/v$ and contributions from the Higgs boson, the weak gauge bosons and the top quark are considered. Feynman diagrams of contributing processes are sketched in Figure 2.1. The right-hand side is characterized by the interplay of negative and positive contributions of the top quark and from the gauge bosons. Using the RG evolution the triviality and stability bounds are calculated. Based on these bounds Higgs mass windows for a fundamental and stable Standard Model can be derived [22]. Evidently, the fermion in the Standard Model with the largest Yukawa coupling of ≈ 1, the top quark, plays a special role in that considerations. Therefore, the analysis of the interactions between the top quark and the Higgs boson could reveal insights to phenomena beyond the Standard Model [23] as discussed in Chapter 2.4.

2.1.2. Quantum Chromodynamics

Even though there are many similarities in the description of the electroweak and the strong interactions the symmetry group $SU(3)_C$ provokes particular features in the phenomenology of QCD. The charge associated to QCD is the color charge. The observed hadrons are bound states consisting of quarks and gluons. These bound states, baryons consisting of three quarks and mesons composed of a quark anti-quark pair, are only observed as colorless states. Gluons are the eight gauge bosons in QCD which also carry the color charge. Due to the non-abelian structure of QCD the gluons have self interactions. The free parameter of the QCD Lagrangian is the strong coupling constant g_S. Generally it is reformulated by the parameter

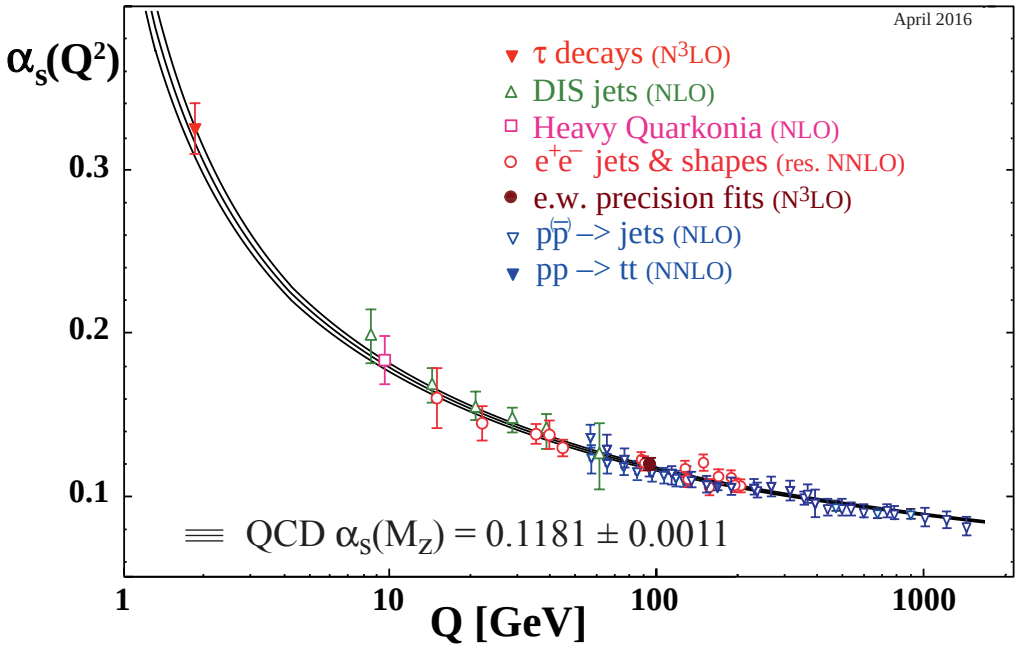

Figure 2.2.: Measurements of α_S for different energy scales Q. The QCD prediction band is obtained by running the world average value for α_S within its uncertainties. Figure taken from Reference [24].

α_S which is related to g_s by the expression

$$\alpha_S = g_S^2 4\pi \tag{2.1.23}$$

Loop corrections from gluon self interactions influence the renormalization group equation of α_S. The dependence of the strong coupling α_S as a function of the scale μ is described by the following equation at one loop order

$$\alpha_S(\mu^2) = \frac{1}{b_0 \log \frac{\mu^2}{\Lambda^2_{\mathrm{QCD}}}} \tag{2.1.24}$$

with the reference scale Λ_{QCD}. The coupling α_S is decreasing with increasing energy. A phenomenon referred to as *asymptotic freedom*. As a consequence the coupling is small at high energies making the perturbative calculation of QCD processes feasible. In contrary at lower energies α_S becomes large leading to *confinement*. Therefore, the quarks and gluons carrying a color charge cannot exist as free particles. The value $\Lambda_{\mathrm{QCD}} \approx 200$ MeV is usually referred to as the cut-off scale of the perturbative description of QCD. The measured values of α_S are shown in Figure 2.2 for different energy scales. The agreement between the theory prediction and the observed value persists up to the highest available measured scales in the TeV range.

At lower energies the perturbative description of QCD is no longer valid. In that regime numerical descriptions like *lattice* QCD or phenomenological models describing the *hadronization* become relevant. The QCD concepts used at a hadron collider to derive meaningful observables from the QCD Lagrangian are outlined in Chapter 2.2.

2.2. Hadron collider physics

The calculation of a physical observable like the cross section of a certain process at a hadron collider strongly relies on several concepts. *Factorization* separates the hard high-energy interaction from the soft low-energy interactions. At high enough energies the strong coupling α_s is small enough to calculate the hard process perturbatively. The *fragmentation* describing the transformation of the partons into hadrons is in turn based on phenomenological models.

Considering the cross section σ of a proton-proton collision with final state X the factorization theorem allows one to separate σ in a perturbative and a non-perturbative part. The probability to find a parton i with momentum fraction x inside the proton is quantified by the parton distribution function (PDF) $f_i(x)$. The PDFs describe the non-perturbative component. The cross section of the hard

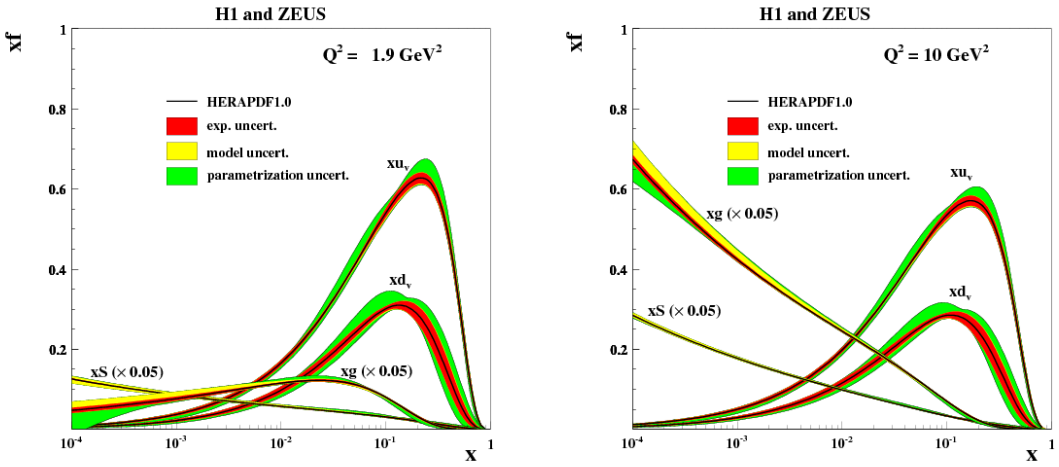

(a) (b)

Figure 2.3.: PDF measurements from HERAPDF at $Q^2 = 1.9$ GeV and $Q^2 = 10$ GeV. The gluon and sea distributions are scaled down. From Reference [28]

process is given by $\hat{\sigma}$.

$$\sigma = \int_0^1 dx_1 \int_0^1 dx_2 \sum_{ij} f_i(x_1, \mu_F) f_j(x_2, \mu_F) \hat{\sigma}_{ij}(x_1 x_2 s, \mu_R) \tag{2.2.1}$$

The factorization scale is given by μ_F and the renormalization scale by μ_R. The squared center of mass energy of the pp collision is denoted by s. It is not possible to calculate PDFs at arbitrary scales. Therefore, evolution functions extrapolate measurements at lower energies to higher scales which are relevant at high energy colliders. The extrapolation is obtained through the Dokshitzer-Gribov-Lipatov-Altarelli-Parisi (DGLAP) [25–27] equations. Measurements of PDFs are shown in Figure 2.3 for different energy scales Q^2. At low x values the gluons dominate whereas at higher x values the u and d valence quarks significantly contribute for $Q^2 = 10$ GeV^2.

2.2.1. Proton-proton collisions and Monte Carlo

The partonic cross-section $\hat{\sigma}_{ij}(x_1 x_2 s, \mu_R)$ can be calculated up to a given order in α_s. Dealing with ultraviolet divergences motivates the introduction of the renormalization scale. Physical observables are generally independent of the factorization or renormalization scales whereas theoretical calculations can preserve a dependence on these scales. It is expected that such scale dependence are reduced by going to calculations at higher order. A typical proton-proton collision event has to describe several processes in addition to the hard scattering as illustrated in Figure 2.4.

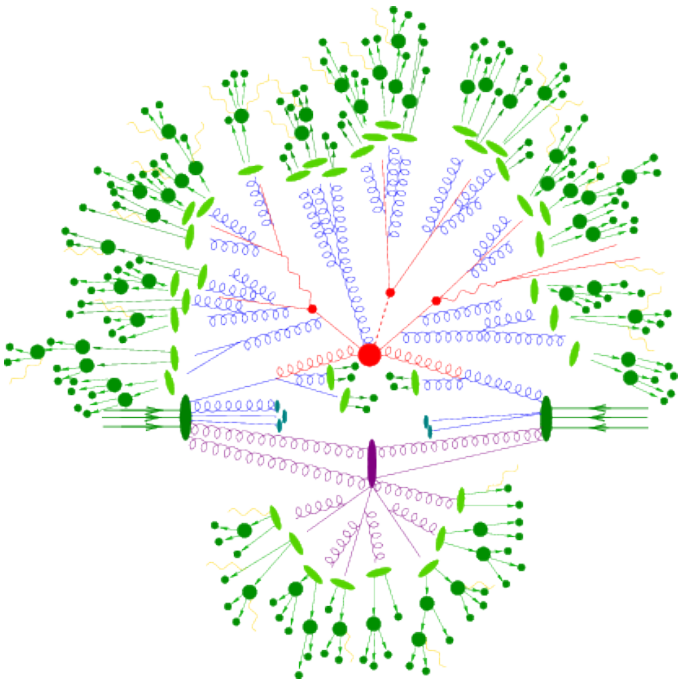

Figure 2.4.: Schematic description of a proton-proton collision event. Taken from Reference [29].

The incoming partons as well as the final state partons produced in the hard scattering undergo a successive radiation emission or splitting in other partons. This can result in large corrections from soft or collinear splittings in the final state which are normally canceled by the virtual correction at each order in perturbation theory. This is further discussed in the context of *infrared safety* in Chapter 2.2.3. The so-called Matrix Element Monte Carlos are used for the fixed-order predictions. Several examples of such Monte Carlo generators which are used in this thesis are outlined in Chapter 3.3. The Monte Carlo parton-shower programs provide a powerful predictive method describing the series of emission and splitting of the hard partons. In the soft and collinear limit one can calculate the probability of not radiating a gluon above a certain transverse momentum scale k_T up to the first order in α_s. The prediction of this probability can be extended to higher order by taking the exponential of it. This quantity is referred to as the Sudakov form factor $\Delta(Q, k_T)$. Monte Carlo methods can be exploited to derive the transverse momentum distribution of the parton with the largest expected transverse momentum in an event

$$\frac{dP}{dk_T} = \frac{d}{dk_T}\Delta(k_T, Q) \tag{2.2.2}$$

Starting from a uniform random number $r \in [0, 1]$ the transverse momentum is inferred solving $\Delta(k_T, Q) = r$. This formalism can be applied iteratively to all partons until they reach a non-perturbative cut-off scale typically around $\approx \Lambda_{\mathrm{QCD}}$

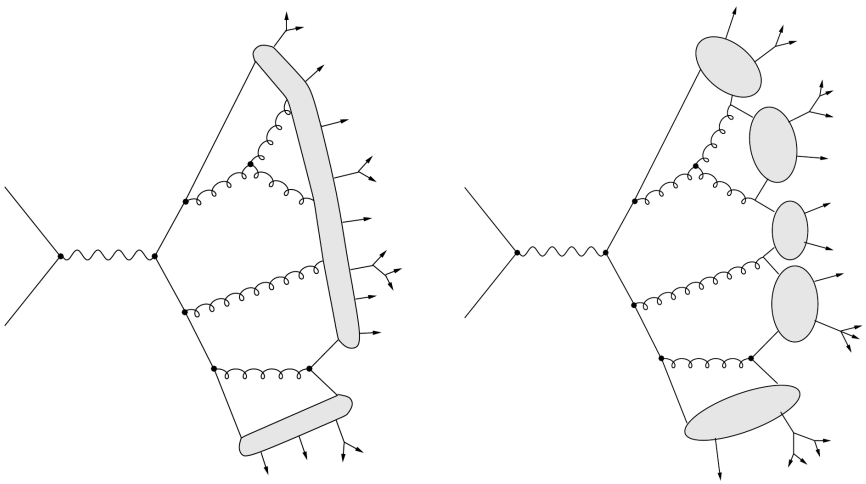

Figure 2.5.: Schematic description of different fragmentation models. The string (left) and cluster (right) fragmentation are shown. Taken from Reference [31].

where the hadronization process starts. The hadronization describes the transition from the final state particles after the parton shower into colorless hadrons. Besides the final state radiation (FSR) and the initial state radiation (ISR) also the particles accompanying the hard interaction have to be considered. The hadronic activity related to the later one is referred to as underlying event (UE). The beam-beam remnants (BBR) as well as the multi-parton interactions (MPI) contribute to it. The underlying event is typically modeled by simulating additional scattering at scales of a few GeV [30].

The hadronization is described by non-perturbative phenomenological models. The string model [32] and the cluster model [33] are the most prominent ones and illustrated in Figure 2.5. In the string model a color string is stretched across quarks and gluons. The color string is broken into hadrons as the energy potential between the quarks grows to the order of the hadron masses. In the cluster model each gluon is split into a quark-antiquark pair. Out of these quarks the colorless clusters are constructed. The heaviest clusters can further decay into lighter clusters. Eventually these clusters constitute the hadrons. The non-perturbative parameters involved in the transition from the parton shower to hadronization and in the hadronization process itself are usually tuned to data.

2.2.2. Hadron collider kinematics

The quantities used to describe the kinematics at a hadron collider are introduced in this chapter. A typical choice of coordinates consists of assigning the z-axis along the beam pipe. The origin is at the center of the detector and corresponds to the nominal interaction point. The x-axis points from the center of the collider ring and the y-axis is chosen to point upwards. The kinematics in the plane transverse

to the beam axis can be described by the azimuthal angle around the z-axis ϕ and the transverse momentum $p_T = \sqrt{p_x^2 + p_y^2}$. The rapidity y and the pseudo-rapidity η are the preferred variables to quantify the other direction. The rapidity and the pseudo-rapidity are defined as

$$y = \tanh^{-1} \frac{p_z}{E} = \frac{1}{2} \ln \frac{E + p_z}{E - p_z} \tag{2.2.3}$$

$$\eta = \tanh^{-1} \frac{p_z}{|\vec{p}|} = -\ln \left(\tan \frac{\Theta}{2} \right) \tag{2.2.4}$$

where the pseudo-rapidity can be linked to the polar angle Θ. For massless particles the pseudo-rapidity is identical to the rapidity. The two variables have the advantage that differences in η or y are invariant under Lorentz boosts in the z-direction. The angular distance between two objects is generally described in η-ϕ space by ΔR

$$\Delta R = \sqrt{(\Delta\phi)^2 + (\Delta\eta)^2} \ . \tag{2.2.5}$$

In some cases the difference ΔR_y in the true rapidity y-ϕ space is used instead

$$\Delta R_y = \sqrt{(\Delta\phi)^2 + (\Delta y)^2} \ . \tag{2.2.6}$$

This is especially relevant for massive jets and in the context of the overlap removal procedures as explained in Chapter 3.4.8.

2.2.3. Jet clustering

The freely existing particles in QCD are color neutral. But generally it is often necessary to infer information about the hard-scatter partons such as quarks and gluons that are colored particles. After hadronization and fragmentation the color-neutral, stable or unstable hadrons are formed. Experimentally these particles are observed in the detector by their produced energy deposits and tracks. Jet reconstruction algorithms exploit the fact that hadrons origination from a hard-scatter particle appear collimated and localized in space. The probability that a quark emits a gluon can be described by the following integral [30]

$$\propto \int \alpha_s \frac{dE}{E} \frac{d\Theta}{\Theta} \tag{2.2.7}$$

The angle between the quark and the gluon is given by Θ and the gluon energy by E. In the perturbative limit the value of α_s should be a small number. Nevertheless the probability can become large for small angle radiation when the emitted gluon tends to be aligned with the quark or for soft gluons with a small energy. The fragmentation and hadronization is typically described by parton shower programs like Pythia or Sherpa. All of them are characterized by some form of locality.

As a consequence partons result in a collimated spray of hadrons which can be observed at the LHC in terms of jets. The basics of the reconstruction of jets is outlined in this chapter.

The input objects to the jet reconstruction e.g. topological clusters in the ATLAS detector or simulated partons or hadrons are denoted as particles in the following description. The jet algorithms aims at constructing a jet object that can than ideally be associated to the initial parton. Consequently, jets are no fundamental objects and the properties of the jet object depends on the chosen jet algorithm. Several criteria characterize the construction of an *optimal* jet algorithm. According to Reference [34] that includes a fully specified algorithm that is theoretically well behaved. Especially the algorithm should respect the concepts of infrared and collinear safety. In these concepts the procedure of the grouping of the particles should not depend on soft gluon radiation from a parton or on collinear parton splitting. Furthermore, the jet algorithm should at least approximately show detector independence on e.g. the cell type and numbers as well as independence on the order. The last point is satisfied for algorithms behaving equally on parton, hadron-particle and detector level.

The sequential recombination algorithms provide a class of algorithms addressing the above mentioned points. They are the default jet algorithms in the ATLAS and CMS experiments [15, 35]. The sequential recombination algorithms are designed as a two to one clustering taking all particles as a starting point and than sequentially combine pairs of two neighboring objects according to two distance measures d_{ij} and d_{iB}. The d_{ij} describes the distance between two particles whereas the d_{iB} is identified as the distance to the beam.

$$d_{ij} = \min(p_{Ti}^{2n}, p_{Tj}^{2n}) \frac{\Delta R_{ij}}{R} \tag{2.2.8}$$

$$d_{iB} = p_{Ti}^{2n} \tag{2.2.9}$$

Here R denotes the so called *jet parameter*. It is optimized for the relevant application. The geometrical distance of two objects in the $y - \phi$ plane $\Delta R_{ij} = \sqrt{\Delta\phi_{ij}^2 + \Delta y_{ij}^2}$ and the transverse momentum of an object p_{Ti} control the merging sequence. The integer n defines whether the Anti-k_T ($n = -1$), the Cambridge/Aachen ($n = 0$) or the k_T ($n = 1$) algorithm is considered. Two objects are combined by adding their four-momenta. This procedure is referred to as *E-scheme* [35]. For all combinations of two objects i and j the smallest distance d_{ij} or the beam distance d_{iB} is determined. If the smallest beam distance d_{iB} is less than the smallest d_{ij} the object is removed from the list of objects and labeled as a final jet. If in contrast the smallest d_{ij} is less than the smallest beam distance d_{iB} the two objects are combined. The procedure continues until all objects are assigned to jets.

The *jet parameter* R characterizes the minimal geometrical distance between the final jets. However, the jets constructed this way can have a quite irregular shape. The jet shape can be quantified in terms of the *jet area* [37] as implemented in

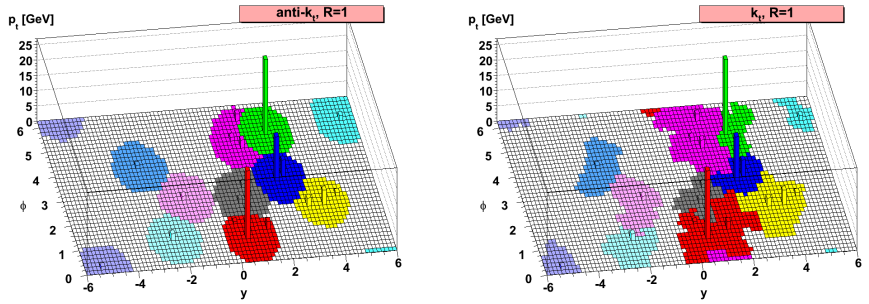

(a) anti $-$ k_T algorithm

(b) k_T algorithm

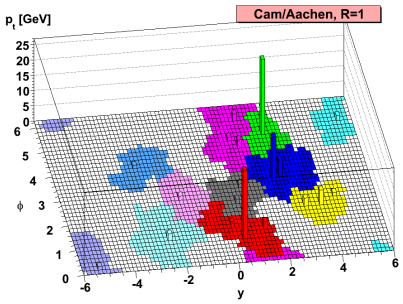

(c) Cambridge-Aachen algorithm

Figure 2.6.: Comparison of the active area of several jet reconstruction algorithms with radius parameter $R = 1$. Each color corresponds to a jets. An event with soft *ghost* particles is overlaid in order to highlight the boundaries of the jets. Taken from Reference [36].

FastJet [38, 39]. The *jet area* can help to highlight the boundaries of the jets as shown in Figure 2.6. A uniform and dense distribution of soft particles referred to as *ghosts* is overlaid and included in the jet clustering. The parameters of the *ghosts* are chosen in order to keep the properties of the final jets unaffected. Anti-k_T jets are more circular shaped. In the Anti-k_T algorithm hard objects tend to be clustered first. Thus, the hard jets in an event are insensitive to soft radiation around the boundaries and they form a circular shape with an area close to πR^2 [40]. However, non-isolated and soft jets in an event are characterized by a more irregular and often crescent shape. On the other hand the k_T algorithms favors the clustering of soft objects first whereas the Cambridge/Aachen algorithm emphasizes the minimal geometrical distance. The relatively circular shape and the linear dependence on soft particles of the Anti-k_T algorithm are advantageous for the experimental calibration of the jets as explained in Chapter 3.4.5.

The optimal choice of the *jet parameter* R depends on the topology and the nature of the considered hard-scatter partons [15]. In scenarios where an identification of the hard-scatter partons with the jets is favored a *small* radius parameter of around 0.4 is typically chosen. Such a case is denoted as a *resolved* setup. Simulated $t\bar{t}$ events reconstructed with different choices of the *jet parameter* R are illustrated in Figure 2.7.

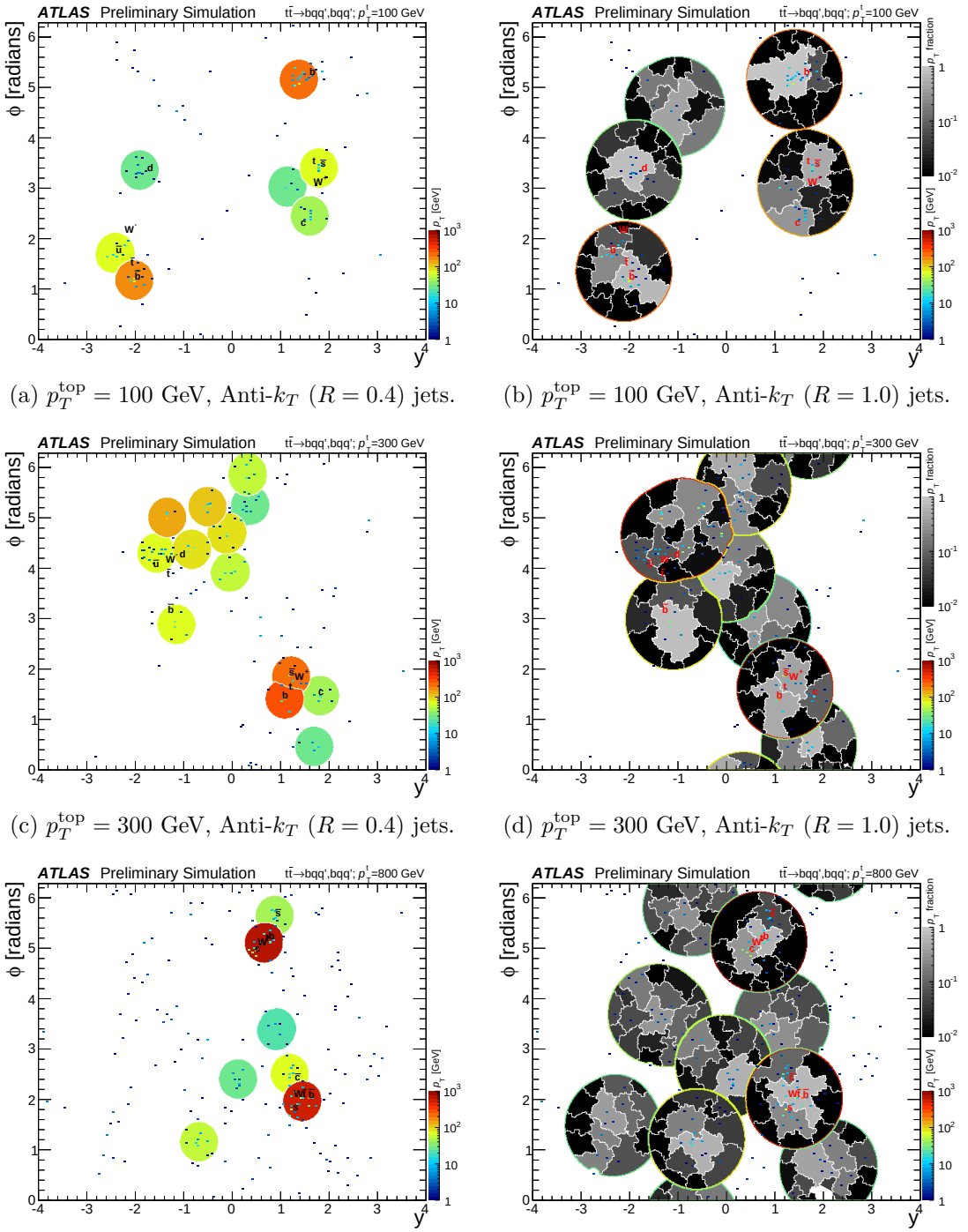

(a) $p_T^{\text{top}} = 100$ GeV, Anti-k_T ($R = 0.4$) jets.

(b) $p_T^{\text{top}} = 100$ GeV, Anti-k_T ($R = 1.0$) jets.

(c) $p_T^{\text{top}} = 300$ GeV, Anti-k_T ($R = 0.4$) jets.

(d) $p_T^{\text{top}} = 300$ GeV, Anti-k_T ($R = 1.0$) jets.

(e) $p_T^{\text{top}} = 800$ GeV, Anti-k_T ($R = 0.4$) jets.

(f) $p_T^{\text{top}} = 800$ GeV, Anti-k_T ($R = 1.0$) jets.

Figure 2.7.: Event displays for simulated $t\bar{t}$ events reconstructed with different jet reconstruction algorithms in ATLAS. The event is shown for different transverse momenta of the top quarks and omitting jets with $p_T < 25$ GeV. The top quarks are generated with increasing transverse momentum of $p_T = 100, 300, 800$ GeV from top to bottom. The jets are build from the Anti-k_T ($R = 0.4$) (left) and Anti-k_T ($R = 1.0$) (right) algorithm. Taken from Reference [41].

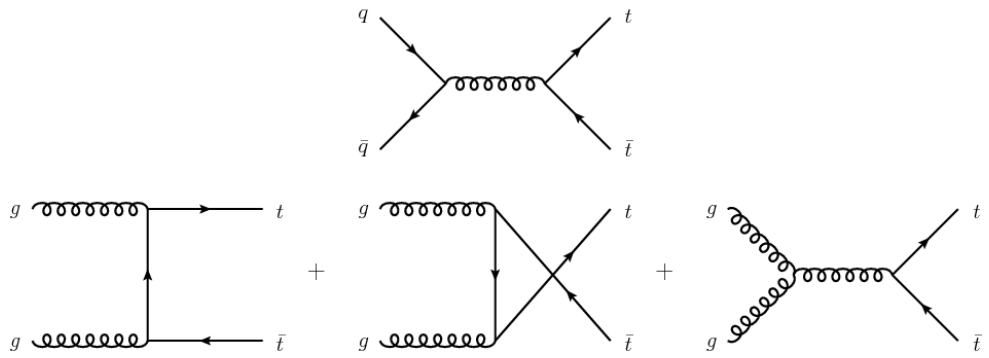

Figure 2.8.: Leading order Feynman Diagrams for $t\bar{t}$ production, from [42].

2.3. Top quark physics

Reviews of top quark physics are given in Reference [44, 45] on which this Chapter is partially based on. The top quark is the heaviest known quark with a mass at the electroweak scale measured for the first time at the Tevatron. The average mass based on Tevatron and LHC measurements is given by

$$m_t = 173.34 \pm 0.27(\text{stat}) \pm 0.71(\text{syst}) \quad \text{GeV} \quad [46]. \tag{2.3.1}$$

The relatively high mass compared to other SM quarks characterizes the phenomenology of the top quark. Specifically, a large center of mass energy is required to produce a $t\bar{t}$ pair at rest. The momentum fraction x_i of the partons in the hard process must be larger than

$$\sqrt{x_i x_j} \geq \frac{2m_t}{\sqrt{s}} \tag{2.3.2}$$

Assuming $x = x_i \approx x_j$ this results in $x \approx 0.03$ at $\sqrt{s} = 13$ TeV. At the LHC which is a proton-proton collider top quark pairs are therefore predominantly produced in gluon fusion with a fraction of around 80% (90%) at $\sqrt{s} = 7(14)$ TeV [45]. The additional $t\bar{t}$ events are mainly induced by the $q\bar{q}$ initial state. Typical Feynman diagrams describing the $t\bar{t}$ production at leading order in QCD are shown in Figure 2.8. At a hadron collider the top quark is predominantly produced in pairs. The production cross-section of single top quarks which involves the electroweak interaction and requires a bottom quark in the initial state is almost one order of magnitude smaller than the top quark pair production. Studying the top quark at the LHC is particularly interesting due the large number of events produced. As a reference, there were around 30 million top quark pair events in the 2015 and 2016 data. The cross-section of the SM $t\bar{t}$ process increases with the center of mass energy which is well described by theory predictions at NNLO+NNLL order as shown in Figure 2.9 for several Tevatron, ATLAS and CMS measurements.

Even though the top quark is produced abundantly it has to compete with many

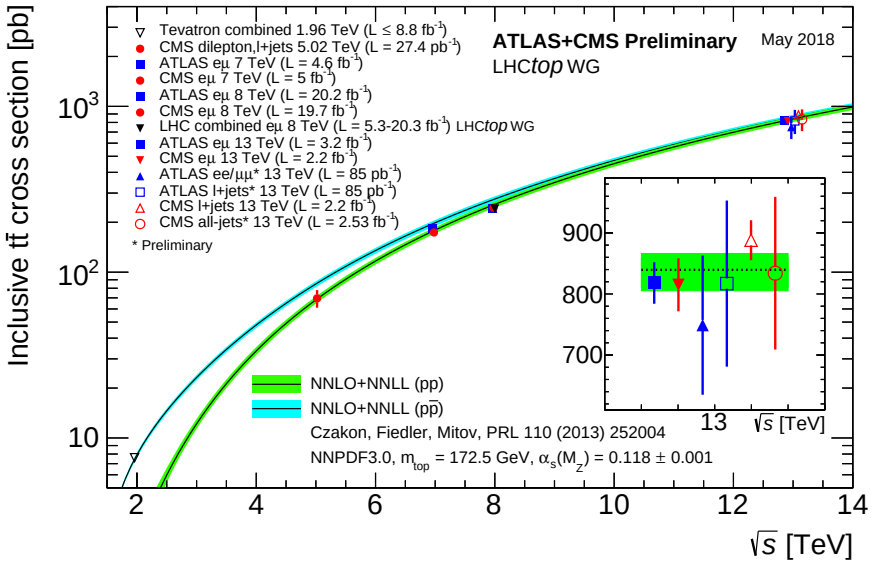

Figure 2.9.: The $t\bar{t}$ production cross-section as a function of the center of mass energy. Several measurements at the Tevatron and the LHC are compared to theory predictions. From Reference [43]

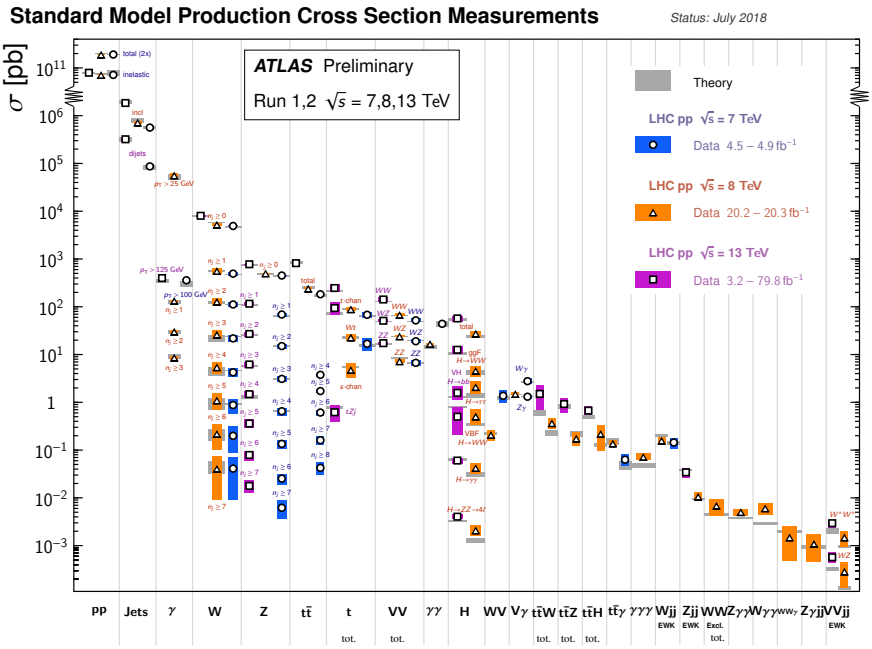

Figure 2.10.: Comparison of SM total and fiducial production cross section measurements with the theory predictions. From Reference [47]

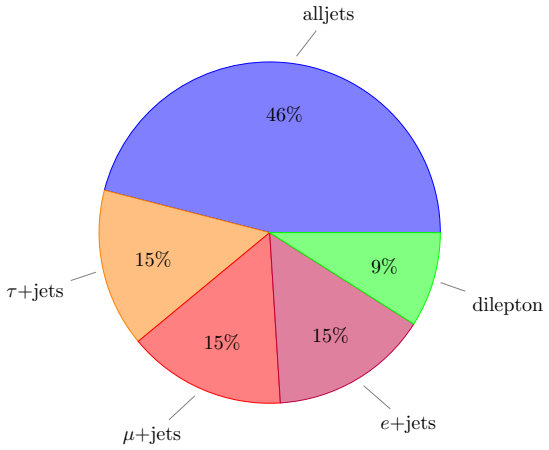

Figure 2.11.: Illustration and branching ratios of different decay modes of the $t\bar{t}$ system.

other processes at a proton-proton collider. Typical cross-sections of SM processes are presented in Figure 2.10. The SM multijet production [48] is among the largest background processes. Even the W boson production cross-section of approximately 10^4 pb is still more than one order of magnitude larger than the inclusive $t\bar{t}$ cross section of approximately 830 pb at $\sqrt{s} = 13$ TeV.

Besides the relatively large mass of the top quark, the top quark phenomenology is driven by the width of the top quark $\Gamma = 1.41^{+0.19}_{-0.15}$ GeV [24]. The size of the width allows that it decays before hadronization which is characterized by the scale $\Lambda_{\mathrm{QCD}} \approx 200$ MeV. This unique property distinguishes the top quark from other quarks. Thus, by studying its decay products it is possible to infer the properties of the top quark. Due to the CKM-matrix element V_{tb} being close to unity it nearly uniquely decays into a W boson and a bottom quark. The W boson can decay leptonically or hadronically resulting in three different decay channels for a top quark pair. At leading order 2/3 of the W decays are hadronic. At next-to-leading order the branching ratio for one flavor $\mathrm{BR}(W \to l\nu) = 0.108$ is used. Hence, the "all-jets", "allhadronic" or "fully hadronic" channel has the largest branching fraction for top quark pairs with approximately 46%, see Figure 2.11. The single lepton channel has a BR of 44% whereas the dileptonic channel has a BR of 11%.

The top quark also provides the largest Yukawa coupling to the Higgs boson. This large coupling to the Higgs boson makes the top quark an important tool for studying electroweak symmetry breaking. Top quark pairs can be a large background or signal in phenomena beyond the standard model. Therefore, the understanding and reconstruction of the top quark plays a crucial role in corresponding searches.

2.4. Beyond the Standard Model physics

All predicted particles and interactions of the SM which are experimentally accessible have been observed. Despite the successful description of many processes as measured e.g. at the LHC there still remain some open questions in the SM. Even though there exists no experimental evidence which strictly contradicts the SM, there are some theoretical and experimental limitations which are presented in the following.

To begin with the SM does not include a description of the gravitational force. But at energies of the Planck scale $\approx 10^{19}$ GeV gravitational forces cannot be ignored in a fundamental quantum field theory. Therefore, the SM is often considered an effective theory which is only valid at energies well below the Planck scale.

The fine-tuning of radiative corrections to the Higgs mass is expected to be strongly related to the top quark. As outlined in Chapter 2.1.1 the Higgs boson is a massive scalar particle. Such a scalar particle is not protected by the custodial symmetry. In contrast, the fermion sector has a $U(1)_L \times U(1)_R$ chiral symmetry which forbids an explicit mass term like $m\overline{\Psi}\Psi$. This is not the case for the Higgs boson which receives the largest radiative corrections by the processes shown in Figure 2.1. The corrections arise from top quark, $SU(2)$ gauge boson loops as well as the Higgs self coupling. Following the numerical example given in Reference [49] the corrections at an assumed cut off scale $\Lambda = 10$ TeV are given by

$$\Delta m_H = -\underbrace{\frac{3}{8\pi^2}\lambda_t^2\Lambda^2}_{\text{top quark loop}} + \underbrace{\frac{9}{64\pi^2}g^2\Lambda^2}_{SU(2)\text{ gauge boson loop}} + \underbrace{\frac{1}{16\pi^2}\lambda^2\Lambda^2}_{\text{Higgs self coupling}} \tag{2.4.1}$$

$$\approx -(2\text{TeV})^2 + (700\text{GeV})^2 + (500\text{GeV})^2 \tag{2.4.2}$$

The numbers can be transferred into a correction Δm_H of the bare Higgs mass m_0. Therefore, at energies around the center of mass energy of the LHC (≈ 10 TeV) the correction to the observed mass m_{obs} is given by

$$m_{\text{obs}}^2 = m_0^2 + \Delta m_H^2 \tag{2.4.3}$$

$$\approx m_0^2 - 209 m_{\text{obs}}^2 \tag{2.4.4}$$

$$\Rightarrow \frac{m_0}{\Delta m_H} \approx \frac{\sqrt{210}}{\sqrt{209}} \approx 1.002 \tag{2.4.5}$$

So already at typical LHC energies a significant level of fine-tuning ($\approx 0.2\%$) would be expected. The top quark which has the largest Yukawa coupling of the SM fermions should play an important role in the fine tuning problem. Prominent examples of theories dealing with the fine-tuning are Supersymmetry [50] or Little Higgs models [49]. In Supersymmetry the partner particles contribute to the loops leading to a cancellation between the contributions. Little Higgs theories describe the Higgs boson as a pseudo-Nambu-Goldstone boson connected to a global symmetry which is broken at higher energies.

The SM is also fine-tuned in another aspect of QCD. The QCD symmetry group allows a CP violating term in the Lagrangian quantified by the phase Θ

$$\mathcal{L}_\Theta = \Theta \frac{g^2}{32\pi^2} G_a^{\mu\nu} \tilde{G}^a_{\mu\nu}. \tag{2.4.6}$$

The strong CP problem [51] is related to the observation that the CP violating phase Θ in the QCD Lagrangian is small $< 10^{-9}$. Even though there is no mechanism in the SM which would explain why it significantly deviates from a value of $\mathcal{O}(1)$.

Furthermore, the amount of free parameters in the SM which has to be determined experimentally serves as a motivation for many models of phenomena beyond the SM. The SM is described by 18 parameters including the nine fermion masses, the four parameters of the CKM matrix and the couplings and the parameters of the scalar sector. Out of these there is only one non-dimensionless parameter $v_0 = 246$ GeV characterizing the corresponding electroweak scale. The observation of neutrino oscillations implies that neutrinos are massive as well. Further parameters are introduced by describing these masses and the associated mixing of neutrinos. In addition the parameters have certain unexplained patterns like comparable mass scales for fermions in the same flavor generation. The matrices describing the mass mixing of quarks or neutrinos also indicate an underlying structure. For the former one it is close to a diagonal matrix whereas the PMNS matrix in the neutrino case has sizable off-diagonal terms.

Among the experimental short comings there is also the anomalous magnetic moment of the muon. It is possible to theoretically predict it at a high precision. The measured value significantly deviates from that prediction.

Cosmological and astrophysical observations suggest the existence of dark matter (DM) and dark energy. The term *dark* highlights the non-absorbing and non-luminous nature of the matter. These observations include amongst others gravitational effects on luminous objects, baryonic acoustic oscillations, the large scale structure formation and the dynamics of the Bullet Cluster. Measurements of anisotropies in the cosmic microwave background by the Planck satellite [52] and of the spatial distribution of galaxies determine the relic density of baryonic matter

$$\Omega_\mathrm{b} h^2 = 0.02226 \pm 0.00023 \quad [24] \tag{2.4.7}$$

and of non-baryonic cold matter

$$\Omega_\mathrm{nbm} h^2 = 0.1186 \pm 0.0020 \quad [24] \tag{2.4.8}$$

which exceeds the former one by over a factor 5. Therefore, dark matter is expected to be the dominant matter contribution in the universe. The observations indicate that dark matter interacts gravitationally and is composed of massive stable particles. It does not participate in electromagnetic interactions and also strong interactions are unlikely. On the other hand it is supposed to interact weakly either via the SM weak force or via another force which is probably even weaker than

the SM force. This motivates searches for dark matter assuming a Weakly Interacting Massive Particle (WIMP) as the dark matter candidate. The cosmological standard model (ΛCDM)[52] with $\Omega_{\mathrm{m}} \approx 0.3$, $\Omega_{\Lambda} \approx 0.7$ and $\Omega_{\mathrm{tot}} \approx 1$ introduces the dark energy component associated to the cosmological constant Λ. The last relation implies an almost flat universe and that all cosmological constituents sum up to the critical density. Hence, the cosmological constant is the dominant component with around 70% of the energy density of the universe and the driving force of the accelerated expansion of the universe as observed e.g. in supernovae of type Ia measurements. The SM offers no direct explanation for neither dark matter nor the dark energy.

The problems of the SM are addressed by extensions addressing single or several of the above mentioned aspects. Such extensions are commonly referred to as Beyond Standard Model (BSM) theories. In the following three extensions are discussed where the reconstruction of SM top quarks is expected to be an important discovery tool.

The three following BSM theories are particularity relevant for $t\bar{t}$ resonance searches and therefore outlined in more detail. The Topcolor assisted technicolor model and simplified dark matter models with massive mediators decaying to $t\bar{t}$ are discussed in the context of massive spin-1 resonances. The theory of Kaluza-Klein excitations and warped extra dimensions also offers candidates with a spin differing from 1. Only an overview of the essential concepts of the models related to the $t\bar{t}$ resonance search are highlighted. Further information on the models can be found in the related References.

2.4.1. Topcolor assisted technicolor

In this chapter, prototypes and specific implementations of theories of dynamical electroweak symmetry breaking are outlined. The description follows References [24, 53–56]. The symmetry breaking is generally achieved by the vacuum expectation value of a fermion condensate. The scale of the strong dynamics Λ, the modeling of the Higgs boson candidate and the related dimensional scale f assist to characterize the theories.

The technicolor mechanism [57, 58] provides a solution to the above mentioned Higgs mass fine tuning problem. It extends the symmetry group description and the particle content of the SM. An additional chiral symmetry $SU(2)_L \times SU(2)_R$ acting on a new type of fermions called *technifermions* is introduced. The theory is characterized by asymptotic freedom. At low energies the theory is confining and the *technifermions* generally form quark anti-quark condensates. The mass of the fermions is protected by a custodial symmetry. Therefore, in this theory there is no need for a mass fine tuning of the non-fundamental Higgs. Technicolor models are heavily constrained by the observation of the light SM Higgs boson and its measured couplings.

Top color [54] and topcolor assisted technicolor (TC2) [55] emphasize the special role of the top quark in EWSB with a mass at the same order as the electroweak

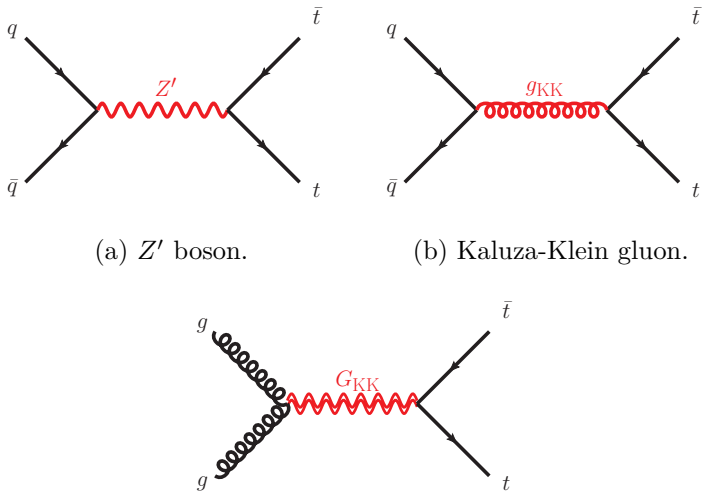

(a) Z' boson.

(b) Kaluza-Klein gluon.

(c) Kaluza-Klein graviton.

Figure 2.12.: Collection of Feynman diagrams representing different classes of signal models for $t\bar{t}$ resonances X. The leading order production process for $pp \to X \to t\bar{t}$ is shown. Taken from Reference [59]

scale ($v \approx 246$ GeV). In such theories a large dynamical scale is assumed ($\Lambda > 1$ TeV, $v/f < 1$). A new color gauge sector $SU(3)_1 \times SU(3)_2$ is present. The quark generations are differently charged under that symmetry. The breaking of the new gauge group to the SM $SU(3)_C$ results in a set of massive color-octet vector bosons. These bosons called *topgluons* couple mainly to $t\bar{t}$ and $b\bar{b}$. In addition a $U(1)_1 \times U(1)_2$ interaction is introduced providing a mechanism to mitigate the degeneracy between top quarks and bottom quarks. The topcolor Z' arises from that extra $U(1)$ symmetry. Specific implementations like e.g. *Model IV* in Reference [56] which is used as a benchmark in this thesis typically predict narrow width resonances. A representative Feynman diagram for the leading-order production is shown in Figure 2.12(a). The benchmark model predicts a leptophobic Z' with vector-like interactions. The strong coupling between the Z' and the quarks exists only for the first and the third generation. The principal part of the Lagrangian is given by

$$\begin{aligned}\mathcal{L}_{Z'} =&(\frac{1}{2}g_1 \cot\Theta_H)Z'^{\mu}_t(\bar{t}_L\gamma_\mu t_L + \bar{b}_L\gamma_\mu b_L + f_1\bar{t}_R\gamma_\mu t_R + f_2\bar{b}_R\gamma_\mu b_R \\ &- \overline{u}_L\gamma_\mu u_L - \overline{d}_L\gamma_\mu d_L - f_1\overline{u}_R\gamma_\mu u_R - f_2\overline{d}_R\gamma_\mu d_R)\end{aligned} \tag{2.4.9}$$

The suppression of $b\bar{b}$ over the $t\bar{t}$ channel is achieved by the choice of the parameters with $f_1 = 1$ and $f_2 = 0$. The parameter $\cot\Theta_H$ is adjusted for each mass point in order to get a width over mass ration of $\Gamma/m = 1.2\%$ [60]. The $Z' \to t\bar{t}$ branching ratio reaches 33% for high signal masses with $m_{Z'} \gg m_{\mathrm{top}}$.

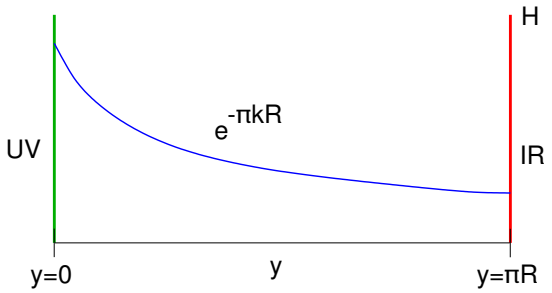

Figure 2.13.: Illustration of the spacetime in Randall-Sundrum types of models. The two four dimensional branes have different coordinates in the fifth dimension described by the coordinate y. The mass of the particles on the infrared brane are suppressed with respect to their mass on the ultraviolet brane which is quantified by the *warp factor* $\exp(-\pi kR)$. Taken from Reference [15].

2.4.2. Warped extra dimensions

Extra dimensions are predicted in many BSM theories e.g. in string models [61]. In the simplest case there is a single extra dimension with radius R. Candidates of spin-1 and spin-2 resonances can be constructed in theories involving warped extra dimensions like in the Randall-Sundrum (RS) model [62, 63]. Detailed overviews are given in e.g. the References [24, 64] on which this summary is based on. The extra dimension is denoted by the coordinate y. The *bulk* is the space between the four-dimensional branes at $y = 0$ (ultraviolet brane) and at $y = \pi R$ (infrared brane). The *warp factor* $\exp(-\pi kR)$ causes a reduction of masses going from the ultraviolet brane to the infrared brane. The Higgs boson is located directly on the infrared brane and the other SM particles are close to it. A schematic overview of the structure is shown in Figure 2.13. States that can propagate in the bulk imply the existence of Kaluza-Klein (KK) excitations of SM particles [65, 66]. In that description the $n = 0$ mode corresponds to the SM particle. The masses of the infinite n excitation modes are proportional to n/R. For a complex scalar field the action would have the following form

$$S_5 = -\int \mathrm{d}^4x\mathrm{d}y M_5 \left(|\partial_\mu \phi|^2 + |\partial_y \phi^2| + \lambda_5 |\phi|^4\right) \tag{2.4.10}$$

Here the scale M_5 assures the correct mass dimension in 4 dimensions. In the RS model the extra dimension is described by a circle S^1 with the property that y can be identified with $-y$. For that scenario and assuming a cosmological constant Λ in the bulk and on the boundary branes (Λ_{UV}, Λ_{IR}) the following metric ds^2 provides

a solution to Einstein's equations

$$S_5 = -\int \mathrm{d}x^4 \mathrm{d}y \left(\sqrt{g} \left(\frac{1}{2} M_5^3 \mathcal{R} + \Lambda \right) + \sqrt{-g_{UV}} \delta(y) \Lambda_{UV} + \sqrt{-g_{IR}} \delta(y - \pi R) \Lambda_{IR} \right) \tag{2.4.11}$$

$$\Rightarrow \mathrm{d}s^2 = e^{-ky} \mathrm{d}x^\mu \mathrm{d}x^\nu \eta_{\mu\nu} + \mathrm{d}y^2 \tag{2.4.12}$$

where the relation $k = \sqrt{-\Lambda/6M_5^3}$ [24] is used. It illustrates the meaning of the *warp factor* which shifts four-dimensional scales depending on the position in the fifth dimension y.

The KK excitation of the gluon (g_{KK}) in the RS model [67, 68] is expected to have a relatively large production cross section at the LHC. The width over mass ratio tends to be large compared to the top-color assisted technicolor model with values ranging from $\Gamma_{g_{KK}}/m_{g_{Kk}} = 10\%$ to 40%. This spin-1 color-octet boson is mainly produced in $q\bar{q}$ annihilation as an s-channel resonance. A representative Feynman diagram for the leading-order production is shown in Figure 2.12(b). In the basic RS KK gluon model the branching ratio to top quark pairs is larger than 90%. Based on the SM gluon coupling g_s the model parameters are chosen such that the coupling g_q of the KK gluon to the light quarks fulfills $g_q = -0.2 g_s$. The KK gluon coupling with the left-handed top quarks is set to $g_L^t = g_s$ and the coupling with the right-handed top quarks g_R^t is adjusted in order to model the width.

The *Bulk* RS model [69, 70] is a modification of the original RS model. The Kaluza-Klein excitation of the Graviton G_{KK} is a candidate for a spin-2 color-singlet boson. It is primarily produced through gluon fusion. A representative Feynman diagram for the leading-order production in the $t\bar{t}$ channel is shown in Figure 2.12(c). The decay modes to the SM gauge bosons (W, Z), the Higgs boson as well as to the SM top quark are dominant. The model sets $k/\tilde{M}_{\mathrm{Pl}} = 1$ where $\tilde{M}_{\mathrm{Pl}}$ is the reduced Planck mass. The branching ratio of the $t\bar{t}$ channel depends on the mass of the KK Graviton reaching around 68% for masses larger than 1000 GeV. In the mass range from 400 GeV to 600 GeV the branching ratio changes from 18% to 50%. The KK Graviton can still be considered as a candidate with a relatively narrow width ranging from 3% at $m_{G_{KK}} = 500$ GeV to 6% at $m_{G_{KK}} = 3000$ GeV.

2.4.3. Dark matter

The Effective Field Theory (EFT) approach can be used to describe a large class of dark matter models in a rather agnostic way. The interaction between dark matter and the SM could be mediated by a TeV-scale particle making the EFT approach questionable at LHC energies. Simplified dark matter models [71, 72] provide a model framework to search for dark matter at a collider. Furthermore, they facilitate the comparison of indirect and direct DM detection methods. Different classes of simplified models can be constructed based on the spin of the mediator and the dark matter particle. In the following a s-channel resonance of a spin-1

Model	X	Spin	Color	Width [%]	$B(X \to t\bar{t})$ [%]
Topcolor assisted technicolor	Z'_{TC2}	1	singlet	1.2	10-33
RS KK gluon	g_{KK}	1	octet	10-40	93
Bulk RS KK Graviton	G_{KK}	2	singlet	3-6	18-68
Simplified DM	$Z'_{\chi,\mathrm{v}}$, $Z'_{\chi,\mathrm{a}}$	1	singlet	5.6	9

Table 2.2.: The considered benchmark signal models for the $t\bar{t}$ resonance search. All models predict a s-channel resonance. The branching ratios of the topcolor assisted technicolor and of the KK graviton model increase for higher masses.

mediator Z'_{χ} coupling to a Dirac dark matter particle χ and to SM fermions is discussed. Therefore, the DM model has similarities to the model presented in Chapter 2.4.1. The main difference arises in the predicted width of the mediator. The simplified model is not UV complete and no additional gauge symmetry is introduced to motivate the Z'_{χ}. Specifically a leptophobic dark matter mediator is considered. The mediator can have vector interactions ($Z'_{\chi,\mathrm{v}}$) or axial-vector interactions ($Z'_{\chi,\mathrm{a}}$). The models correspond to model A1 and V1 introduced in Reference [72]. The model is characterized by four free parameters. The coupling of the dark matter mediator to quarks is denoted as g_q, the coupling to dark matter as g_χ. In addition, there are the masses of the DM particle m_χ and the mass of the mediator. The following Lagrangians describe the relevant interactions for the axial and the axial-vector scenario

$$\mathcal{L}_{\text{vector}} = g_q \sum_{l \in \{\mathrm{u,\ d,\ c,\ s,\ t,\ b}\}} Z'_\mu \overline{q}_l \gamma^\mu q_l + g_\chi Z'_\mu \overline{\chi} \gamma^\mu \chi \tag{2.4.13}$$

$$\mathcal{L}_{\text{axial-vector}} = g_q \sum_{l \in \{\mathrm{u,\ d,\ c,\ s,\ t,\ b}\}} Z'_\mu \overline{q}_l \gamma^\mu \gamma^5 q_l + g_\chi Z'_\mu \overline{\chi} \gamma^\mu \gamma^5 \chi \tag{2.4.14}$$

A coupling to dark matter of $g_\chi = 1$ and a coupling to fermions with $g_q = 0.25$ is assumed. The mass of the DM particle is set to $m_\chi = 10$ GeV and the mass of the mediator is varied in the range around 500 GeV to 2000 GeV. At $m_{Z'_\chi} = 500$ GeV the width of the mediator particle is 5.3% of the mass due to kinematic restrictions. At higher masses the width reaches 5.6%.

The main characteristics of the presented models are summarized in Table 2.2. The specific models should highlight that studying massive resonance decaying to top-quark pairs is physically well motivated. Nevertheless, the particular implementations of models are mainly chosen as benchmarks to illustrate the sensitivity for different classes of resonances. Enough information is provided to transfer the results to other models predicting similar resonances.

2.5. Statistics

The statistical analysis of the data involves the construction of a suitable test statistic. The investigation of the test statistic allows one to make statements about the agreement with the background-only hypothesis or to determine exclusion limits.

2.5.1. Test of the SM-only hypothesis

The *BumpHunter* procedure [73] provides a test statistic for testing the SM-only hypothesis. It searches for excesses or deficits in the data. The *BumpHunter* procedure uses binned data as input. It calculates a Poisson probability $P(d_i, b_i)$ based on the data yield d_i and the background count b_i in each window i.

$$P(d_i, b_i) = \begin{cases} \Gamma(d_i, b_i) = \sum_{n=d_i}^{\infty} \frac{b_i^n}{n!} e^{-b_i}, & \text{if } d_i \geq b_i \\ 1 - \Gamma(d_i + 1, b_i), & \text{if } d_i < b_i \end{cases} \tag{2.5.1}$$

Here the smallest possible windows are given by the bin size. The expression is modified in order to account for the presence of systematic uncertainties Θ_i.

$$P(d_i, b_i) \to P(d_i, b_i + \lambda_i \Theta_i) e^{-\frac{\lambda^2}{2}} \tag{2.5.2}$$

where λ_i is a real number in a fixed interval maximizing

$$\frac{(b_i + \lambda_i \Theta_i)_i^d}{d_i!} e^{-(b_i + \lambda_i \Theta_i)} e^{-\frac{\lambda^2}{2}} \ . \tag{2.5.3}$$

Based on the probabilities the test statistic t is calculated in the following way

$$t = \begin{cases} 0, \text{if } d_i \leq b_i \\ -\log P_i^{\min}, \text{otherwise} \end{cases} \tag{2.5.4}$$

Ensemble tests are use to generate the distribution of the test statistics $f(t)$ and to compare it to the test statistic t_{obs} found in data.

$$p\text{-value} = \frac{\int_{t_{\text{obs}}}^{\infty} f(t)}{\int_0^{\infty} f(t)} \tag{2.5.5}$$

The *BumpHunter* procedure allows the calculation of local and global p-values as well as the corresponding significance. Even though the *BumpHunter* highlights the presence of localized deviations, the determined p-value accounts for the *look-elsewhere-effect* [73, 74].

2.5.2. Exclusion limits

A frequentist significance test based on a likelihood ratio as a test statistic can be used to set limits on the cross-section times branching ratio of processes involving new phenomena. The description below is based on [75]. The tested models often contain several unknown parameters besides the parameter of interest μ which could be e.g. the cross-section of a new process. The nuisance parameters Θ describe the uncertainties of physics quantities. The values of the nuisance parameters are inferred from data. This can be achieved by fits using the profile likelihood technique. In a binned scenario a global Likelihood is constructed taking all regions, bins and parameters of the model into account. Generally, a product of Poisson measurements and a probability density function for the systematics constitute the Likelihood function. For a model with an expected data yield D, an expected background yield b, a cross section $\sigma_{Z'}$ of the signal process with acceptance $a_{Z'}$ and parameter of interest μ the Likelihood has the following form

$$L(\mu, \Theta) = \prod_{i=0}^{\text{channels,bins}} \frac{e^{-\mu a_{Z',i}\sigma_{Z'}+b_i}(\mu a_{Z',i}\sigma_{Z'} + b_i)^{D_i}}{\Gamma(D_i + 1)} C(\Theta) \tag{2.5.6}$$

where the function $C(\Theta)$ describes the constraints on the nuisance parameters. The actual hypothesis test relies on the profile likelihood ratio test statistic Λ defined by

$$\Lambda(\mu) = \frac{L(\mu, \hat{\hat{\Theta}}(\mu))}{L(\hat{\mu}, \hat{\Theta})} \tag{2.5.7}$$

The double circumflex denotes the maximum likelihood estimate with a fixed value of μ. The single circumflex is used to denote the unconditional maximum likelihood estimate of a parameter. The asymptotic formulae for likelihood-based tests of new physics [76] indicate that for large enough samples the statistic $-2\ln(\Lambda(\mu))$ is distributed according to a χ^2 distribution with one degree of freedom. This avoids the computational expensive task of running ensemble tests. Eventually the Cl_s method [77, 78] can be used to set limits. The Cl_s limit is a conservative approximation to the frequentist exclusion limit.

3. Experimental setup

Theories of phenomena Beyond the Standard Model and the Standard Model itself can be investigated using particle accelerators at high energies. The foundations of the experimental facilities are outlined starting with a description of the Large Hadron Collider in Chapter 3.1. The ATLAS experiment is summarized in Chapter 3.2. The description is mostly based on the overview of the LHC machine [79] and the ATLAS experiment [80]. The event simulation is described in Chapter 3.3. The reconstruction and selection of physics objects and events in ATLAS is explained in Chapter 3.4.

3.1. Large Hadron Collider

The Large Hadron Collider [79, 81] (LHC) is a particle accelerator at the high energy frontier. The accelerator is installed at the European Organization for Nuclear Research (CERN[1]) near Geneva in the former tunnel of the Large Electron–Positron Collider (LEP). The circular structure of the LHC allows the collision of two counter-rotating beams of either protons or heavy ions. The LHC is designed to achieve a center-of-mass energies up to 14 TeV for proton beams and a luminosity of $10^{34}\text{cm}^{-2}\text{s}^{-1}$. Thereby it reaches unprecedented collision energies compared to previous particle accelerators making the LHC an excellent discovery machine. The discovery of the Higgs boson [8, 9] in 2012 proved the potential of the LHC. The LHC is installed underground in an around 100 m deep tunnel with a circumference of approximately 27 km. Over 1000 superconducting dipole magnets with a magnetic field up to 8.4 T bend the beams. Additional multipole magnets achieve the beam focusing.

Four large experiments are installed around the accelerator ring at separate interaction points as illustrated in Figure 3.1. The multi-purpose detectors ATLAS (A Toroidal LHC ApparatuS) [83] and CMS (Compact Muon Solenoid) [84] are optimized for measurements in the Higgs sector and searches for new physics. They are equally offering possibilities to perform measurements of the Standard Model and to study heavy ion physics. These physics goals are achieved by a precise tracking system, efficient muon detection systems and large-coverage calorimeters. The LHCb (Large Hadron Collider beauty) [85] experiment targets the flavor sector of the Standard Model. The decay products of B-hadrons have an enhanced production cross-section in the forward direction influencing the geometry of the LHCb spectrometer. The LHCb experiment is constructed as a one-sided forward

[1]Conseil Européen pour la Recherche Nucléaire

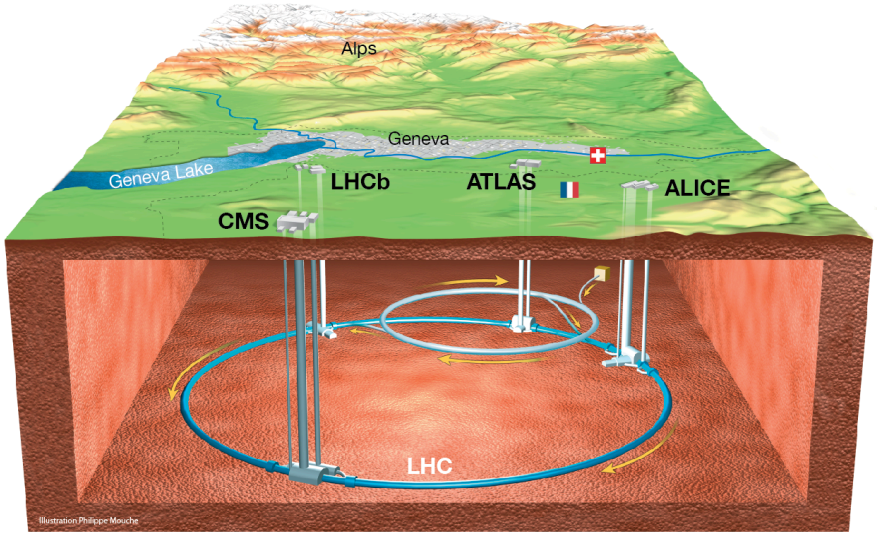

Figure 3.1.: Overview of the LHC accelerator ring and its interaction points. Taken from Reference [82].

detector. The LHCb physics program involves primarily the study of CP violation and tests of the SM. Studying heavy-ion collisions is the main focus of the ALICE (A Large Ion Collider Experiment) [86] experiment. It is designed to measure the quark gluon plasma [87]. The ALICE and the LHCb experiment generally run at reduced collision rates compared to the ATLAS and CMS experiment.

Before being injected in the LHC machine the particles undergo a complex acceleration scheme which is summarized in the following. For simplicity the description focuses on the acceleration of protons as they are used in the ATLAS experiment. The CERN facilities including the LHC and other experiments are sketched in Figure 3.2.

The proton beams provided by the CERN pre-acceleration structure have an energy of 450 GeV before they are injected in the LHC beam pipe. First, the proton production is accomplished by ionizing hydrogen atoms. The linear collider LINAC2 accelerates the protons up to 50 MeV. The Proton Synchrotron Booster (PSB) consists of four superimposed synchrotron rings which increase the energy of the protons from the LINAC2 up to 1.4 GeV before injecting them into the Proton Synchrotron (PS). The intermediate acceleration of the PSB improves the number of protons which can be accepted by the PS. The bending magnets in the pre-acceleration are operated at room temperature. The PS has a circumference of 628 m and accelerates the protons up to 25 GeV. Eventually the Super Proton Synchrotron (SPS) is the final pre-acceleration structure with an circumference of 7 km. The protons entering the LHC machine are grouped in spatial *bunches* of around 1.15×10^{11} protons.

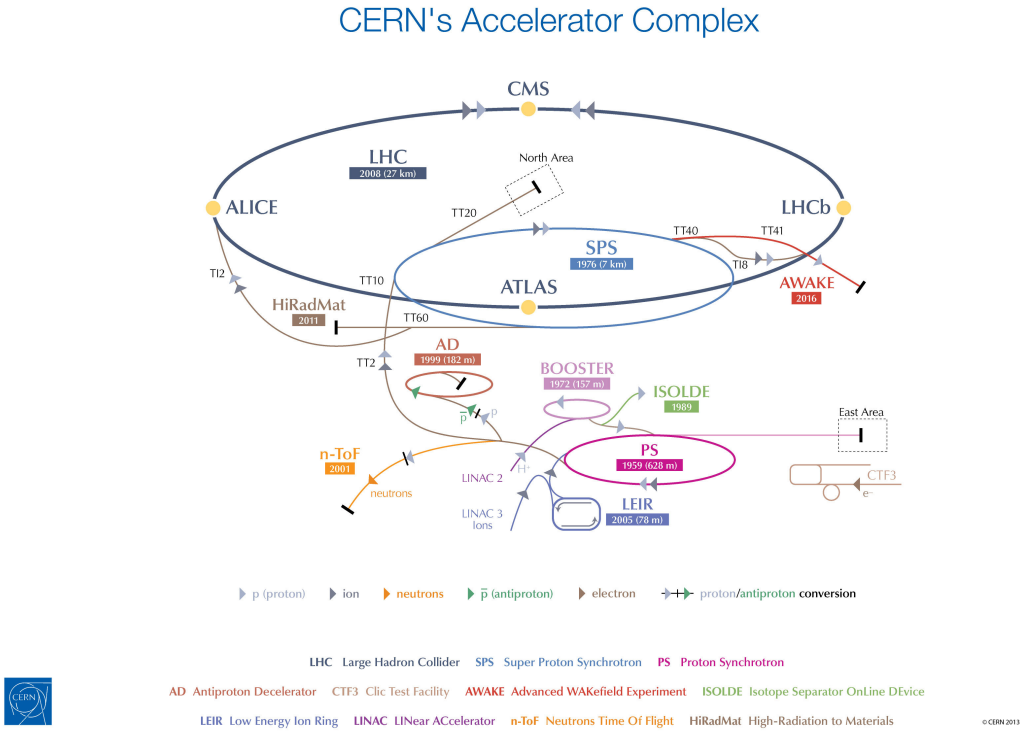

Figure 3.2.: Overview of the LHC accelerator complex within the CERN framework. Taken from Reference [88].

The acceleration process in the LHC during a *fill* achieves the final center-of-mass energies with 7 TeV in the 2011, 8 TeV in the 2012 and 13 TeV in the 2015/2016 data taking periods respectively. The 1232 superconducting dipole magnets of the LHC are cooled down to 1.8° K. They provide a magnetic field of 8.33 T and bend the beam on a circular path. The *bunch* structure allows the usage of radio frequency cavities for acceleration. The counter-rotating beams of protons circulate in two separate vacuum tubes. The *bunches* are separated by 25 ns for the 13 TeV data taking period. In addition 502 quadrupole magnets achieve a focusing of the beam in the straight sections of the accelerator ring. Thereby, the orbits are stabilized and the rate of proton-proton collisions can be increased.

Besides the center-of-mass energy the instantaneous luminosity L is an important parameter which defines the rate of a process with cross-section σ and N_{ev} produced events

$$\frac{dN_{\text{ev}}}{dt} = \sigma \times L \ . \tag{3.1.1}$$

The LHC is designed for a maximal instantaneous luminosity of about $10^{34}\text{cm}^{-2}\text{s}^{-1}$. The value of the instantaneous luminosity is determined by several beam parameters: The number of protons in each beam (n_1, n_2), the overlapping beam area A and the revolution frequency (f)

$$L = \frac{n_1 n_2}{A} f \ . \tag{3.1.2}$$

The beam overlap A for a Gaussian beam profile with root-mean-square of σ_x in the horizontal and σ_y in the vertical direction is given by

$$A = 4\pi\sigma_x\sigma_y. \tag{3.1.3}$$

The beam emittance ϵ and the β function define the beam size

$$\sigma^2 = \beta\epsilon. \tag{3.1.4}$$

Given the bunch structure of the beam it is convenient to express the numerator of L in terms of the number of protons in each bunch (N_p), the number of bunches per beam (k_b), the revolution frequency and the relativistic γ factor. A potential reduction of L due to an adjustable crossing angle is quantified by the factor F. The beam overlap in the denominator of L is expressed in terms of the normalized emittance ($\epsilon_n = \beta\gamma\epsilon$) and the β function at the interaction point $\beta^\star$. The $\beta^\star$ parameter is reduced from ≈ 80 cm in the 2015 to ≈ 40 cm in the 2016 data taking period [89], thus increasing L. Generally round beams are assumed in the following

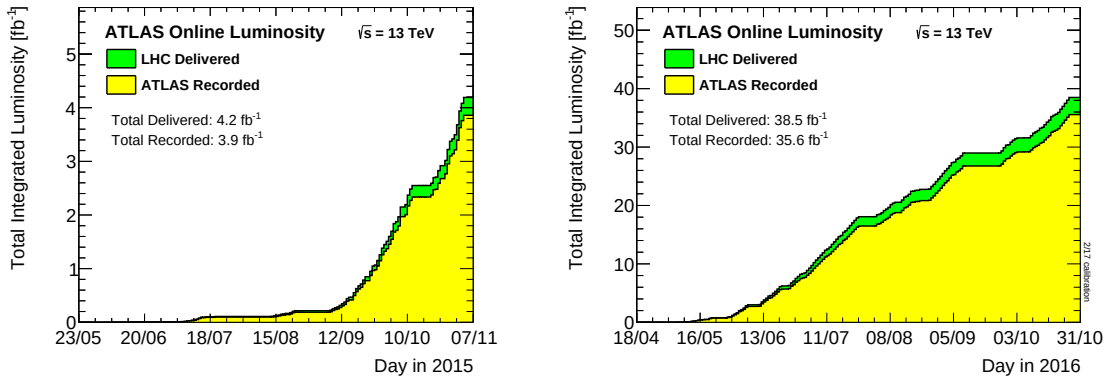

Figure 3.3.: Total integrated luminosity in the 2015 (left) and the 2016 (right) data taking period. Taken from Reference [21].

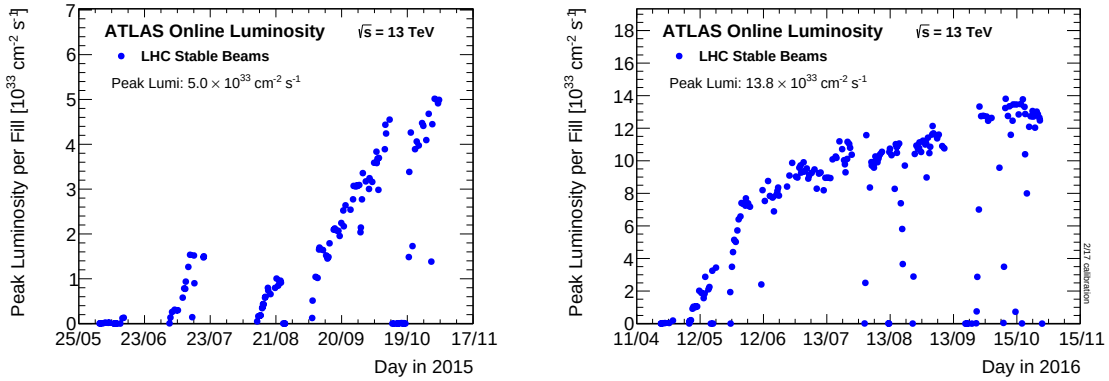

Figure 3.4.: The peak instantaneous luminosity delivered to ATLAS in the 2015 (left) and the 2016 (right) data taking period. Taken from Reference [21].

expression of L

$$L = \frac{N_p^2 k_b f}{4\pi\sigma_x^\star\sigma_y^\star} F \tag{3.1.5}$$

$$= \frac{N_p^2 k_b f \gamma}{4\pi\epsilon_n\beta^\star} F \tag{3.1.6}$$

The productivity of a collider is described by the integral over time of the delivered instantaneous luminosity which defines the integrated luminosity $\mathcal{L}$

$$\mathcal{L} = \int L dt \tag{3.1.7}$$

The integrated luminosity recorded at the LHC as well as the maximal delivered luminosity in the 2015 and 2016 data taking period are shown in Figure 3.3. During

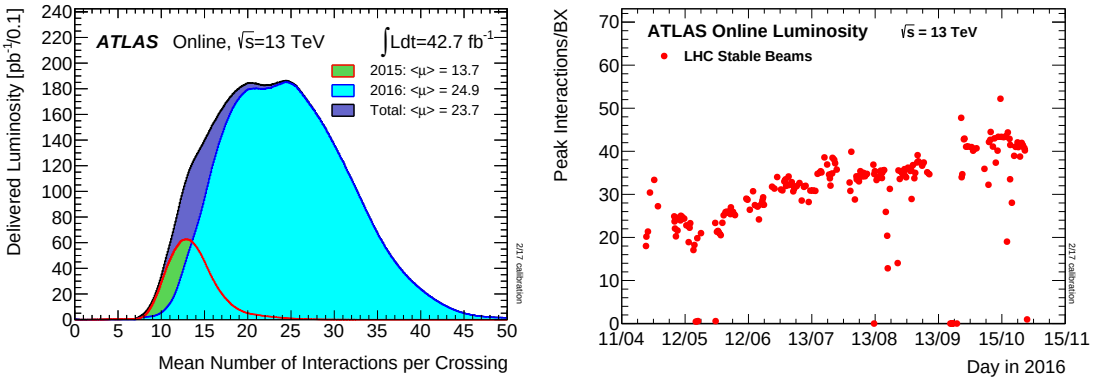

(a) (b)

Figure 3.5.: Luminosity-weighted distribution of the mean number of interactions per crossing for the 2015 and 2016 ATLAS data taking period 3.5(a) and the maximum number of inelastic collisions per beam crossing 3.5(b). Taken from Reference [21].

the data taking the luminosity is not constant. The peak luminosity per fill in 2015 and 2016 is shown in Figure 3.4. The highest luminosities are achieved at the end of the 2016 data taking period with an overall peak luminosity of $13.8 \times 10^{33}\text{cm}^{-2}\text{s}^{-1}$.

The measures providing a high luminosity equally increase the probability of simultaneous proton-proton collisions recorded by the detector. The parameter μ describes the average number of inelastic proton-proton interactions per bunch crossing. The calculation of μ is based on the inelastic cross section $\sigma_{\text{inel}} = 80$ mb at 13 TeV collision energy, the LHC revolution frequency $f = 11.245$ kHz, and the instantaneous luminosity per bunch L_{bunch}.

$$\mu = \sigma_{\text{inel}} \frac{L_{\text{bunch}}}{f} \tag{3.1.8}$$

The average μ is presented in Figure 3.5(a) for different data taking periods. It ranges from $\langle\mu\rangle = 13.7$ in the 2015 to $\langle\mu\rangle = 24.9$ in the 2016 data taking period respectively. The maximal μ per fill during stable beams is shown in Figure 3.5(b) for the 2016 data taking period. The effect of additional proton-proton collisions is generally denoted as pileup. Thereby two types of pileup are distinguished. The protons in hadron colliders like the LHC are produced in successive bunches composed of several protons. As a consequence a given hard scattering process is potentially exposed to additional superimposed proton-proton collisions from the same bunch crossing. Such a process is referred to as *in-time* pileup. Furthermore the response of the subdetectors is characterized by a timescale which can in principal exceed the bunch crossing rate. Thus, also previous and following bunch crossings will affect the measurement of the hard scattering process under investigation. The influence of other bunch crossings besides the current one results in

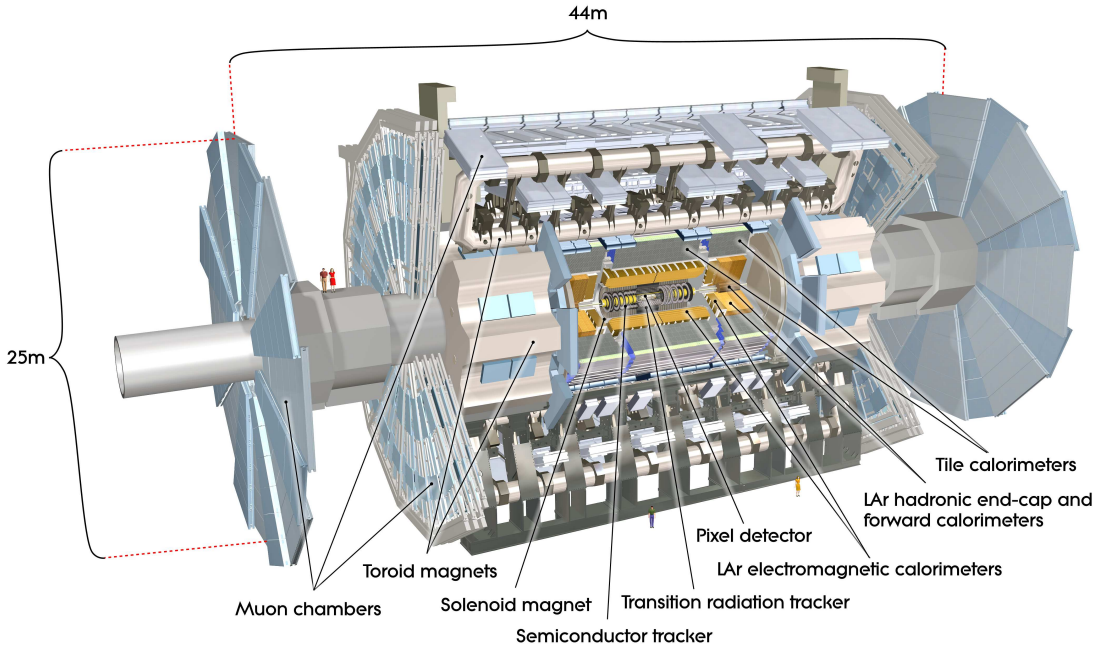

Figure 3.6.: Overview of the ATLAS detector. Taken from Reference [80].

so-called *out-of-time* pileup.

3.2. ATLAS detector

The ATLAS detector is designed to study the collision products in order to investigate different aspects of particle physics. The main design concepts of the ATLAS detector are outlined in this chapter. The description is primarily based on Reference [80]. The individual subsystems constituting the ATLAS detector are summarized in Figure 3.6. The ATLAS detector is a general-purpose detector with a cylindrically and forward-backward symmetric structure. It consists of tracking, calorimeter and muon detectors. The principle how different particles are reconstructed in each subsystem for a slice of the ATLAS detector is sketched in Figure 3.7.

Generally a right-handed coordinate system is used in ATLAS where the nominal interaction point in the center of the detector defines the origin. The z-axis is in the beam direction, the x-axis points towards the center of the LHC ring and the y-axis points upwards. The detector symmetry is reflected by cylindrical coordinates with ϕ denoting the azimuth angle around the beam pipe in the x-y plane. The angle θ is the polar angle from the beam axis. Additional collider variables describing the kinematics in an event are introduced in Chapter 2.2.2.

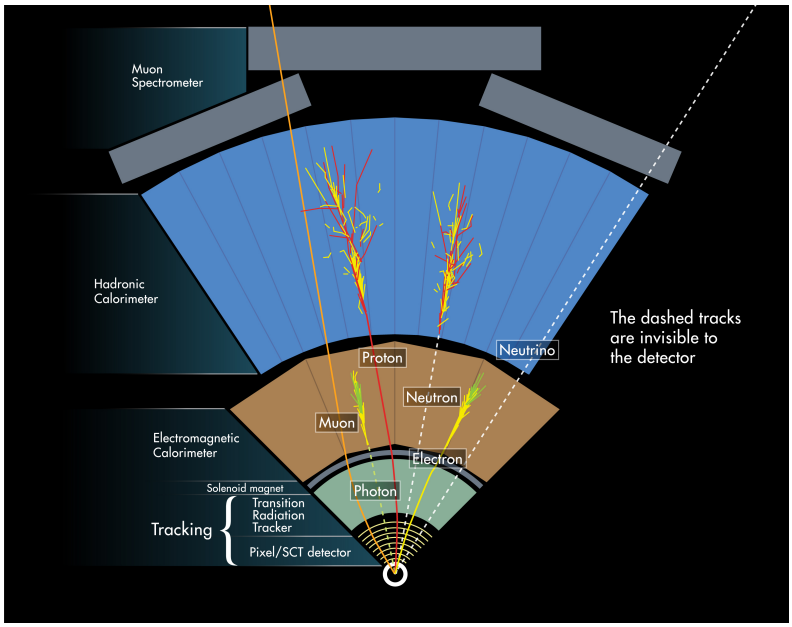

Figure 3.7.: Schematic overview of the ATLAS particle detection principles. Taken from Reference [90].

3.2.1. Magnet system

The ATLAS magnet system bends trajectories of charged particles moving in the detector. The system consists of four superconducting magnets. The general layout is shown in Figure 3.6. The central solenoid (CS) surrounds the inner detector and lies inside the calorimeter volume. The two endcap toroids (ECT) and the barrel torroid (BT) exceed the spatial dimensions of the CS and are located around the muon system. The CS provides a 2 T solenoid magnetic field and is designed to have minimal radiative thickness to reduce the influence on the calorimeter detection. The CS is 5.8 m long and has a diameter of 2.5 m. It is operated at a temperature of 4.5 K using a liquid helium based cooling system. The outer toroidal magnetic field has a diameter of 22 m and a longitude of 26 m. It provides the magnetic field of around 0.5 T to 1 T for the muon system in the barrel and the end-cap regions.

3.2.2. Inner Detector

The Inner Detector (ID) measures charged particle trajectories and is situated in the 2 T magnetic field of the CS. The ID consists of four individual subsystems. The components are, with increasing distance from the interaction point, the Insertable B-Layer (IBL) [92, 93], the Pixel Detector (PD), the Semiconductor Detector (SCT) and the Transition Radiation Tracker (TRT). Tracking capabilities close to the interaction point are especially important for vertex reconstruction and the identification of jets that are likely to contain B hadrons. The IBL is a pixel detector with a high resolution and a spatial coverage of pseudorapidities up to

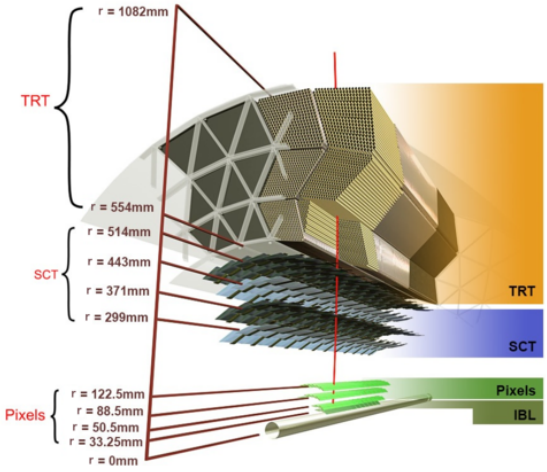

Figure 3.8.: Sketch of the inner detector in the barrel region. Taken from Reference [91].

$|\eta| < 3$. In order to achieve the above mentioned tasks the IBL is installed as close as possible to the interaction point at a mean radial distance of 3.3 cm. The IBL is located between the thin beryllium beam pipe and the PD. The IBL is expected to improve the tracking robustness and the performance in a high luminosity environment characterized by higher pileup and occupancy. The spatial resolution of the IBL is measured to be around 10 μm in $r - \phi$ and approximately 66.5 μm in z [94].

The PD has three layers denoted by B-, 1- and 2-layer in the barrel region and 3 disk-shaped layers in the end-cap region. The PD covers the range up to $|\eta| < 2.5$ and is placed at a radial distance between 5 and 12 cm from the interaction point. The high granularity of the PD results in around 80 million read-out channels. The semiconducting pixel sensors are of small size and provide an intrinsic spatial resolution of 10 μm in $r - \phi$ and 115 μm in z in the barrel and 115 μm in r for the end-caps.

The SCT is a silicon microstrip detector composed of 4 barrel layers and 9 end-cap disks on each side. It extends up to $|\eta| < 2.5$ and is located at radial distances between 30 and 51 cm. The SCT has a design similar to the PD. The larger covered area leads to a lower track density. Therefore, strips can be used instead of pixels. The spatial resolution is 16 μm in $r - \phi$ and 580 μm in the z-direction (r-direction) for the barrel (end-cap) region. The $r - \phi$ resolution of the SCT is comparable to the PD. The number of readout channels for the SCT is much smaller with about 6 million.

The TRT is formed by straw tubes with a diameter of 4 mm filled with a Xenon based gas mixture. It covers the pseudorapidity range $|\eta| < 2$ and extends up to a radius of 107 cm. In contrast to the previous ID systems the TRT provides mainly $r - \phi$ information. The achieved spatial resolution is around 130 μm per straw in the $r - \phi$ direction and $75 - 150$ cm in the z-direction (r-direction) in the barrel

Detector component	Coverage		Resolution and Granularity	
	η	p_T [GeV]	p_T^{-1} [%]	d_0 [μm]
Tracking	$\lvert\eta\rvert < 2.5$	$p_T > 0.1$	$5 \times 10^{-4} p_T \oplus 0.01$	$20 - 140$
			E [%]	Granularity
ECAL	$\lvert\eta\rvert < 3.2$		$0.1/\sqrt{E} \oplus 0.007$	0.025×0.025
HCAL	$\lvert\eta\rvert < 3.2$		$0.5/\sqrt{E} \oplus 0.03$	0.1×0.1

Table 3.1.: Basic detector and performance parameters in the ATLAS barrel region. The $\eta \times \phi$ granularity is given for the second ECAL layer and the inner three layers of the HCAL system respectively. The parameter d_0 denotes the transverse impact parameter resolution. Table modified from Reference [95] based on the numbers given in Reference[80, 96–98].

(end-cap) region. The around 400000 straw tubes of the TRT are installed parallel (perpendicular) to the beam line in the barrel (end-cap) region and are 144 (37) cm long. The TRT has a relatively small number of around 350 thousand readout channels. Charged particles can ionize the gas in the TRT. The TRT delivers important information for the identification of electron candidates by studying the difference in emitted radiation of the traversing particles. The large number of hits per track and the large track length compensate the coarser resolution of the TRT.

The ID allows one to reconstruct charged particle tracks, as well as primary and secondary decay vertices as described in Chapter 3.4.1. It has to handle a high track density with up to about several thousand particles from the interaction point every 25 ns. The basic tracking performance for the barrel region is summarized in Table 3.1. The transverse impact parameter d_0 resolution ranges from around 120 μm down to 20 μm depending on the transverse momentum and the pseudorapidity of the measured track [98]. A relative transverse momentum resolution σ_{p_T}/p_T of $5 \times 10^{-4} \times p_T \oplus 0.01$ is targeted [80]. The design of the ID in the barrel region is presented in Figure 3.8.

3.2.3. The calorimeters

The ATLAS calorimeter consists of the electromagnetic calorimeter (ECAL) and the hadronic calorimeter (HCAL). The two subsystems are shown in Figure 3.6. Both systems are using a sampling technology with alternating active and absorber material within a layer. The absorber material enhances interactions with the traversing particles leading to a cascade of lower-energetic secondary particles which eventually induce an ionization or scintillation signal in the active material. The ECAL is designed to measure the showers of electromagnetically decaying and light particles such as photons and electrons. The HCAL is optimized for the identification of hadronic showers. The ECAL relies on liquid-argon (LAr) as active material. The absorber material in the LAr calorimeter is lead. The hadronic calorimeter sur-

rounds the ECAL. It uses a mixture of LAr and tile calorimeters. The tile calorimeter consists of steel absorbers and scintillating tiles. The calorimeters are designed to provide a good containment for the electromagnetic and hadronic showers. In addition, they sufficiently prevent punch-through into the muon system. In total the calorimeter extends up to $|\eta| < 4.9$.

The electromagnetic calorimeter

The ECAL consists of the LAr barrel (EMB) and two end-cap (EMC) calorimeters which cover a range up to $|\eta| < 1.475$ for the barrel and of $1.375 < |\eta| < 3.2$ for the end-cap component. A reduction of the inactive material in front of the calorimeter is achieved by placing the ECAL in the same vacuum vessel as the CS magnet. The full ϕ coverage without azimuthal cracks is realized by an accordion geometry of the calorimeters.

The barrel part of the ECAL is divided in three segments depending on the distance from the beam pipe. The $\Delta\eta \times \Delta\phi$ granularity is different in all these barrel segments with about 0.025×0.1 in the first, 0.025×0.025 in the middle and 0.05×0.025 in the back layer for the most central region $|\eta| < 1.4$. Considering the full ECAl system the $\Delta\eta \times \Delta\phi$ granularity ranges from 0.025×0.025 to 0.1×0.1 depending on the layer and the pseudorapidity η. The radiation length X_0 denotes the average distance that an electron can travel in a medium before the electron energy reaches a fraction of $1/e$ of the initial energy due to interactions. The total thickness of the ECAL is above $22X_0$ ($> 24X_0$) in the barrel (end-cap) region. High energetic particles loose energy in the absorber material in a cascade of decays. Eventually the charged particles can ionize the LAr and the electrons drift towards the readout electrodes. The LAr calorimeter is operated at a voltage of around 2000 V resulting in ion drift times of approximately 500 ns. In addition, a presampler (PS) is installed before the ECAL in the range $0 < |\eta| < 1.8$. It guarantees an improved measurement of particles starting to shower before reaching the ECAL. The PS consists of a thin instrumented argon layer with a depth of 11 mm.

The energy resolution of the calorimeter can be quantified by the following equation

$$\frac{\sigma(E)}{E} = \frac{S}{\sqrt{E}} \oplus \frac{N}{E} \oplus C \tag{3.2.1}$$

where N denotes the noise term originating from electron and pileup contributions. Shower evolution and detector sampling influence the statistical term S. At high energies the constant term C accounts for dead material, non-uniform responses or effects of the geometry. The barrel ECAL has a target energy resolution of $0.1/\sqrt{E} \oplus 0.007$.

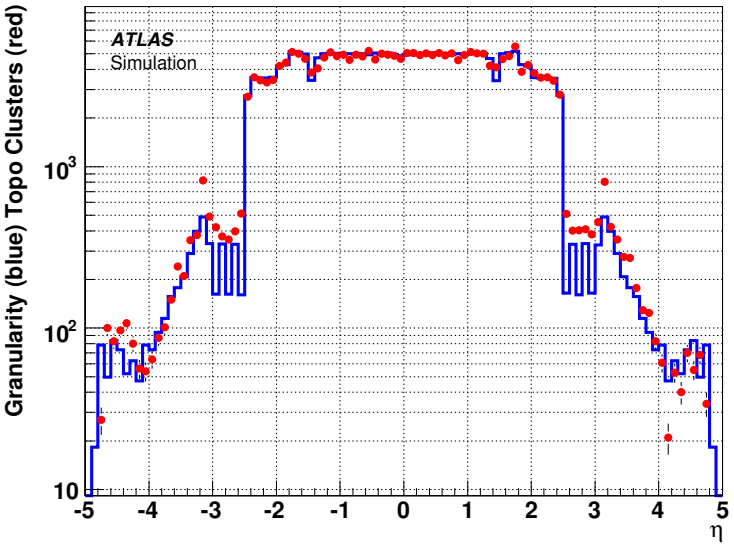

Figure 3.9.: The geometric granularity (number of cells per $\Delta\eta = 0.1$) as a function of pseudorapidity (blue) and corresponding number of topological clusters (red) calculated from simulated noise-only events. Taken from Reference [99].

The hadronic calorimeter

The tile calorimeter of the HCAL relies on steel as the absorber material and on plastic scintillator tiles as active material. Wavelength shifting fibers forward the signals to photomultipliers at the end of the tiles. The tile scintillator hadronic barrel calorimeter covers $|\eta| < 1.7$. The LAr hadronic endcap calorimeter (HEC) covers $1.5 < |\eta| < 3.2$, and the LAr forward calorimeter (FCAL) covers $3.1 < |\eta| < 4.9$ The HCAL in the barrel region is segmented into three layers. Generally, the HCAL granularity is coarser than the ECAL because a larger area has to be covered. The azimuthal granularity is $\Delta\phi = 0.1$ in all three layers. The first two layers have a finer pseudorapidity granularity of $\Delta\eta = 0.1$ compared to the third layer with $\Delta\eta = 0.2$. The LAr technology used in the HEC is the same as in the ECAL. Two independent copper plate wheels form the HEC. The HEC shares the cryostats with the ECAL end-cap calorimeter and the FCAL. The basic parameters of the central HCAL are summarized in Table 3.1. The HCAL target energy resolution is given by $0.5/\sqrt{E} \oplus 0.03$. It is broader than the ECAL resolution.

The FCAL consists of a copper/tungsten LAr forward calorimeter targeting electromagnetic and hadronic showers. The copper supports the measurement of electromagnetic showers whereas the tungsten is used for the hadronic showers.

The overall calorimeter granularity as a function of pseudorapidity η is presented in Figure 3.9. The construction of the topological clusters used to quantify the relative granularity is described in Chapter 3.4.3. In the central region $|\eta| < 2.5$

the highest and almost constant granularity is achieved. The granularity decreases with increasing $|\eta|$. The central region is expected to be crucial for precise physics measurements.

3.2.4. The muon system

The layout of the muon spectrometer is strongly related to the design of the toroid magnet system. The magnetic deflection of muons is achieved by a magnetic field which is mostly orthogonal to the particle trajectories. The magnetic field consists of the field of about 1 T produced by the end-cap toroids in the range $1.6 < |\eta| < 2.7$ and the magnetic field of around 0.5 T provided by the barrel toroid in the range $|\eta| < 1.4$. The muon spectrometer provides independent tracking and trigger capabilities. Monitored Drift Tube (MDT) chambers and Cathode Strip Chambers (CSC) in the forward region ($|\eta| > 2.7$) can determine the muon momentum. The muon resolution is $\sigma(p_T)/p_T = 10\%$ for muons with a transverse momentum of $p_T = 1$ TeV [80].

3.2.5. Data acquisition and trigger system

The proton-proton collisions at the LHC occur at an expected rate of 40 MHz. The reconstruction of a single event in a CPU requires around $\mathcal{O}(1\text{ s})$ and produces about 1.5 MB of data. This causes challenges for the feasible bandwidth, disc space and available computing resources. The Trigger and Data Acquisition (TDAQ) system has the task to select the events with interesting physics information. Thereby, the rate of recorded events is reduced to a level of about 1 kHz. The TDAQ system is composed of two subsystems. The hardware-based first-level trigger (L1) aims at reducing the rate from 40 MHz down to 100 kHz. It is followed by the software-based high-level trigger (HLT) achieving a further reduction down to approximately 1 kHz. The trigger decision is calculated during data taking and has to rely on less information than the full information available for the offline event reconstruction. The ATLAS physics program motivates the definition of certain object and event criteria denoted as *trigger items*. The *trigger items* can consists of e.g. particle multiplicities or kinematic requirements on the particles. The total of all active *trigger items* during the data taking is described by the *trigger menu*. The layout of the ATLAS TDAQ system is presented in Figure 3.10.

First-level trigger

The L1 trigger decision is fully hardware-based and relies mostly on Application Specific Integrated Circuits (ASIC) and Field Programmable Gate Arrays (FPGA). The L1 uses coarse granularity information from all calorimeters and the muon system. The 40 MHz bunch crossing rate defines the L1 input rate. The L1 is designed to make the decision whether the event passed in less than 2.5μs. The following description focuses on the processing of the calorimeter information. More details of

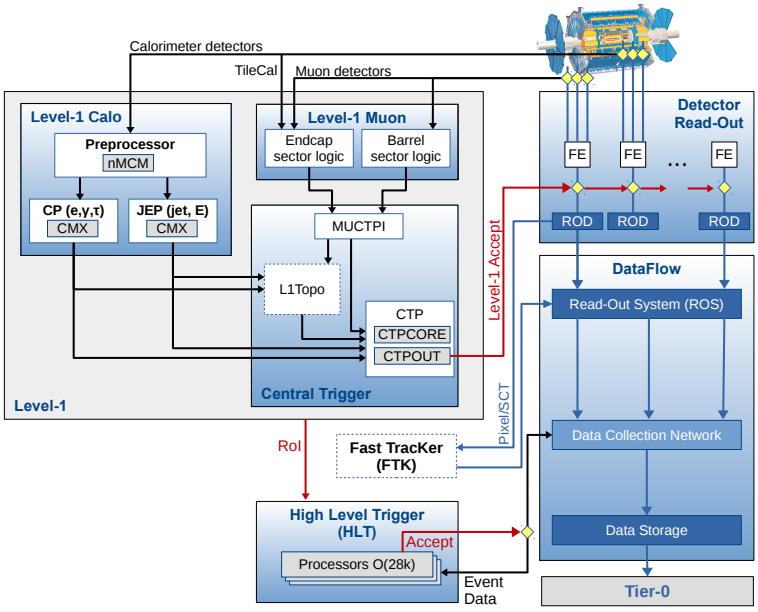

Figure 3.10.: Schematic overview of the data acquisition and trigger system. Taken from Reference [100].

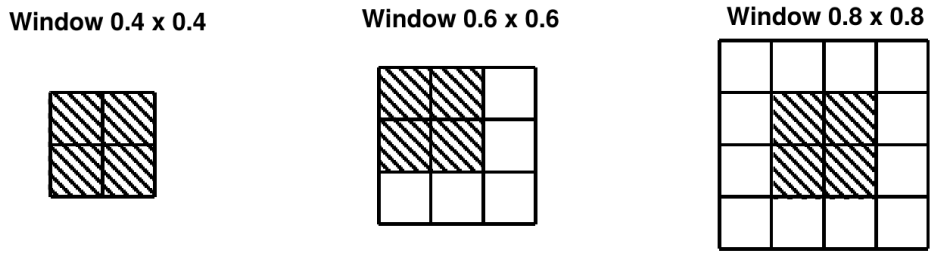

Figure 3.11.: Illustration of the jet reconstruction in the L1 trigger. The three possible sliding window sizes in $\Delta\eta \times \Delta\phi$ are shown. The shaded area represents the *Region-of-interest* corresponding to the local maximum. In the 0.6×0.6 case the *Region-of-interest* can be associated to four possible windows. In the 0.8×0.8 case the *Region-of-interest* is always in the center position. Taken from Reference [80].

the L1 trigger and other ATLAS subdetector inputs are discussed in Reference [101, 102]. The first-level calorimeter trigger (L1Calo) and the first-level muon trigger (L1Muon) pre-process the data from the respective sub-detectors. Eventually, they provide the data to the central trigger processor (CTP) which makes the L1 trigger decision. For some data runs the first-level topological processor (L1Topo) extracts geometric and kinematic information in an intermediate step before the CTP.

The calorimeter granularity is reduced by forming around 7000 coarser *trigger towers* consisting of transverse energy sums of the calorimeter segments. The *trigger towers* (TT) have a granularity of around $\Delta\eta \times \Delta\phi = 0.1 \times 0.1$ for $|\eta| < 2.5$. A separate *trigger tower* grid is used for the electromagnetic and the hadronic calorimeter. Subsequently, a sliding window algorithm identifies localized energy deposits in the Cluster Processor (CP) and the Jet-Energy processor (JEP). The CP focuses on the identification of electrons, photons and τ particles exploiting a sliding window with a fixed size of 4×4 in units of *trigger towers* and applying additional isolation requirements. The JEP is specialized on the identification of jets and missing transverse energy. The jet identification runs on even coarser jet elements which are $\Delta\eta \times \Delta\phi = 0.2 \times 0.2$ sums over trigger towers. The three possible sliding window sizes are 2×2, 3×3 and 4×4 in units of the jet elements. Thus, they span corresponding $\Delta\eta$ and $\Delta\phi$ range from 0.4 to 0.8. The window steps over the jet elements and searches for local transverse energy E_T maxima. In a first step the algorithm checks if the E_T sum of a full window exceeds a threshold. Secondly a smaller window corresponding to 2×2 in jet elements has to be identified as a local maximum. This is fulfilled if the E_T of the local maximum candidate is equal or greater than the neighboring elements. The jet finding procedure is illustrated in Figure 3.11. In the case of multiple candidates further checks achieve the unambiguous identification of the local energy maximum.

The L1 defines rectangular ($\eta \times \phi$) Regions-of-interest (RoI) which are finally used to seed the HLT. These *Regions-of-interest* are the possible candidates for trigger objects. For the sliding window jet finding the *Region-of-interest* position corre-

sponds to the above mentioned localized energy maxima. The transverse energy sum of the associated window defines the energy of the *Region-of-interest* jet. The L1 is expected to achieve a rate reduction down to 100 kHz.

High-level trigger

A computer farm of around forty thousand CPU cores constitute the HLT [103]. The HLT filters the events accepted by the L1 trigger. A supervisor application assigning the incoming events optimizes the usage of the available CPU cores. The detector subsystems are read out separately and the full granularity is provided to the HLT processing. The data of the corresponding subdetectors is saved in event-data fragments. These fragments are managed inside the Read-Out System (ROS). The Data Collection Network (DCN) is part of the ROS and contains the event-data fragments requested by the HLT. Only the subset of event information which is necessary for a HLT process is requested by the HLT for a specific CPU core. The HLT decision is based on a group of several steps forming a so called *trigger chain*. The L1 trigger objects like e.g. the jet *Region-of-interest* seed the HLT *trigger chains*. Subsequently feature extraction algorithms perform offline-like tasks as e.g. track reconstruction or calorimeter clustering on partial-event data. The hypothesis algorithms check if the extracted features satisfy the predefined requirements. The decision making of the subsequent chains is optimized in order to achieve a fast processing. If a *trigger chain* is fulfilled for an event the data stored in the DCN is transferred into an *output stream* to CERN's Tier-0 computing center. The total rate is reduced to around 1 kHz by the HLT trigger. The pileup condition and the used trigger menu influence the average event processing time of the HLT. It was about 235 ms for the highest luminosity run in 2015 corresponding to a peak luminosity of 5.2×10^{33} cm^{-2} s^{-1} [100]. The interplay of the HLT trigger with the L1 trigger and the detector read-out is illustrated in Figure 3.10. The jet reconstruction at HLT level is comparable to the offline reconstruction and is discussed in more detail in Chapter 3.4.5. At HLT level the full calorimeter information is used for the jet reconstruction in contrast to the L1 restriction to a finite *Region-of-interest*. The default HLT jet reconstruction is not relying on tracking information. For certain *trigger chains* a multiple stage track reconstruction is performed in spatially limited regions around the L1 *Region-of-interest* [100].

3.3. Event simulation

Simulations of the proton-proton collisions at the LHC are an essential ingredient for testing the predictions of the Standard Model and of physics of phenomena Beyond the Standard Model. The modeling of the physics in a collision at a hadron collider as described in Chapter 2.2 is the task of the Monte Carlo (MC) event generators that are outlined in Chapter 3.3.1. The interaction of final state particles with the detector is described by specialized detector simulations summarized in

Chapter 3.3.2. A general introduction into Monte Carlo generators used in LHC analyses and the ATLAS detector simulation can be found in Reference [104] and Reference [105] on which the following description is partially based on.

3.3.1. Monte Carlo generation

Monte Carlo event generators are the primary tool for the modeling and prediction of events in proton-proton collisions at the LHC. The Monte Carlo generators have to address several tasks involving amongst others the generation of the hard-scattering matrix element at a given QCD perturbative order, the corresponding matching to approximate treatments of higher orders, the parton showering and the hadronization modeling.

The Pythia [106, 107] generator is designed as a general purpose MC generator with a focus on the $2 \to 2$ process. Pythia can handle beam combinations between hadrons like e.g. protons or same generation leptons. It is mainly a leading-order generator relying on the Lund string model [32] for hadronization. Higher orders in perturbative QCD are simulated by the parton shower. Depending on the version different parton shower emulations are enabled. Ordering the emission of the PS in the transverse momentum is commonly used in version 8 and is an option besides the mass in version 6. Pythia provides a model of the underlying event. The UE and hadronization parameters are tuned to ATLAS data [108–111]. In addition Pythia can be interfaced to other MC generators which extend the pure Pythia-internal $2 \to 2$ process.

Herwig [112–114] follows the concept of a general purpose MC generator with similar functionality as Pythia. The PS emission uses an angular ordering. The hadronization and the UE is simulated by the cluster model as described in Chapter 2.2.1. The multiple particle modeling is usually achieved through a combination with the Jimmy generator [115]. Herwig can be interfaced to other MC generators simulating the hard-scattering matrix element.

The Powheg [116, 117] method and the Powheg Box framework [118] provide an interface between parton-shower Monte Carlo generators and fixed next-to-leading order QCD computations. The hard-scattering matrix element is reweighted to the NLO prediction. The procedure is independent of the parton shower. Therefore, Powheg can be additionally combined with parton shower, hadronization and UE modeling tools such as Pythia or Herwig.

The Madgraph [119] generator simulates the matrix elements at leading order. The extension MadGraph5_aMC@NLO [120] allows the inclusion of loop diagrams and adds the functionality of the Mc@nlo [121] generator. The MadGraph5_aMC@NLO framework combines several tasks ranging from the computation of cross-sections, the generation of hard events and the implementation of corresponding matching procedures to the interfacing with additional simulation tools. Specifically the MadGraph5_aMC@NLO results can be interfaced to other programs such as Pythia for the simulation of the parton shower or hadronization processes.

Sample Uncertainty	Powheg+Pythia6 Nominal	Powheg+Herwig++ PS model	Powheg+Pythia6 Radiation high	Powheg+Pythia6 Radiation low	aMC@NLO+Herwig++ Generator model
ME gen.	Powheg-Box r2330.3	Powheg-Box r2330.3	Powheg-Box r2330.3	Powheg-Box r2330.3	aMC@NLO 2.2.1
PS/UE gen.	Pythia 6.427	Herwig++ 2.7.1	Pythia 6.427	Pythia 6.427	Herwig++ 2.7.1
Ren. scale	$\sqrt{m_t^2 + p_{T,t}^2}$	$\sqrt{m_t^2 + p_{T,t}^2}$	$\frac{1}{2}\sqrt{m_t^2 + p_{T,t}^2}$	$2\sqrt{m_t^2 + p_{T,t}^2}$	$\sqrt{m_t^2 + \frac{1}{2}(p_{T,t}^2 + p_{T,\bar{t}}^2)}$
Fac. scale	$\sqrt{m_t^2 + p_{T,t}^2}$	$\sqrt{m_t^2 + p_{T,t}^2}$	$\frac{1}{2}\sqrt{m_t^2 + p_{T,t}^2}$	$2\sqrt{m_t^2 + p_{T,t}^2}$	$\sqrt{m_t^2 + \frac{1}{2}(p_{T,t}^2 + p_{T,\bar{t}}^2)}$
hdamp	m_t	m_t	$2m_t$	m_t	–
ME PDF	CT10	CT10	CT10	CT10	CT10
PS/UE PDF	CTEQ6L1	CTEQ6L1	CTEQ6L1	CTEQ6L1	CTEQ6L1
PS Tune	P2012	UE-EE-5	P2012 radHi	P2012 radLo	UE-EE-5
Matching	Powheg Matching	Powheg Matching	Powheg Matching	Powheg Matching	MC@NLO

Table 3.2.: Overview of used $t\bar{t}$ MC settings for different simulated samples. Table modified from Reference [122, 123]. The transverse momentum of the top quark $p_{T,t}$ is given in the $t\bar{t}$ center of mass frame.

Top quark pair modeling

The Standard Model $t\bar{t}$ is simulated with POWHEG [116, 117, 124] and PYTHIA 6 [106]. In POWHEG the processes $gg \to t\bar{t}$, $q\bar{q} \to t\bar{t}$ and the emission of the hardest additional real parton are generated at next-to-leading order in the strong coupling parameter α_s. The CT10 PDF set [125] is used for the ME together with the PERUGIA2012 tune [111] and the CTEQ6L1 [126] to describe the showering. The *hdamp* parameter is required to be equal to the top mass of 172.5 GeV. This model parameter influences the Matrix Element and Parton Shower matching. Qualitatively it modifies the hardness of the first radiation, against which the $t\bar{t}$ system has to recoil. Thereby it is expected that the transverse momentum of the top quark and the $t\bar{t}$ system are affected by variations of *hdamp*. The renormalization μ_r and factorization scale μ_f of the hard process are equal to the default generator value μ defined as

$$\mu = \sqrt{m_t^2 + p_{T,t}^2} \tag{3.3.1}$$

Here m_t and $p_{T,t}$ are the top quark mass and top quark transverse momentum before radiation. Different radiation settings are modeled by varying μ_r, μ_f and `hdamp` simultaneously as discussed in more detail in Chapter 6.8.12. The used settings for the nominal SM $t\bar{t}$ sample and the samples used to derive systematic uncertainties for the $t\bar{t}$ modeling are summarized in Table 3.2 and Table 3.3.

The $t\bar{t}$ cross section for a top quark mass of 172.5 GeV and for pp collisions at a center of mass energy of $\sqrt{s} = 13$ TeV is $\sigma_{t\bar{t}} = 832^{+46}_{-51}$ pb. The calculation was done with the Top++2.0 program [127–133] at next-to-next-to-leading (NNLO) order in QCD including resummation of next-to-next-to-leading-logarithm (NNLL) soft gluon terms. The uncertainties from α_S and the PDFs are calculated using the PDF4LHC prescription [134] with the MSTW2008 68% CL NNLO [135, 136], CT10 NNLO [125, 137] and NNPDF2.3 5f FFN [138] PDF sets and added in quadrature

Sample Uncertainty	Powheg+Pythia8 Nominal	Powheg+Herwig7 PS model
ME gen.	Powheg-Box v2	Powheg-Box v2
PS/UE gen.	Pythia 8.2	Herwig7 7.0.1
Ren. scale	$\sqrt{m_t^2 + p_{T,t}^2}$	$\sqrt{m_t^2 + p_{T,t}^2}$
Fac. scale	$\sqrt{m_t^2 + p_{T,t}^2}$	$\sqrt{m_t^2 + p_{T,t}^2}$
hdamp	$1.5m_t$	$1.5m_t$
bornsuppfact	500	500
foldx	2	2
foldy	2	2
foldphi	2	2
ME PDF	NNPDF3.0	NNPDF3.0
PS Tune	A14	H7-UE-MMHT
Matching	Powheg Matching	Powheg Matching

Table 3.3.: Overview of used $t\bar{t}$ MC settings for different simulated samples used to derive modeling uncertainties. Table modified from Reference [122, 123]. The transverse momentum of the top quark $p_{T,t}$ is given in the $t\bar{t}$ center-of-mass frame.

to the effect of the scale uncertainty. This calculation corresponds to the combined ATLAS and CMS recommendation [139].

3.3.2. Detector simulation

The particles produced in the proton-proton collision interact with the ATLAS detector. The GEANT4 [140] framework allows a modeling of such interactions with the full ATLAS detector incorporating the individual subcomponents, the geometry, the material content and the specific responses. The inputs to the detector simulation are generated particles at the stable hadron level. The GEANT4 framework calculates the full interaction with the detector for each particle individually and is therefore denoted as a *full simulation*. The energy deposits of the simulated particles are converted into electronics signals during the *digitization* step. Eventually, the signals serve as input to the object reconstruction as described in Chapter 3.4. From there on data and simulated events are generally treated in the same way.

The effect of additional pileup events as explained in Chapter 3.1 is modeled with minimum-bias events generated by PYTHIA. Each generated event is overlaid with a certain number of such pileup events during the *digitization*. Generally correction factors are applied on simulated events in order to reduce the difference in the pileup distribution between data and simulation. The pileup reweighting procedure can involve information from the average pileup $\langle\mu\rangle$ distribution as well as the number of primary vertices.

3.4. Reconstruction and selection of physics objects and events in ATLAS

Most of the particles produced in the proton-proton collision create signals in the detector. These signals are processed and converted into physics objects in the *reconstruction* step. The analyses presented in this thesis heavily rely on jets and the flavor tagging of the jets. The following discussion of the object reconstruction and identification emphasizes these two aspects.

3.4.1. Tracks and vertices

Tracks in the ID are reconstructed within the full available acceptance $|\eta| < 2.5$, see [91, 98, 141]. *Hits* in the ID subdetectors are the starting point of the reconstruction [142, 143]. An *inside-out algorithm* identifies primary charged particles with a mean lifetime greater than 3×10^{-11} s that are produced directly in a proton-proton interaction or in subsequent decays of particles with a mean lifetime shorter than 3×10^{-11} s. In addition, particles produced in the interaction of primary particles are referred to as secondary particles. They are reconstructed starting with segments in the TRT which are extended inwards by a *back-tracking* procedure. The

starting point of the *inside-out algorithm* are track candidates from seeds with a quality-dependent minimum requirement of hits in the Pixel Detector and the SCT. Subsequently, outlying clusters, ambiguities and fake tracks are removed before the track is extrapolated to the TRT. The minimum transverse momentum requirement of such tracks is 400 MeV. Other track types exist for specialized cases like e.g. the tracks formed in the muon system. The track reconstruction efficiency for the *loose* (*tight*) working point is around 90% (85%) for high $p_T \geq 5$ GeV tracks [141]. The fake rate strongly depends on the chosen working point and is expected to increase for higher pileup conditions.

The position of primary vertex candidates is determined by an iterative vertex finding algorithm [144, 145] using tracks interpolated to the beamline as inputs. The vertex finding and the vertex fitting are the two steps of the vertex reconstruction. The tracks used for the vertex reconstruction have to satisfy additional requirements reducing the contamination with fake tracks and tracks originating from secondary vertices. The algorithm is seeded by the z-position of the reconstructed tracks at the beamline. The beam spot parameters impose additional constraints on the vertex candidates and the considered tracks. An iterative χ^2 fit associates a weight to each track classifying its compatibility with the fitted vertex. If a track is incompatible with a given vertex candidate by more than 7 σ it is removed from the vertex and treated as unused in the following. The procedure repeats until no additional vertices can be found taking into account the unused tracks. The hard-scatter vertex is the one with the largest transverse momentum sum $\sum p_T^2$ of the tracks associated to it.

In events with high track multiplicities the longitudinal vertex position resolution reaches around 30 μm [145]. The application of the beam-spot constraint during the fit results in a transverse vertex position resolution below 20 μm [145]. The transverse-position resolution is independent of the track multiplicity.

The single vertex reconstruction efficiency is above 99% for minimum-bias events as well as hard-scatter interactions for large enough track multiplicities [145]. The impact of pileup on the vertex reconstruction performance is validated in data. The simulation shows a good agreement with data up to the tested range of $\mu = 70$ [145]. The relation between the mean number of reconstructed vertices and the number of interactions per bunch crossing is presented in Figure 3.12.

3.4.2. Muons

Information from the ID and the muon system (MS) is combined in the muon identification algorithms [146, 147]. Generally it can be extended by the calorimeter information. The MS layers provide track segments which are combined into MS tracks. The muon candidates are classified into four categories depending on the information used for the reconstruction. The *standalone muons* are build solely from MS tracks which are extrapolated to the primary vertex. The *combined muons* rely on all relevant tracks of the ID and MS. The *segment-tagged muons* are based on the ID tracks which are extrapolated to the MS. At least one MS track segment

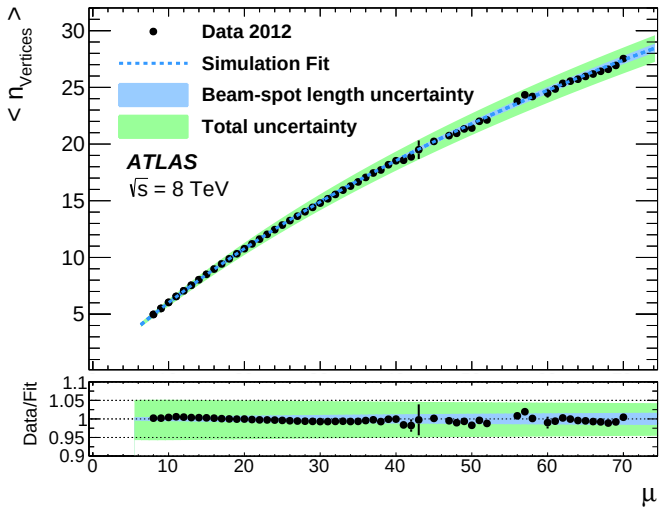

Figure 3.12.: The mean number of reconstructed vertices $\langle n_{\text{vertices}} \rangle$ as a function of the number of interactions per bunch crossing μ. A simulation fit based on simulated minimum-bias events is compared to minimum bias data recorded in the 2012 data taking period. Taken from Reference [145].

has to be successfully matched to an ID track. The *calorimeter-tagged muons* are detected as minimally-ionizing particles in the calorimeter if a corresponding ID track can be matched to the calorimeter cluster.

The quality cuts imposed on the tracking as well as the performance of the muon selection criteria are summarized in the References [146, 147]. It involves the definition of discrete working points denoted by *loose* or *tight* depending on the muon identification efficiency. The muon reconstruction efficiency in the central region exceeds 99%.

The following selection requirements are applied on the reconstructed muons unless stated otherwise. The longitudinal impact parameter z_0 relative to the primary vertex must be less than 2 mm. The isolation requirement involves a geometrical selection in the $\eta \times \phi$ plane depending on the transverse momentum of the muon. Specifically, the transverse momentum sum of all tracks excluding the muon track in a cone of size $R_{\text{cut}} = 10 \text{ GeV}/p_T^{\mu}$ around the muon candidate's direction must be less than 6% of the muon p_T. Thereby the maximal allowed cone radius is set to $R_{\text{cut}}^{\text{max}} = 0.3$. The isolation improves the separation between the hard-interaction muons and muons that are produced in hadron decays. All muon candidates must pass the acceptance requirements of $\eta < 2.5$ and $p_T > 25$ GeV. The criteria for rejection of muons overlapping with a jet are described in Chapter 3.4.8. Unless stated otherwise events containing muons are generally rejected in the analyses presented.

3.4.3. Topological clusters

Topological clusters are build from calorimeter cells and serve as input for the jet reconstruction [99, 148]. The clusters are seeded by cells with an energy exceeding 4 standard deviations σ_{noise} of the predefined cell noise level. The noise level has an electronic and a pileup contribution. It depends on the detector region and the detector subsystem.

$$\sigma^2_{\text{noise}} = (\sigma^{\text{pileup}}_{\text{noise}})^2 + (\sigma^{\text{electronic}}_{\text{noise}})^2 \tag{3.4.1}$$

For the majority of components and regions of the detector the $\sigma^{\text{pileup}}_{\text{noise}}$ is larger than $\sigma^{\text{electronic}}_{\text{noise}}$ assuming a pileup condition of $\mu = 30$ [148]. In the forward region the $\sigma^{\text{pileup}}_{\text{noise}}$ is clearly the dominant source.

Subsequently, a protocluster is formed by adding all neighboring cells with an energy above $2\sigma_{\text{noise}}$ in three dimensions. The procedure is repeated as long as the energy requirement is fulfilled. In a last step a single layer of cells directly surrounding the protocluster is added. A dedicated cluster splitting algorithm handles the case where topological clusters overlap [99].

3.4.4. Electrons

Electron candidates are build based on information from the ID and the EM calorimeter. Cells in the EM calorimeter are clustered in a static approach [99]. The energy clusters in the EM that are matched to an ID track seed the electron candidates [149]. The EM cells are grouped in *towers* of size $\Delta\eta \times \Delta\phi = 0.025 \times 0.025$ corresponding to the granularity of the middle layer in the EM calorimeter. The transverse energy of the *tower* is determined from the transverse energy sum of all longitudinal layers. Subsequently a sliding window algorithm [99] searches for clusters with local transverse energy maxima. The seed threshold of the clusters is set to 2.5 GeV. Ambiguities of spatially close clusters are resolved based on the transverse energy of the clusters. In a next step the EM clusters are matched to the ID tracks. If the matched track originates from the primary vertex the cluster is identified as an electron candidate. Otherwise photon identification procedures as described in Reference [150] are pursued. Eventually electron candidates are optimized by rebuilding clusters and including track information [149]. The background from fake electrons such as jets or pions can be further reduced using TRT information. Depending on the signal selection efficiency and the background rejection several discrete working points are defined. The working point definition takes into account the size and shape of the EM shower, potential energy deposits in the hadronic calorimeter, the quality of the considered tracks as well as the quality of the matching procedure [151]. Therefore, the electron reconstruction and identification efficiency depends on the transverse momentum and chosen background rejection level varying from around 65% to 95% [149].

The identified electrons are required to be within the acceptance of the ID corre-

sponding to $|\eta| < 2.47$. In order to take into account the crack between barrel and end-cap calorimeters the region $1.37 < |\eta| < 1.52$ is excluded. The η coordinate of the electrons is calculated from the cluster position with respect to the primary vertex. The transverse energy of the electron E_T is calculated from the cluster energy E_{cl} and the η_{track} of the associated track as $E_T = E_{\mathrm{cl}}/\cosh(\eta_{\mathrm{track}})$. The electrons must have a minimum transverse momentum of $E_T > 25$ GeV. Unless stated otherwise isolation is imposed on the electron by requiring that the p_T sum of all tracks besides the electron's track in a cone of variable size $R_{\mathrm{cut}} = 10\ \mathrm{GeV}/p_T^{\mathrm{electron}}$ around the candidate's direction must be less than 6% of its E_T. The maximal allowed cone radius is set to $R_{\mathrm{cut}}^{\mathrm{max}} = 0.2$. The criteria for rejection of electrons overlapping with a jet are described in Chapter 3.4.8. Unless stated otherwise events containing electrons are generally rejected in the analyses presented.

3.4.5. Jets

Tracks, calorimeter clusters and simulated particles can be used to define various types of jets. Generally jet reconstruction algorithms are designed in a way that allows an interpretation of the jets as partons originating in a hard process. The guiding principles of the jet algorithms used in ATLAS are discussed in Chapter 2.2.3. The concept of infrared and collinear safety allows the comparison of reconstructed jets to theoretical predictions. Measurements of jet production, which is one of the most basic processes at a proton-proton collider, are shown in Figure 3.13. The higher order QCD calculations are in good agreement with the jet properties measured in data properties over a wide range of pseudorapidity and transverse momentum. The basics of the jet reconstruction and calibration in ATLAS are outlined in the following.

Jets that are build from simulated and stable final state particles from the hard-scatter interaction are denoted as truth jets. Stable particles are required to have a minimum decay length of $c\tau > 1$ cm. Only particles depositing most of their energy in the calorimeters are considered. Therefore, muons, neutrinos and particles originating from pileup are excluded [153]. Calorimeter jets are formed from topological clusters using the Anti-k_T jet algorithm [36] with a distance parameter of $R = 0.4$, denoted as Anti-k_T ($R = 0.4$) and the four-momentum recombination using the FastJet software [38, 39]. The calorimeter jets are the predominant type of jets used in the presented analyses and therefore occasionally simply denoted as jets. In addition jets using solely tracks as input are referred to as track jets. Generally, the different types of jets use the same jet reconstruction algorithms and software mentioned above.

The ratio of a measured jet quantity, such as the energy, to the corresponding quantity at MC truth level is denoted as the jet response. The response of jets build from topological clusters usually differs from unity. The energy of the clusters is given at the electromagnetic (EM) scale. The EM scale is expected to correctly describe electromagnetic showers. Due to several effects such as signal losses on cluster boundaries and inactive detector material as well as non-compensating calorimeter

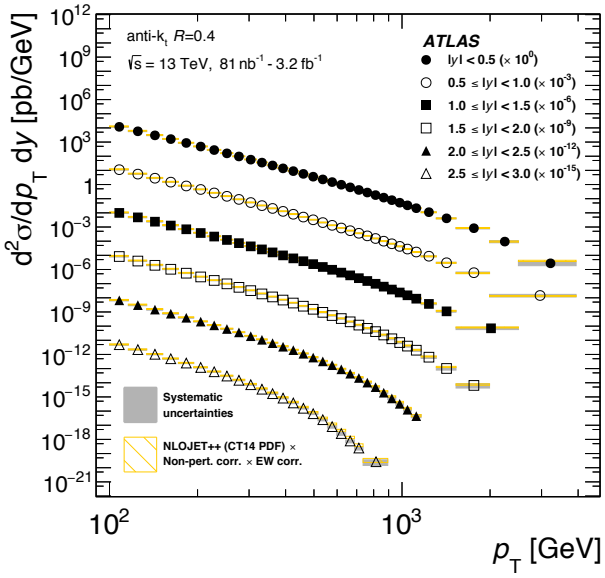

(a) The inclusive jet cross-section of Anti-k_T ($R = 0.4$) jets as a function of p_T and y.

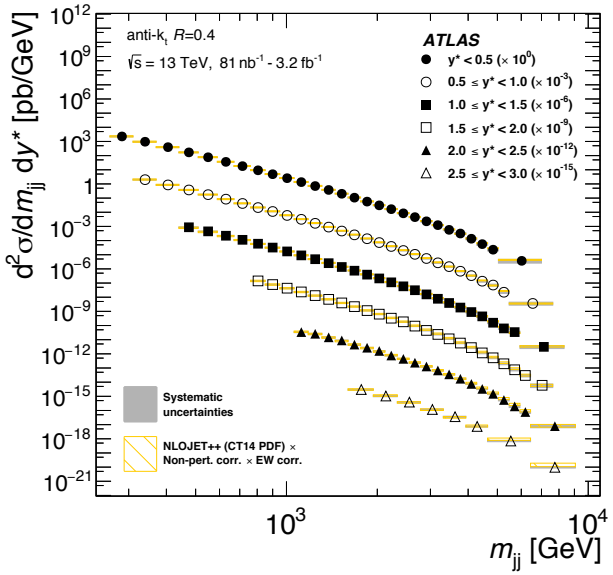

(b) The double-differential dijet production cross-section as a function of the dijet mass and of half the absolute rapidity separation $y^\star$ between the two leading jets.

Figure 3.13.: Inclusive jet and dijet cross-sections. The jet reconstruction is based on the Anti-k_T ($R = 0.4$) algorithm. The measured values are compared to higher order QCD calculations corrected for non-perturbative and electroweak effects. Taken from Reference [152].

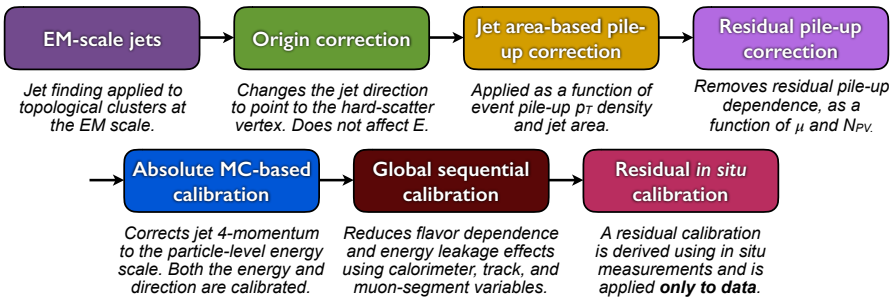

Figure 3.14.: Schematic overview of the calibration procedure for EM-scale jets. Taken from Reference [153].

response to hadrons a calibration procedure is required. The calibration procedure for jets build from topological clusters at the EM scale is shown in Figure 3.14. The jet energy scale (JES) is corrected and calibrated in several steps [153]. First vertex information is used to adjust the jet direction. The pileup contribution is subtracted from the jets using the jet area description. The residual pileup dependence is reduced by correction factors depending on the number of vertices and μ. The mean jet energy response $\mathcal{R}$ is defined as the ratio

$$\mathcal{R} = \left\langle \frac{E_{\text{reco}}}{E_{\text{truth}}} \right\rangle \tag{3.4.2}$$

which is determined in simulated events by a Gaussian fit to the response distribution. The response is converted in a numerical inversion procedure to a correction factor varying as a function of the jet energy and pseudorapidity η. The Global Sequential Calibration (GSC) [153, 154] aims to account for differences between quark and gluon initiated jets. Among other quantities the GSC exploits information of tracks associated to the jets such as their multiplicity or their geometrical width. The dominant improvement of the GSC is observed on the jet energy resolution (JER) rather than the JES. Until this point the same calibration is applied to jets in data and simulated events. Subsequently jets in data are corrected using in-situ measurements.

The jet energy scale uncertainty is below 1% for central jets ($|\eta| < 1.2$) with a transverse momentum in the range $100 < p_T < 500$ GeV. The uncertainty increases for low momentum jets and is around 4.5% for central jets with $p_T = 20$ GeV [153]. The minimum transverse momentum of reconstructed jets is 7 GeV. Due to the large uncertainties at low transverse momentum only jets with $p_T > 25$ GeV and $|\eta| < 2.5$ are considered in the analyses. The JES uncertainty as a function of the η position and the transverse momentum of the jets is shown in Figure 3.15. Hardware problems in the calorimeter, cosmic-ray induced showers and LHC beam-gas interactions can cause so-called *bad jets* [155]. Events containing such *bad jets* are rejected by requiring the event to fulfill certain jet quality criteria [156]. Resolving overlapping objects as described in Chapter 3.4.8 also relies only on the

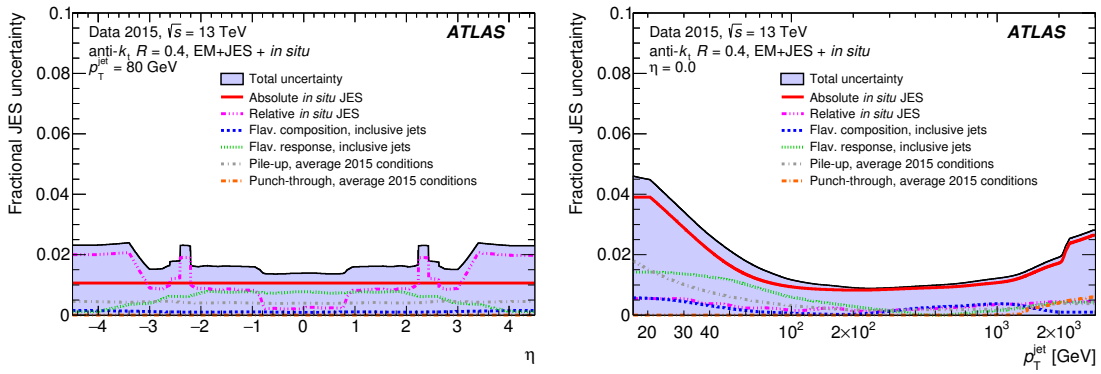

(a) (b)

Figure 3.15.: Combined uncertainty of fully calibrated Anti-k_T ($R = 0.4$) jets as a function of the transverse momentum and η of the jet. Taken from Reference [153].

selected jets.

The above mentioned pileup correction only accounts for average energy corrections of hard-scatter jets. Pileup can lead to additionally reconstructed jets. The Jet Vertex Tagger (JVT) is designed to suppress such pileup jets while keeping the hard-scatter jets [157]. The JVT is a multivariate combination of the corrected Jet Vertex Fraction (cJVF) quantity and the R_{p_T} quantity. The variable cJVF takes into account the dependency on the number of vertices and is defined in the following equation

$$\mathrm{cJVT} = \frac{\sum_i p_T^{\mathrm{trk}_i}(\mathrm{PV}_0)}{\sum_j p_T^{\mathrm{trk}_j}(\mathrm{PV}_0) + \frac{\sum_{n\geq 1}\sum_l p_T^{\mathrm{trk}_l}(\mathrm{PV}_n)}{(k\cdot n_{\mathrm{trk}}^{\mathrm{PU}})}} \ . \tag{3.4.3}$$

The $k \cdot n_{\mathrm{trk}}^{\mathrm{PU}}$ is a correction factor based on the total number of pileup tracks per event ($n_{\mathrm{trk}}^{\mathrm{PU}}$). The calculation of the total number of pileup tracks per event comprises all tracks that are associated to vertices (PV_n) excluding the hard-scatter primary vertex PV_0. The value of k is set to 0.01. The term $\sum_i p_T^{\mathrm{trk}_i}(\mathrm{PV}_0)$ denotes the scalar p_T sum of the tracks i which are associated to the jet and that originate from the primary vertex PV_0. The term $\sum_{n\geq 1}\sum_l p_T^{\mathrm{trk}_l}(\mathrm{PV}_n)$ is the scalar p_T sum of the tracks associated to the jet which originate from the reconstructed vertices excluding the primary vertex. The ratio R_{p_T} compares the scalar p_T sum $\sum_i p_T^{\mathrm{trk}_i}(\mathrm{PV}_0)$ described above to the transverse momentum of the fully calibrated jet. Thereby, the calibration includes the pileup subtraction:

$$R_{p_T} = \frac{\sum_i p_T^{\mathrm{trk}_i}(\mathrm{PV}_0)}{p_T^{\mathrm{jet}}} \ . \tag{3.4.4}$$

The JVT is only applied on jets with transverse momentum in the range 20 GeV

$< p_T < 60$ GeV and $|\eta| < 2.4$. The JVT is studied in simulated $Z \to \mu\mu$ events and in data. The corresponding uncertainty varies between 2% and 6% as a function of the transverse momentum and η of the jet [158].

3.4.6. Flavor tagging of jets

A hadron containing a bottom quark (B-hadron) with transverse momentum of 50 GeV has an average flight path of around 3 mm in the transverse direction before it decays. The B-hadron decay topology is characterized by the long lifetime, a high mass and large multiplicity of the decay products as well as the relatively hard fragmentation function of bottom quarks. The long lifetime of B-hadrons causes a significant displacement between the B-hadron's decay vertex and the primary vertex. Furthermore, the B-hadron decay in the secondary vertex gives rise to displaced tracks with measurable impact parameters. These inner detector quantities are the objects used in the ATLAS b-tagging algorithms. A multivariate combination of algorithms based primarily on tracks classifies jets as originating from bottom-, charm or light-jets. Specifically, the `MV2c10` algorithm [159, 160] is applied on the selected jets. The b-tagging algorithms can be grouped in two classes. The first class relies on the impact parameter information such as the longitudinal or transverse impact parameter. The track selection for the impact parameter determination can differ from the standard track selection and considers the B-hadron topology and the expected corresponding track properties. In the second class the reconstruction of the displaced vertex builds the basis for the identification of the b-jets and the rejection of light-jets.

Depending on the threshold of the multivariate discriminant several working points are defined labeled according to the expected b-jet efficiency measured in simulated $t\bar{t}$ benchmarks. The 85% (*loose*) and the 70% (*tight*) working point are used in the presented analyses. Unless stated otherwise jets are simply referred to as b-tagged if the 70% working point is applied on the selection. The benchmark efficiencies determined in simulated $t\bar{t}$ events for the 70% (85%) working point are a c-jet, light-jet and τ rejection of 12 (3.1), 381 (33) and 55 (8.2) respectively [160] where the rejection is defined as the inverse of the selection efficiency to pass a given b-tagging working point.

A slight dependence of the b-tagging performance on the pileup activity in an event is expected. Especially for background from light-flavor jets the reconstruction efficiency of secondary vertices increases with pileup [159]. This eventually results in a reduced light-flavor jet rejection in a high pileup environment. On the other hand the secondary vertex rate is expected to be almost constant for b- and c-jets where the secondary vertices originate from the decays of long-lived heavy hadrons [159].

The modeling of the b-tagging algorithm is validated in data and simulated events [160–162]. Correction factors as a function of the jet p_T and η are derived by comparing the efficiencies for b-, c- and light jets in data and simulation in a transverse momentum range from 20 GeV to 300 GeV. The resulting scale fac-

tors are applied on the simulated events to account for the found differences. The b-tagging efficiency increases with the transverse momentum of the jets reaching a peak around 100 GeV. For higher jet p_T the efficiency decreases again.

3.4.7. Missing transverse momentum

The negative vector sum of several calibrated and selected physics objects defines the missing transverse momentum. In addition to the objects introduced in this chapter a term accounting for the extra soft energy in an event is considered in the sum. This soft terms takes the tracks and the energy deposits in the calorimeter which are not associated to the physics objects into account. Only ID tracks matched to the primary vertex are considered in the calculation of the soft term in order to reduce pileup effects. Eventually the electrons, photons, jets, muons and the soft term contribute to the missing transverse momentum [163, 164]. Neither event selection nor reconstruction directly uses the missing transverse momentum in the analyses presented in this thesis.

3.4.8. Overlap removal

An *overlap removal* procedure aims to avoid that the same object like e.g. a calorimeter cell contributes to several reconstructed objects. Therefore, any jet within a cone of $\Delta R_y < 0.2$ of an electron is discarded. In a second step electrons that are within $\Delta R_y < 0.4$ of the remaining jets are rejected. An overlap criteria between jets and muons is defined depending on the muon transverse momentum p_T^μ. Muons within $\Delta R_y < 0.04 + 10\ \text{GeV}/p_T^\mu$ of a jet associated to at least three hard-scatter tracks are removed from the event selection. Otherwise jets with less than three tracks overlapping with a muon are discarded. Modifications of the above mentioned *overlap removal* are indicated in the corresponding chapters.

4. Description of the bucket algorithm

The concept of the bucket algorithm is discussed in this chapter. The algorithm was first proposed in Reference [16] on which the description in this Chapter is based on. It aims at using the reconstructed and calibrated objects outlined in Chapter 3.4 in order to identify and reconstruct top quark pairs in the all-hadronic decay mode. The theoretical details of the top quark decay are outlined in Chapter 2.3. At a center of mass energy of 13 TeV the SM top quark pairs created in proton-proton collisions and measured in the ATLAS detector have a transverse momentum distribution peaking at around 100 GeV [166]. The distribution further decreases with increasing p_T. The transverse momentum of the top quarks has a strong impact on the top quark reconstruction procedure as it influences the topology and especially the geometrical separation between the decay products. In a two-body decay the ΔR distance, introduced in Chapter 2.2.2, between the decay products can be approximated by

$$\Delta R \simeq \frac{2m}{p_T} \tag{4.0.1}$$

with the mass of the initial object denoted by m. This relation also serves as a rule of thumb for other decay processes [35]. The geometrical distance of the three partons from top quark decay in simulated $t\bar{t}$ events is shown in Figure 4.1. Top tagging approaches using isolated small-R jets are referred to as *resolved* tagging. Anti-k_T jets with a distance parameter $R = 0.4$ are used to define small-R jets in the bucket algorithm. In a *resolved* scenario the top reconstruction aims for an association between the partons of the top quark decay and the small-R jets.

At leading order, the presence of six jets is expected in an all-hadronic $t\bar{t}$ decay. The tagging of top quarks at small transverse momentum $p_T < 200$ GeV generally requires to combine jets from a large $\eta - \phi$ area. Therefore, combinatorics are the largest challenge for *resolved* top taggers. At larger transverse momenta $p_T \approx 400$ GeV the decay products merge and cannot be resolved by the small-R jets anymore. On the other hand, the high transverse momentum of the top quarks allows the usage of substructure based top tagging [12, 15, 95]. In such a *boosted* scenario the top quark decay can be captured by a single large-R jet where the radius parameters range from around 0.8 to 1.5 depending on the process and the kinematic regime for which they are optimized. The large-R jets in ATLAS rely mainly on the Anti-k_T algorithm but other sequential recombination algorithms are also applicable.

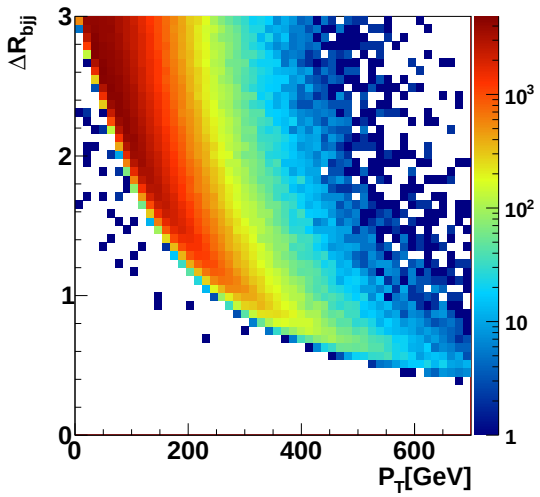

Figure 4.1.: Partonic ΔR_{bjj} for simulated SM $t\bar{t}$ events as a function of the p_T of the top quark. The ΔR_{bjj} approximates the geometrical size of the top quark decay in $y - \phi$ space. Taken from Reference [165]

Substructure techniques are usually limited at low transverse momentum due to the momentum threshold needed to achieve a containment of the top quark decay. Classical *resolved* reconstruction techniques [10] often require a relatively strict selection on the small-R jets in order to achieve a complete matching between jets and the partons of the $t\bar{t}$ decay. The bucket algorithm aims to complement these existing techniques by targeting the transverse momentum regime between 100 GeV and 400 GeV of the top quarks.

In around 50% of the SM $t\bar{t}$ events an additional hard jet with $p_T > 25$ GeV in the kinematic regime of the ATLAS jet selection is present [167]. In addition, the jet corresponding to the softer quark from the W boson decay can potentially fail the jet selection [16]. Both cases are addressed by the bucket algorithm design. The inputs to the top quark reconstruction are the small-R jets and the related b-tagging information as described in Chapter 3.4.5 and Chapter 3.4.6 respectively.

Certain BSM models as introduced in Chapter 2.4 predict heavy resonances such as the heavy Z' bosons decaying directly to $t\bar{t}$ pairs. A full identification of the $t\bar{t}$ system is essential to achieve a good Z' reconstruction. The mass of the resonance sets a scale for the transverse momentum of the produced top quarks. Therefore, the bucket algorithm is well suited for the reconstruction of resonances up to around 1 TeV. The algorithm is described in the following. Further details of its performance can also be found in [16, 168].

The starting point is a relatively high multiplicity of calibrated and pileup corrected small-R jets. The minimum multiplicity requirement can be optimized for each analysis. The bucket algorithm groups the jets into three containers referred to as buckets. Thereby, the top quark candidates are identified with the first two

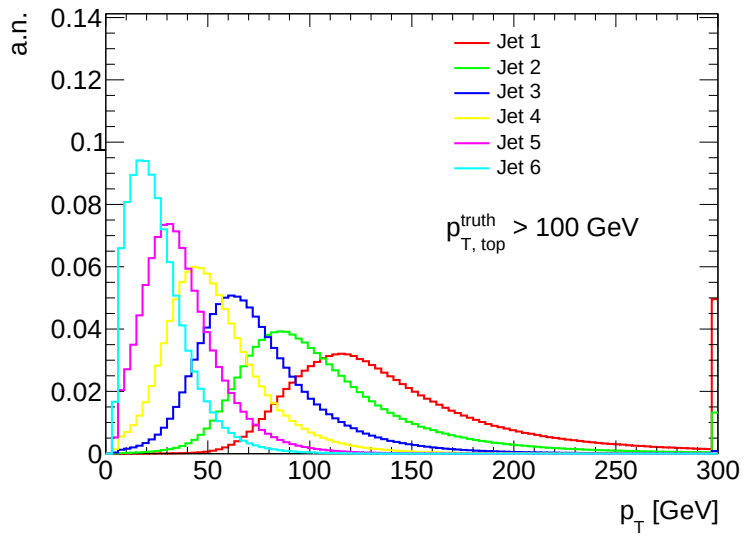

Figure 4.2.: Distribution of Anti-k_T ($R = 0.4$) truth jets for the simulated process $pp \to t_h\bar{t}_h$ with all-hadronic decays of the top quark. The momenta of the top quarks are evaluated after final state radiation before they decay. Only truth jets with pseudorapidity $|\eta| < 2.5$ are considered. The six Anti-k_T ($R = 0.4$) truth jets with the highest transverse momentum are shown. The harder top quark in an event has a transverse momentum above 100 GeV.

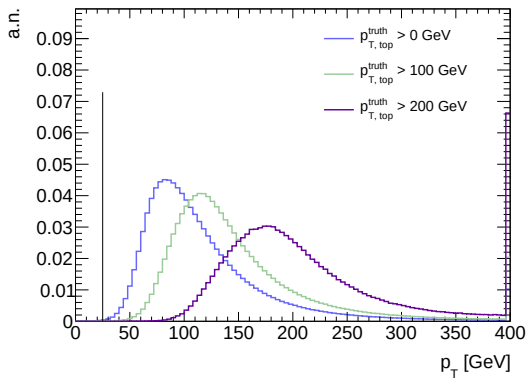

(a) The truth jet with the highest transverse momentum

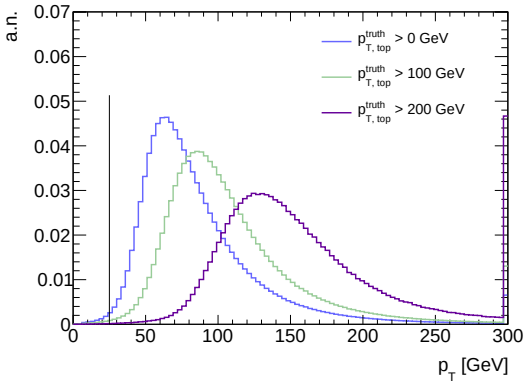

(b) The truth jet with the second highest transverse momentum

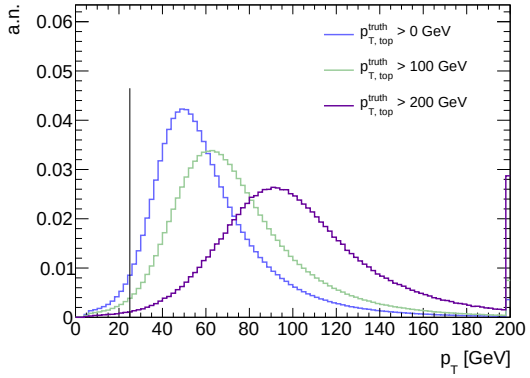

(c) The truth jet with the third highest transverse momentum

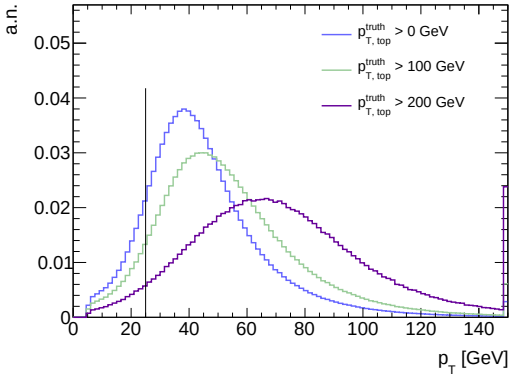

(d) The truth jet with the fourth highest transverse momentum

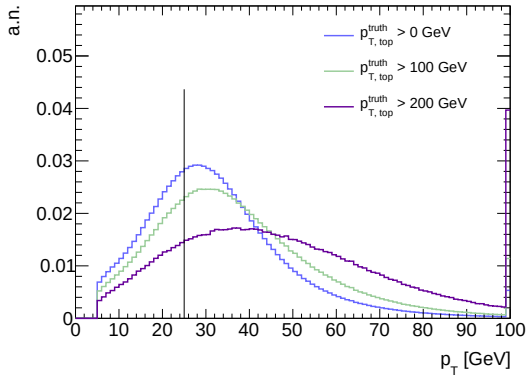

(e) The truth jet with the fifth highest transverse momentum

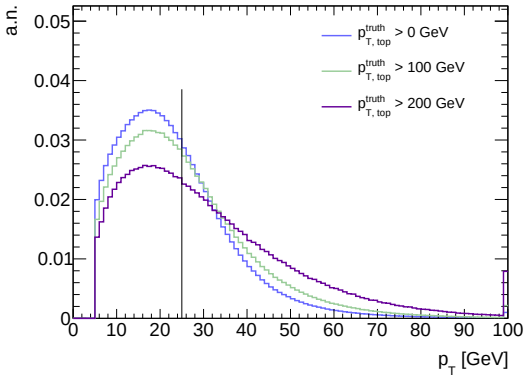

(f) The truth jet with the sixth highest transverse momentum

Figure 4.3.: Distribution of Anti-k_T ($R = 0.4$) truth jets for the simulated process $pp \to t_h\bar{t}_h$ with all-hadronic decays of the top quark. The momenta of the top quarks are evaluated after final state radiation before they decay. Only truth jets with pseudorapidity $|\eta| < 2.5$ are considered. The top quarks have to pass a transverse momentum threshold. The line indicates the minimal transverse momentum requirement for offline jets.

buckets B_1 and B_2. All extra hadronic activity in the event is associated with the third bucket B_{ISR}. In particular, this third bucket B_{ISR} is expected to acount for the initial state radiation (ISR) that is present in the event. In general a two step procedure manages the association of jets to the buckets. In each step different assumptions on the $t\bar{t}$ topology are made. The first one aims to identify all partons of the top quark decay. Even for high jet multiplicities with more than five jets this identification is often not possible as the partons can be outside the acceptance. Especially the minimum requirement on the transverse momentum of the jets $p_T > 25$ GeV can prevent the successful reconstruction of the softer parton from the W decay [16].

Such a topology is addressed by the second reconstruction step that allows for a partial reconstruction of the decay products. The transverse momentum distributions of the six hardest Anti-k_T ($R = 0.4$) truth jets in simulated $pp \to t_h\bar{t}_h$ events with an all-hadronic decay of the top quarks are shown in Figure 4.2. Moderately boosted top quarks are selected by requiring the transverse momentum of the harder top quark to be above 100 GeV. In approximately 50% of the events the four hardest truth jets have a transverse momentum above 50 GeV. That defines a kinematic regime of jets for which a good jet reconstruction is expected as explained in Chapter 3.4.5. For softer jets the experimental uncertainties typically increase. Furthermore, the successful identification of reconstructed small-R jets with all the partons from the decay of the top quark pair becomes critical considering the minimal transverse momentum requirement. The distribution of the sixth hardest truth jet suggests that in around 50% of the events it is not available for the top quark reconstruction. The transverse momentum of the six hardest truth jets as a function of the transverse momentum of the top quarks is presented in Figure 4.3. The harder truth jets show a stronger dependence on the transverse momentum of the top quarks compared to the softer ones. As a consequence the potential unavailability of all the jets from the top quark decay persist even for events with relatively boosted $p_T > 200$ GeV top quarks. In particular, the sixth hardest jet is likely to still fail the offline reconstruction. Therefore, a highly efficient top tagging approach in the intended kinematic regime should address this partial topology.

The selected jets are assigned to the top buckets in both steps. All possible permutations of assigning the jets to the three buckets are studied. A metric is calculated for each permutation in order to identify the top quarks. Eventually the bucket candidates are identified by the assignment which minimizes the metric. An additional restriction based on the b-tagging information is imposed on the assignment of the jets. Every top bucket is required to be seeded by exactly one

b-tagged jet. The metric Δ is used in the first step

$$\Delta^2 = \omega\Delta_{B_1}^2 + \Delta_{B_2}^2 \tag{4.0.2}$$

$$\Delta_{B_i} = |m_{B_i} - m_t| \tag{4.0.3}$$

$$m_{B_i}^2 = \left(\sum_{j\in B_i} p_j\right)^2 \tag{4.0.4}$$

$$\omega = 100 \longrightarrow \Delta_{B_1} < \Delta_{B_2} \tag{4.0.5}$$

which is fully based on the invariant mass of the buckets. The bucket mass is calculated from the vector sum of the jets inside the bucket. The choice of the metric Δ_{B_i} results in minimizing the distance of the bucket mass to the true top mass set to $m_t = 173.5$ GeV. The two top quarks are reconstructed simultaneously. The weighting factor ω achieves a decoupling between the mass reconstruction of B_1 and B_2. As a consequence the first bucket is always closer to the true top mass. The advantage of introducing the weighting factor is motivated by the second step. In order to accept a top candidate they have to pass certain mass window requirements defined by the following equation.

$$155 \text{ GeV} < m_{B_{1,2}} < 200 \text{ GeV} \tag{4.0.6}$$

By construction the combinatorial background will also peak at the true top mass. So far unused information inside the top buckets can be used to further suppress non $t\bar{t}$ events. Therefore the mass $m_{k\ell}$ of the two-jet distribution inside the top buckets B_i is scanned to find W boson candidates. If the following equation is satisfied the top bucket is supposed to contain a W candidate and is labeled $\mathfrak{t}_w$.

$$\left|\frac{m_{k\ell}}{m_{B_i}} - \frac{m_W}{m_t}\right| < 0.15 \tag{4.0.7}$$

Here $m_{k\ell}$ is the invariant mass formed out of any combination of two jets inside the bucket B_i but excluding the b-tagged jet. The ratio of the two-jet mass over the bucket mass is compared to the ratio of the true W mass $m_W = 80.4$ GeV over the true top quark mass m_t. If no W candidate is found the bucket is labeled $\mathfrak{t}_-$. Restricting the selection to only the $\mathfrak{t}_w$ buckets would in general reduce the reconstruction efficiency. As mentioned before the incomplete reconstruction of the W boson is expected for the jet selection with $p_T > 25$ GeV where the softer jet from the W decay is missed.

The second reconstruction step aims at addressing the topology characterized by the presence of $\mathfrak{t}_-$ buckets in order to recover a high reconstruction efficiency. A new metric Δ_B^{bj} is introduced in this step to account for two-jet top buckets without a W candidate. The schematic overview of the metric design for the two steps and topologies is illustrated in Figure 4.4. The observation that the selected jets are mostly the bottom quark and the harder quark from the W decay motivates the

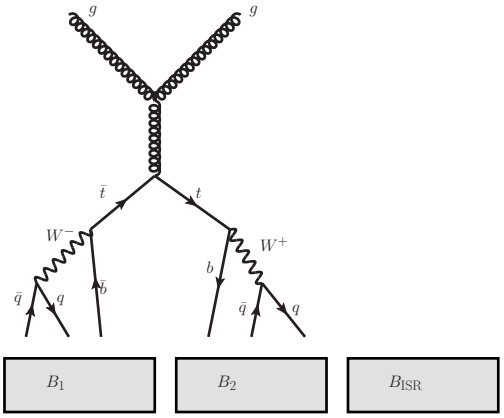

(a) Illustration of an event where the $t\bar{t}$ decay is fully reconstructed in the first step.

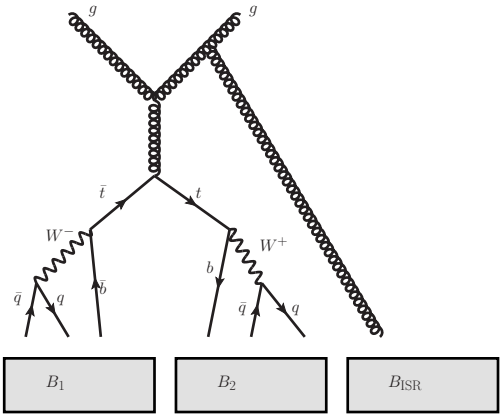

(b) Illustration of an event with extra hadronic activity

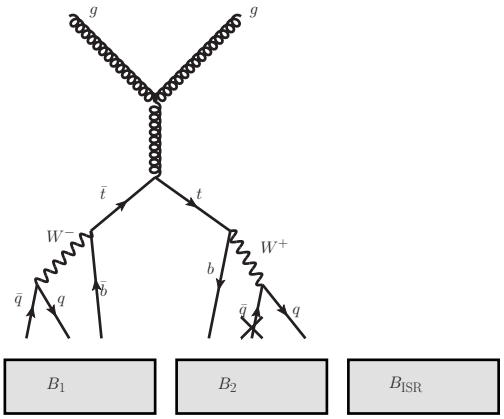

(c) Typical event in which the $t\bar{t}$ decay is partially reconstructed in the second step.

Figure 4.4.: Illustration of the bucket algorithm. Each diagram should be read from top to bottom.

structure of the second metric. The invariant mass of this two-jet system (b/jet) has a specific shape behavior which is used to solve the combinatorics of the jet assignment. The b/jet distribution shows a peak around a mass of 145 GeV due to the top decay kinematics with an endpoint at $\sqrt{m_{\mathrm{t}}^2 - m_{\mathrm{W}}^2} \simeq 155$ GeV [169]. Therefore, the new metric is based on a reduced mass and is given by the following equation

$$\Delta_B^{bj} = \begin{cases} |m_B - 145 \text{ GeV}| & \text{if } m_B \leq 155 \text{ GeV} \\ \infty & \text{else} \end{cases} \tag{4.0.8}$$

The two step approach profits from the fact that the effective number of jets considered for the second metric can be reduced. After the first step the event can be categorized depending on the bucket type t_w or t_- as well as the bucket position B_1 and B_2. The labeling uses the convention that the first bucket in parenthesis corresponds to bucket one (B_1, B_2). The four event categories after step one are summarized here

- (t_w, t_w): A W candidate in both top buckets
- (t_w, t_-): A W candidate in B_1 and no W candidate in B_2
- (t_-, t_w): A W candidate in B_2 and no W candidate in B_1
- (t_-, t_-): No W candidate found in the top buckets.

The jets associated to a t_w bucket are excluded from the second reconstruction step. This reduces the combinatorics. Three different types are distinguished

- (t_w,t_w): keep
- (t_w,t_-) or (t_-,t_w): recompute minimizing Δ_B^{bj}
- (t_-,t_-): recompute minimizing $\Delta_{B_1}^{bj} + \Delta_{B_2}^{bj}$ using all jets in the event

influencing the second metric as well as the considered jets. Eventually the two-jet buckets minimizing the metric are selected as the new top candidates. The t_- top candidates have to satisfy the following mass window requirement

$$75 \text{ GeV} < m_{bj} < 155 \text{ GeV} \tag{4.0.9}$$

in order to be accepted. Events not falling in any of the four event categories are labeled (t_0, t_0). The (t_0, t_0) category contains events where the mass window requirements are not satisfied by the top buckets.

5. Performance of the bucket algorithm

5.1. Introduction

The bucket algorithm serves as a tool to identify and reconstruct top quark pairs and can be used in several applications. The usage of the algorithm in $t\bar{t}$ resonance searches, in searches for the Standard Model Higgs boson in association with top quarks and in a trigger-level study is investigated in this thesis. Generally, the bucket algorithm has to handle the hadronic activity in an event and the corresponding combinatorics of the jet assignment to top quark candidates. Understanding the performance of the algorithm in simulated events as well as a validation in data is a crucial step before any further physics application.

Two different selections are exploited in this Chapter. The performance evaluation on simulated $t\bar{t}$ events is using a relatively loose selection. The validation in data is using a trigger threshold which increases the minimal transverse momentum imposed on the selected jets. The used simulations and the data is described in Chapter 5.2. The two selections are listed in Chapter 5.3. The basic top quark reconstruction performance is studied on simulated events in Chapter 5.4. A comparison between data and simulation is presented in Chapter 5.5.

5.2. Data and simulation

The data was collected during proton-proton collisions in the 2015 and 2016 data taking period of the ATLAS experiment at a center of mass energy of 13 TeV. Quality criteria on the data ensure that the detectors were fully operational and that stable beam conditions were present. The dataset corresponds to an integrated luminosity of 36.1 fb^{-1}.

QCD multijets and SM $t\bar{t}$ are expected to be the dominant contributions after the selection described in Chapter 5.3. The SM $t\bar{t}$ events are simulated separately for the all-hadronic final state and the leptonic final states. The Powheg [116, 117, 124] generator interfaced to Pythia 6 [106] is used for the simulation of the SM $t\bar{t}$ process. The same SM $t\bar{t}$ samples that are used in the $t\bar{t}$ resonance search are studied. A detailed description of the MC generator setup can be found in Chapter 6.3.4. The QCD multijet is modeled with Pythia 8 [107] as a $2 \rightarrow 2$ process at leading order using the NNPDF2.3 [138] PDF set. The events are filtered on the transverse momentum of the truth jets in order to achieve smaller

statistical uncertainties for events with high-p_T jets. The properties of heavy-flavor hadron decays are simulated with EvtGen v1.2.0 [170] for all simulated samples. In all simulated events a pileup contribution based on simulated minimum-bias events is included.

5.3. Event preselection

The bucket algorithm requires a minimal selection in order to identify valid top quark candidates. The description in Chapter 4 motivates that there should be at least four jets in an event and two of them should be b-tagged. The analysis presented in this thesis have even more restrictive requirements on the jet multiplicity and the b-jet multiplicity that are described in the respective Chapters. The bucket algorithm performance is not independent of the topology and the kinematics of the event as is explained in this performance study. Therefore, a dedicated performance analysis is separately performed in each phase space of the respective analysis presented in this thesis. The general performance that is investigated here aims at a selection which is close to the analyses but still loose enough to draw some more general conclusions about the capabilities of the bucket algorithm. The event selection largely follows the $t\bar{t}$ resonance selection introduced in Chapter 6.2.2 but looser requirements are imposed on the small-R jets. All selections require small-R jets with a transverse momentum of at least 25 GeV which are central $|\eta| < 2.5$. Both selections require the default overlap removal. A JVT criteria is applied in order to suppress pileup jets. The selection is only imposed on soft jets with a transverse momentum $p_T < 60$ GeV that are within pseudorapidity range $|\eta| < 2.4$.

The so called *loose* selection requires at least five small-R jets allowing to study adequately the case of $\mathfrak{t}_w$ and $\mathfrak{t}_-$ top candidates. The 70% b-tagging WP corresponding to the *tight* b-tagging selection is applied. At least two of the reconstructed small-R jets are required to be b-tagged. Only simulated events with fully-hadronic top quark pair decays are considered. Besides that no selection on truth jets or top quarks is applied in order to highlight the acceptance and efficiency effects.

The *preselection* used for the data to MC comparison imposes stricter criteria on the jet multiplicity requiring at least six small-R jets. At the trigger level at least five jets are selected with $p_T > 60$ GeV in the 2015 data taking period and at least five jets with $p_T > 65$ GeV and $|\eta| < 2.4$ in the 2016 data taking period. In order to reduce the trigger effect on the distribution the five hardest offline small-R jets are required to have $p_T > 75$ GeV assuring an operation in the trigger plateau. The other object reconstruction and event selection requirements not directly affecting the jets are identical to those introduced in Chapter 6.2.2. Furthermore, the additional correction factors outlined in Chapter 6 are equally applied in the Data to MC comparison. The event selection with respect to the small-R jets and the top candidates for the *loose* scenario and the *preselection* for the data to MC comparison are summarized in Table 5.1.

Variable	*Loose*	*Preselection*
Number of small-R jets ($p_T > 25$ GeV)	≥ 5	≥ 6
Multijet trigger	not present	pass
Number of small-R jets ($p_T > 75$ GeV)	≥ 0	≥ 5
Leading small-R jets ($\|\eta\| < 2.4$)	≥ 0	≥ 5
Number of tight b-tagged small-R jets	≥ 2	≥ 2
Top candidates	mass windows	mass windows

Table 5.1.: Summary of event preselections used in the performance evaluation of the bucket algorithm. The *loose* selection is used for the investigation of simulated SM $t\bar{t}$ events. The *preselection* (trigger) is stricter on the selected small-R jets and required for the data to MC simulation comparison. Only the selection with respect to the small-R jets and the top candidates is shown.

5.4. Performance on simulated events

The performance of the bucket algorithm is investigated in simulated fully hadronic SM $t\bar{t}$ events. The SM $t\bar{t}$ events are considered as the signal in the following. In principal the reconstruction in terms of the assignment of jets to top buckets can potentially fail. Therefore, it is necessary to define a measure of accuracy of the jet assignment. The quality of the reconstruction is quantified by a geometrical matching in the $\eta - \phi$ plane. Thereby the reconstructed top quark candidates t_i^{reco} are matched to the truth top quarks after radiation and before the decay t_j^{truth} with the quantity $\Delta R(t_i^{\text{reco}}, t_j^{\text{truth}}) = \sqrt{(\eta_i - \eta_j)^2 + (\phi_i - \phi_j)^2}$. If the relation

$$\Delta R(t_i^{\text{reco}}, t_j^{\text{truth}})) < R_{\text{cut}} \tag{5.4.1}$$

is satisfied by both top quark candidates the matching is considered successful. The matching distance R_{cut} is set to $R_{\text{cut}} = 0.3$.

Generally, increasing the transverse momentum of the top quarks results in harder small-R jets as shown in Figure 4.3. Such harder jets are expected to be better measured in the ATLAS detector as described in Chapter 3.4.5. Furthermore, the decay products of boosted top quarks are more collimated. As a consequence, the combinatorics challenge is reduced for boosted top quarks. In an extreme case the collimation would be strong enough to allow a full reconstruction within a large-R jet which is the task of dedicated substructure top taggers. The small-R jets merge for highly boosted top quarks $p_T > 400$ GeV preventing an efficient resolved top quark reconstruction in that regime. Nevertheless, for softer top quarks the resolved top quark reconstruction is likely to improve with increasing top quark p_T. The distributions of several quantities related to the bucket algorithm are presented in Figure 5.1 and Figure 5.2. The mean of the transverse momenta of the reconstructed top quark candidates differ by approximately 100 GeV which is expected

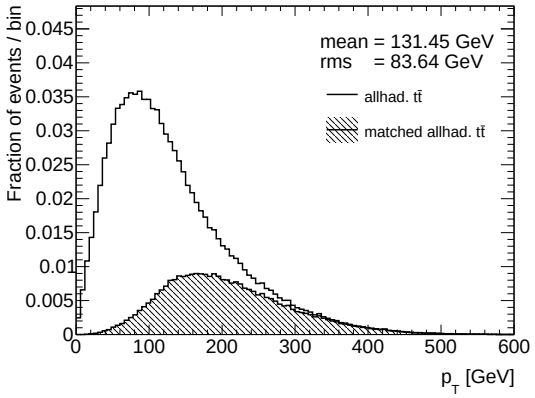

(a) Softer reconstructed top bucket p_T.

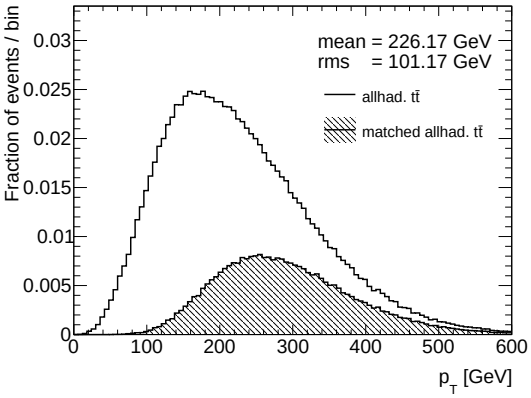

(b) Harder reconstructed top bucket p_T.

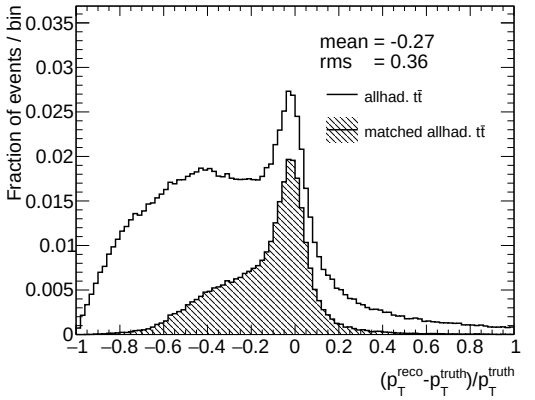

(c) Softer reconstructed top bucket p_T-resolution.

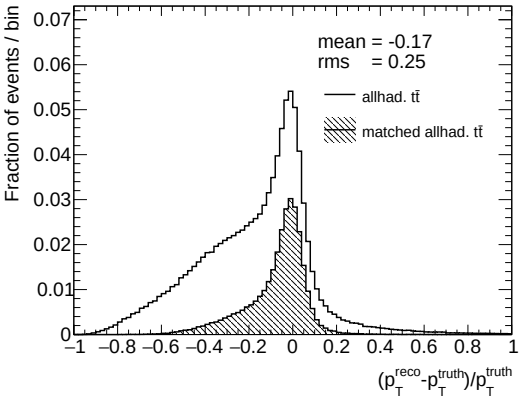

(d) Harder reconstructed top bucket p_T-resolution.

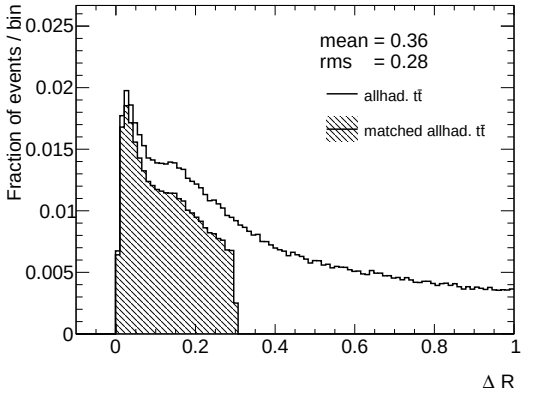

(e) Softer reconstructed top bucket $\Delta R(t_i^{\mathrm{reco}}, t_j^{\mathrm{truth}})$.

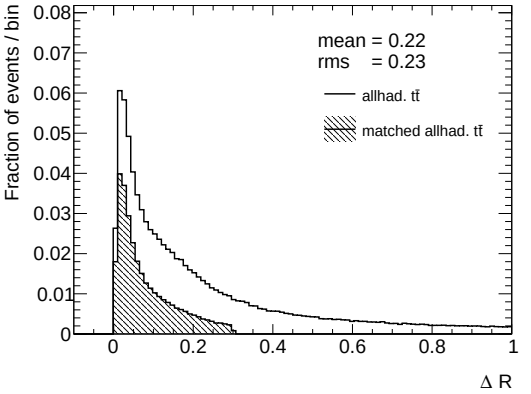

(f) Harder reconstructed top bucket $\Delta R(t_i^{\mathrm{reco}}, t_j^{\mathrm{truth}})$.

Figure 5.1.: Distribution of several reconstructed top quark candidates in simulated allhadronic (allhad.) $pp \to t_h\bar{t}_h$ events. The events are selected according to the *loose* selection summarized in Table 5.1. The fraction of events in which the reconstructed top quark pair is matched to the truth top quarks after final state radiation with $\Delta R(t_i^{\mathrm{reco}}, t_j^{\mathrm{truth}})) < 0.3$ is shown by the shaded area. The mean and root-mean-square of the full distribution is indicated.

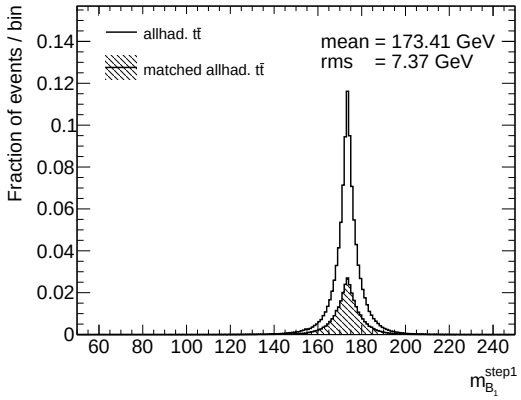

(a) Mass of first bucket in step 1.

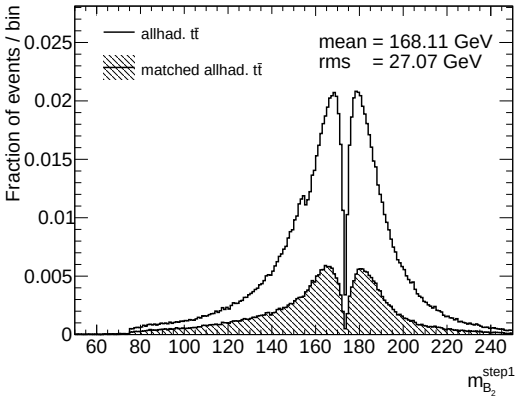

(b) Mass of second bucket in step 1.

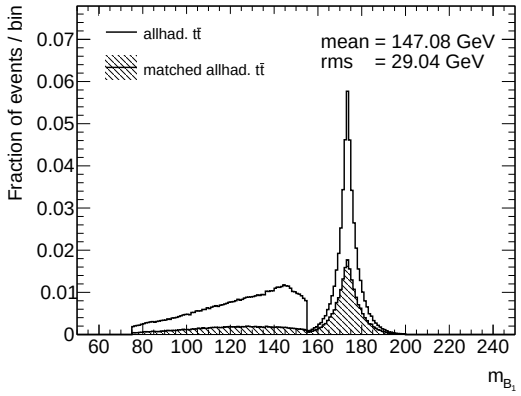

(c) Mass of first bucket.

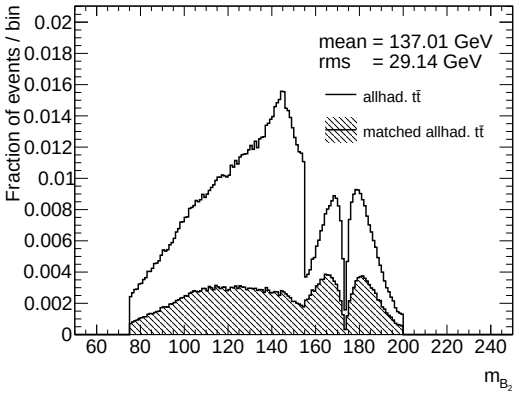

(d) Mass of second bucket.

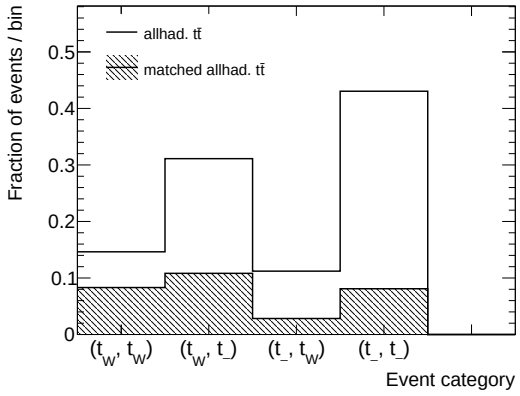

(e) Event categories

Figure 5.2.: Distribution of several reconstructed top quark candidates in simulated allhadronic (allhad.) $pp \to t_h\bar{t}_h$ events. The events are selected according to the *loose* selection summarized in Table 5.1. The fraction of events in which the reconstructed top quark pair is matched to the truth top quarks after final state radiation with $\Delta R(t_i^{\text{reco}}, t_j^{\text{truth}})) < 0.3$ is shown by the shaded area. The mean and root-mean-square of the full distribution is indicated.

from the generated top quarks. The well reconstructed top quarks are characterized by harder transverse momentum. In particular the non-matched p_T-distribution of the softer top bucket peaks below 100 GeV. Evidently a selection on the minimal transverse momentum of the softer reconstructed top bucket provides an increased fraction of well-matched top quarks. Besides the geometrical matching the transverse momentum resolution of the top buckets additionally indicates the quality of the top quark reconstruction. For the harder (softer) top buckets the mean is below zero with a value of around -0.2 (-0.3). The non-matched distribution has a large tail towards negative values. It is expected that some of the t_{-} buckets missing one of the jets cannot fully reconstruct the top quark four momenta. However, the geometrical well-matched top buckets also achieve a better momentum resolution. The distribution of the $\Delta R(t_i^{\mathrm{reco}}, t_j^{\mathrm{truth}})$ shows that the harder top bucket reconstructs the generated top quark more precise than the softer top bucket. Both distributions peak close to zero but the mean of the harder top bucket is around 0.1 closer to zero than the softer top bucket. The geometrical matching is always imposed on both top buckets. As is illustrated by the $\Delta R(t_i^{\mathrm{reco}}, t_j^{\mathrm{truth}})$ distribution it is more likely that the softer top bucket fails the matching requirement while the harder top bucket could still be matched successfully.

The mass of the top buckets determined in the first step of the reconstruction is shown in Figure 5.2(a) and Figure 5.2(b). By construction the distribution of the first bucket is expected to peak at the used true top mass of 173.5 GeV. The weighting ω introduced in Equation 4.0.2 results in a dip-like structure around the true top mass for the second bucket and a broader mass distribution with a root-mean-square of around 27 GeV. In the second step the top buckets are checked for compatibility with a W boson candidate. The t_{-} buckets are identified based on a metric with a reduced mass. The mass distribution after both reconstruction steps is composed of both t_w and t_{-} buckets where all buckets with $m < 155$ ($m > 155$) GeV correspond to t_{-} (t_w) buckets. The event can be grouped in the (t_w, t_w), (t_w, t_{-}), (t_{-}, t_w) and (t_{-}, t_{-}) categories. In summary around 41% (31%) of the harder (softer) top buckets are identified as t_w buckets. The largest fraction of events of approximately 43% is in the (t_{-}, t_{-}) category. The fraction of well-matched top quarks increases with the number of t_w buckets reaching around 57% in category (t_w, t_w). Including also the categories with t_{-} buckets significantly increases the potential reconstruction efficiency.

5.5. Data–MC comparison

The simulated SM $t\bar{t}$ events and the simulated QCD multijet are compared to data in the *preselection* region. Assuming the leading order prediction of the simulated QCD multijet events results in total predicted yield of 521000 ± 26100 as summarized in Table 5.2. The predicted yield deviates from the data yield 743672 by around 30%. Only statistical uncertainties are considered and the normalization of the QCD multijet simulation is expected to have large systematic uncertainties.

Type	Yield
allhad. $t\bar{t}$	106 180(450)
non-allhad. $t\bar{t}$	17 503(88)
QCD dijet	397 000(26100)
Total	521 000(26100)
Data	743 672

Table 5.2.: Predicted event yields for the *preselection* with $\sqrt{s} = 13$ TeV and 36 fb^{-1}. The uncertainty indicates the statistical uncertainty.

Therefore, in a second approach the QCD multijet is normalized to the difference between data and the simulated $t\bar{t}$ contribution assuming that the $t\bar{t}$ normalization is sufficiently well known.

The distribution of several variables for the data to MC comparison assuming the predicted yield are presented in Figure 5.3. The corresponding distributions of the normalized approach are shown in Figure 5.4. The statistical uncertainty of the QCD dijet sample is dominated by events with relatively small transverse momentum of the truth jets having large weights. The following discussion focuses on the normalized distributions. The jet and b-jet multiplicities are well described over the bulk of the distribution within the statistical uncertainty. As these quantities are the main inputs of the bucket algorithm the performance of the top reconstruction related variables can be validated in the following. The transverse momentum of the harder reconstructed top candidate is well described up to around 600 GeV. The transverse momentum of the $t\bar{t}$ system slightly deviates for higher transverse momenta above 300 GeV. The geometrical separation between the top candidates indicates that they are rather back-to-back. The predicted distribution shows a slight slope with respect to the data. The grouping of the event categories is equally well modeled within statistical uncertainties. An improved background rejection for the categories containing t_w buckets is observed. In summary, a good description of several variables describing the bucket algorithm is found in the data to MC comparison. A validation in phase spaces with stricter requirements on the top candidate p_T or the event category are omitted as they would result in large statistical uncertainties on the QCD dijet sample.

5.6. Conclusion

The performance on simulated SM $t\bar{t}$ events is tested with a *loose* selection. The study shows that the bucket algorithm is able to identify top quark pairs and reconstruct their momenta. Basic principles of the jet grouping in two steps and the event categories are well modeled in simulation as confirmed in the data to MC comparison. The analyses presented in this thesis require specific phase spaces for which the performance can potentially deviate from the baseline selection tested here. Thus,

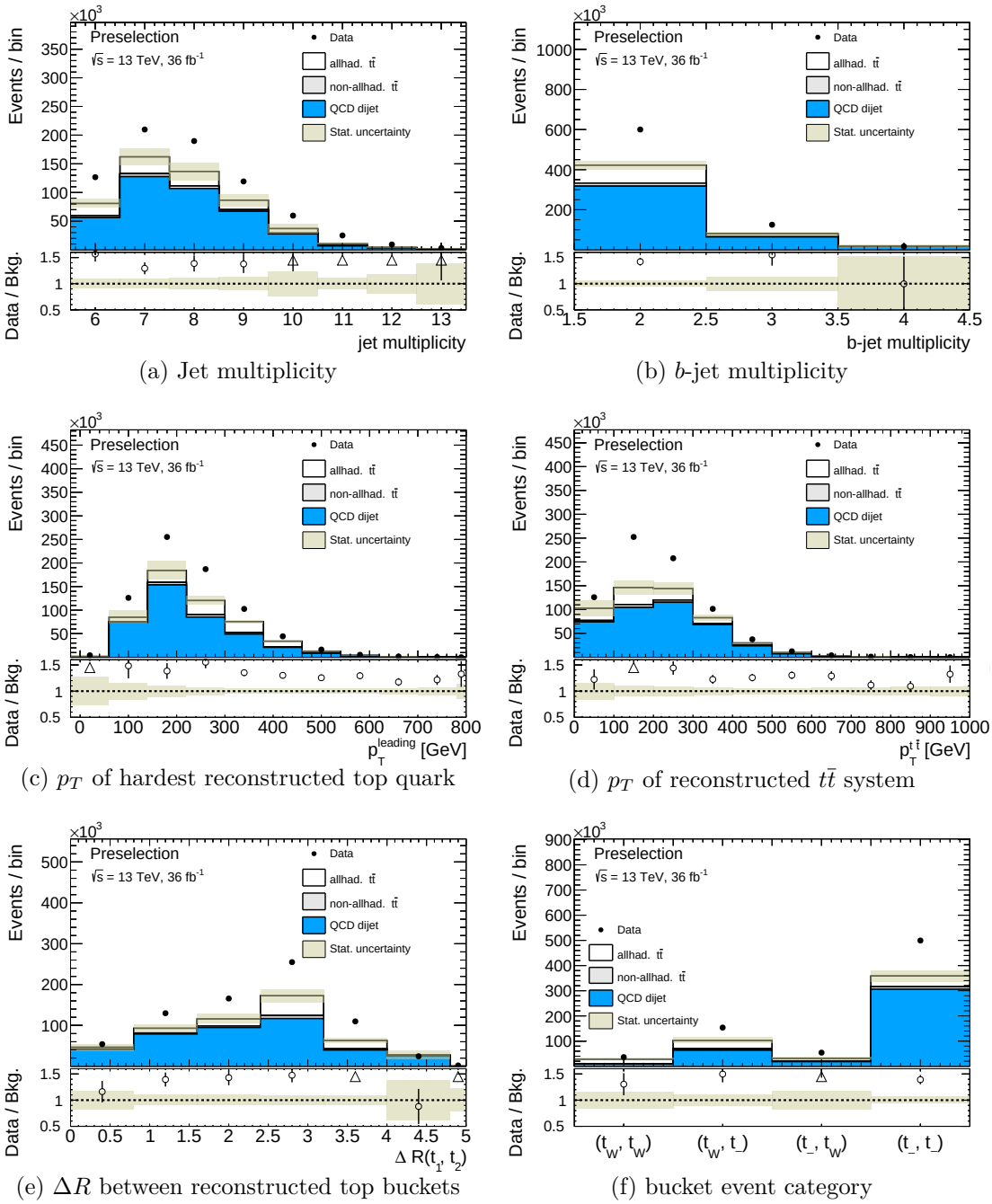

(a) Jet multiplicity

(b) b-jet multiplicity

(c) p_T of hardest reconstructed top quark

(d) p_T of reconstructed $t\bar{t}$ system

(e) ΔR between reconstructed top buckets

(f) bucket event category

Figure 5.3.: Validation plots after *preselection*. The QCD Dijet MC is normalized to the LO prediction. The statistical (Stat.) uncertainty indicates the statistical uncertainty of the background model.

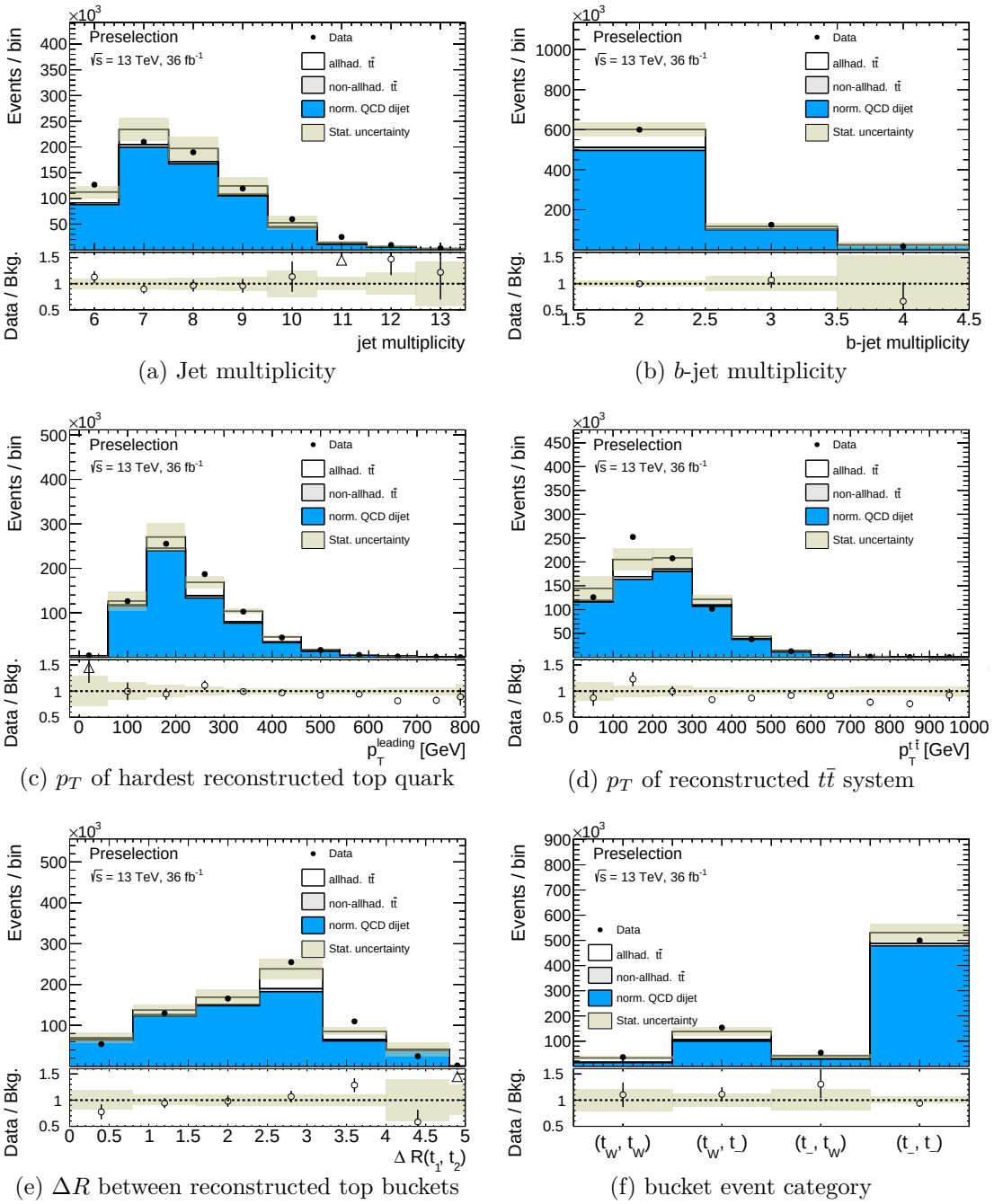

(a) Jet multiplicity

(b) b-jet multiplicity

(c) p_T of hardest reconstructed top quark

(d) p_T of reconstructed $t\bar{t}$ system

(e) ΔR between reconstructed top buckets

(f) bucket event category

Figure 5.4.: Validation plots after *preselection*. The QCD Dijet MC is normalized to data minus SM $t\bar{t}$ MC contribution. The statistical (Stat.) uncertainty indicates the statistical uncertainty of the background model.

the relevant performance features have to be validated and the corresponding top quark related selection is optimized in each analysis chapter separately. Generally, the performance of the bucket algorithm shows a dependence on the topology and kinematics as the main challenge consists in handling the combinatorics for signal and background events. The reconstruction of the top quark momenta can be improved by requiring a moderately boost of the top quark candidates. The $\mathfrak{t}_w$ buckets provide a better reconstruction of the four-momentum and improve the background suppression. Nevertheless, even the $\mathfrak{t}_-$ buckets can adequately reconstruct the top quark four-momenta and improve the overall efficiency of the top quark identification.

6. Search for new heavy particles decaying to a top quark pair in the fully hadronic final state

6.1. Introduction

Heavy particles predicted in models of new physics often couple to top quark pairs. Therefore, the search for resonances in the $t\bar{t}$ invariant mass spectrum $m_{t\bar{t}}$ is a promising tool to test extensions of the Standard Model. Such a search can be done in a model independent way by looking for a peak structure in the reconstructed $m_{t\bar{t}}$ distribution. In order to perform this test one typically considers a specific benchmark model which describes the decay of the new particle to top quark pairs. Nevertheless, as long as the selection does not favor such a specific model it is still possible to draw general conclusions about the limits on the production cross section for alternative and comparable models. The discriminant variable in the limit setting process is the reconstructed $m_{t\bar{t}}$ where the signal is supposed to be manifested by a peak in the smooth background distribution. In the allhadronic $t\bar{t}$ decay mode the $t\bar{t}$ system can be fully reconstructed. Hence, it is expected that the $m_{t\bar{t}}$ resolution is improved compared to the leptonic channels. The presented analysis considers among others a narrow width signal benchmark for which the advantage of a good mass resolution should be more pronounced. The spin-1 color singlet vector boson Z'_{TC2} with a width of 1.2% predicted by the topcolor assisted technicolor model introduced in Chapter 2.4.1 serves as a benchmark model. This model was used in previous $t\bar{t}$ resonance searches at lower center of mass energies in ATLAS, CMS, CDF and DØ [171–174] and at 13 TeV in the semi-leptonic decay mode [59]. The last fully-hadronic analysis in ATLAS used the full 7 TeV dataset [175]. These previous analyses excluded the Z'_{TC2} model for masses up to 3.0 TeV [59].

The analysis presented in this chapter aims at improving the sensitivity for small ditop masses below around 1.3 TeV. The increased luminosity at the LHC and the accordingly higher trigger thresholds make a substructure based analysis in that low $m_{t\bar{t}}$ regime difficult and gives room for a fully-hadronic resolved analysis where multijet triggers with lower thresholds can be used. The specific model mentioned before is already excluded in previous studies for this mass range. Nevertheless, for the purpose to set cross section limits in a generic and largely model independent way it is advantageous to improve the limits on the full mass range.

The reconstruction of the top quark pair is achieved via the bucket algorithm as introduced in Chapter 4 and Chapter 5. It provides an accurate reconstruction of the top quark four momentum for a moderate transverse momentum regime around $p_T = 100 - 400$ GeV. In addition the overwhelming QCD multijet background can be suppressed by selections on the top quark pair kinematics. This is achieved by grouping the Anti-k_T ($R = 0.4$) jets in three buckets. Two of these buckets provide the top quark candidate while the third bucket describes the extra hadronic activity in the event.

The standard model $t\bar{t}$ production is an irreducible background in the analysis. Both the contribution from the fully hadronic and the leptonic $t\bar{t}$ production are considered with MC simulation. The relevant MC set-ups are discussed in Chapter 6.3 and the systematic uncertainties related to the $t\bar{t}$ modeling will be investigated in Chapter 6.8. As described before the other dominant background originates from QCD multijet production. This background is hardly modeled by MC simulation especially for the specific phase space with high jet multiplicities which is used in this analysis. One goal of the top quark reconstruction is the suppression of this background source in order to increase the sensitivity and to become less dependent on uncertainties related to its estimate. The QCD multijet estimation is based on a data driven technique as explained in Chapter 6.6. The estimation of the multijet background will be directly combined with the hypothesis testing procedure. This analysis design provides a more consistent treatment of the case where signal leakage into the control regions can occur and where regions with small sample sizes are present. This combined procedure is introduced in Chapter 6.7. The treatment of systematic uncertainties is described in Chapter 6.8. As the reconstructed $m_{t\bar{t}}$ is initially blinded the performance of the background estimation and the SM $t\bar{t}$ modeling is validated using several control variables in Chapter 6.9. The results in the form of cross section limits on the production cross–section times branching fraction are presented in Chapter 6.10.

6.2. Event selection

The two main considerations for the event selection are the efficient background suppression while keeping the selection as signal-model-agnostic as possible at the same time. The second point is important to interpret the CL_s limits calculated via the profile likelihood fit in the context of different signal models. This is achieved by focusing on selections on the top quark pair reconstruction. As a consequence the SM $t\bar{t}$ is an irreducible background.

6.2.1. Object reconstruction

The analysis focuses on the all-hadronic decay channel. Therefore the main ingredients are the small radius jets in the event together with their b-tagging information. In order to be able to combine the all-hadronic channel with the other top quark

pair decay channels it is important that the object reconstruction guarantees orthogonality between the channels. This is achieved by reconstructing leptons like electrons and muons in the same way it is done by other analyses that concentrate on the leptonic decays. Eventually the leptons are only used to veto such events but otherwise do not enter in the calculation of the final discriminant variable used in the limit setting fit. To achieve the goals mentioned above the object reconstruction heavily relies on standard ATLAS methods. These methods are described in detail in Chapter 3.4.

Data events are only considered when all the detector systems were fully operational. Tracks with $p_T > 400$ MeV are used to determine the interaction vertices. The vertex which maximizes the sum of associated tracks $\sum p_{T,\text{track}}^2$ is selected as primary vertex. The event must contain at least one vertex with more than one associated track.

The jets are the main component used to calculate the final discriminant variable. The calibration of the jets to the jet energy scale uses corrections based on simulation and *in situ* methods with $\sqrt{s} = 13$ TeV data [176, 177]. The reconstructed and calibrated offline jets have to satisfy $p_T > 25$ GeV and $|\eta| < 2.5$ to be considered in the further selection process. Jets with $p_T < 60$ GeV and $|\eta| < 2.4$ originating from pileup only are suppressed by the Jet Vertex Tagger (JVT) requirement [158] which exploits information from associating tracks to jets.

The reconstruction of electrons is based on clusters in the electromagnetic calorimeter combined with the track information of the ID [151, 178]. The LAr crack veto is enabled by requiring that the electron candidates are outside $1.37 < |\eta_{\text{cluster}}| < 1.52$. Track-matching and shower-shape variables are used to define a tight set of selection criteria as explained in Reference [151]. Muon candidates are build from tracks of the MS which are matched to ID tracks [147]. In a next step improved tracks are calculated using the combined information of the two sub-detectors. Isolation criteria are applied on the electrons and muons in order to reduce the contribution from non-prompt leptons.

Muons and electrons with $p_T > 25$ GeV and $|\eta| < 2.5$ are selected and used in the lepton-jet overlap removal procedure. The motivation of the overlap removal is to reduce the probability of double-counting a single detector response in the reconstruction of several objects. Objects are not considered in subsequent overlap removal steps once they are rejected. If a calo-tagged muon shares an ID track with an electron it is removed. If any electron shares an ID track with the remaining muons it is removed. For the overlap removal the jets are categorized in all jets and the sub-category of non-pileup jets which satisfy the JVT requirement. The single jet closest to an electron within $\Delta R < 0.2$ is removed to avoid double-counting of electron energy deposits as a jet. Additionally electrons which are within $\Delta R < 0.4$ of a non-pileup jet are removed in a next step. High-energy muons can deposit a significant amount of energy in the calorimeter. Hence, jets which are within $\Delta R < 0.2$ or ghost-matched to a muon are rejected under two possible circumstances. Namely, if less than three tracks are associated to the jets or secondly, if the transverse momentum ratio of the muon to the jet is larger than

0.5 ($p_T^{\text{muon}}/p_T^{\text{jet}} > 0.5$) and if the ratio of transverse momentum of the muon to the transverse momentum of the sum of the tracks associated to the jet is larger than 0.7 ($p_T^{\text{muon}}/p_T^{\text{sum trk, jet}} > 0.7$). Muons are then rejected if they are within $\Delta R < 0.4$ of the remaining non-pileup jets to suppress the contribution of muons originating from heavy flavor decays.

The standard ATLAS b-tagging algorithm `MV2c10` [159, 160] as described in Chapter 3.4.6 performs the classification of the above mentioned Anti-k_T ($R = 0.4$) jets into b-, c- and light-quark jets. It is based on a multivariate technique combining topological information of secondary and tertiary decay vertices with the information from the impact parameters of displaced tracks. Depending on the considered region the *tight* or *loose* working point is chosen.

In the considered benchmark model the heavy Z' bosons decay directly to $t\bar{t}$ pairs. So a good reconstruction of the $t\bar{t}$ system is essential for the final limit setting in terms of achieving a good background suppression and signal resolution. Depending on the mass of the resonance the top quarks from the decay have a different p_T regime. At a high enough boost of the top quarks purely substructure based techniques are efficient. In order to address also adequately the intermediate p_T regime the buckets of tops method [16] is used in the resonance search. The buckets of tops method is based on a relatively high multiplicity of Anti-k_T ($R = 0.4$) jets and is further explained in Chapter 4. Further details of its general performance can also be found in Chapter 5. The reconstruction performance in the context of the resonance search is investigated in Chapter 6.4.

6.2.2. Event preselection and categorization

The 2015 and 2016 dataset collected by the ATLAS detector is used which corresponds to an integrated luminosity of 36.1fb^{-1}. The analysis is based on an unprescaled trigger to exploit the full available data. At low invariant masses $m_{t\bar{t}}$ the Anti-k_T ($R = 0.4$) jets of the top quark decay are still separated and a multijet trigger is able to select signal events. For 2016 data taking the unprescaled multijet trigger with the lowest p_T requirement for at least five jets requires $E_T > 65$ GeV and a maximal pseudorapidity of $|\eta| < 2.4$ for the jets at the high-level trigger. In addition the level-one (L1) trigger rate is reduced by requiring $E_T > 15$ GeV for at least four L1 *Region-of-interest* jets. For the 2015 data taking period a lower threshold trigger is available and used. It is based on the same level-one trigger chain but the five jets with the largest transverse momentum high-level trigger are only required to have $E_T > 60$ GeV.

In order to be less dependent on the trigger modeling the reconstructed offline jet with the 5$^{\text{th}}$ hardest transverse momentum must satisfy $p_T > 75$ GeV. This selection also reduces the signal acceptance at low invariant masses. Alternatives using b-jet trigger or new trigger approaches specific to the top quark decay are discussed in Chapter 8. In addition the five leading offline jets have to be within $|\eta| < 2.4$ in order to achieve a better agreement between online and offline jet selection. Even with this pre-selection the triggers are not perfectly modeled in simulation.

A dedicated set of scale factors is derived to correct for trigger inefficiencies in Chapter 6.5. Using the trigger SFs helps to maintain a high signal acceptance for events having the fifth hardest jets in the range $p_T = 75 - 95$ GeV.

Orthogonality with respect to the resonance searches in the leptonic decay mode is guaranteed by vetoing all events which contain an isolated electron or muon.

The top quark reconstruction and especially the efficiency of finding a W boson candidate in $t\bar{t}$ events would profit from an even lower jet p_T threshold. But the disadvantage would be a larger QCD multijet background and relatively large systematic uncertainties of the calorimeter jets at low transverse momentum ($p_T < 50$ GeV). At least six Anti-k_T ($R = 0.4$) jets are required in the final selection. This reduces the multijet background and is consistent with the expectation of the $t\bar{t}$ decay at leading order.

The same jets are also used for the b-tagging. Due to the top quark reconstruction procedure at least two b-tagged jets are required. In addition the b-tagging selection suppresses the QCD multijet background. A combination of the *loose* and *tight* working points is used to define the *b-tag control region* and the *b-tag signal region* in Chapter 6.6. As is motivated in more detail in Chapter 6.8.4 the two hardest b-jets in an event are required to satisfy $|\eta| < 1.6$ in order to achieve a better description of the data-driven QCD multijet background estimate.

The above selection defines also the input to the top quark pair reconstruction. Additional event selection is performed on the output consisting of the masses or the transverse momentum of the top quarks as well as the masses of the W candidates. Inaccurately reconstructed top quarks and QCD multijet events are rejected by requiring $p_T > 200$ GeV for the top quark candidates. Triggers with lower thresholds would allow one to use lower p_T^{top} criteria or split the analysis in different p_T^{top} regions in a future iteration. For the signal region the top event category ($\mathfrak{t}_w$, $\mathfrak{t}_w$) is preferred as it gives the highest QCD rejection and also the best resolution of the reconstructed top quark four momenta. As a result the resolution of the invariant mass $m_{t\bar{t}}$ of a signal is improved which helps eventually in the limit setting procedure and the hypothesis test. Top candidates with a looser selection are used for the background estimation and as control regions in the profile likelihood fit as described in Chapter 6.6 and Chapter 6.7.

The basic preselections with respect to the jets and the top candidates for the events finally used in the fit are summarized in Table6.1. All events are categorized based on the top quark candidate and b-tagging information. The bucket algorithm allows a categorization in the four event categories ($\mathfrak{t}_w$, $\mathfrak{t}_w$), ($\mathfrak{t}_w$, $\mathfrak{t}_-$), ($\mathfrak{t}_-$, $\mathfrak{t}_-$) and ($\mathfrak{t}_0$, $\mathfrak{t}_0$). The *b-tag control region* contains events passing the *loose* b-tagging but failing the *tight* selection. The *b-tag signal region* is composed of events with *tight* b-tagged jets. Therefore, in total eight orthogonal regions denoted as A, B, C, D, A_0, A_-, C_0 and, C_- are distinguished. The regions are defined and summarized in Table 6.2. The region D consisting of ($\mathfrak{t}_w$, $\mathfrak{t}_w$) buckets and *tight* b-tagged jets is expected to provide the highest sensitivity and is commonly referred to as the signal region. Besides region D also the regions A, B and C are considered in the profile-likelihood fit as explained in Chapter 6.7. The looser top tagging regions

Variable	Selection
Number of jets ($p_T > 25$ GeV)	≥ 6
Multijet trigger	pass
Number of jets ($p_T > 75$ GeV)	≥ 5
Hardest jets ($\|\eta\| < 2.4$)	≥ 5
Number of b-tagged jets	≥ 2
Hardest b-tagged jets ($\|\eta\| < 1.6$)	≥ 2
Top candidates p_T	≥ 200 GeV
Event category	($\mathfrak{t}_w$, $\mathfrak{t}_w$), ($\mathfrak{t}_w$, $\mathfrak{t}_-$)

Table 6.1.: Summary of event selections used in the $t\bar{t}$ resonance search. Only the selection with respect to the small-R jets and the top candidates is shown. The set of selection criteria excluding the event categories defines the preselection.

	($\mathfrak{t}_0$, $\mathfrak{t}_0$)	($\mathfrak{t}_-$, $\mathfrak{t}_-$)	($\mathfrak{t}_w$, $\mathfrak{t}_-$)	($\mathfrak{t}_w$, $\mathfrak{t}_w$)
b-tag CR	A_0 $(2.1 \pm 0.0)\%$	A_- $(4.2 \pm 0.1)\%$	A $(12.3 \pm 0.2)\%$	B $(38.9 \pm 0.9)\%$
b-tag SR	C_0 $(8.0 \pm 0.1)\%$	C_- $(16.9 \pm 0.2)\%$	C $(44.9 \pm 0.5)\%$	D $(79.6 \pm 1.3)\%$

Table 6.2.: The event categorization based on the top tagging and b-tagging information after the preselection. The expected SM $t\bar{t}$ purity in each region as inferred from simulation is shown in parenthesis. The error indicates the statistical uncertainty. The regions A, B, C and D contribute to the profile likelihood fit. The looser top tagging selection in the regions A_0, A_-, C_0 and, C_- is used for validation purposes.

($\mathfrak{t}_0$, $\mathfrak{t}_0$) and ($\mathfrak{t}_-$, $\mathfrak{t}_-$) with the corresponding regions A_0, A_-, C_0 and, C_- contribute to the estimation of the multijet background modeling uncertainty as detailed in Chapter 6.8.4.

6.3. Signal and background modeling

The applied event selection results in a dataset which consists mostly of QCD multijets and SM $t\bar{t}$ events. A small contribution from single top production or associated production of top quark pairs and vector bosons are not directly considered but enters through the data-driven background estimation. The QCD multijet production is the largest background and will be determined from data as described in Chapter 6.6. The signal benchmarks and the SM $t\bar{t}$ contribution is modeled by a MC simulation. A description of how these processes are simulated and normalized and what algorithms are used is given in the following. As explained in Chapter 2.4 there is a plethora of models predicting heavy resonances decaying to $t\bar{t}$. A condensed set of models with certain characteristics is summarized in Table 2.2. These models cover a wide range of classes ranging from new spin-1 to spin-2 color-singlet or color-octet bosons with a narrow width over mass $\Gamma/m = 1\%$ to broader signals up to $\Gamma/m = 40\%$. The benchmark signal models are generated in a mass range from 500 GeV up to 2000 GeV.

6.3.1. Signal modeling of narrow spin-1 resonances

The used benchmark model is the process $pp \to Z'_{\mathrm{TC2}} \to t\bar{t}$ for which the cross-sections are calculated based on Reference [60]. Signal samples are simulated for several mass points in the range from 500 GeV to 1250 GeV using the Pythia 8 [107] generator. The simulation relies on the default settings for a generic SSM Z' generation and on the NNPDF2.3 LO PDF set [138] and the A14 [110] set of tuned parameters. This set-up provides a narrow width Z' which is well suited for the considered benchmark Z'_{TC2}. The LO cross sections of the Z'_{TC2} model are multiplied by a k-factor of 1.3 to get the next-to -leading order cross section based on calculations in Reference [179, 180].

The same signal samples are used for the mediator in the simplified DM models. The samples are reweighted to describe the expected mediator width. The cross-sections are calculated with the MadGraph5_aMC@NLO [120] framework at leading order. The spin correlations are preserved by using the MadSpin [181] program for the top quark decays.

6.3.2. Signal modeling of spin-2 resonances

The spin-2 *Bulk* RS graviton G_{KK} benchmark model is simulated with the MadGraph5_aMC@NLO framework at leading order using the NNPDF2.3 PDF set and the subsequent parton shower is modeled by Pythia 8. The LO cross sections

for $\sigma_{G_{KK}} \times \mathrm{BR}(G_{KK} \to t\bar{t})$ are extracted from MadGraph5_aMC@NLO.

6.3.3. Signal modeling of broad spin-1 resonances

A characteristic spin-1 signal model predicting a larger width is given by the color-octet KK gluon g_{KK} model. The considered benchmark is generated with Pythia 8 and the NNPDF2.3 LO PDF set and the A14 set of tuned parameters. The default generated width is $\Gamma/m = 30\%$. The cross sections times branching fractions $\sigma_{g_{KK}} \times \mathrm{BR}(g_{KK} \to t\bar{t})$ are extracted from Pythia 8.

6.3.4. Top quark pair modeling

The simulation of SM $t\bar{t}$ events is described in Chapter 3.3.1. The nominal SM $t\bar{t}$ samples are corrected for electroweak higher order effects [182] following the procedure described in Reference [171]. This involves an event-by-event weight based on the $t\bar{t}$ kinematics such as the partonic energy $\sqrt{s} = m_{t\bar{t}}$, the scattering angle $z = \cos(\Theta^{\star})$ the top quark in the $t\bar{t}$ rest frame and the type of the initial state partons.

6.3.5. General treatment of simulated events

Events from multiple proton-proton interactions are added to the simulated MC events. These pileup interactions are simulated with the Pythia 8 generator, the `MSTW2008` PDF set and the `AUET2` tune [108]. All events from simulated MC samples are reweighted to produce the pileup distribution measured in data during the 2015 and 2016 data taking period.

The simulated MC events are processed through the detector simulation [105] using Geant4 [140] or a fast detector simulation [183]. All nominal simulated MC samples are using the full detector simulation unless stated otherwise. The same reconstruction software is run on the simulated MC samples as on the data. Corrections based on data control samples are applied on simulated events to achieve an agreement for object identification efficiencies, energy scales and energy resolutions.

6.4. Performance of top quark pair reconstruction

The event selection in the $t\bar{t}$ resonance search is close to the general selection in the performance study in Chapter 5. In contrast the phase space is characterized by a harder transverse momentum selection and tighter selection on the top quark candidates in terms of the event category ($\mathfrak{t}_w$, $\mathfrak{t}_w$) and ($\mathfrak{t}_w$, $\mathfrak{t}_{\_}$). The top reconstruction performance in the most sensitive signal region D corresponding to *tight* b-tagging selection and to category ($\mathfrak{t}_w$, $\mathfrak{t}_w$) is investigated in terms of the mass resolution in Chapter 6.4.1 and the reconstruction efficiency in Chapter 6.4.2. The performance of the $t\bar{t}$ reconstruction for all possible regions is summarized in Table 6.3.

Event category	Fraction of events [%]		Matched top-quark pairs [%]	
	SM $t\bar{t}$	Z'_{TC2} (850 GeV)	SM $t\bar{t}$	Z'_{TC2} (850 GeV)
($\mathfrak{t}_0$, $\mathfrak{t}_0$)	16.5(3)	12.6(7)	57.1(10)	63.6(27)
($\mathfrak{t}_-$, $\mathfrak{t}_-$)	17.5(3)	15.0(9)	66.7(9)	74.2(26)
($\mathfrak{t}_-$, $\mathfrak{t}_w$)	7.8(2)	7.9(8)	72.2(13)	80.0(39)
($\mathfrak{t}_w$, $\mathfrak{t}_-$)	30.2(4)	30.9(12)	78.9(6)	82.6(15)
($\mathfrak{t}_w$, $\mathfrak{t}_w$)	28.0(4)	33.6(13)	88.7(5)	90.7(11)

Table 6.3.: Performance of the bucket algorithm as a function of the five possible event categories. The fraction of events in each category with respect to the preselection explained in Chapter 6.2.2 is shown. The *tight b*-tagging selection is applied. In each category the relative fraction of events that have correctly matched top-quark pairs is indicated. In matched events all top buckets satisfy the geometrical condition $\Delta R(\text{bucket}, \text{truth top}) < 0.3$. The momenta of the truth top quarks are evaluated immediately before the decay. The statistical uncertainty of the simulated events describes the error.

The ($\mathfrak{t}_w$, $\mathfrak{t}_w$) and ($\mathfrak{t}_w$, $\mathfrak{t}_-$) regions account for around 60% of the events for the simulated SM $t\bar{t}$ background as well as for a representative Z'_{TC2} (850 GeV) signal model. The different transverse momenta of the top quarks is the main topology difference between the two considered samples. The tight top tagging provided by ($\mathfrak{t}_w$, $\mathfrak{t}_w$) and ($\mathfrak{t}_w$, $\mathfrak{t}_-$) helps to suppress the QCD multijet background and improves the reconstruction of the $t\bar{t}$ system. Top quark candidates from SM $t\bar{t}$ and from the signal sample are matched to truth top quarks using the geometrical condition $\Delta R(\text{bucket}, \text{truth top}) < 0.3$. A high matching efficiency of around 90% (80%) in category ($\mathfrak{t}_w$, $\mathfrak{t}_w$) (($\mathfrak{t}_w$, $\mathfrak{t}_-$)) is achieved.

6.4.1. Mass resolution

The reconstructed mass of the $t\bar{t}$ system $m_{t\bar{t}}^{\mathrm{reco}}$ is calculated from the four-vector sum of the two top candidates. The $m_{t\bar{t}}^{\mathrm{reco}}$ of the three classes of signal models is presented in Figure 6.1 for the most sensitive signal region D (($\mathfrak{t}_w$, $\mathfrak{t}_w$)). The quality of the reconstruction depends on the considered mass range and width. The low mass distribution $m_{Z'} \approx 500$ is dominated by statistical uncertainties due to the trigger thresholds and the strong cuts to suppress the QCD multijet background. Therefore it is omitted from the following discussion. The narrow-width signals with a pole mass around 750 GeV are well reconstructed for the Z'_{TC2} and the G_{KK} case. The experimental resolution is evidently larger than the generated width. The g_{KK} sample with a width $\Gamma/m = 30\%$ exceeds the experimental resolution. For higher pole masses the distributions of all signal samples develop a tail towards lower reconstructed masses. This behavior is especially pronounced for the broader width signals. There are two processes contributing to the tail effect. On the

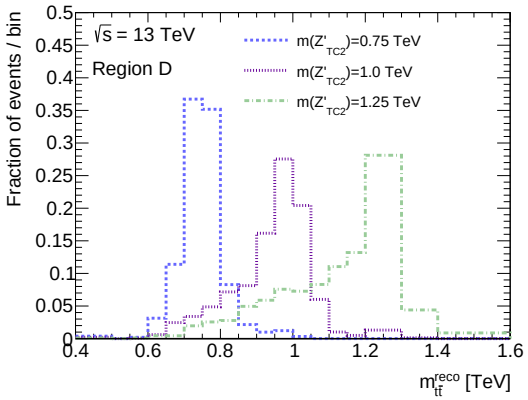

(a) Topcolor assisted technicolor Z'_{TC2}

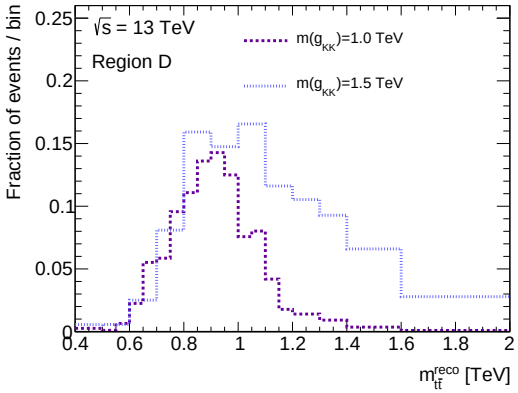

(b) KK gluon g_{KK} ($\Gamma/m = 30\%$)

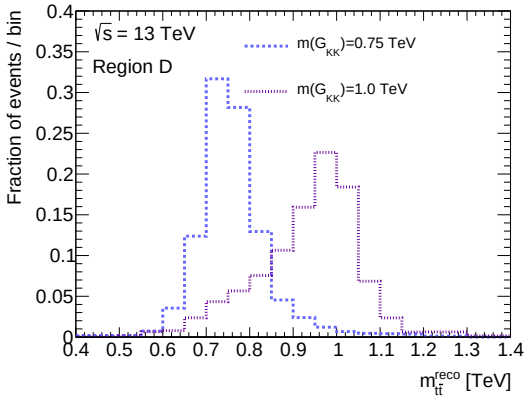

(c) KK Graviton G_{KK}

Figure 6.1.: Distribution of reconstructed $m_{t\bar{t}}$ in several simulated signal models.

one hand parts of the final state radiation off the $t\bar{t}$ system can be lost in the $t\bar{t}$ reconstruction. On the other hand independent of the reconstruction the steeply falling parton luminosities induce a tail in $m_{t\bar{t}}$ for increasing partonic center of mass energies. The first process is expected to increase for higher pole masses while the second is enhanced for broad signals.

The sensitivity inferred in the profile-likelihood fit depends on the achievable mass resolution. A good resolution facilitates the separation of signal and background events and helps to constrain the background contribution in bins with a small expected signal contribution. For simplicity the following description concentrates on the narrow Z'_{TC2} signal benchmark model. The mass resolution is calculated with respect to top quarks before final state radiation as shown in the left side of Figure 6.2 and after final state radiation before the decay as shown on the right side respectively for three signal mass points from 600 GeV, 850 GeV to 1250 GeV. Generally the resolution decreases with increasing pole mass and a tail develops towards lower masses for the Figures using the $m_{t\bar{t}}$ before FSR as reference. The resolution after final state radiation is better for all three mass points with the largest improvement at high masses. Therefore, the incomplete reconstruction is caused by the missing final state radiation. In both cases for the $m_{t\bar{t}}$ after and before FSR the resolution is larger than the generated width $\Gamma/m = 1.2\%$. The performance is expected to slightly differ for the broader KK gluon g_{KK} samples with a width of at least 10%. In addition the mass and transverse momentum dependence of the top tagging and the b-tagging efficiency can influence the shape of the reconstructed $m_{t\bar{t}}^{\mathrm{reco}}$ as is discussed in the following chapter.

6.4.2. Reconstruction efficiency

The acceptance times efficiency of all signal regions as a function of the mass of the $t\bar{t}$ system is presented in Figure 6.3. The top quark four momenta are evaluated at truth level before the final state radiation. The acceptance times efficiency reaches the maximum around 1.2 TeV. Even for higher masses the efficiency stays finite. This is explained by the tail towards small $m_{t\bar{t}}$ for signal models with a high pole mass. The difference between the spin-1 and the spin-2 benchmarks models is caused by the different topologies. The spin-2 KK graviton G_{KK} tends to be more central and harder than the spin-1 model. Thus, the efficiency is larger at low masses (< 1.5 TeV). At high masses (> 1.5 TeV) in turn the harder top quarks of the G_{KK} cannot be resolved by the bucket algorithm anymore.

In addition two separate efficiencies are investigated to highlight the kinematic dependence of the top quark reconstruction in the most sensitive signal region D. The top tagging efficiency ϵ(Doubletag) quantifies the efficiency to simultaneously tag two hadronically decaying top quarks in an event. The bucket algorithm has a minimal requirement of a baseline selection in terms of jets and b-tagging in order to calculate top quark candidates. Thus, the ϵ(Doubletag) is calculated with respect to all applied preselections excluding the top quark related selections. The requirements on the reconstructed top quark mass, the mass of the W-boson candidate

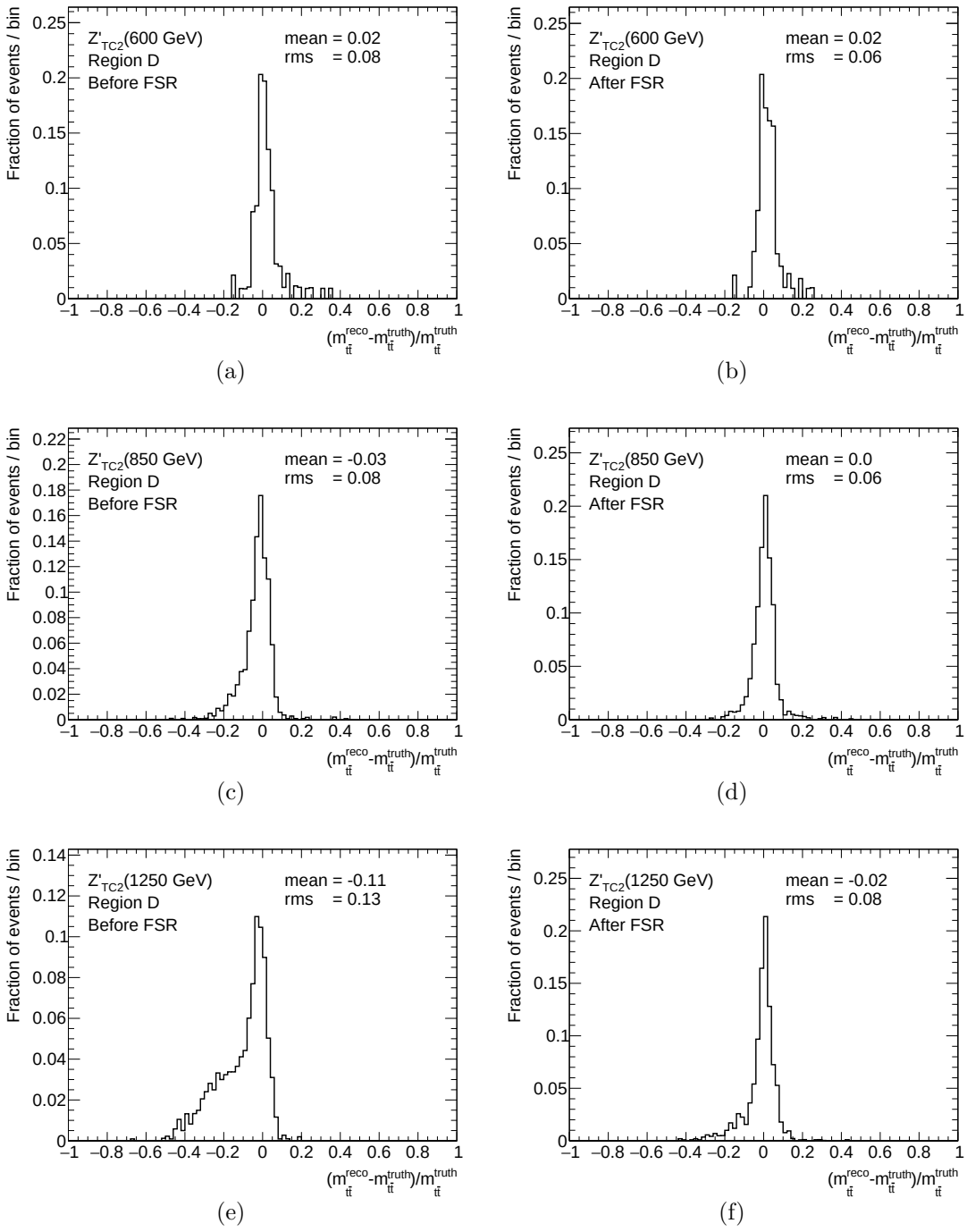

Figure 6.2.: Resolution of the $t\bar{t}$ mass in region D. The left side uses the truth mass before final state radiation as the reference mass. The right side uses the truth mass after final state radiation before the decay as the reference mass.

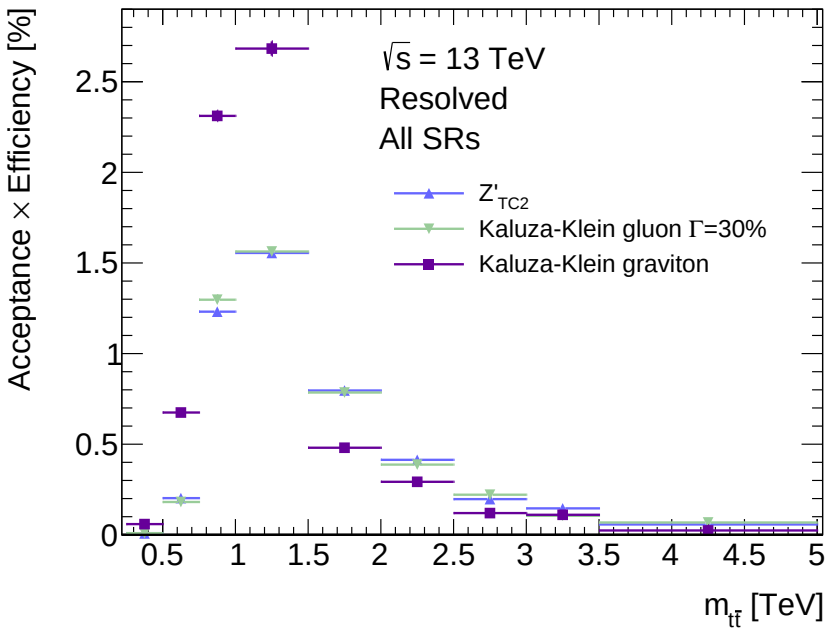

Figure 6.3.: Acceptance times efficiency for various signal benchmark models as a function of the mass of the $t\bar{t}$ system. The top quark four momenta are evaluated before final state radiation.

and the transverse momentum of the two top quark candidates causes potential inefficiencies in the ϵ(Doubletag). Furthermore the matching efficiency ϵ(Matching) shows the accuracy of the reconstruction. An event is successfully matched if both top buckets t_i^{reco} are within $\Delta R(t_i^{\text{reco}}, t_j^{\text{truth}}) = \sqrt{(\eta_i - \eta_j)^2 + (\phi_i - \phi_j)^2} < 0.3$ of a true top quark t_j^{truth}. The momenta of the t_j^{truth} are evaluated after FSR. The ϵ(Matching) is calculated with respect to the top tagged events. The following equations summarize the definition of the efficiencies

$$\epsilon(\text{Doubletag}) = \frac{\text{Top reconstruction selection}}{\text{Preselection}} \tag{6.4.1}$$

$$\epsilon(\text{Matching}) = \frac{\text{Geometrical matching}}{\text{Top reconstruction selection AND Preselection}}. \tag{6.4.2}$$

The doubletag and matching efficiency are studied in simulated SM $t\bar{t}$ events as a function of the truth top quark transverse momentum and as a function of the truth mass of the $t\bar{t}$ system. The efficiencies are presented in Figure 6.4.

The transverse momentum dependence of the efficiency is comparable for the softer top candidate and the truth top quark. Top buckets with a higher transverse momentum achieve a higher reconstruction accuracy. The doubletag efficiency has a threshold around $p_T = 200$ GeV due to the transverse momentum selection on the top buckets. It reaches a maximum around $350 - 400$ GeV. For higher transverse momenta the doubletag efficiency decreases again due to the merging of the small-

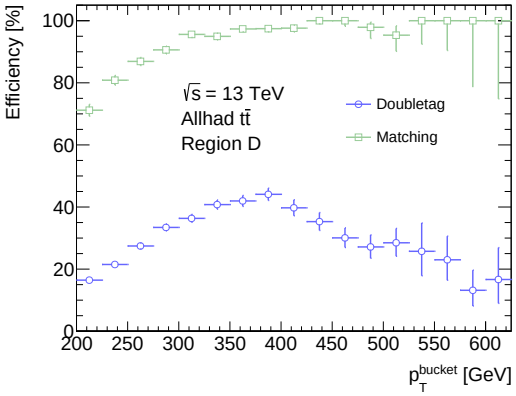

(a) p_T of softer top bucket.

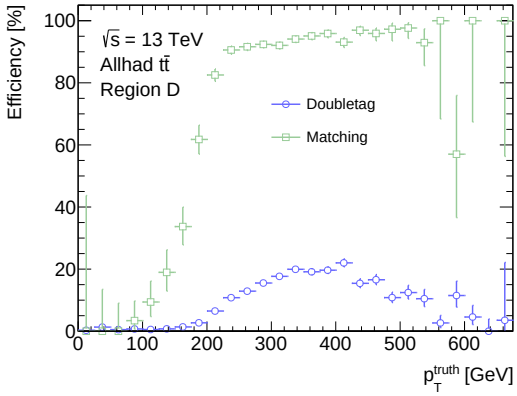

(b) p_T of softer truth top quark after FSR.

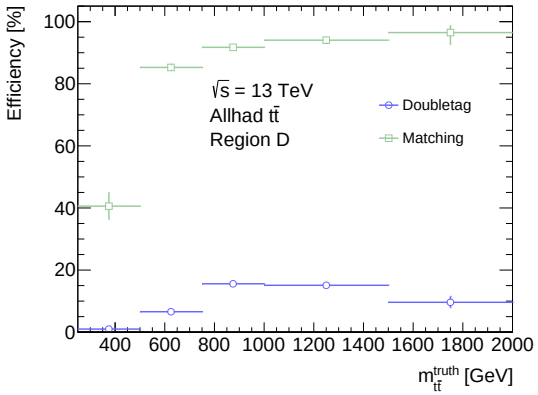

(c) Mass of the $t\bar{t}$ system after FSR.

Figure 6.4.: Doubletag and matching efficiency in region D for different variables in simulated allhadronic $t\bar{t}$ events.

R jets while the matching efficiency stays on a high level ($> 90\%$). In a similar way the doubletag efficiency starts to be efficient for truth masses above 500 GeV reaching the maximum for masses around 800 GeV and staying almost constant for higher masses up to around 1500 GeV. The matching efficiency equally increases with the truth mass and acquires a plateau above approximately 800 GeV.

6.5. Multijet trigger

The multijet trigger is ideally operated in the efficiency plateau regime. This can be achieved by a suitable selection on the offline jets such as the imposed transverse momentum thresholds. Requiring the five hardest jets to have $p_T > 75$ GeV in turn reduces the signal acceptance especially for small top quark p_T or low signal masses. The considered multijet trigger especially the one used during the 2016 data taking period with five jets at the high-level-trigger level have a relatively flat turn-on curve. Therefore, even the tight jet selection is insufficient to achieve a fully efficient trigger regime. On the other hand keeping the low value of $p_T^{\text{jet5}} > 75$ GeV is important to maintain a reasonable sensitivity at low $m_{t\bar{t}}$ masses. Thus, the efficiency of the multijet rigger is calculated in data and in simulated events and corresponding scale factors are derived to correct for a potential trigger mis-modeling in simulation. The trigger scale factors are derived in a dedicated dataset using a looser selection omitting the requirements on the top candidates. Generally, trigger scale factors can be calculated even in datasets with large statistical uncertainty using the *bootstrap* method [184]. The event selection remains close to a $t\bar{t}$ topology in order to avoid a potential unconsidered topology dependence of the scale factors. The *bootstrap* method relies on a prescaled reference trigger with reduced requirements on the jet multiplicity and the jet transverse momentum. Specifically it requires fewer jets at the high-level trigger level as well as at the level-one trigger guaranteeing a sufficiently looser selection to capture the potential inconsistencies and inefficiencies in the simulated trigger decisions. The reference trigger chain is seeded by three level-one jets satisfying $E_T > 15$ GeV. At the high-level trigger four jets with $E_T > 45$ GeV are required. That specific prescaled trigger provides a total integrated luminosity of 44839.0nb^{-1} in 2016 and 11457.8nb^{-1} in 2015. The dedicated dataset is selected by events passing the reference trigger criteria. The default jet selection is applied. In addition at least two jets must be identified as *loose* b-tagged jets. The top tagging related variables are excluded in the selection in order to enhance the available number of events in the dataset. Such a selection allows a reasonable sample size to calculate the trigger efficiency turn-on in data. The main contribution in data for this preselection originates from QCD multijets. Nevertheless the preselection enhances events with a $t\bar{t}$ topology-like structure.

The trigger scale factors are derived from the ratio of the trigger efficiency in data ϵ(data) over the efficiency in simulated fully-hadronic SM $t\bar{t}$ MC $\epsilon(t_h\bar{t}_h$ MC)

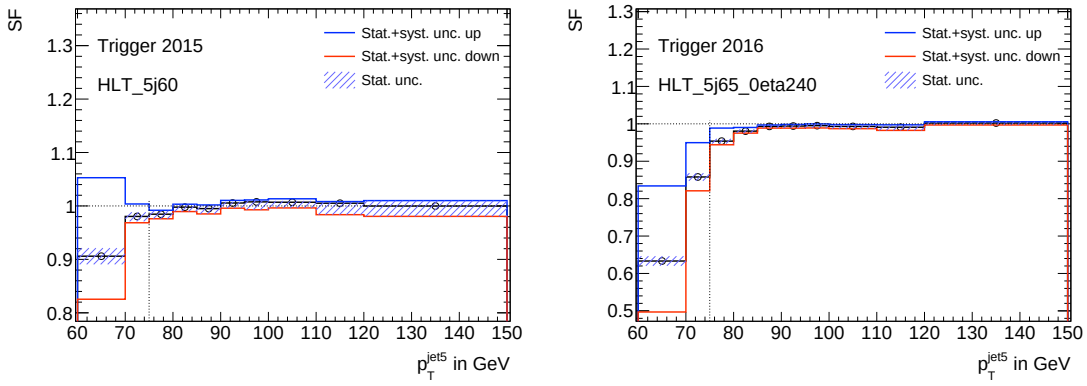

(a) 2015 data (b) 2016 data

Figure 6.5.: Trigger SFs and uncertainty for the 2015 and 2016 trigger selection as a function of the fifth hardest jet in the event. The dotted line illustrates the offline selection of $p_T > 75$ GeV used in the event selection of the resonance search. The effect of the statistical uncertainty (stat. unc.) is shown together with the combined statistical and systematic uncertainty with the components added in quadrature (stat. + syst. unc.).

events. The corresponding efficiencies

$$\epsilon(\text{sample}) = \frac{\text{analysis trigger fired}}{\text{reference trigger fired}} \tag{6.5.1}$$

$$\text{SF}^{\text{trig}} = \frac{\epsilon(\text{data})}{\epsilon(t_h\bar{t}_h \text{ MC})} \tag{6.5.2}$$

define the nominal scale factors. The scale factors are recalculated taking into account simulated $t\bar{t}$ events shifted according to the jet energy scale uncertainties as described in Chapter 6.8.7 and Chapter 6.8.8. Such scale factors are calculated equivalently and added as an systematic uncertainty on the nominal trigger scale factors. The resulting scale factors for the trigger 2015 and the trigger 2016 with the corresponding statistical and systematic uncertainties are presented in Figure 6.5. The larger statistical uncertainties for the trigger 2015 is mainly caused by the smaller available dataset in 2015 compared to 2016. The trigger 2015 is fully efficient within the uncertainties as long as the five hardest offline jets have a transverse momentum above for 80 GeV. The uncertainty of the trigger 2016 is dominated by the systematic component for transverse momenta below 85 GeV. In both setups the scale factors significantly deviate from one starting at around 80 GeV. That illustrates the necessity to correct the distributions with the trigger scale factors if events with softer jets are used in the analysis.

The pseudorapidity restrictions on the jets at the high-level trigger motivated the related offline jet criteria as supported by the scale factor distributions shown

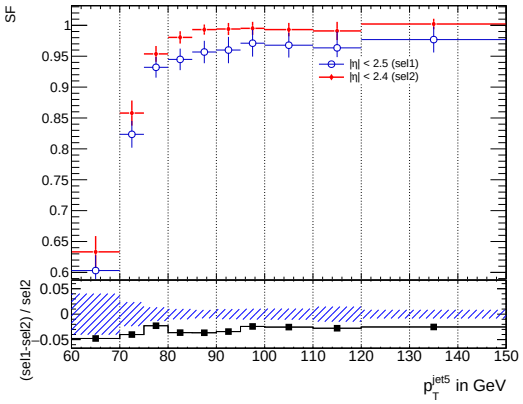

(a) Difference between $|\eta| < 2.4$ of five hardest jets and no $|\eta|$ selection for 2016 trigger.

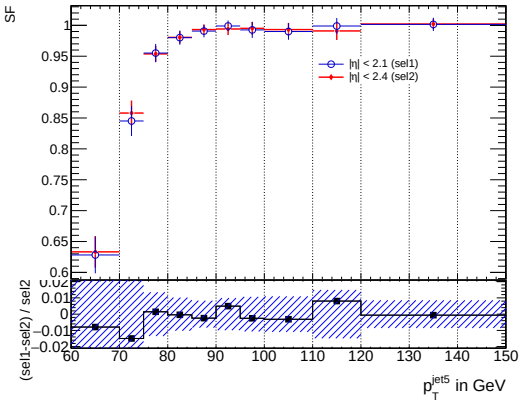

(b) Difference between $|\eta| < 2.4$ and $|\eta| < 2.1$ of five hardest jets for 2016.

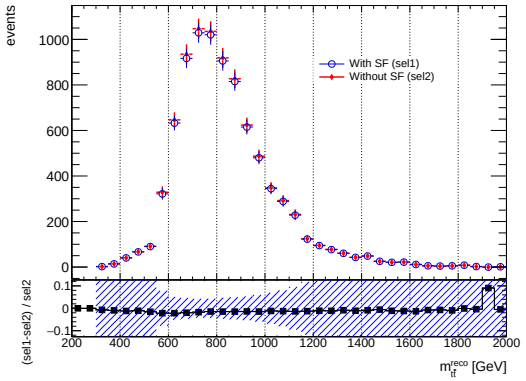

(c) Effect on reconstructed $m_{t\bar{t}}$ shape in region D after applying trigger SFs for full event selection.

Figure 6.6.: Dependence of multijet trigger scale factor on $|\eta|$ of five hardest jets in the event and overall effect of nominal trigger SF on the reconstructed $m_{t\bar{t}}$ shape. The blue shaded area is the statistical uncertainty of the nominal SM $t\bar{t}$ sample.

in Figure 6.6(a). Furthermore, the potential additional topology dependence of the trigger efficiency on e.g. the pseudo rapidity of the offline jets is found to be negligible as is illustrated in Figure 6.6(b). The nominal trigger scale factor is applied on all simulated events. The effect of the correction on the $m_{t\bar{t}}^{\text{reco}}$ distribution in simulated allhadronic SM $t\bar{t}$ events in signal region D is shown in Figure 6.6(c). Applying the trigger scale factor reduces the SM $t\bar{t}$ event yield by around 1.5%. The reduction is mainly caused by the scale factor in the range $p_T = 75 - 80$ GeV as can be seen in Figure 6.5. The shape of the $m_{t\bar{t}}^{\text{reco}}$ is less affected by the SF and the variations are below the statistical uncertainty. The treatment of the uncertainties in the profile likelihood fit is further discussed in Chapter 6.8.14.

6.6. QCD multijet background estimation

Besides the irreducible SM $t\bar{t}$ contribution the QCD multijet production is the main background of the $t\bar{t}$ resonance search. Relying on MC simulation for multijets is supposed to show large modeling uncertainties. Furthermore the relevant phase space demanding a high transverse momentum and b-tagged jets needs to be sufficiently populated by the simulation. The yield and shape of the QCD multijet production is inferred in a data-driven approach to account for these difficulties. An auxiliary measurement is performed in control regions in order to produce a template for the multijet distribution with smaller systematic uncertainties as would be possible with a MC simulation.

Eventually an ABCD-Likelihood model as explained in Chapter 6.7 estimates the multijet shape and yield. Initially the nominal ABCD approach is used to construct four orthogonal regions via cuts on two discriminant variables. Ideally the control regions used to measure these properties are enriched by multijet events with only a small SM $t\bar{t}$ or signal contribution. The b-tagging and top tagging are the primary selection variables controlling the multijet contribution. Therefore, they are the first choice for the ABCD-Likelihood variables. In order to determine the shape of the final discriminant $m_{t\bar{t}}^{\text{reco}}$ distribution one of the variables should be uncorrelated with $m_{t\bar{t}}^{\text{reco}}$ in addition. Under the assumption that the probability density function $\rho(x, y)$ of the two considered variables x and y factorizes like

$$\rho(x, y) = f(x)h(y) \tag{6.6.1}$$

the multijet yield in the signal region can be calculated. Conceptually this is supported by the fact that b-tagging is mainly influenced by tracking information and top tagging has a stronger dependence on the calorimeter information. As the bucket algorithm is seeded by the b-tagged jets the number of b-jets has to be at least two. The top reconstruction requirements are taken into account by exploiting the different b-tagging working points in order to construct orthogonal regions as described in Chapter 6.2.2. The splitting of regions is summarized in Table 6.2. The $t\bar{t}$ purity in each region is shown illustrating the differences between the regions

in terms of multijet background rejection. The largest $t\bar{t}$ signal contribution is expected in region D. Finally regions A, B , C and D are used in the Likelihood. The extra regions based on the looser top tagging ($\mathfrak{t}_0$, $\mathfrak{t}_0$) and ($\mathfrak{t}_-$, $\mathfrak{t}_-$) are used to assign a systematic uncertainty to the multijet template due to the different b tagging WPs as described in Chapter 6.8.4.

The nominal multijet yield in region A, B and C is assumed to be given by the difference between the data yield and the expected SM $t\bar{t}$ yield. The multijet shape in the *b-tag control region* is evaluated by subtracting the SM $t\bar{t}$ shape from the data distribution. The nominal multijet shape in region C is equal to the multijet shape in region A. The nominal prediction of the multijet template in region D follows the *standard* ABCD-method approach

$$\frac{dn_D^{\mathrm{QCD}}}{dm_{t\bar{t}}} = \frac{n_C^{\mathrm{QCD}}}{n_A^{\mathrm{QCD}}} \times \frac{dn_B^{\mathrm{QCD}}}{dm_{t\bar{t}}} \tag{6.6.2}$$

where the yield in region B n_B^{QCD} per bin is scaled by the ratio of the multijet yield in region C n_C^{QCD} and region A n_A^{QCD}. The resulting multijet yield in region D including statistical uncertainties is given by

$$n_D^{\mathrm{QCD}} = 1750 \pm 49(\mathrm{stat.}). \tag{6.6.3}$$

The description above defines the construction of the nominal multijet template. The extension to the likelihood formalism and the corresponding implications are described in Chapter 6.7.

6.7. ABCD-Likelihood

The nominal multijet construction in the ABCD approach as described in Chapter 6.6 relies on several assumptions [75]. First there must be enough events in the control regions A, B and C to propagate the statistical uncertainties linearly to signal region D. Especially for the irreducible SM $t\bar{t}$ sample this can be challenging. Secondly if the phase space used to extract the background distribution is close to the phase space of the signal region the effect of signal leakage in the control regions has to be considered. The signal strength μ is generally the parameter of interest in the minimization used in the limit setting procedure. Hence, a variation of the signal strength during the limit setting has to be correctly accounted for in the background estimation. If on the other hand the background consists of many different sources the ABCD method could select regions with a largely modified composition of the background itself. This could potentially result in an incorrect prediction of the shape if it differs for the types of background sources. Finally a correlation between the two variables used to separate the ABCD regions can result in a wrong estimation of the nominal yield in the signal region.

The ABCD-Likelihood [75, 185] addresses most of the above mentioned assump-

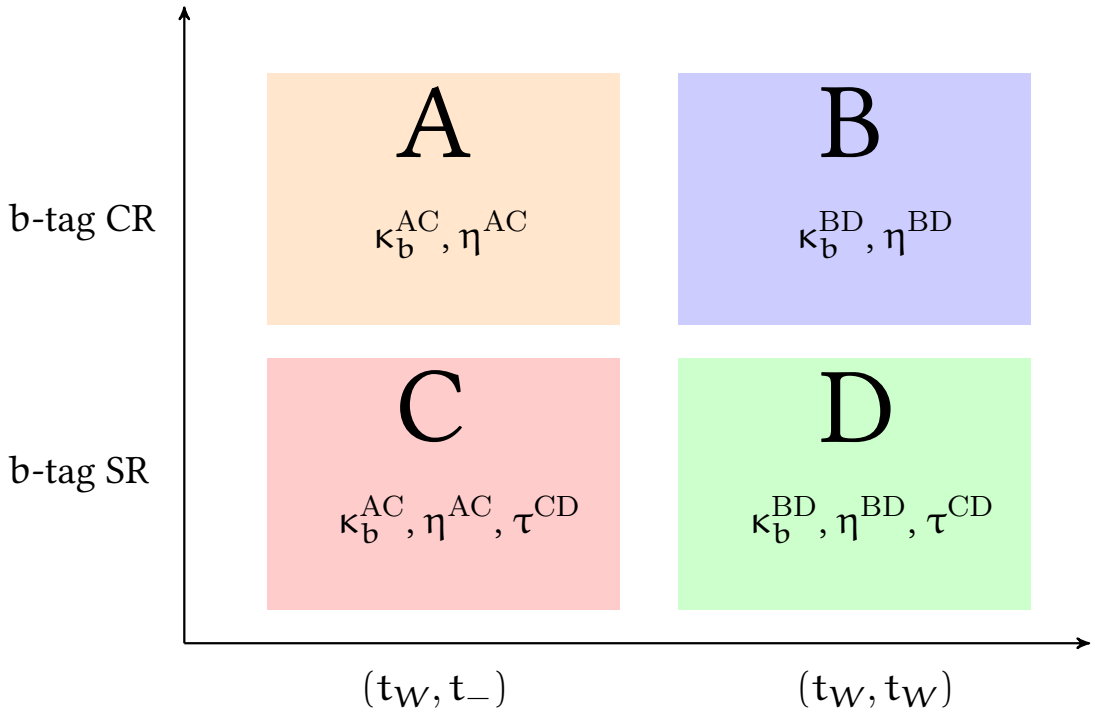

Figure 6.7.: Schematic overview of the ABCD method regions and additional parameters introduced to establish the multijet background estimation in the likelihood fit. The index "b" indicates that a parameter is added per bin to describe unconstrained bin-by-bin variations

tions in case they are not fulfilled or cannot be directly validated. The ABCD-Likelihood approach combines the background estimation and the hypothesis testing in one single step using the likelihood function of the observation. The likelihood function L illustrates a counting experiment

$$L(n_A, n_B, n_C, n_D|\nu, \Theta_\nu) = \prod_{b\in\text{bins}} \prod_{l\in\{A,B,C,D\}} \frac{e^{-\nu_{l,b}}\nu_{l,b}^{n_{l,b}}}{n_{l,b}!} C(\Theta) \tag{6.7.1}$$

where the $\nu_{l,b}$ denote the predicted rate in region l and bin b. A suitable choice of additional unconstrained parameters representing the $\nu_{l,b}$ incorporates the ABCD approach in the Likelihood. Thereby the Likelihood is also extended to fit the shape of the QCD multijet background by adding unconstrained parameters κ_b to the model for each bin as illustrated in Figure 6.7. Specifically the unconstrained bin-by-bin parameters κ_b^{AC} (κ_b^{BD}) are introduced in the regions A (B) and C (D) corresponding to the top tagging category ($\mathfrak{t}_w$, $\mathfrak{t}_-$) (($\mathfrak{t}_w$, $\mathfrak{t}_w$)). Thus, the multijet shape distribution that is originally extracted from the *b-tag control region* is fitted simultaneously for all four ABCD regions inside the profile-likelihood fit. Figuratively the κ_i^{AC} are used to fit the QCD multijet shape in region A and C. Equivalently the κ_i^{BD} fit the QCD multijet shape in region B and D. The following parametrization of the likelihood in Equation 6.7.1 is chosen

$$\nu_{A,b} = \mu_{A,b} + \nu_{A,b}^{\text{MC}} + c_{A,b} \times \eta^{\text{AC}} \times \kappa_b^{\text{AC}} \tag{6.7.2}$$

$$\nu_{B,b} = \mu_{B,b} + \nu_{B,b}^{\text{MC}} + c_{B,b} \times \eta^{\text{BD}} \times \kappa_b^{\text{BD}} \tag{6.7.3}$$

$$\nu_{C,b} = \mu_{C,b} + \nu_{C,b}^{\text{MC}} + c_{C,b} \times \eta^{\text{AC}} \times \kappa_b^{\text{AC}} \times \tau^{\text{CD}} \tag{6.7.4}$$

$$\nu_{D,b} = \mu_{D,b} + \nu_{D,b}^{\text{MC}} + c_{D,b} \times \eta^{\text{BD}} \times \kappa_b^{\text{BD}} \times \tau^{\text{CD}} \tag{6.7.5}$$

with the $\mu_{l,b}$ denoting the predicted signal rate whereas the $\nu_{l,b}^{\text{MC}}$ accounting for the simulation based background model. The constants $c_{l,b}$ are calculated to account for the nominal ABCD construction as described in Chapter 6.6. As a consequence the unconstrained parameters η^{AC}, η^{BD}, τ^{CD}, κ_b^{AC} and κ_b^{BD} are characterized by a nominal value of one. These nominal values should increase the numerical stability of the fit. The parameters η^{AC}, η^{BD}, τ^{CD} describe the normalization in the specific region where they are present. The upper index denotes the regions in which the parameter is applied. The above parametrization is illustrated in Figure 6.7. The parameters η^{AC}, η^{BD} are introduced to facilitate the visualization of the post-fit results on dedicated validation variables. So their purpose is mainly technical. It is validated that the results are unaffected by removing the η^{AC}, η^{BD} parameters. On the other hand the τ^{CD} parameter quantifies deviations of the derived extrapolation factor from the *b-tag control region* to the *b-tag signal region* by correlating the multijet yield in region C and D. Technically the parameters are incorporated using the HistFactory framework [186]. The extra parameters are only applied on the QCD multijet template.

By construction the ABCD-Likelihood accounts for the data statistical uncer-

tainty, the statistical uncertainty and the systematic sources of uncertainty in the simulated events in the derivation of the multijet parameters. Alternative parametrization such as a *standard* ABCD formula consisting of one parameter per region and one extrapolation parameter were tested and resulted in compatible expected limits. An additional constrained nuisance parameter can be added to the Likelihood to account for the correlation between the used variables. The description of that source of uncertainty is presented in Chapter 6.8.5. In summary the ABCD-Likelihood improves the likelihood model by correctly considering the signal contribution in all ABCD regions and by propagating the statistical and systematic uncertainties on the multijet template.

6.8. Systematic uncertainties

Systematic uncertainties can be caused by the background construction procedure, the MC modelling or general detector effects. The final discriminant variable in the profile likelihood fit is the reconstructed invariant mass of the $t\bar{t}$ system $m_{t\bar{t}}^{\text{reco}}$. The normalization as well as the shape of the $m_{t\bar{t}}^{\text{reco}}$ can be affected by the uncertainties. Each source of systematic uncertainty is assumed to be uncorrelated from the others unless stated otherwise and they are considered as nuisance parameters in the profile-likelihood fit following the description in Reference [186]. For the systematic uncertainties 92 nuisance parameters are included in the profile-likelihood fit. The reconstructed mass distribution consists of 19 bins. The binning is chosen based on the expected signal resolution and on the expected stability of the fit taking into account the description of the uncertainties. In each of the four regions one NP is added per bin for the statistical uncertainty using the semi-analytical procedure introduced in Reference [187] and modified in Reference [186]. Furthermore due to the ABCD-Likelihood one NP per bin is included in the two top tag regions ($\mathfrak{t}_w$, $\mathfrak{t}_w$) and ($\mathfrak{t}_w$, $\mathfrak{t}_-$) and three overall NPs in specific regions as described in Chapter 6.7. In total 209 NPs are considered in the likelihood fit.

The treatment of the different sources of systematic uncertainties is summarized in this chapter. The general prescriptions applied to parts or all of the considered systematic uncertainties is outlined in the following. All the uncertainties related to simulated events apply to the SM $t\bar{t}$ MC samples. Due to the additional unconstrained multijet fit parameters the multijet background has no directly associated statistical uncertainties at pre-fit level. Nevertheless, the template is fitted simultaneously and as a consequence it is indirectly affected by the uncertainties of the simulated events too. By construction the effect of an uncertainty between the simulated and the multijet template tends to be opposite leading ideally to a reduction of the overall uncertainty. The uncertainties of the SM $t\bar{t}$ modeling rely on simulated events using the full detector simulation. Thus, they are produced with a reduced sample size compared to the nominal SM $t\bar{t}$ sample due to limited computing resources. This can result in sizable statistical uncertainties on the systematic uncertainties. A *smoothing* procedure is applied in that case to deal with

Uncertainty	Sample X	Sample Y	Procedure
Nominal	–	Powheg+Pythia6	–
$t\bar{t}$ generator	Powheg+Herwig++	aMC@NLO+Herwig++	$\pm\lvert X - Y\rvert$
$t\bar{t}$ parton shower	Powheg+Herwig7	Powheg+Pythia8	$\pm\lvert X - Y\rvert$
$t\bar{t}$ ISR/FSR	Powheg+Pythia6 high	Powheg+Pythia6 low	$\pm\frac{1}{2}\lvert X - Y\rvert$
PDF eigenvector rew.	–	aMC@NLO+Herwig++	$\pm\lvert Y_i^{\mathrm{PDF}} - Y_0^{\mathrm{PDF}}\rvert$
PDF CT10 vs PDF4LHC15	–	aMC@NLO+Herwig++	$\pm\lvert Y - Y_0^{\mathrm{PDF}}\rvert$

Table 6.4.: Different considered $t\bar{t}$ modeling uncertainties and MC samples used for evaluating them. The Y_0^{PDF} denotes the nominal setup of the PDF4LHC15 while the Y_i^{PDF} are the corresponding EV variations. The *pure* X and Y denote the nominal distribution predicted in each sample.

the finite MC sample size. The advantage of the *smoothing* is an increased stability of the fit. Generally, as information is lost during the *smoothing* step it is assumed that the resulting limits are more conservative. The *smoothing* is achieved by rebinning the histograms of the systematic variations based on the configurable number of allowed shape variations and the statistical uncertainty of the nominal sample. Finally the successfully smoothed distributions have to agree with the unmodified distributions within statistical errors. Different *smoothing* techniques are tested to confirm the stability of the chosen procedure. In addition a *pruning* procedure on the nuisance parameters helps to reduce the computing time and to improve the stability of the fit. In the *pruning* step uncertainties are omitted if they fail a predefined threshold. In each region and for each sample the pruning decision is made separately for the normalization and the shape component of the uncertainty. The size of the later one is inferred from the bin-by-bin variations. For both shape and normalization *pruning* a threshold value of 1% is applied. Unless stated otherwise the uncertainties are *symmetrized* in order to stabilize the fit.

The SM $t\bar{t}$ modeling uncertainties as described in Chapter 6.8.10, 6.8.11 and 6.8.12 and the PDF uncertainties in Chapter 6.8.13 rely on the comparison of simulated events with different configuration setups. The corresponding procedures are summarized in Table 6.4.

The pre-fit effect of the uncertainties on the predicted background yield and the yield of a representative signal benchmark model is shown in Table 6.5. Here the background consists of the sum of the SM $t\bar{t}$ MC and the nominal QCD multijet template. Only the uncertainties with the largest effect on the yield are selected in order to highlight which category of uncertainties has the strongest impact.

6.8.1. Integrated luminosity

The method used to determine the uncertainty on the integrated luminosity is described in Reference [188]. The corresponding uncertainty for the combined 2015 and 2016 dataset is found to be ±2.1%. The luminosity calibration is derived from *van-der-Meer* scans. The calibration is influenced by variations of the cross-

Source of uncertainty	Relative impact on yield [%]	
	Background	Z' (0.85 TeV)
Anti-k_t R=0.4 JER	2.6	10.9
Anti-k_t R=0.4 JES	9.0	11.0
b-tagging	5.4	6.6
$t\bar{t}$ generator	12.1	–
$t\bar{t}$ ISR/FSR	11.6	–
$t\bar{t}$ parton shower	14.5	–
$t\bar{t}$ cross section	5.1	–
$t\bar{t}$ NNLO reweighting	6.6	–
$t\bar{t}$ CT10 vs. PDF4LHC15	5.1	–
$t\bar{t}$ PDF eigenvector	4.7	–
Pileup	0.8	1.6
Luminosity	1.7	2.1
Trigger scale factor	1.0	1.0
ABCD correlation	3.4	–
Total	27	17

Table 6.5.: Effect of the pre-fit systematic uncertainties on the total background and the signal yield for a Z'_{TC2} sample with a mass of 0.85 TeV in the signal region D. The expected SM $t\bar{t}$ purity is around 80% in region D. The uncertainties with an effect larger than 1% are presented. The systematic uncertainties described by single nuisance parameters are grouped and summed in quadrature. The total sum in quadrature of all uncertainties is shown in the last row.

section, a non constant emittance during the scan and by beam correlation effects. The luminosity uncertainty is considered for all simulated events. It only affects the normalization.

6.8.2. Pileup simulation

The simulated events are reweighted to account for the luminosity profile found in data. An uncertainty associated to the reweighting procedure is applied on the simulated events. The effect is small compared to the statistical uncertainties. The uncertainty is based on the difference in the predicted and measured inelastic cross-section in the fiducial volume defined by $M_X > 13$ GeV where M_X is the mass of the non-diffractive hadronic system [189].

6.8.3. Flavor tagging of the jets

The main concepts and performance of the b-tagging in ATLAS are described in Chapter 3.4.6. The b-tagging is an important component of the analysis as it has a strong influence on the construction of the control and signal regions. It controls the size of the background contribution by greatly reducing the QCD multijet background. Therefore, it is expected to show an interplay with the estimation of the multijet background. The main quantities associated to a specific b-tagging working point and choice of algorithm are the b-tagging efficiency, the c-jet rejection and light-jet rejection. Each of these efficiencies is calibrated separately in order to provide simulation to data scale factors and the associated uncertainties. For the breakdown of the uncertainties an eigenvector variation method is used. The SF and uncertainties a applied per reconstructed jet object where the truth b-jet, c-jet and light-jet information from the MC simulation is considered. As explained above the analysis makes use of two different working points which correspond to different specific cut values on the b-tagging discriminant.

The set of eigenvectors or systematic uncertainties related to the reconstruction of b-jets depends on the specific calibration. Generally the calibration of the b-tagging efficiency uses more bins as the calibration of c-jets and light-jets. The eigenvector variation method is applied in order to reduce the total number of uncertainties to the ones with the largest contribution while still keeping as much of the relevant correlation information between bins in the calibration as necessary. The b-, c- and light-jet uncertainties are derived from the full 2015 and 2016 dataset. Finally 5, 4 and 14 uncertainties are considered for b-, c and light-jets respectively. In addition 2 eigenvectors take into account the extrapolation of the scale factor for high transverse momentum jets ($p_T > 300$ GeV). The extrapolation uncertainty is correlated across the flavors and found to be small below the *pruning* threshold as the majority of the selected jets is not in the high p_T regime. The uncertainties of the *loose* b-tagging WP are applied in the *b-tag control region* A and B. The uncertainties of the *tight* WP are applied in the *b-tag signal region* C and D. The

uncertainties between the two different working points are treated as fully correlated. The opposite scenario with fully uncorrelated uncertainties is considered as a cross-check. It is verified that the choice of correlation has a negligible effect on the expected limits.

6.8.4. Multijet shape uncertainty

As the shape and the yield of the multijet template is fitted during the hypothesis test by the ABCD-Likelihood there remain only a few uncertainties to be considered directly on the multijet template. The statistical and systematic uncertainties of the non-multijet samples are incorporated during the profile likelihood fit in which the unconstrained multijet parameters are determined. Nevertheless there exist two types of intrinsic uncertainties. The fact that there can be a correlation between the top quark and b-jet tagging could lead to a deviation in the prediction of the QCD multijet yield in region D. This is investigated in Chapter 6.8.5. Secondly the shape of the multijet estimate is related to the b-tagging performance. The ABCD method relies on the assumption that the shape can be extrapolated from the *b-tag control region* to the *b-tag signal region*. It is known from b-tagging calibration measurements that especially the light jet rejection varies with the transverse momentum and the pseudorapidity η of the jet under consideration [159]. Such a kinematic dependence can deviate between different b-tagging working points. Requiring already at the event selection that the two highest transverse momentum b-tagged jets are central $|\eta| < 1.6$ reduces a b-tagging induced shaping effect. As is demonstrated in Chapter 6.9 in a data to background model comparison the highest transverse momentum b-tagged jet kinematics in terms of p_T and η are well described by simulated SM $t\bar{t}$ events and the multijet template after the default event selection. Generally, the reconstruction of the $t\bar{t}$ invariant mass can depend on the correlations between the b-tagged jets itself which is potentially affected by the WPs. Therefore, an uncertainty on the QCD multijet shape due to the transformation from the *b-tag control region* to the *b-tag signal region* is derived in additional control regions not directly used in the Likelihood. These control regions are constructed by requiring a looser top quark pair selection. The corresponding $t\bar{t}$ purities of the used top categories ($\mathfrak{t}_0$, $\mathfrak{t}_0$) and ($\mathfrak{t}_-$, $\mathfrak{t}_-$) are listed in Table 6.2. As the $t\bar{t}$ contribution is relatively small in these validation regions the nominal QCD multijet template is estimated from data by subtracting the simulated SM $t\bar{t}$ distribution in each region . This approach allows one to study the $m_{t\bar{t}}$ shape difference between the *b-tag control region* and the *b-tag signal region*. The ratio between the two distributions is calculated independently in both top categories.

The first uncertainty referred to as the multijet shape uncertainty is inferred from the ratio $\tilde{R}(x)$ of the multijet shape in C_0 and A_0 as a function of the variable x. The second uncertainty is constructed in a similar way using the regions C_- and A_- instead. The shape transfer function $R(x)$ from *b-tag control region* to *b-tag signal region* is measured from data in ($\mathfrak{t}_0$, $\mathfrak{t}_0$) and defines a relative uncertainty applied on the multijet shape in region C and D in the Likelihood. The function

Event regions	ABCD	A_BC_D	A_0BC_0D
Multijet yield	1750(49)	1659(40)	1801(42)

Table 6.6.: Predicted multijet template yield in signal region D based on three different set-ups of the ABCD-method depending on the regions used in the calculation. The uncertainty consists of the statistical uncertainty only.

$R(x)$ is calculated separately for the fit variable $m_{t\bar{t}}^{\text{reco}}$ and for additional validation variables. Assuming the multijet template distribution is described by the function $q_{\text{QCD}}^{\text{C}_0}(x)$ with yield $n_{\text{QCD}}^{\text{C}_0}$ in C_0 and by $q_{\text{QCD}}^{\text{A}_0}(x)$ with yield $n_{\text{QCD}}^{\text{A}_0}$ in region A_0 respectively. The transfer function $R(x)$ in

$$q_{\text{QCD}}^{\text{C}_0}(x) = \tilde{R}(x) q_{\text{QCD}}^{\text{A}_0}(x) = \left(R(x) + \frac{n_{\text{QCD}}^{\text{C}_0}}{n_{\text{QCD}}^{\text{A}_0}} \right) q_{\text{QCD}}^{\text{A}_0}(x) \tag{6.8.1}$$

accounts for the measured shape difference between the regions. Finally, the uncertainty is symmetrized in order to stabilize the fit. The QCD multijet shape uncertainties between region C and region D are treated as fully correlated which is supported by the comparable kinematics of the b-tagged jets in both regions. The application of the uncertainty in region C and D should allow one to constrain it better as the multijet contribution in region C is significantly larger compared to the signal region D. The uncertainty used in the likelihood is solely based on the derived $R(x)$ in region ($\mathfrak{t}_0$, $\mathfrak{t}_0$) which provides smaller associated statistical uncertainties than the $R(x)$ derived in region ($\mathfrak{t}_-$, $\mathfrak{t}_-$). Nevertheless, the two transfer functions derived in both regions are compatible. In contrast to other uncertainties no smoothing is applied on the multijet shape uncertainty. Qualitatively the effect of the uncertainty shifts the shape of the QCD multijet distribution towards lower invariant masses. This ranges from an effect on the multijet template of around $+20\%$ for masses $m_{t\bar{t}}^{\text{reco}}$ below 500 GeV to about -20% for masses above 1600 GeV.

6.8.5. ABCD correlation

The QCD multijet yield would be affected by a correlation between the selection variables used in the ABCD method construction. An ABCD correlation uncertainty is introduced to account for a potential correlation between the b-tagging and the top quark reconstruction. Generally, the correlation is expected to be small as b-tagging is based primarily on tracking information whereas the top reconstruction relies on the calorimeter based jets. Approaches to infer the corresponding correlation from simulated events are limited by the small sample sizes. Therefore, in a similar way as described in Chapter 6.8.4 the validation regions ($\mathfrak{t}_0$, $\mathfrak{t}_0$) and ($\mathfrak{t}_-$, $\mathfrak{t}_-$) are considered to estimate the size of this effect. The nominal ABCD method is modified to be described by the A_0BC_0D or A_BC_D regions instead. This results

in a recalculated multijet yield in region D as shown in Table 6.6 including statistical uncertainties. The influence of the SM $t\bar{t}$ modeling is expected to be reduced for the A_0BC_0D scenario which is dominated by the multijet component in region A_0 and C_0 as explained in Table 6.2. The maximal variation between A_0BC_0D and A_BC_D has a size of 8%. So an additional uncertainty with a Gaussian constraint term is applied on the QCD multijet yield in region D to account for ABCD-correlation uncertainties in the likelihood fit. The uncertainty has a conservative size of 20% and solely affects the multijet normalization. Due to the different background composition in separate bins this can still affect the shape of the total background prediction.

6.8.6. Jet vertex tagger

The Jet vertex tagger is described in Chapter 3.4.5. The purpose of the JVT is the suppression of pileup jets while keeping the hard-scatter jets [157, 158]. Scale factors are applied to correct for differences in the efficiency of this cut between data and simulation. The measurement of the JVT scale factors and corresponding uncertainties is based on simulated samples and the 2015 and 2016 datasets by selecting events with a Z boson decaying into muons with at least one extra jet. The corresponding sample is further divided in events enriched by pileup and hard-scatter jets. Finally three working points to reject jets in both data and MC simulation are determined for jets with 20 GeV $< p_T <$ 60 GeV and $|\eta| < 2.4$. Additionally the per-jet scale factor to correct simulated events is derived as a function of the jet p_T. The present statistical uncertainty and a 30% uncertainty on the residual contamination from pileup jets after the corresponding suppression selection contribute to the uncertainty of the JVT SF.

6.8.7. Jet energy resolution

In-situ measurements are used to derive the jet energy resolution JER uncertainty in four pseudorapidity η bins up to $|\eta| = 2.8$ [177]. The JER can be factorized in three terms as described by the following equation

$$\frac{\sigma_{p_T}}{p_T} = \frac{N}{p_T} \oplus \frac{S}{\sqrt{p_T}} \oplus C \tag{6.8.2}$$

where N parametrizes the noise, S the stochastic effects and C accounts for a constant term [190]. The correlations between the η bins are considered. So in principle the central JER could be described by 12 eigenvectors. The correlations between the η regions allow one to reduce this to a set of 9 NPs or a strongly reduced set with a single NP which is used in this analysis. The JER uncertainty is implemented via a smearing procedure on the jet four momentum in simulated events. The so derived effect on the $m_{t\bar{t}}^{\text{reco}}$ distribution is one-sided by construction. Finally the uncertainty is symmetrized to allow for a more stable minimization of

the fit. In contrast to the other systematic uncertainties a stronger smoothing with fewer allowed shape variations is used.

6.8.8. Jet energy scale

The ATLAS jet reconstruction and calibration procedure is explained in Chapter 3.4.5. The calibration compensates differences between the particle jet and the energy measured in the calorimeter. There are three main sources of deviations from the particle jet energy level. Dead material causes loss of energy deposits. Equally hadron energy deposits are not fully measured and noise and pileup lead to further inefficiencies.

The baseline JES calibration in ATLAS consists of 88 nuisance parameters. Global and category reductions are applied to achieve a reduced number of NPs. The reduction requires that the analysis is largely independent of correlations between the considered uncertainty sources. This is proven by repeating the limit setting with three different scenarios of strongly reduced NPs each consisting of four NPs in total. One of these parameters quantifies the pseudorapidity η intercalibration non-closure and the other three are combinations of all remaining parameters. The equivalence of the four scenarios basically shows that the analysis is independent from jet correlations induced by changes of the jet energy scale. Eventually a reduced set with 21 NPs is selected in order to facilitate a future combination with analyses concentrating on other $t\bar{t}$ decay modes. The reduced set is only used for the derivation of the trigger scale factor as described in Chapter 6.5.

6.8.9. Cross-section of SM top quark pair

The uncertainty on the inclusive $t\bar{t}$ cross-section is based on the combined ATLAS and CMS recommendations [139] as described in Chapter 3.3.1. Three types of uncertainties enter in its calculation. The scale uncertainty is evaluated by varying the factorization and renormalization scales independently. For the combined PDF and α_s uncertainty the corresponding 68% CL uncertainty is calculated for each. Finally the envelope of both is taken. Additionally an uncertainty due to the variation of the top mass is considered. The sum in quadrature of the three uncertainties makes the total uncertainty. Only the $t\bar{t}$ normalization is affected by this uncertainty. The relative uncertainty on the SM $t\bar{t}$ yield is estimated to be $^{+5.6\%}_{-6.1\%}$.

6.8.10. Hard scatter generation

The treatment of the hard scatter generation modeling uncertainty is explained in the following. Ideally this uncertainty can be parametrized by comparing the $m_{t\bar{t}}^{\text{reco}}$ distribution of two different $t\bar{t}$ MC generators. For this purpose the influence from the scale variations, extra radiation and the parton shower modeling should be minimized. Specifically this is achieved by comparing the POWHEG generator

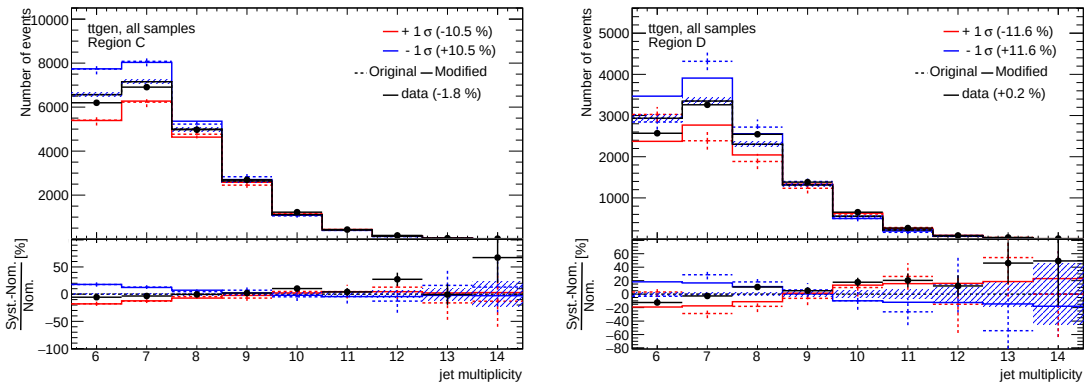

(a) (b)

Figure 6.8.: Effect of $t\bar{t}$ generator modeling uncertainty on the jet multiplicity distribution at pre-fit level. The statistical uncertainty of the nominal distribution is shown on the ratio by the blue shaded area. The modified distribution is constructed after *smoothing* and *symmetrizing* the uncertainty.

to the aMC@NLO generator which are both interfaced to the same parton shower simulation using Herwig++. The configuration of the generators is summarized in Table 3.2. The choice of generator setups is motivated by the idea that the effects not coming from the hard scatter generation should factorize out. As also the matching methods between the setups differ this cannot be perfectly achieved.

The used procedure for the uncertainty is summarized in Table 6.4. For each bin the variation Δ is calculated:

$$\Delta^{\text{Hard scatter}} = \left| n^{\text{Powheg+Herwig++}} - n^{\text{aMC@NLO+Herwig++}} \right| \tag{6.8.3}$$

The final effect on $m_{t\bar{t}}^{\text{reco}}$ is parametrized for each bin with nominal number of events n^{nominal} as

$$n^{\text{nominal}} \pm \Delta^{\text{Hard scatter}} \ . \tag{6.8.4}$$

Generally, it is expected that the matrix element can influence the small-R jet properties and in turn affects the $m_{t\bar{t}}^{\text{reco}}$. Hence, also other distributions besides the $m_{t\bar{t}}^{\text{reco}}$ distribution are investigated to cross-check this assumption. The jet multiplicities in Region C and D are shown in Figure 6.8. Indeed besides a strong $\mathcal{O}(10\%)$ uncertainty on the normalization also the predicted number of selected jets deviates between the two configurations.

The statistical uncertainties associated to the simulated events used for the evaluation of the systematic uncertainty exceed the corresponding uncertainty of the nominal SM $t\bar{t}$ simulation. The hard scatter generation uncertainty is among the largest uncertainties with respect to the pre-fit effect on the background yield in

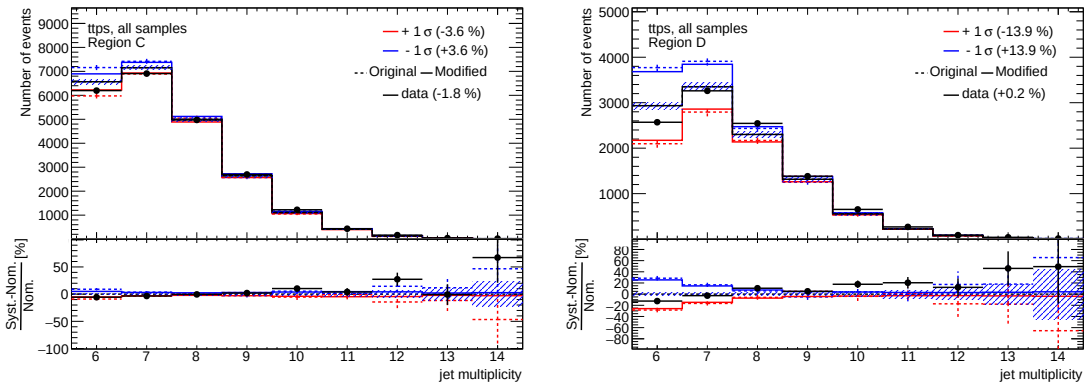

(a) (b)

Figure 6.9.: Effect of $t\bar{t}$ parton shower modeling uncertainty on the jet multiplicity distribution at pre-fit level. The statistical uncertainty of the nominal distribution is shown on the ratio by the blue shaded area. The modified distribution is constructed after *smoothing* and *symmetrizing* the uncertainty.

region D that is estimated to be around 12.1%, see Table 6.5.

6.8.11. Fragmentation and hadronization model

The uncertainty of the fragmentation and hadronization model on the SM $t\bar{t}$ simulation relies on a comparison between the Pythia and Herwig parton shower models. In principal the nominal SM $t\bar{t}$ MC simulation based on Powheg+Pythia6 could be used as the baseline and the Powheg+Herwig++ simulation for the variation [123]. Instead an alternative configuration [191] is used aiming at reducing the statistical uncertainties on the evaluation by relying on a Powheg+Pythia8 simulation and a Powheg+Herwig7 $t\bar{t}$ sample generated with a different Powheg setup compared to the nominal simulation as described in Table 3.3. The two samples are simulated based on the same Powheg configuration with respect to the PDF set and the scales but the parton shower and underlying event tune differ.

The used procedure for the uncertainty is summarized in Table 6.4. For each bin the variation Δ is calculated:

$$\Delta^{\mathrm{PS}} = \left| n^{\mathrm{Powheg+Herwig7}} - n^{\mathrm{Powheg+Pythia8}} \right| \tag{6.8.5}$$

The final effect on $m_{t\bar{t}}$ is parametrized for each bin with nominal number of events n^{nominal} as

$$n^{\mathrm{nominal}} \pm \Delta^{\mathrm{PS}} \ . \tag{6.8.6}$$

The effect of the parton shower uncertainty on the expected background jet multiplicity in region C and D is shown in Figure 6.9. The uncertainty can shift the

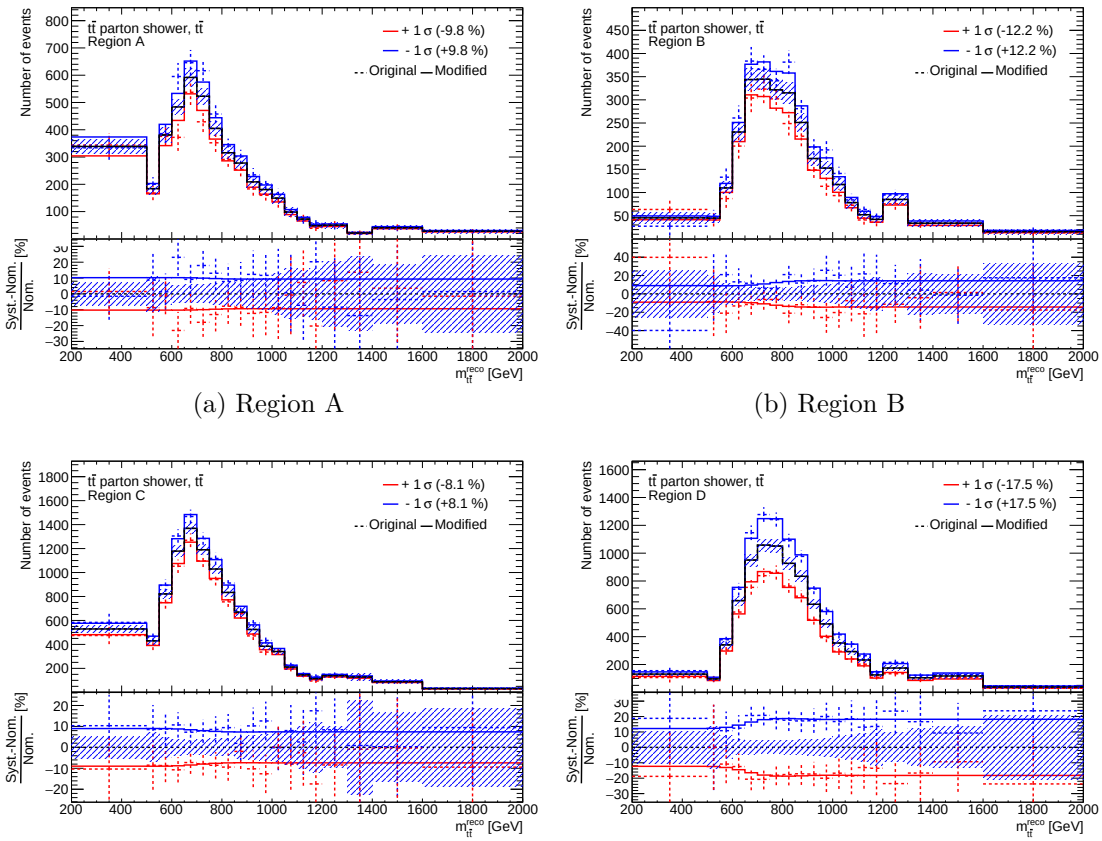

(a) Region A

(b) Region B

(c) Region C

(d) Region D

Figure 6.10.: Effect of the uncertainty of the fragmentation and hadronization model on the $m_{t\bar{t}}^{\text{reco}}$ distribution for simulated SM $t\bar{t}$ events at pre-fit level. The statistical uncertainty of the nominal distribution is shown on the ratio by the blue shaded area. The modified distribution is constructed after *smoothing* and *symmetrizing* the uncertainty.

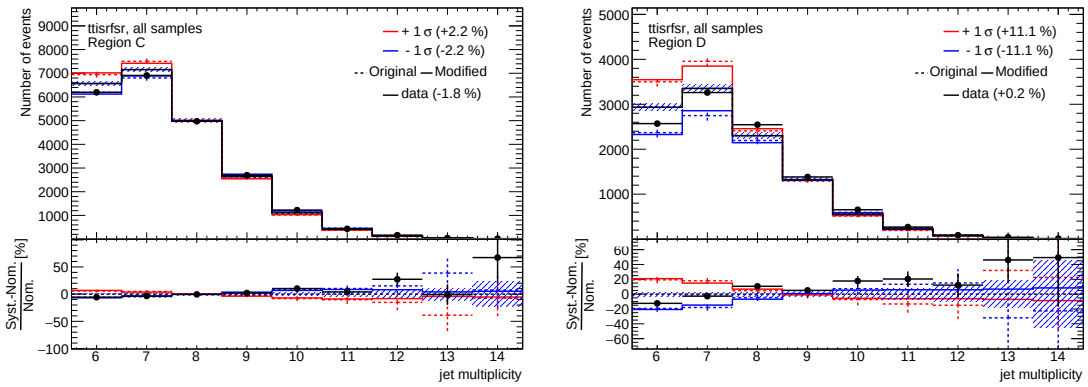

(a) (b)

Figure 6.11.: Effect of $t\bar{t}$ scale and additional radiation modeling uncertainty on the jet multiplicity distribution at pre-fit level. The statistical uncertainty of the nominal distribution is shown on the ratio by the blue shaded area. The modified distribution is constructed after *smoothing* and *symmetrizing* the uncertainty.

jet multiplicity distribution and has a 14.5% influence on the background yield in region D. The effect on the $m_{t\bar{t}}^{\text{reco}}$ distribution is shown in Figure 6.10. The uncertainty primarily affects the SM $t\bar{t}$ normalization but varies between the ABCD regions.

6.8.12. Scales and additional radiation

The effect of scale variations and additional radiation is considered as a combined uncertainty. The two samples used for higher or lower extra radiation contribution are based on the same MC generator POWHEG and shower simulation PYTHIA6 as the nominal sample but with deviations in the configuration as is summarized in Table 3.2. For the *high* radiation sample the renormalization and factorization scale are simultaneously reduced by a factor 1/2. At the same time the parton shower tune is altered to a higher radiation setup (*P2012 radHi*). In a similar way the *low* radiation sample is produced with renormalization and factorization scale increased by factor 2 and the corresponding *P2012 radLo* parton shower tune. In addition for the *high* sample the NLO radiation is modified by setting the *hdamp* parameter to twice the top mass.

The procedure for the uncertainty is summarized in Table 6.4. For each bin the variation Δ is calculated:

$$\Delta^{\text{ISRFSR}} = \frac{1}{2}\left|n^{\text{Powheg+Pythia6 high}} - n^{\text{Powheg+Pythia6 low}}\right| \tag{6.8.7}$$

The final effect on $m_{t\bar{t}}$ is parametrized for each bin with nominal number of events

n^{nominal} as

$$n^{\text{nominal}} \pm \Delta^{\text{ISRFSR}} \tag{6.8.8}$$

The effect of the extra radiation uncertainty on the expected background jet multiplicity in region C and region D is shown in Figure 6.11. The uncertainty can affect the five jet multiplicity up to 20%.

6.8.13. Parton distribution functions

The $m_{t\bar{t}}$ distribution as any observable at a hadron collider depends on the precise knowledge of the proton structure. As explained in the discussion of the factorization theorem in Chapter 2.2 this can be described by the parton distribution functions. The uncertainty of the PDF determination and its application in the resonance search is discussed in the following. The task of the PDF determination is generally treated in different ways by collaborations which results in solutions in terms of so-called PDF sets. These sets differ by the input data and theory assumptions which enter the determination. A reweighting method is applied to evaluate the effect of different PDFs on simulated events. Thereby a weight $w^{\text{PDF}}(x_1, x_2, Q)$ is calculated on the event level as defined by

$$w^{\text{PDF}}(x_1, x_2, Q) = \frac{f_i^{\text{new}}(x_1, Q^2) f_j^{\text{new}}(x_2, Q^2)}{f_i^{\text{old}}(x_1, Q^2) f_j^{\text{old}}(x_2, Q^2)} \tag{6.8.9}$$

with the parton distribution functions $f_i^{\text{type}}(x)$. In order to reweight just the acceptance and not the cross section to the new PDF set an additional weight W^{PDF} is applied to correct for that

$$W^{\text{PDF}} = \frac{\sum_{\text{all events}} w^{\text{PDF}} w^{\text{MC}}}{\sum_{\text{all events}} w^{\text{MC}}} \ . \tag{6.8.10}$$

Here the w^{MC} accounts for the event weight provided by the MC generator. By construction this reweighting procedure captures only the linear dependence at fixed order in QCD of the PDFs. This implies that depending on the used MC generator a sample generated with a PDF set will not necessarily be identical to a sample generated with another PDF set and reweighted to the first. This so-called *closure* property is not expected to be present for the POWHEG generator that is used to simulate the nominal SM $t\bar{t}$ events. Therefore, the evaluation of the PDF uncertainties relies on the MC@NLO generator which is expected to achieve the *closure* behavior. Instead of relying on a specific PDF set and the associated internal PDF uncertainties the PDF4LHC15 prescription [192] is used. It is a statistical combination of the CT14 [193], MMHT14 [194] and NNPDF3.0 [195] PDF sets based on the Monte Carlo method [196]. The PDF4LHC15 approach provides a full combined uncertainty description and several reduced sets in addition. The selection

criteria for the three chosen PDF sets is outlined in Reference [192]. The globality requirement leads to the exclusion of some PDF sets like the HERAPDF set. This ansatz is sufficient for the resonance search. The PDF4LHC15 prescription provides different options of reduced uncertainty scenarios for different use-cases. The Hessian sets rely on the *Hessian reduction method* [197, 198] and the MC set on the *Monte Carlo compression method* [199]. The chosen Hessian representation provides by design uncertainties with a Gaussian shape. So they are well suited for an application in a profile likelihood fit.

The considered MC generators were not yet tuned to the PDF4LHC15 sets. Thus, the PDF4LHC15 sets are only used to calculate the uncertainties and not as the nominal description. The PDF set of the nominal $t\bar{t}$ MC generator is CT10 as listed in Table 3.2. So two kinds of uncertainties are considered as shown in Table 6.4. One taking into account the reduced 30 symmetric Hessian eigenvectors from the PDF4LHC15 prescription and an extra uncertainty for the difference between CT10 and PDF4LHC15. No significant shaping of the $m_{t\bar{t}}^{\text{reco}}$ distribution is observed due to the PDF uncertainties. The quadratic sum of the effect of the eigenvectors on the background yield in region D is around 5%. The combined eigenvector effect on the yield is of approximately the same size as the uncertainty from the comparison between the CT10 and PDF4LHC15 sets. The PDF uncertainty is applied on the simulated SM $t\bar{t}$ events.

6.8.14. Trigger scale factor

The estimation of the uncertainty of the trigger scale factor considers the effect of the above mentioned JER and JES uncertainties as described in Chapter 6.5. The trigger SFs of the JES and JER variations are added in quadrature and are treated as a single uncertainty. As the effect is small compared to the statistical uncertainties this simplified treatment is justified. Otherwise the full correlations with the JES and JER uncertainties should be considered. The uncertainty is applied on all simulated samples.

6.8.15. Electroweak corrections

Following the description in Reference [171] the uncertainty from higher order electroweak corrections [182] is estimated by varying the difference of each correction factor from unity by 10%. The resulting effect on the SM $t\bar{t}$ normalization and shape is below 1%.

6.8.16. NNLO effect on SM top quark pairs

The SM $t\bar{t}$ calculation in Reference [200] at NNLO in QCD using dynamical scales is considered as a correction. The corrections are applied as a function of the transverse momentum of the top quark and the transverse momentum of the $t\bar{t}$ system after final state radiation directly before the top quark decay. The resulting

Type	Region A	Region B	Region C	Region D
Z'(500GeV)	79(73)	37(39)	180(147)	115(104)
Z'(600GeV)	167(79)	135(119)	408(109)	431(180)
Z'(750GeV)	470(68)	367(91)	1196(141)	1203(182)
Z'(850GeV)	561(93)	407(92)	1366(154)	1484(260)
Z'(1000GeV)	460(65)	296(37)	1018(127)	1014(148)
Z'(1250GeV)	205(18)	98(13)	462(43)	317(35)
$t\bar{t}$ allhad	3955(1023)	2702(633)	9027(2985)	8360(2698)
$t\bar{t}$ nonallhad	444(74)	90(22)	1143(158)	255(49)
multi-jet (template)	31 374(6278)	4394(885)	12 495(2500)	1750(353)
Total	35 772(6365)	7186(1094)	22 665(3941)	10 364(2742)
Data	35 772	7186	22 665	10 821

Table 6.7.: Yields for $\int L\mathrm{dt} = 36.1$ fb^{-1} and $\sqrt{s} = 13$ TeV in the ABCD regions. The expected Z' signal yields are calculated based on the $\mu = 1$ hypothesis. The uncertainty denotes the sum in quadrature of the statistical and systematic uncertainties.

deviations from the nominal distribution are treated as a systematic uncertainty. The effect ranges from around 3% below a mass of 500 GeV up to 11% for masses above 1200 GeV.

6.9. Control variables

The modeling of the background is investigated in several control observables at pre-fit level. The accuracy of the nominal QCD multijet background estimate is best investigated in Region C where it has an expected contribution of around 45%. The modeling of the SM $t\bar{t}$ events has a stronger impact on the signal region D with an expected SM $t\bar{t}$ purity of around 80%. The yields in the ABCD regions are summarized in Table 6.7 at pre-fit level. The expected event yields for the Z'_{TC2} signal model under the $\mu = 1$ hypothesis are shown as well as the background sources. The integrated selection efficiencies for simulated events are listed in Table 6.8. The reduced acceptance at lower invariant masses around 500 GeV that is mainly caused by the trigger threshold and the transverse momentum dependent efficiency of the bucket algorithm results in a smaller signal selection efficiency compared to masses around 850 GeV. At higher Z' masses above 1 TeV the top quarks are more boosted and substructure based reconstruction techniques would become more effective. The SM $t\bar{t}$ background in region D is dominated by fully hadronic top quark pair decays with 8360 ± 2698 events. In addition a small contribution from non-allhadronic $t\bar{t}$ decays with 255 ± 49 events are considered in the background model. Such a background can be selected if e.g. the lepton of

Type	Region A	Region B	Region C	Region D	Region ABCD
Z'(500GeV)	0.01(1)	0.004(4)	0.02(2)	0.01(1)	0.05(2)
Z'(600GeV)	0.03(2)	0.03(2)	0.08(2)	0.09(4)	0.23(5)
Z'(750GeV)	0.20(3)	0.16(4)	0.52(6)	0.52(8)	1.40(11)
Z'(850GeV)	0.38(6)	0.28(6)	0.93(10)	1.01(18)	2.59(22)
Z'(1000GeV)	0.58(8)	0.37(5)	1.28(16)	1.27(19)	3.49(26)
Z'(1250GeV)	0.63(6)	0.30(4)	1.42(13)	0.97(11)	3.32(18)
g_{KK} (500GeV)	0.03(2)	0.02(1)	0.06(2)	0.06(2)	0.16(3)
g_{KK} (1000GeV)	0.38(5)	0.26(6)	0.93(10)	0.85(11)	2.42(17)
g_{KK} (1500GeV)	0.46(6)	0.16(3)	1.01(12)	0.71(9)	2.33(17)
G_{KK} (500GeV)	0.08(3)	0.04(2)	0.14(2)	0.06(2)	0.32(4)
G_{KK} (750GeV)	0.61(7)	0.39(6)	1.24(14)	1.31(21)	3.55(27)
G_{KK} (1000GeV)	1.08(8)	0.59(5)	2.31(18)	1.82(19)	5.80(28)
$t\bar{t}$	0.03(1)	0.02(0)	0.07(2)	0.06(2)	0.18(3)

Table 6.8.: Integrated signal efficiencies for $\int L\mathrm{dt} = 36.1\mathrm{fb}^{-1}$, $\sqrt{s} = 13$ TeV in per cent for the topcolor assisted technicolor model Z', the KK gluon g_{KK} and the KK graviton G_{KK} benchmark models . The efficiencies are divided by the all-hadronic branching ratio of 46%. The uncertainty denotes the sum in quadrature of the statistical and systematic uncertainties.

the top quark decay is reconstructed as a jet and thereby passes the lepton veto. The large uncertainty on the total background model is caused by the large pre-fit uncertainties of the $t\bar{t}$ modeling. Nevertheless, the total predicted background rate in region D agrees with data even at pre-fit level.

The control observables presented in this chapter are a selection of individual object properties and general event variables. In region C the nominal QCD multijet yield is inferred from the difference between data and the simulated prediction. The QCD shape in region C is extracted from region A. The jet multiplicity in Figure 6.12(a)shows a predicted deficit for larger multiplicities. This is still compatible with the $t\bar{t}$ modeling uncertainties or within the jet energy scale uncertainty. The centrality C is a global event variable based on all selected jets in an event. It is calculated from the four-vector sum of the jets:

$$\mathrm{C} = \frac{p_T(\sum p_{\mathrm{jet}})}{\mathrm{mass}(\sum p_{\mathrm{jet}})} \ . \tag{6.9.1}$$

SM $t\bar{t}$ events are more central than QCD multijets as can be seen in Figure 6.12(b). As the centrality sums over all jets also the b-tagged jets are included. Therefore, it is sensitive to a mis-modeling of the nominal QCD multijet background which is derived from different b-tagging working points. The centrality is well modeled by the background model in region C. Two quantities related to the top quark reconstruction are the transverse momentum of the softer reconstructed top quark

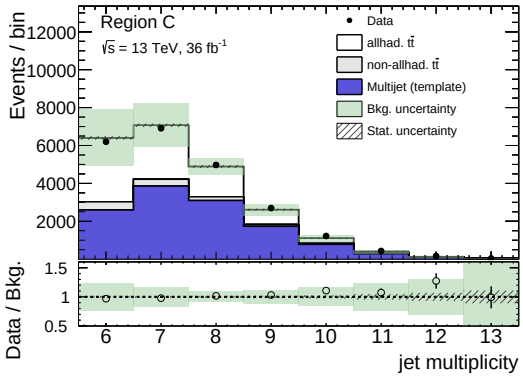

(a) Jet multiplicity

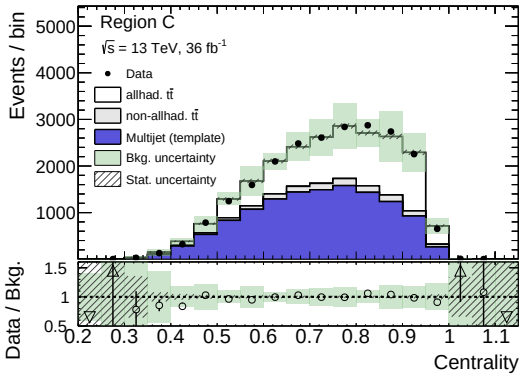

(b) Centrality

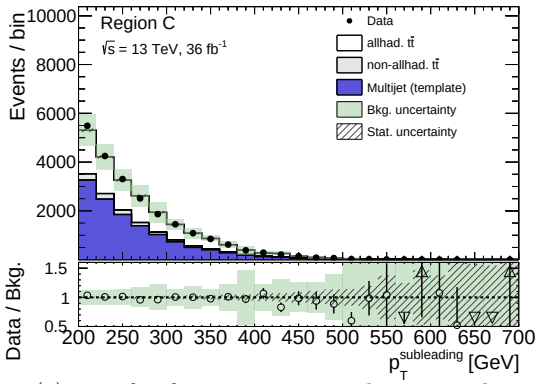

(c) p_T of softer reconstructed top quark

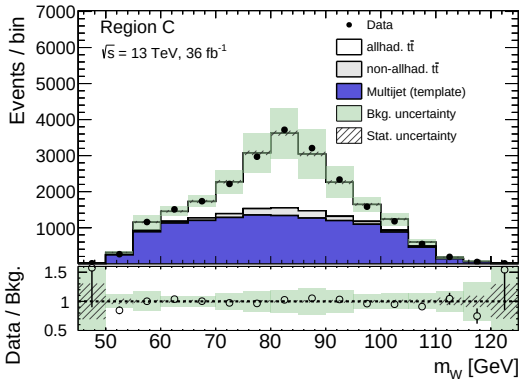

(d) Mass of W candidate in bucket 1

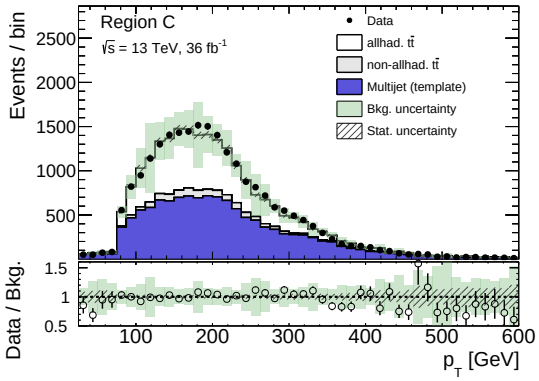

(e) p_T of hardest b-tagged jet

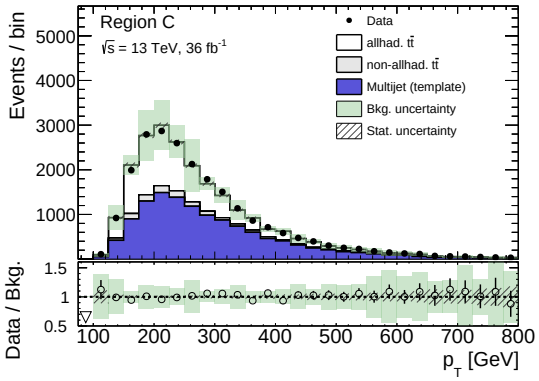

(f) p_T of the hardest jet in the event

Figure 6.12.: Data to background model comparison of several variables in region C corresponding to top category ($\mathfrak{t}_w$, $\mathfrak{t}_-$).

and the mass of the W candidate in the first top bucket. These observables are also well described within the uncertainties. The distribution of the mass of the W candidate suggests that the SM $t\bar{t}$ yield is predicted well as the shape between QCD multijets and SM $t\bar{t}$ differ stronger compared to other variables. As mentioned before the kinematics of the leading b-tagged jet in terms of the transverse momentum distribution is well described by the background model.

Similar observations can be made for the region D. In region D the nominal QCD multijet yield is estimated by the ABCD method using the $\mu = 0$ hypothesis. Due to the larger SM $t\bar{t}$ purity a potential mis-modeling induced by the simulation should be more pronounced in region D than in region C. The set of control distribution in region D is shown in Figure 6.13 and 6.14. The distributions of all observables are well modeled by the background predictions within the uncertainties. Even though a tight top quark selection is applied the predicted SM $t\bar{t}$ yield is well described as supported by the distribution of the mass of the W candidate in Figure 6.13(d). The deviations in the transverse momentum distribution of the softer reconstructed top quark can be explained by the $t\bar{t}$ modeling uncertainties and by the multijet shape uncertainty as discussed in Chapter 6.8.4. Furthermore the p_T of the reconstructed $t\bar{t}$ system is shown in Figure 6.14(b). The metric Δ, as introduced in Equation 4.0.2, which is used in the first top quark reconstruction step is presented in Figure 6.14(a). It illustrates that the mass of the top buckets system is correctly described.

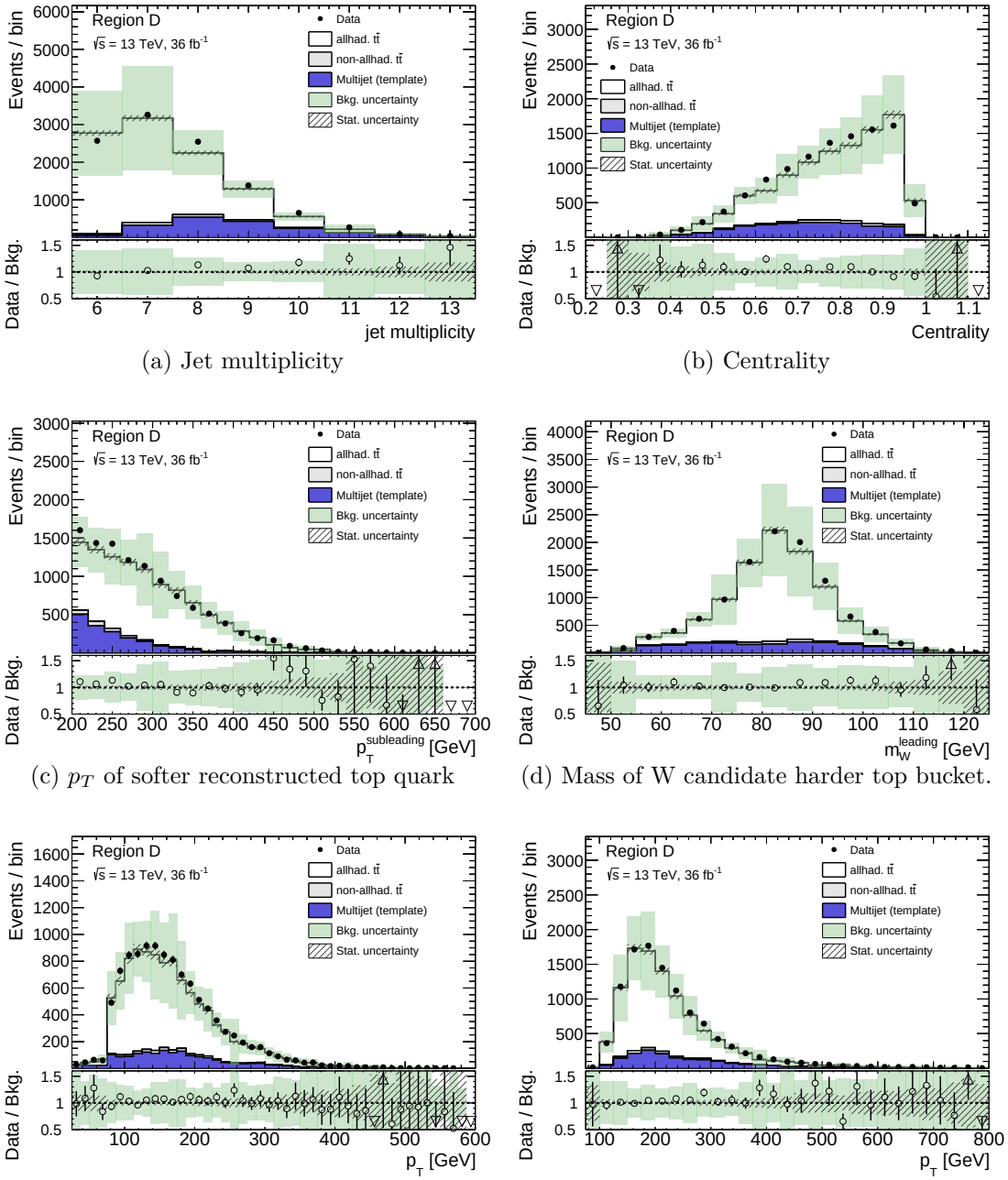

(a) Jet multiplicity

(b) Centrality

(c) p_T of softer reconstructed top quark

(d) Mass of W candidate harder top bucket.

(e) p_T of hardest b-tagged jet

(f) p_T of the hardest jet in the event

Figure 6.13.: Data to background model comparison of several variables in region D corresponding to top category ($\mathfrak{t}_w$, $\mathfrak{t}_w$).

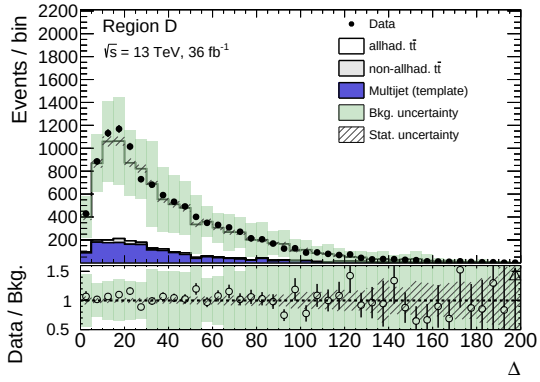

(a) Metric used in first reconstruction step

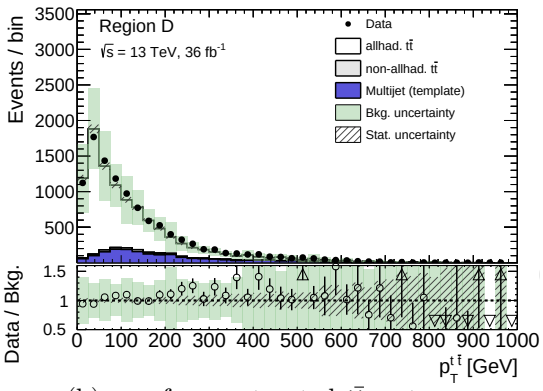

(b) p_T of reconstructed $t\bar{t}$ system

Figure 6.14.: Data to background model comparison of several top bucket variables in region D corresponding to top category ($\mathfrak{t}_w$, $\mathfrak{t}_w$).

6.10. Results

As motivated in the previous chapter the QCD multijet background estimation and the hypothesis testing are combined in one single step in order to improve the usage of information available in the data. The modified frequentist method is used where a CL_s limit [78, 201] is calculated based on the Maximum Likelihood Estimators of the profile likelihood ratio as described in Chapter 2.5.

6.10.1. Expected performance with the Asimov dataset

The Asimov dataset method [76] allows one to investigate the performance of the fit based on the model predictions. Instead of using the Monte-Carlo pseudo experiment approach the Asimov method provides a fast and reliable test of the median experimental sensitivity and fluctuations around it. The validity of the approach requires the assumption of the asymptotic approximation. In this procedure a *representative dataset* is constructed which corresponds to the predicted distribution and statistical uncertainty of the model based on the expected values. Using the Asimov dataset the correlations between nuisance parameters and potential constraints on them can be studied. This provides a cross-check for both the performance of the fitting procedure as well as for the potential differences to the results finally inferred from real data distributions.

According to Wilks theorem [202] in the asymptotic limit the profile likelihood ratio $-2\log\lambda$ is distributed as a χ^2 distribution if the null hypothesis is true. The more general Wald theorem [203] gives an approximation of the profile likelihood ratio for the non-null hypothesis. For the Asimov dataset the maximum likelihood estimators of the nuisance parameters are just the true values. Therefore, in the asymptotic limit the non-null profile likelihood ratio is described by the Asimov dataset and the known distribution can be linked to the significance without the necessity to generate toy Monte Carlo experiments [76].

The expected performance and significance can be determined doing background-only and signal plus background fits to the Asimov data. The numerical stability of the fit can be further investigated via a modified Asimov dataset which has a signal injected according to the MC predictions of the signal. First the background-only fit to the Asimov dataset is investigated. The pull of the nuisance parameters is shown in Figure 6.15 and the post-fit parameters are presented in Figure 6.16. The parameters describing the MC statistical uncertainty are referred to as the γ parameters in the following. By constructions the systematic uncertainties are centered at zero and the shape and normalization parameters are equal to one.

The uncertainties related to the $t\bar{t}$ modeling like e.g. parton shower, hard scatter generation and additional radiation are strongly constrained. This is expected as the SM $t\bar{t}$ is an irreducible background dominating in the signal region D with a contribution of around 80%. Also some of the nuisance parameters related to the detector performance like the jet energy calibration or some of the b-tagging eigenvectors are constrained. Many uncertainties affect mostly the normalization

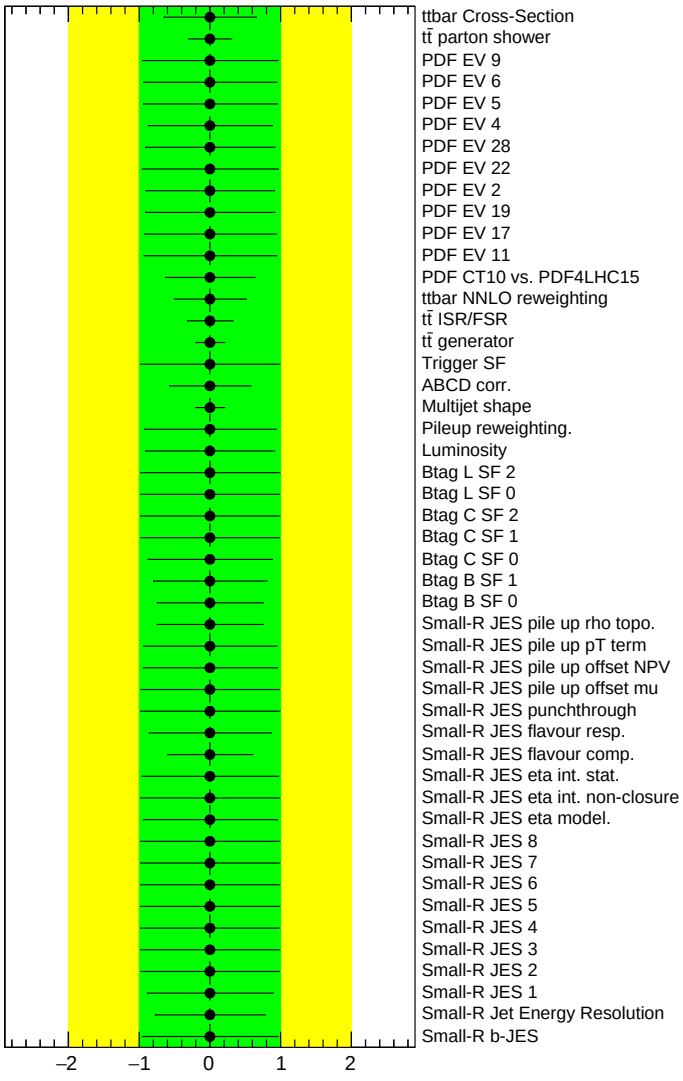

Figure 6.15.: The pull of the nuisance parameters using the Asimov dataset. Only uncertainties after the *pruning* procedure are shown.

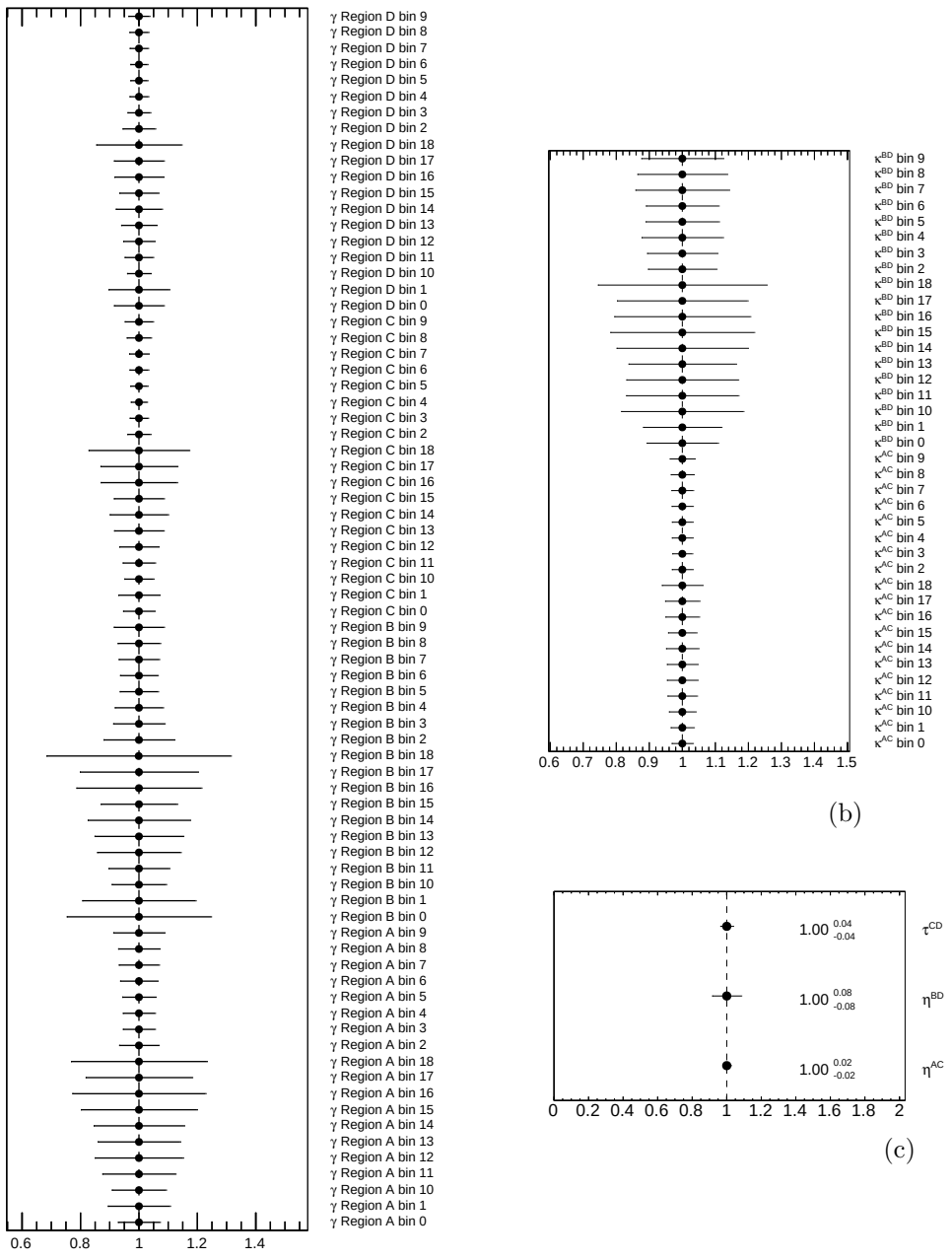

Figure 6.16.: Post-fit nuisance parameters for statistical uncertainty γ (a), NP for multijet shape factor κ (b) and normalization factors (c) using the Asimov dataset.

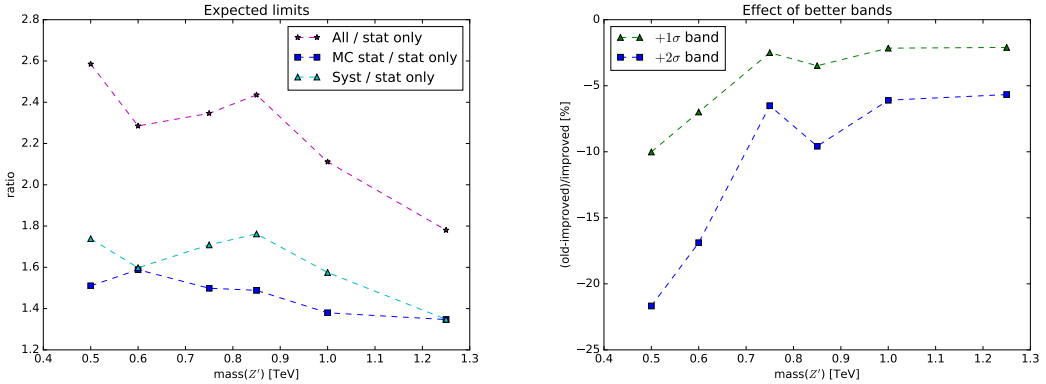

(a) Ratio of groups of expected limits with respect to the data statistics-only limits. The effect of the MC statistical uncertainties (MC stat), the systematics (syst) and the combination of all uncertainties is studied.

(b) Effect of the improved iterative treatment on the size of the $+1\sigma$ and $+2\sigma$ expected limit band.

Figure 6.17.: Properties of expected limits for different setups using the Asimov dataset.

which can be well fitted and constrained by the ABCD-Likelihood approach. The addition of the region ($\mathfrak{t}_w$, $\mathfrak{t}_-$) which has a relatively small signal contamination compared to ($\mathfrak{t}_w$, $\mathfrak{t}_w$) provides further information on the background normalization which improves the maximum likelihood fit. This especially applies to the b-tagging and PDF uncertainties which are characterized by small effects on the shape.

The uncertainties of the ABCD correlation and multijet shape are also constrained. The former one is only present in region D where the QCD purity is relatively small $\approx 20\%$ which explains why it is only moderately constrained. In contrast the constrain on the multijet shape uncertainty is quite strong which is supported by the fact that this uncertainty is simultaneous present in region C and region D and fully correlated between both regions.

The correlations between all NPs are investigated. A strong correlation points to scenarios where the stability of the fit of real data could be affected and must be well studied in advance to avoid that the correlations are not simply caused by inconsistencies of the model set-up. No strong correlation above 40% is present for the systematic uncertainties. The parameters η^{AC} and η^{BD} have by construction a strong $> 90\%$ correlation with the shape parameters κ. It was validated that they do not affect the expected limits.

Furthermore the impact of different groups of uncertainties are studied by removing the nuisance parameters of each group simultaneously in the fit. The best expected limits are achieved if only the uncertainties caused by the assumption of Poisson-distributed data are considered. This is referred to as data statistics-only limit in the following. The median expected sensitivity is degraded once the MC

statistical uncertainties are considered. This is done using Gaussian constraint parameters per bin as described in Chapter 6.8. The ratio between expected limits with MC statistical uncertainties and data statistics only is shown in Figure 6.17(a). The expected limit becomes worse by a factor of approximately 1.5 and depends only slightly on the considered mass range. The same procedure can be done for the complete group of systematic uncertainties referred to as the systematics group. The degrading effect on the limits is again visualized in Figure 6.17(a). The systematics effect is of similar size as the MC statistical uncertainty group. Correlations between the MC statistical uncertainties and the systematic uncertainties are expected to be small. This is supported by the combined expected limit including MC statistical and systematic uncertainties.

Besides providing the median expected limit the Asimov dataset method can be used to derive the expected $\pm 1\sigma$ and $\pm 2\sigma$ uncertainties on it. In the asymptotic limit a formula for the $n\sigma$ uncertainty can be calculated analytically [76] as described by the following equations

$$\mu_{\text{up}+N} = \sigma(\Phi^{-1}(1 - \alpha\Phi(N)) + N) \tag{6.10.1}$$

$$\sigma^2 = \frac{\mu^2}{q_{\mu,A}} \qquad [75]. \tag{6.10.2}$$

The method is based on an approximate relation between the variance and the test statistic. If σ depends strongly on μ it is necessary to account for small deviation of the approximation on σ. This is performed in an iterative procedure updating the Asimov dataset in each step [204]. Without this improved procedure the predicted bands would be too narrow as shown in Figure 6.17(b).

6.10.2. Observed limit based on 2015 and 2016 data

Before setting limits on the production cross-section times branching fraction of the benchmark signal models the SM-only hypothesis is tested with the *BumpHunter* procedure [73] as explained in Chapter 2.5.1. The post-fit $m_{t\bar{t}}^{\text{reco}}$ distribution including the systematic uncertainties based on the background-only fit serves as an input to the hypothesis test. The corresponding $m_{t\bar{t}}^{\text{reco}}$ distributions in the ABCD regions are presented in Figure 6.18. No significant excess or deficit is observed.

The results of the background-only fit are represented by the post-fit nuisance parameters. The pulls of the NPs are shown in Figure 6.19 and the correlation matrix between the NPs in Figure 6.20. The MC statistical uncertainty at post-fit level in terms of the γ parameters, the κ parameters of the multijet shape fit and the multijet normalization parameters are presented in Figure 6.21. The constraints on the nuisance parameters are consistent with the expected performance described in Chapter 6.10.1. Some of the SM $t\bar{t}$ modeling uncertainties are pulled like the scales and additional radiation uncertainty ($t\bar{t}$ ISR/FSR) as well as the jet energy resolution uncertainty. The size of the pulls are below 1σ. The multijet shape uncertainty is pulled around 1.7σ which is primarily caused by the pre-fit shape

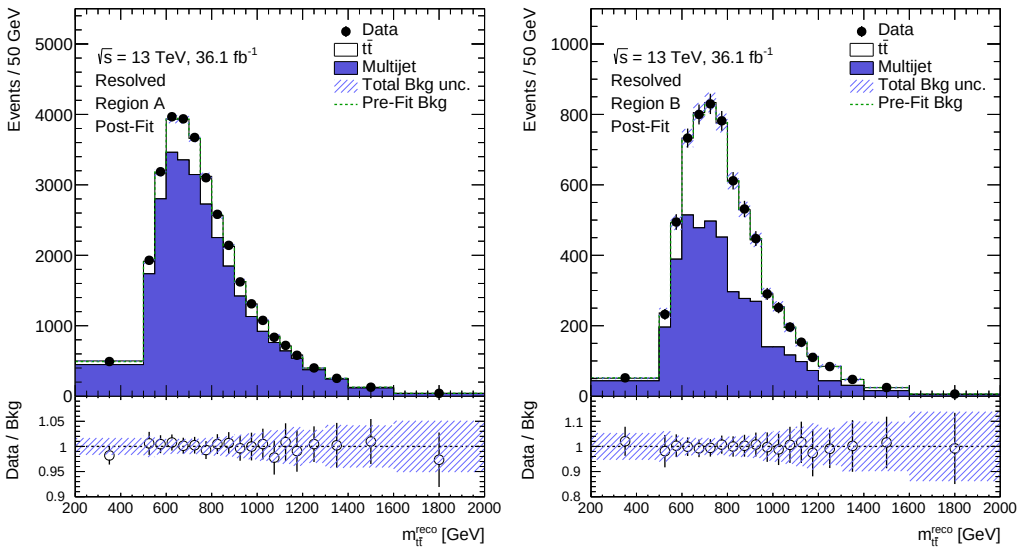

(a) Region A

(b) Region B

(c) Region C

(d) Region D

Figure 6.18.: Post-fit $m_{t\bar{t}}$ distribution including the systematic uncertainties. The statistical uncertainties on the MC events are not directly shown. But they enter through the shape factor parameters of the background fit.

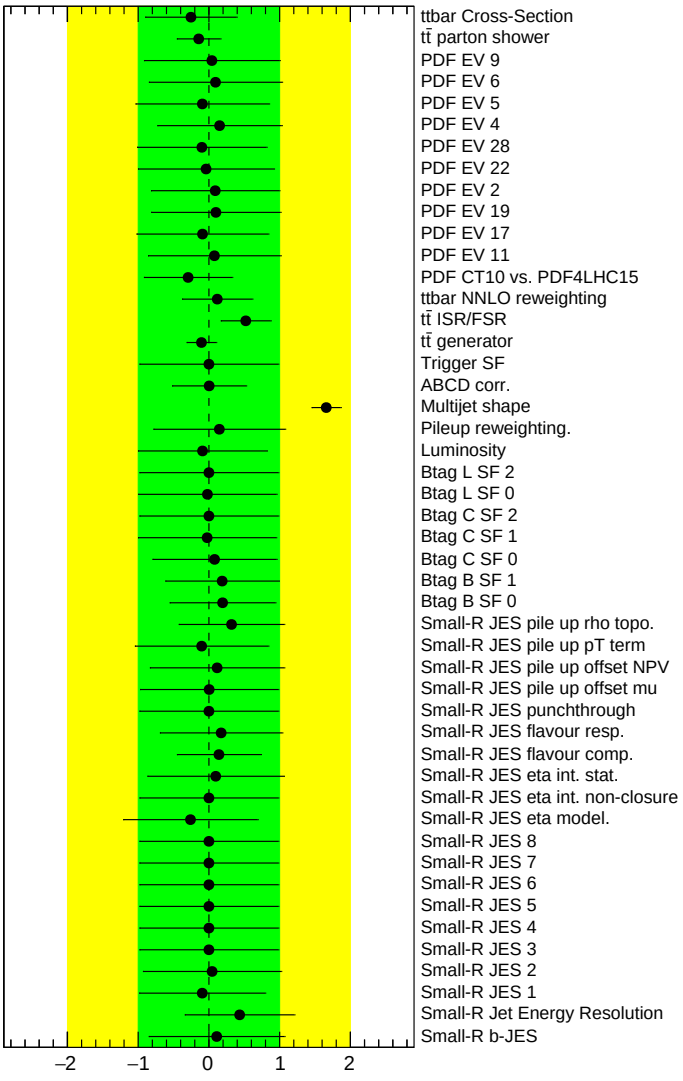

Figure 6.19.: The pull of the nuisance parameters using the 2015 and 2016 dataset. Only uncertainties after the *pruning* procedure are shown.

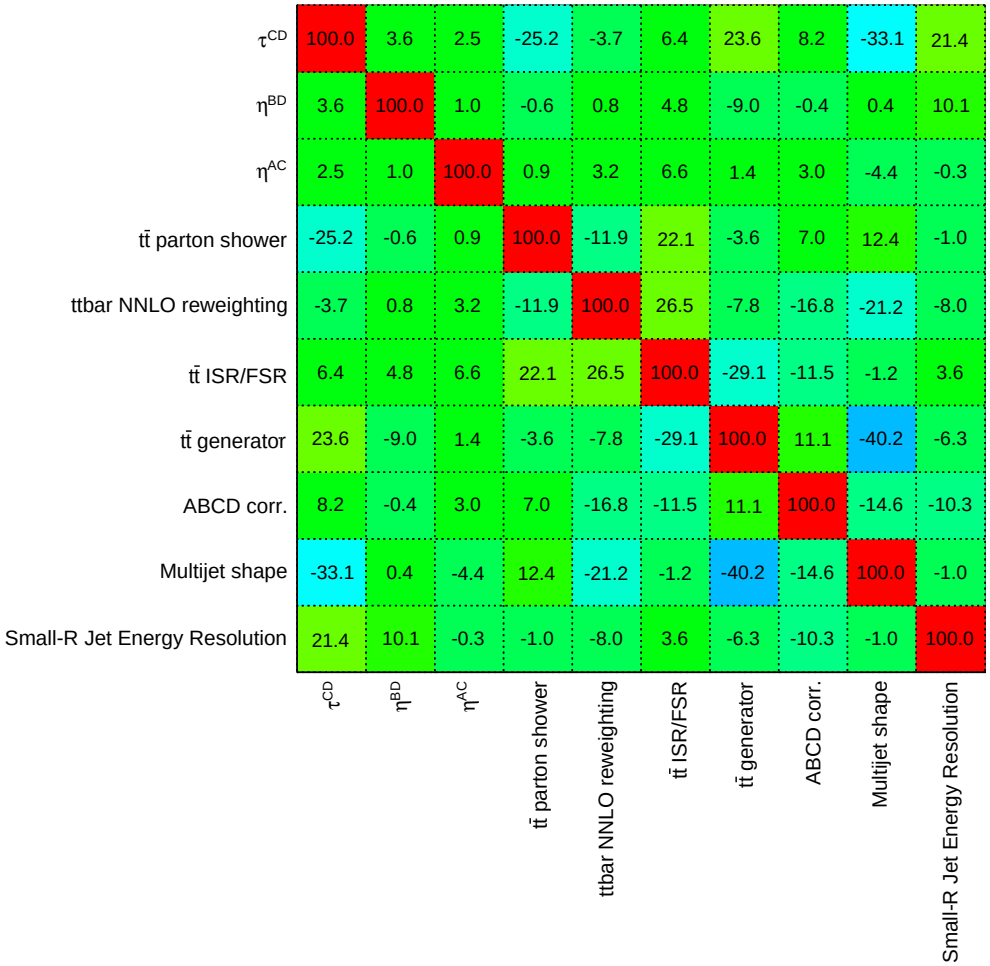

Figure 6.20.: Correlation between nuisance parameters using the 2015 and 2016 dataset. Only NPs with a correlation larger than 20% with any another NP are shown. The bin-by-bin NPs are omitted in the Figure.

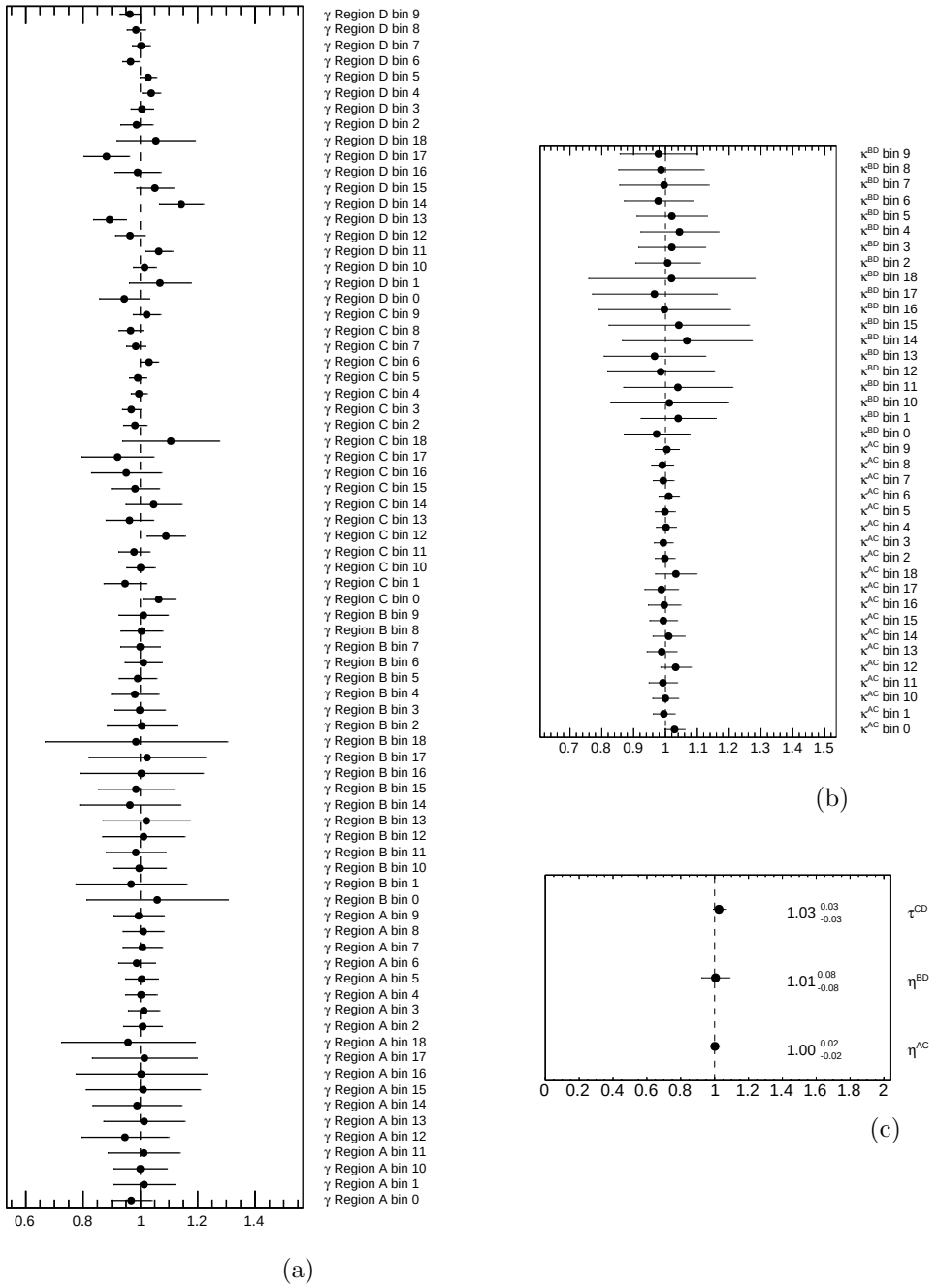

Figure 6.21.: Post-fit nuisance parameters for statistical uncertainty γ (a), NP for multijet shape factor κ (b) and normalization factors (c) using the 2015 and 2016 dataset.

Source of uncertainty	Relative impact	
	$+\Delta$	$-\Delta$
b-tagging efficiency	0.05	0.04
JES and JER	0.20	0.24
$t\bar{t}$ modeling	0.34	0.33
Multijet estimation	0.25	0.27
PDF	0.07	0.08
Pileup reweighting	0.07	0.05
Simulation statistical uncertainty	0.41	0.41
Total systematic uncertainty	0.92	0.92
Data statistical uncertainty	0.39	0.39

Table 6.9.: The relative post-fit impact on the signal strength parameter μ for the Z'_{TC2} model with $m = 0.75$ TeV. The groups of systematic uncertainties with an relative impact on the signal strength larger than 2% are presented. The reference uncertainty used to calculate the relative impact is the post-fit uncertainty on μ inferred from the signal plus background fit. The impact of a specific nuisance parameter is evaluated by first fixing the value of the NP to its calculated $\pm 1\sigma$ post-fit value inferred from the nominal fit. Secondly the fit is repeated with the reduced set of freely floating NPs. The impact is calculated from the difference between the best-fit μ in the reduced fit and the nominal fit. The relative impact is grouped and summed in quadrature for different sources of systematic uncertainties. The total systematic uncertainty is different from the sum in quadrature of the different components due to correlations between nuisance parameters. The data statistical uncertainty is evaluated by fixing all the nuisance parameters in the fit to the best-fit values except for the unconstrained normalization factors.

Signal		Expected [TeV]	Observed [TeV]
Z'_{TC2}	($\Gamma = 1.2\%$)	$[0.59, 1.25]$	$[0.59, 1.25]$
	($\Gamma = 3\%$)	$[0.50, 1.25]$	$[0.57, 1.25]$
Z'_{med}	(vector)	$[0.75, 1.07]$	$[0.74, 0.97]$
	(axial-vector)	–	$[0.80, 0.92]$
g_{KK}	($\Gamma = 30\%$)	< 1.67	< 1.56

Table 6.10.: The expected and observed excluded mass ranges at 95% CL for the considered benchmark signal models.

difference in region C. Due to the construction of the multijet shape uncertainty that effectively resembles a reweighting of the distribution a relatively strong pull is not unexpected. The stability of the fitting procedure with a single strongly pulled NP is validated by scaling the multijet shape uncertainty up such that the post-fit pull is below 1σ. The pulls of the other nuisance parameters are confirmed to be basically unaffected by the scaling. The successful background estimation based on the ABCD-Likelihood is supported by the post-fit κ_b^{AC}, η^{AC}, κ_b^{BD}, η^{BD} and τ^{CD} parameters that are consistent with one within their uncertainties. The effect of the systematic uncertainties on the signal strength parameter μ is listed in Table 6.9. The post-fit impact of the SM $t\bar{t}$ modeling which dominated the pre-fit uncertainties is reduced. The strongest impact is caused by the small-R jet energy scale and jet energy resolution, the SM $t\bar{t}$ modeling, the multijet estimation as well as the MC statistical uncertainties.

In the absence of significant deviations from the SM-only hypothesis expected and observed upper limits at 95% CL are set on the production cross section times branching fraction for signal benchmark models. The limits are presented in Figure 6.22 as a function of the pole mass and in Figure 6.23 for the KK gluon g_{KK} as a function of the width. The points between the pole masses and the width are linearly interpolated. The expected and observed excluded mass ranges are summarized in Table 6.10. At low invariant masses below around 0.6 TeV the sensitivity is reduced by the trigger thresholds and the respectively optimized selection criteria. At higher masses above around 1 TeV the limit becomes less steep due to the increasing uncertainties. The observed (expected) excluded mass range of the topcolor assisted technicolor Z'_{TC2} is $[0.59, 1.25]$ ($[0.59, 1.25]$) for the narrow $\Gamma/m = 1.2\%$ scenario. The sensitivity is insufficient to set exclusion limits on the *Bulk* RS KK graviton model. The simplified dark matter models are still characterized by a narrow width. Therefore, the expected and observed limits a relatively close to the Z'_{TC2} model. The KK gluon model with a width $\Gamma/m = 30\%$ is excluded for masses below 1.56 TeV (1.67 TeV expected). At a KK gluon mass of 0.5 TeV the limits depend only slightly on the width. This is caused by the lack of events for $m_{t\bar{t}}^{\mathrm{reco}}$ below 0.5 TeV as well as by the threshold effects due to the acceptance times efficiency as shown in Figure 6.3. For higher KK gluon masses the limits

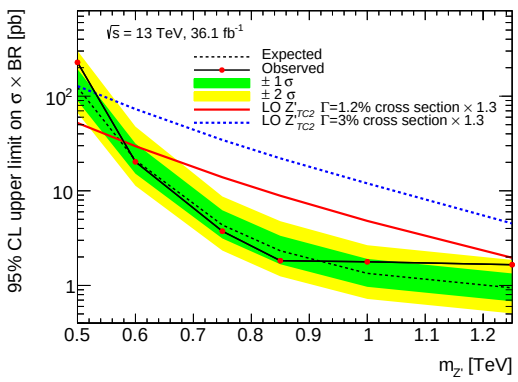

(a) Topcolor assisted technicolor Z'_{TC2}.

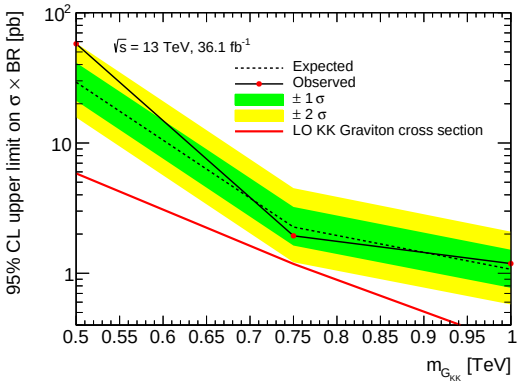

(b) KK graviton G_{KK}.

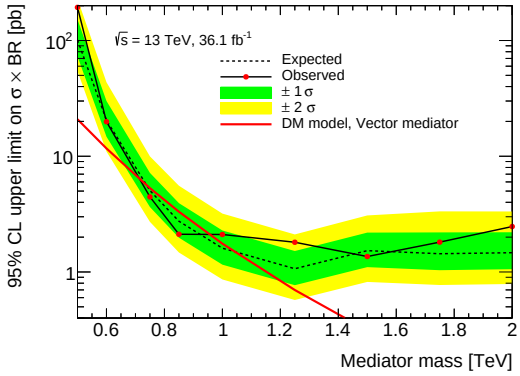

(c) Simplified DM, Vector mediator.

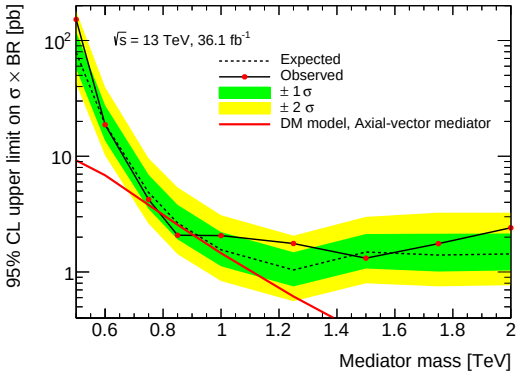

(d) Simplified DM, Axial-vector mediator.

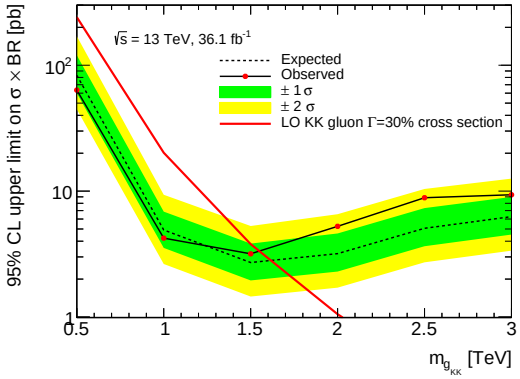

(e) KK gluon g_{KK}.

Figure 6.22.: Observed and expected 95% CL upper limits on the cross section times branching fraction for several signal benchmark models as a function of the pole mass.

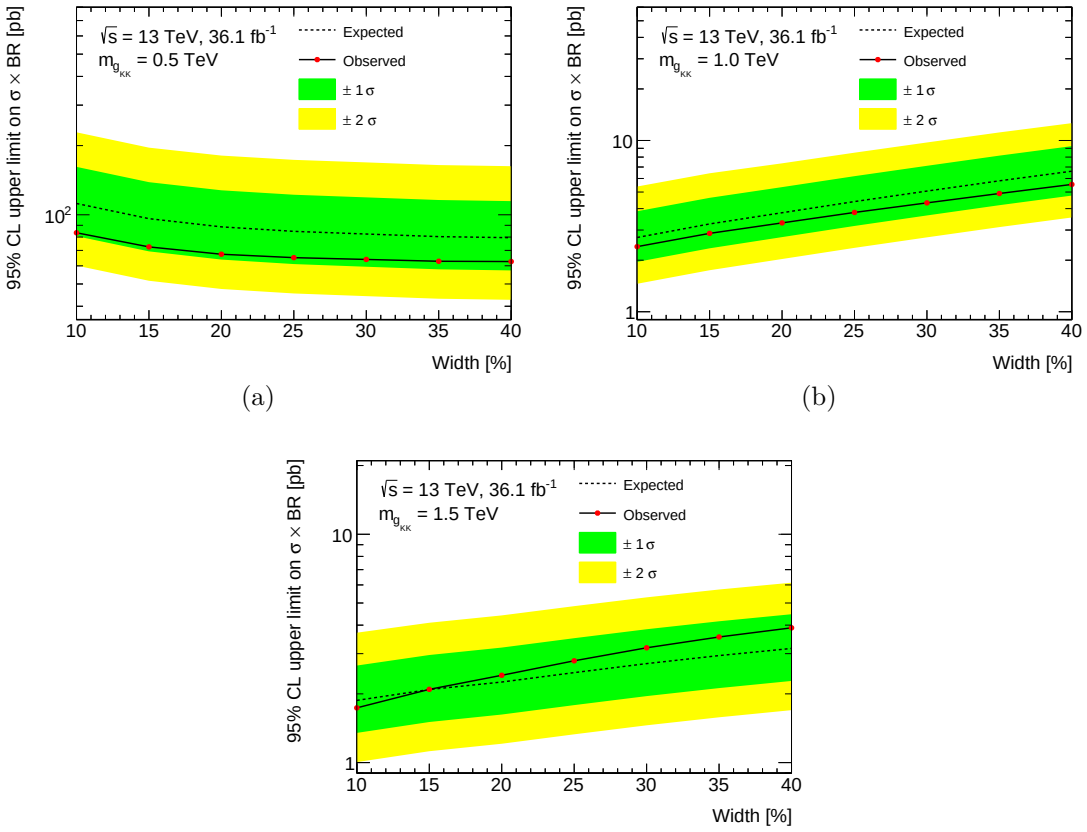

Figure 6.23.: Observed and expected 95% CL upper limits on the cross section times branching fraction for KK gluon g_{KK} signal benchmark model at different pole masses as a function of the width over mass Γ/m.

improve with decreasing width as expected by the better separation between signal and background events.

6.11. Summary and Outlook

A search for new heavy particles decaying to a top quark pair in the fully hadronic decay channel is performed using 36.1 fb^{-1} of data collected from proton–proton collisions at a center of mass energy of 13 TeV with the ATLAS detector at the LHC. The search targets the mass range from 500 GeV to around 1300 GeV for the new particles. The presence of jets identified as likely to contain B hadrons helps to reject the large QCD multijet background and seeds the top quark reconstruction. The buckets of tops method is used to select fully hadronic $t\bar{t}$ events with a moderately high transverse momentum $p_T > 200$ GeV of the top quarks. No deviation from the Standard Model prediction is observed in the considered mass range of the $t\bar{t}$ system. Upper limits on the production cross section times branching ratio are set on the signal benchmark models characterized by different spins and widths of the hypothetical new particle. The limits are transfered to excluded mass ranges for the topcolor assisted technicolor model Z'_{TC2}, mediators Z'_{med} in simplified dark matter models and Kaluza-Klein excitations of the gluon g_{KK} in the Randall–Sundrum model. The Kaluza-Klein excitations of the graviton G_{KK} in the *bulk* Randall–Sundrum model are not excluded in the investigated mass range.

The dataset with an integrated luminosity of 36.1 fb^{-1} at $\sqrt{s} = 13$ TeV was used by the ATLAS collaboration to search for resonant $t\bar{t}$ production in the lepton–plus–jets channel of the top quark pair [59]. The analysis focused on two top quark reconstruction techniques to achieve a wider search range for the new heavy particle mass using a substructure based top reconstruction for the boosted regime. The trigger relies on leptonic trigger chains allowing to set limits down to the threshold region of $t\bar{t}$ production around masses of 400 GeV. A search for heavy particles decaying to $t\bar{t}$ is also performed by the CMS collaboration using 36 fb^{-1} of proton–proton collision data recorded at a center of mass energy of $\sqrt{s} = 13$ TeV at the CMS experiment. Exclusive final states corresponding to the $t\bar{t}$ decay modes are constructed. The analysis focuses on boosted top quark reconstruction. The limits of the three analyses for a narrow-width Z' are compared in Figure 6.24. The dedicated boosted analysis strategy helps to improve the limits particularly for high masses above 1000 GeV in the allhadronic scenario.

This thesis presents the first search for resonant $t\bar{t}$ production in the allhadronic decay channel at $\sqrt{s} = 13$ TeV targeting the low invariant mass range below 1300 GeV. A double-sideband likelihood approach successfully combines the QCD multijet estimation with the hypothesis test. The analysis relies on a relatively high multiplicity of small radius jets. Therefore, it can be combined with a boosted analysis using large radius jets based on the expected limits that are likely to show a turn-over at around 1000 GeV due to the necessary event selection. In addition, the analysis is orthogonal to the lepton–plus–jets $t\bar{t}$ decay modes. A future

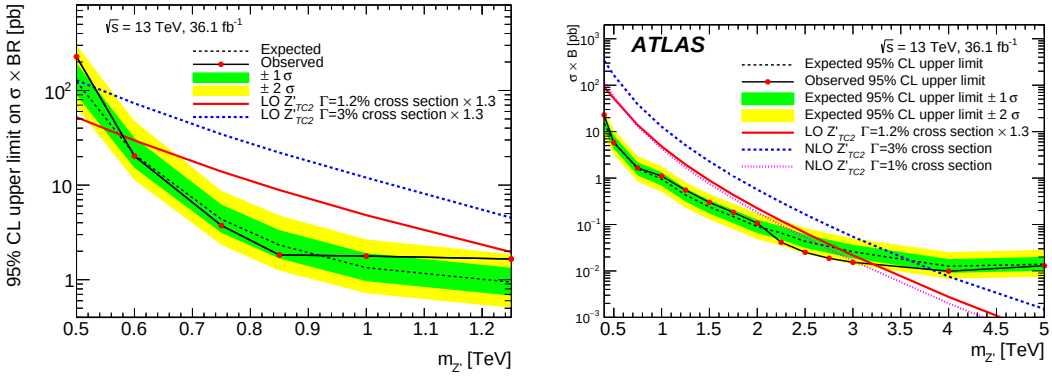

(a)

(b)

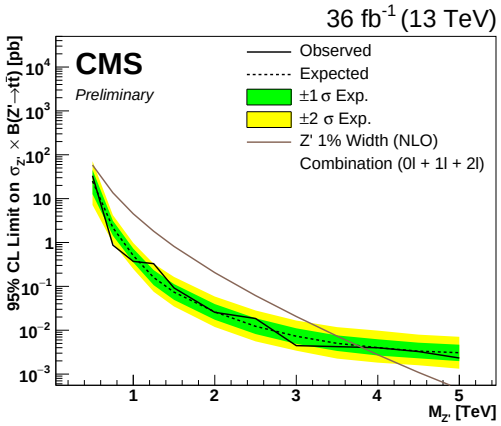

(c)

Figure 6.24.: Observed and expected 95% CL upper limits on the cross section times branching fraction for a topcolor assisted technicolor model Z' produced in proton–proton collisions at $\sqrt{s} = 13$ TeV. The results of the allhadronic search presented in this thesis (a), of the search in the lepton–plus–jets decay mode of the $t\bar{t}$ system at ATLAS [59] (b) and of the search for resonant $t\bar{t}$ production at CMS [205] (c) are shown.

combination of the analyses in ATLAS can further improve the limits.

The analysis is optimized for the used multijet trigger. Increasing luminosities influence the development of the available trigger chains in ATLAS and thereby the performance of the search. Future optimizations at low invariant masses can involve modifications of the trigger strategy. The usage of b-tagging at trigger level [17, 18, 100, 206, 207] can reduce the transverse momentum requirements on the selected jets or help to keep the current thresholds at higher luminosities. New trigger chains complementing the b-tagging approach are discussed in Chapter 8. Furthermore, future development in the tracking at trigger level, as e.g. provided by the FastTracker (FTK) trigger system [208] in ATLAS, can be used to revise the trigger strategy.

7. Search for the Standard Model Higgs boson in association with a top quark pair in the fully hadronic final state

7.1. Introduction

After the discovery of the Higgs boson, precise measurements of its properties like the couplings to SM particles are becoming important. Measuring the couplings to fermions is expected to reveal new insights into the electroweak symmetry breaking (EWSB) mechanism. The first direct Higgs boson to fermion interaction (ffH) was observed in the H to $\tau\tau$ decay channel with a combined ATLAS and CMS sensitivity of 5.5σ [209] in Run 1. Recently, the decay of the Higgs boson into a bottom quark pair was observed with a sensitivity of 5.4σ using combined Run 1 and Run 2 data at ATLAS [210]. The top quark is the heaviest Standard Model fermion and influences the renormalization group evolution of the Higgs potential to high energy scales. It is therefore expected to play an important role in EWSB and studying the $t\bar{t}H$ coupling could be a window to phenomena beyond the Standard Model.

A combined fit of ATLAS and CMS measurements of the Higgs properties in Run 1 was used to obtain a top Yukawa coupling value in the κ framework κ_t of $0.87^{+0.15}_{-0.15}$ [209]. Due to the large mass of the top quark it dominates one of the main production mechanisms namely gluon fusion $gg \to H$ (ggF) and contributes strongly to the decay channel $H \to \gamma\gamma$. In both processes the top quark appears inside loops. This indirect method of measuring the $t\bar{t}H$ coupling relies on the assumption that no new particles contribute to the ggF production or the $H \to \gamma\gamma$ decay. In contrast to inferring the top Yukawa coupling from the ggF production cross-section and $H \to \gamma\gamma$ branching fraction, a direct measurement of $t\bar{t}H$ would allow one to directly test effects of phenomena beyond the Standard Model. The direct $t\bar{t}H$ production could not be observed with $\sqrt{s} = 7$ TeV and $\sqrt{s} = 8$ data alone with a corresponding significance of 4.4σ compared to an expected significance of 2.0σ [209]. The measured signal strength based on $\sqrt{s} = 7$ and 8 TeV data is $2.3^{+0.7}_{-0.6}$. Using ATLAS data at $\sqrt{s} = 13$ TeV with an integrated luminosities up to 79.1 fb^{-1} results in an observed (expected) significance of 5.8 (4.9) [211]. An observed (expected) significance of 6.3 (5.1) is achieved if also the $\sqrt{s} = 7$ and

8 TeV datasets are added [211]. The measured $t\bar{t}H$ production cross section at $\sqrt{s} = 13$ TeV is $670 \pm 90(\text{stat.})^{+110}_{-100}(\text{syst.})$. The $t\bar{t}H$ production with a subsequent $H \to bb$ decay and non allhadronic top quark decays was studied at $\sqrt{s} = 13$ TeV with ATLAS data [212]. The corresponding decay in the allhadronic $t\bar{t}$ decay mode was studied at $\sqrt{s} = 8$ TeV [213].

Even though the direct measurement of the top Yukawa coupling is a promising tool to test BSM effects, the small $t\bar{t}H$ production cross section for $\sqrt{s} = 13$ TeV proton-proton collisions makes a measurement challenging. The fully hadronic channel, i.e. both top quarks decay hadronically, has the largest branching ratio. But the channel also suffers from small signal purity due to the overwhelming QCD multijet background. At leading order, the final state of the process consists of four bottom quarks and four additional lighter quarks. As a result the final state is characterized by a high multiplicity of jets with the consequence that the reconstruction of the top quark pair and the Higgs boson is generally affected by combinatorial backgrounds. Precise reconstruction of the Higgs boson and the top quark pair from their decay products can serve as a suitable method to suppress the background.

The resonance search presented in Chapter 6 exploits primarily the precise top quark reconstruction of all $t\bar{t}$ decay products which results in a reduced combinatorial background and a better $m_{t\bar{t}}$ mass resolution which is relevant for setting limits on narrow resonances. In the light of a small signal cross-section for $t\bar{t}H$ and reduced signal acceptance due to the high trigger thresholds this channel requires a highly efficient top reconstruction which could be provided by the bucket algorithm as first proposed by Reference [214]. In addition, the reconstruction in this busy high jet multiplicity environment has to deal with different scenarios where the available offline jets only give an incomplete or approximate description of the original $t\bar{t}H$ decay.

In this chapter, a feasibility study for the search for $t\bar{t}H$ production at $\sqrt{s} = 13$ TeV with 2016 ATLAS data where both top quarks decay hadronically is presented. The selection especially emphasizes the sensitivity to $H \to bb$ decays ($ttH(H \to bb)$) but also the other decay modes are included as signal.

Sidebands are used for modeling the background. The QCD multijet background is derived using a data-driven technique. Also, the modeling of SM $t\bar{t}$ is challenging for this final state with high multiplicity of jets, out of which several are heavy flavor jets. Previous studies have shown that in particular the modeling of the tt+heavy flavor process can affect the results [213] . The analysis in this thesis relies on a multivariate discriminant approach based on general event shape variables and kinematic selections for the background suppression. The strategy and performance of the multivariate method is discussed in Section 7.8. The possibility of using sidebands in the reconstructed Higgs mass spectrum is studied in Section 7.7. The sideband method has the advantage that this approach is more reliable to deal with anomalies like potential BSM contributions.

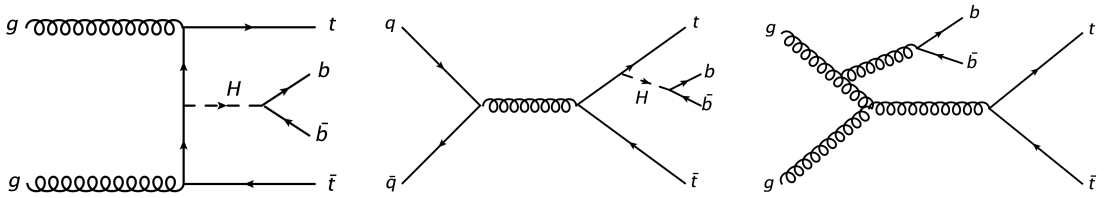

Figure 7.1.: Feynman diagrams of the $t\bar{t}H$ signal process (a), (b) and a typical SM $t\bar{t}+b\bar{b}$ background process (c) from Reference [215].

7.2. Analysis strategy and event selection

The guiding principle of the event preselection is to select signal like events which allow one to perform the top quark reconstruction and the construction of the additional event shape variables used for background suppression as explained in Chapter 7.8. At leading order, the fully hadronic $ttH(H \to bb)$ final state should be characterized by eight jets out of which four are tagged as originating from a bottom quark. The most dominant background for such an allhadronic final state at the LHC is QCD multijet production. This background is using a data-driven technique as described in Chapter 7.5.3. Another background source explicitly considered are top quark pairs with additional light or heavy flavor jets. Recent fiducial cross-section measurements performed in the lepton-plus-jets channel of the $t\bar{t}$ decay [216] suggest a sizable contribution of such processes relative to the $t\bar{t}H$ signal. Typical Feynman diagrams for the signal and background processes are presented in Figure 7.1.

The object definitions are mostly identical to the ones used in Chapter 6.2.1. They are summarized in Chapter 7.2.1 emphasizing the differences present for an allhadronic $t\bar{t}H$ selection. The analysis is based on events recorded by ATLAS in proton-proton collisions at $\sqrt{s} = 13$ TeV in the 2016 data taking period. The integrated luminosity in this time period corresponds to 32.8fb^{-1}.

7.2.1. Object reconstruction and general preselection

The objects used in the $t\bar{t}H$ selection are largely based on the general definitions given in Chapter 3.4. The main difference with respect to the $t\bar{t}$ resonance selection is the lower momentum regime targeted and the higher expected jet multiplicity of the final state. In order to preserve orthogonality to other $t\bar{t}$ decay channels with leptonic decay modes a specific optimization of the object definitions and overlap removal is omitted.

Data events are only considered when all the detector systems were fully operational. All tracks with $p_T > 400$ MeV are used to determine the interaction vertices. The vertex which maximizes the sum of associated tracks $\sum p^2_{T,\text{track}}$ is selected as primary vertex.

The most relevant objects for the calculation of the selection variables are small-R jets and in particular b-tagged jets. All jets have to pass quality criteria to avoid jets from detector noise or non-collision backgrounds [156]. If any jet fails these criteria the event is discarded. A suppression of pure pileup jets with $p_T < 60$ GeV and $|\eta| < 2.4$ is achieved by the Jet Vertex Tagger [158] which exploits information from tracks associated to the jets.

Depending on the region considered the *loose* or *tight* working point of the b-tagging algorithm is chosen. The hardest b-tagged jet is required to be central with a pseudorapidity of $|\eta| < 1.6$ which is motivated in the context of the QCD multijet background estimation in Chapter 7.5.3.

The reconstruction of electrons is based on clusters in the electromagnetic calorimeter combined with the track information of the ID [151, 178]. The LAr crack veto is applied by requiring that the electron candidates are outside $1.37 < |\eta_{\text{cluster}}| < 1.52$. Track-matching and shower-shape variables are used to define a tight set of selection criteria as explained in Reference [151]. Muon candidates are build from tracks of the MS which are matched to ID tracks [147]. In a next step, improved tracks are calculated using the combined information of the two sub-detectors. Isolation criteria are applied on the electrons and muons in order to reduce the contribution from non-prompt leptons. Muons and electrons with $p_T > 25$ GeV and $|\eta| < 2.5$ are selected and used for the lepton-jet overlap removal procedure. The motivation of the overlap removal is to reduce the probability of double-counting a single detector response in the reconstruction of several objects. Objects are not considered in subsequent overlap removal steps once they are rejected. The jet closest to an electron within $\Delta R < 0.2$ is removed to avoid double-counting of electron energy deposits as a jet. Subsequently, electrons which are within $\Delta R < 0.4$ of a jet are removed. High-energy muons can deposit a significant amount of energy in the calorimeter. Hence, any jet which has less than three tracks associated to it is removed under two circumstances: first, if the jets is within $\Delta R < 0.2$ to a muon or second, if the the jet has a muon inner-detector track ghost-associated to it. Subsequently, muons are rejected if they are within $\Delta R < 0.4$ of the remaining jets to suppress the contribution of muons originating from heavy flavor decays.

Top quark pair reconstruction The reconstruction of the top quark pair allows the suppression of the background and provides a Higgs candidate as will be shown in the following. One advantage of the bucket algorithm is the relatively high efficiency for a large variety of top quark decay topologies. This flexibility makes it a promising tool to test the $t\bar{t}H$ final state. The low signal cross-section requires a high reconstruction efficiency of the top quarks. The standard bucket algorithm as introduced in Chapter 4 is used. No further modifications are necessary to apply it on the $t\bar{t}H$ topology.

The high jet multiplicities and b-jet multiplicities present are likely to increase the combinatorial background. Therefore, the $t\bar{t}$ reconstruction performance is expected to degrade compared to the study conducted in Chapter 5. Selections

Variable	Control Region	Signal Region
Number of jets ($p_T > 25$ GeV)	≥ 8	≥ 8
Multijet trigger	pass	pass
Number of jets ($p_T > 75$ GeV)	≥ 5	≥ 5
Number of loose b-tagged jets	≥ 4	≥ 4
Number of tight b-tagged jets	$= 0$	≥ 4
Hardest b-tagged jet	$\lvert\eta\rvert < 1.6$	$\lvert\eta\rvert < 1.6$
Top candidates	within mass windows	within mass windows

Table 7.1.: Summary of the analysis specific event preselections for the control and signal region.

applied after the top reconstruction to assure a better quality are described together with the other event selection requirements in Chapter 7.2.2. The performance of the top quark identification and reconstruction is discussed in Chapter 7.4 taking into account the general design and the goals of the analysis.

Higgs boson candidate reconstruction The bucket algorithm assigns several jets and in particular two b-tagged jets to the top quark pairs. As a consequence, the remaining jets or b-tagged jets that are assigned to the third bucket (B_{ISR}) can be used to construct the Higgs boson candidate. Thereby the Higgs boson candidate is identified by exclusion of the top jets. Depending on the b-jet multiplicities two cases are distinguished: if exactly four b-tagged jets are present in the event the two b-tagged jets not associated to the $t\bar{t}$ system constitute the Higgs candidate, otherwise if more than four b-tagged jets are found, the two b-jets with the highest transverse momentum are selected as the Higgs candidate after excluding the $t\bar{t}$ related jets. Even though not all available information in the event is directly used for the identification of the Higgs candidate, this approach, using the exclusion of top jets, has the advantage that the reconstructed Higgs boson mass spectrum is expected to have a reduced selection-induced shaping. The implications of the combined classification of top quark and Higgs boson candidates is further discussed in the context of the event preselections in Chapter 7.2.2.

7.2.2. Analysis specific event preselection

The event preselection is chosen to enhance the allhadronic $t\bar{t}H$ phase space and to provide a set of jets and b-tagged jets which allow the reconstruction of the top quark system using the bucket algorithm.

Events which still contain electrons or muons after the overlap removal are vetoed to suppress leptonic decay modes of the $t\bar{t}$ system. The lowest momentum jets in a $t\bar{t}H$ signal event are produced with relatively small transverse momentum compared to typical trigger thresholds applied during 2016 ATLAS data taking. Therefore, events are selected with the lowest available unprescaled multijet trigger requiring at

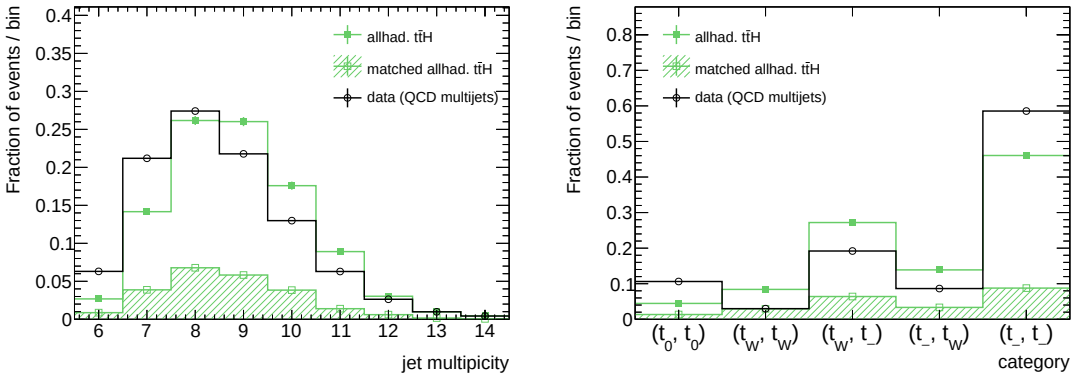

(a) Jet multiplicity. Preselection before the cut on the jet multiplicity.

(b) Event categories based on bucket mass window selections. Preselection before the cut on the event category.

Figure 7.2.: Shape comparison of signal and background distributions. The data is taken from the *b-tag control region* and consists mainly of QCD multijets. The matching in simulated signal events is done between the Higgs candidate and the truth Higgs using the geometrical requirement $\Delta R < 0.3$. The distributions are shown after the preselection described in Chapter 7.2.2 and summarized in Table 7.1 but before the cut on the respective variable.

least five jets with $E_T > 65$ GeV at trigger level. The trigger rate is further reduced by considering only central jets with $|\eta| < 2.4$. Inefficient regions of the trigger are avoided by requiring $p_T > 75$ GeV for the five hardest offline jets. All small radius jets in the event must fulfill a minimal transverse momentum of $p_T^{\text{jet}} > 25$ GeV and have $|\eta| < 2.5$. The minimal jet multiplicity to associate to each final state parton a jet is eight. As mentioned before jets originating from the top quark decay can fail the transverse momentum selection resulting in a reduced number of jets. The sensitivity of the analysis could be improved by also selecting the six and seven jet final state. As this will have consequences on the event kinematics it is not considered in this proof of principle analysis but could be added in a future iteration as e.g. an extra sideband region. The distribution of the jet multiplicity for $t\bar{t}H$ signal MC and the background is shown in Figure 7.2(a). The background is constructed from data in a region with negligible signal contribution relying on a looser b-tagging selection as described in Chapter 7.5.3.

The multiplicity of b-tagged jets has to be at least four which reduces the QCD multijet background. Comparing the distributions for correctly reconstructed simulated $t\bar{t}H$ signal events and the background template as shown in Figure 7.3(a) illustrates that even more than four b-tagged jets are reconstructed occasionally in the signal. For the $t\bar{t}H$ signal MC, in around 90% of the events exactly four b-tagged jets are reconstructed.

The bucket algorithm allows the classification of the events in certain event cate-

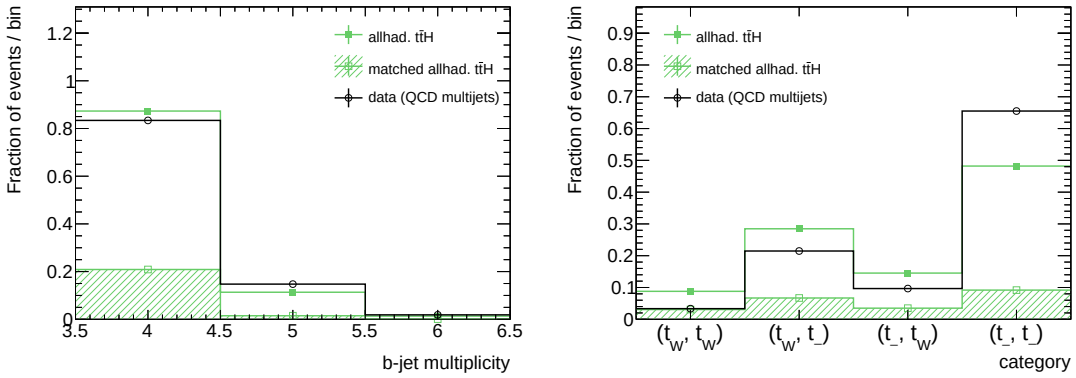

(a) b-jet multiplicity (b) Event category

Figure 7.3.: Shape comparison of signal and background distributions. The data is taken from the *b-tag control region* and consists mainly of QCD multijets. The matching in simulated signal events is done between the Higgs candidate and the truth Higgs using the geometrical requirement $\Delta R < 0.3$. The distributions are shown after the preselection described in Chapter 7.2.2 and summarized in Table 7.1.

gories depending on whether a W boson candidate is found inside a top candidate and the top mass window selection is fulfilled. All four (t_w, t_w), (t_w, t_-), (t_-, t_w) and (t_-, t_-) are considered. Only events where the tops are outside the mass window corresponding to (t_0, t_0) are vetoed. The corresponding distributions of the event categories are shown in Figure 7.2(b) before the restriction on the top mass window and in Figure 7.3(b) after preselection. Vetoing the (t_0, t_0) category allows for a clear interpretation of the reconstructed top quark pair. The effect on the signal efficiency is small as merely around 5% of the signal events are in the (t_0, t_0) region.

The trigger efficiency dependence on the transverse momentum of the fifth hardest jet (p_T^{j5}) in an event is shown in Figure 7.4 for simulated signal $t\bar{t}H$ events. The criterion $p_T^{\mathrm{j5}} > 75$ GeV is chosen as the trigger efficiency becomes close to the plateau region. The trigger selection can significantly reduce the signal efficiency. The integrated trigger efficiencies of $t\bar{t}H$ events are given for three different conditions:

$$\epsilon_1 = \frac{\text{trigger fired}}{\text{preselection with } p_T^{5^{\text{th}}\text{jet}} > 75\text{GeV}} > 99\% \tag{7.2.1}$$

$$\epsilon_2 = \frac{\text{trigger fired}}{\text{preselection with } p_T^{5^{\text{th}}\text{jet}} > 25\text{GeV}} = 48.6 \pm 0.1\% \tag{7.2.2}$$

$$\epsilon_3 = \frac{\text{trigger fired AND } p_T^{5^{\text{th}}\text{jet}} > 75\text{GeV}}{\text{preselection with } p_T^{5^{\text{th}}\text{jet}} > 25\text{GeV}} = 34.2 \pm 0.1\% \ . \tag{7.2.3}$$

The integrated trigger efficiency is $\epsilon_1 > 99\%$ for $t\bar{t}H$ events. The integrated trigger

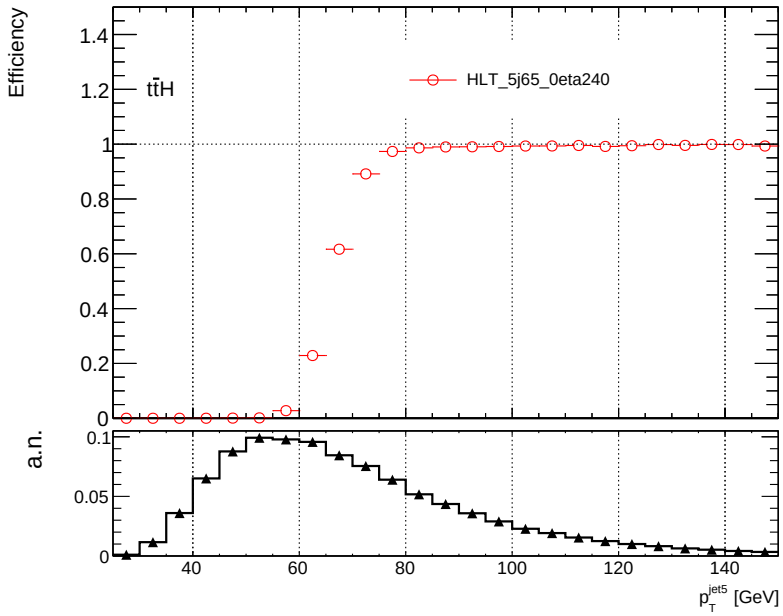

Figure 7.4.: Trigger turn-on curve and distribution of the transverse momentum of the fifth hardest jet evaluated in $t\bar{t}H$ signal events. The same selection as described in Chapter 7.2.2 is applied except for the p_T requirement of the fifth hardest jet.

efficiency on events passing all of the preselection requirements besides the trigger selection and besides requiring $p_T^{\mathrm{j5}} > 75$ GeV is $\epsilon_2 = (48.6 \pm 0.1)\%$. The corresponding efficiency for having the trigger also in the plateau regime in $t\bar{t}H$ MC is $\epsilon_3 = (34.2 \pm 0.1)\%$. Therefore, selecting also events significantly below the trigger plateau ($p_T^{\mathrm{j5}} \ll 75$ GeV) could help to recover the signal. The corresponding trigger efficiencies of such selections are measured and studied in Chapter 6.5. Due to the associated systematic uncertainties present at lower p_T^{j5} this possibility is not applied in this proof of principal analysis. The prospects of alternative trigger strategies which aim to recover the lost signal are studied and discussed in Chapter 8.

As motivated in Chapter 7.5.3 and 7.6 the data-driven multijet background modeling requires the b-tagged jet with the highest transverse momentum to be central with a pseudorapidity within $|\eta| < 1.6$. This jet is chosen based on the *tight* (*loose*) b-tagging information in the Signal Region (Control Region). The preselection is summarized in Table 7.1. The event yields after preselection of the simulated $t\bar{t}H$ signal and the allhadronic SM $t\bar{t}$ process are summarized in Table 7.2. The multijet background yield is assumed to be data minus $t\bar{t}$ MC in each region. The expected sensitivity after preselection in terms of $S/\sqrt{S+B}$ in the control region of around 0.49 is competitive with the sensitivity of 0.77 in the signal region. Only the signal region with the *tight* b-tagging is considered in the study of the Higgs candidate invariant mass distribution in Chapter 7.7 and the multivariate analysis in Chapter 7.8. After the event preselection the QCD multijet is still the dominant

Type	Control Region $\geq$ 8j, $\geq$ 4b-CR	Signal Region $\geq$ 8j, $\geq$ 4b-SR
ttH	160.0 ± 1.7	80.7 ± 1.1
Multijet	...	...
$t\bar{t}$	9140 ± 480	1152 ± 76
Data	102781	10678
$t\bar{t}$/data [%]	8.79	10.66
$t\bar{t}H/t\bar{t}$ [%]	1.75	7.01
$t\bar{t}H$/data [%]	0.15	0.75
$t\bar{t}H/\sqrt{\text{data}}$	0.49	0.77

Table 7.2.: Summary of yields in the control and signal regions of the analysis after the preselection described in Chapter 7.2.2 and summarized in Table 7.1. The data corresponds to 32.8 fb^{-1} with $\sqrt{s} = 13$ TeV recorded in 2016. The multijet yield is derived from data by subtracting the expected $t\bar{t}$ contribution.

background source. Around 11% of the events are originating from the SM $t\bar{t}$ process. The expected $t\bar{t}H$ contribution is below 1% illustrating the importance of the QCD suppression which will be further addressed in Chapter 7.8. The signal is also much smaller than SM $t\bar{t}$ with a S/B-ratio of about 0.07 in the signal region. So any analysis approach has to achieve an effective suppression of both background sources. The strategy chosen in this thesis is outlined in Chapter 7.4. The control region has a signal contamination of 0.15%, making it a good testing ground for the shapes of the background distributions.

7.3. Matching performance

A geometrical matching procedure is studied for two purposes. First, the general matching between the partons after final state radiation and all reconstructed and selected jets after preselection is investigated. Any inefficiencies related to the input objects will limit the achievable identification performance of the top quarks and the Higgs boson. Second, the matching between the partons and the identified jets after the jet assignment of the bucket algorithm is studied.

The matching is performed in the $\eta - \phi$ plane using $\Delta R = \sqrt{\Delta\phi^2 + \Delta\eta^2} < 0.3$ as a requirement to have a successful matching between two objects. A unique matching scenario is not considered as ambiguities are expected in such a busy environment for which the simple geometrical $\eta - \phi$ based matching is known to have limitations for close-by jets.

The efficiency to match all signal partons, the two Higgs b-quarks and the six decay quarks from the $t\bar{t}$ decay, to any reconstructed jet in the event is approxi-

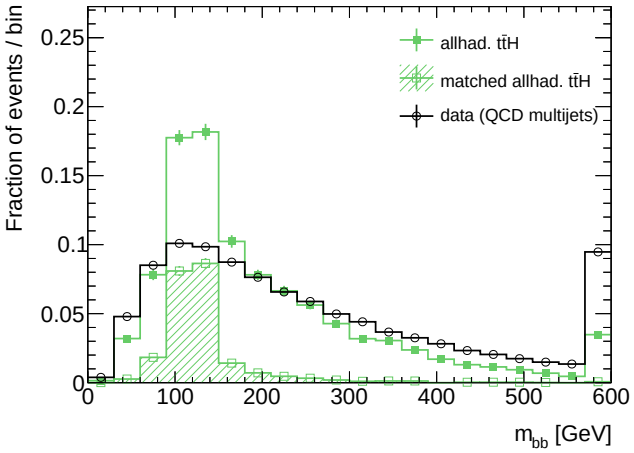

Figure 7.5.: Shape comparison of signal and background distributions of the Higgs candidate mass. The data is taken from the *b-tag control region* and consists mainly of QCD multijets. The matching in simulated signal events is done between the Higgs candidate and the truth Higgs using the geometrical requirement $\Delta R < 0.3$. The distributions are shown after the preselection described in Chapter 7.2.2 and summarized in Table 7.1.

mately $\epsilon(\text{all}) = 40\%$. As already four b-tagged jets are required the efficiency of matching the two Higgs bottom quarks to any jet is relatively large with around 92%. Hence, the main contribution to the above mentioned $\epsilon(\text{all}) = 40\%$ is caused by the matching of the $t\bar{t}$ decay system which has an efficiency of around 45%. If only the bottom quarks and the harder decay parton of the W boson decay are considered the $t\bar{t}$ system can be matched in approximately 87% of the events. This confirms again that a partial reconstruction as performed by the bucket algorithm is required to achieve a high efficiency for the signal process.

The matching after the bucket algorithm jet assignment quantifies the performance of the $t\bar{t}H$ system reconstruction. The corresponding top quark candidates, the Higgs candidate and the association of jets are described in Chapter 7.2.1. To begin with, a $\Delta R < 0.3$ requirement between the Higgs candidate and the Higgs boson at truth level before the decay is used. Around 22% of reconstructed Higgs candidates match the truth Higgs boson. This efficiency is denoted as $\epsilon_{\text{H}} = 22\%$ in the following. Additionally, in about 15% of the events the two Higgs candidate jets can be matched to the truth level bottom quarks from the Higgs decay. In around 7% of the events the Higgs candidate matches the truth Higgs but the individual b-tagged jets cannot be matched to the Higgs bottom quarks. In addition, in approximately 1% of the cases the identified b-tagged jets are correctly matched to the bottom quarks from the Higgs boson decay but the Higgs candidate cannot be matched to the truth Higgs boson. The later one is probably caused by ambiguities and the above mentioned limitations of the purely geometrical matching procedure.

The reconstructed m_{bb} distribution for the multijet background and simulated $t\bar{t}H$ events is shown in Figure 7.5. The corresponding matched contribution, using the ϵ_{H} criterion, peaks around the true Higgs mass used in the MC. Therefore, matching Higgs candidates to truth Higgs bosons (ϵ_{H}) can indeed quantify the performance of the Higgs reconstruction.

7.4. Analysis method

The goal of the fully hadronic $t\bar{t}H$ analysis is the direct measurement of the top Yukawa coupling. In order to achieve this, the analysis has to be optimized taking into account two important aspects. First, the correct reconstruction of the signal $t\bar{t}H$ system or the $t\bar{t}$ system can help to make the peak of the $t\bar{t}H$ signal in the m_{bb} distribution more prominent. Second, the suppression of the overwhelming multijet background plays a critical role in increasing the sensitivity.

From studies of the SM $t\bar{t}$ process, as conducted in Chapter 5, it can be seen that kinematic selections like e.g. on the top quark transverse momentum can improve both the background suppression and the accuracy of the top reconstruction. Therefore, an interplay between the background estimation, the top reconstruction performance and the background suppression is expected. The procedure to achieve the event reconstruction and classification is summarized in Figure 7.6. This choice is motivated and explained in the following based on a set of variables presented in Figures 7.5, 7.7 and 7.8. The preselection enhances a phase space which allows one to perform event classification and reconstruction. The top quark reconstruction is based on the bucket algorithm. The classification relying on a multivariate analysis uses primarily event shape and kinematic variables constructed from the full set of jets. The variables related to the Higgs candidate constructed from the bucket algorithm are excluded from the multivariate analysis. An adequate combination of the multivariate discriminant variable and the Higgs candidate invariant mass can help to measure the $t\bar{t}H$ signal. Ideally, the signal and background discrimination of the classification also enhances the selection of events with well reconstructed Higgs candidates. The sideband method using the Higgs candidate mass is discussed in Chapter 7.7. The event classification based on a multivariate method is investigated in Chapter 7.8.

The two main building blocks of the analysis are the event reconstruction based on the bucket algorithm and the event classification based on a multivariate method. The bucket algorithm provides the mass of the Higgs candidate, as shown in Figure 7.5. This mass distribution can be used to discriminate signal from background and to estimate background yields. The performance of the top reconstruction is summarized in terms of representative reconstructed top variables in Figure 7.7 and representative reconstructed Higgs variables in Figure 7.8. The background distribution is modeled by data from the almost signal free control region, see Table 7.1. The signal and background distributions of the top variables differ only slightly. Therefore, the individual quantities do not provide a strong separation. The same

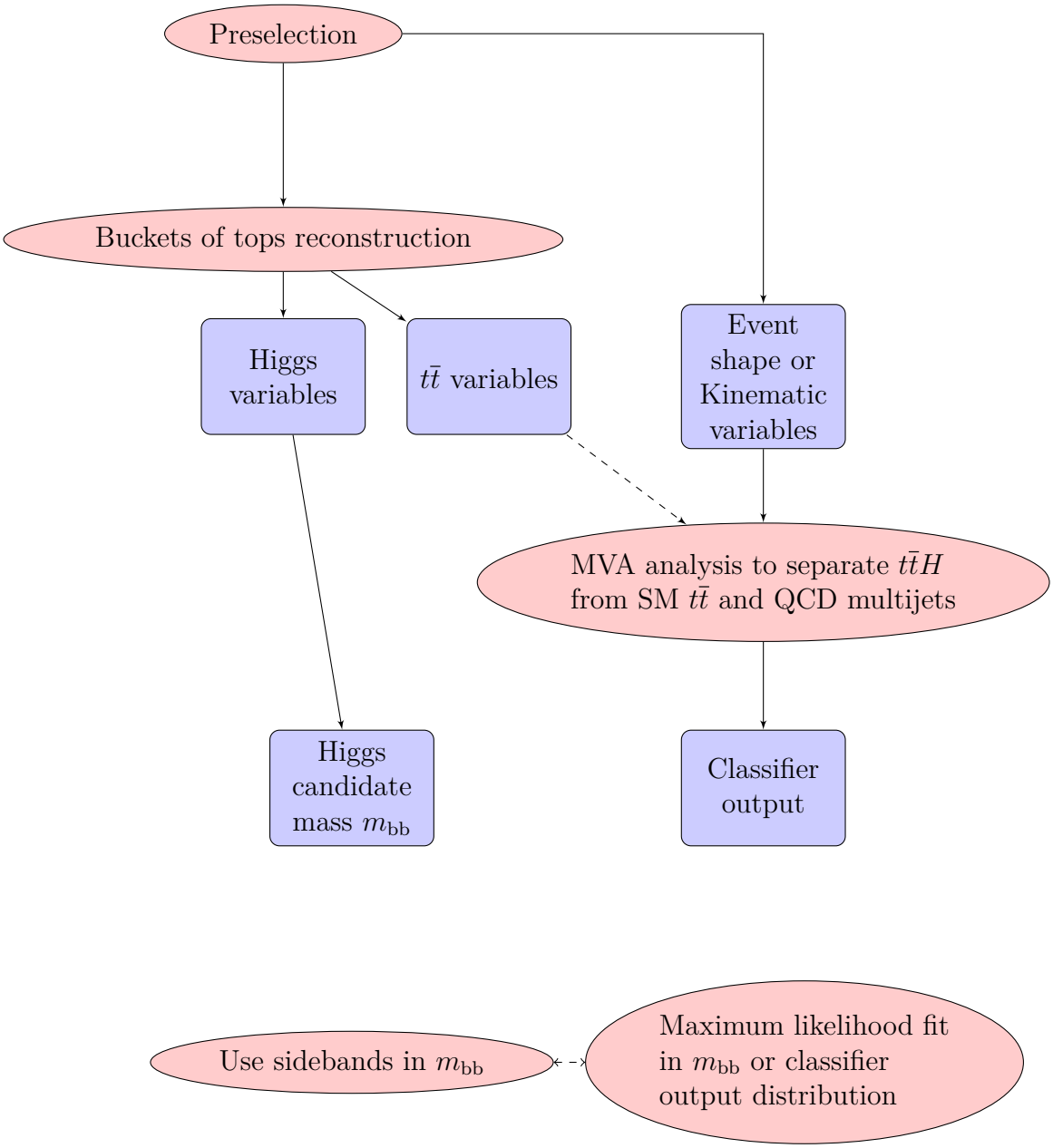

Figure 7.6.: Summary of analysis structure. The preselection enhances a phase space which allows one to perform event classification and reconstruction. The top quark reconstruction is based on the bucket algorithm. The multivariate analysis uses event shape and kinematic variables. An adequate combination of the multivariate discriminant variable and the Higgs candidate invariant mass can help to measure the $t\bar{t}H$ signal. Ideally, the signal and background discrimination enhances the selection of events with well reconstructed Higgs candidates.

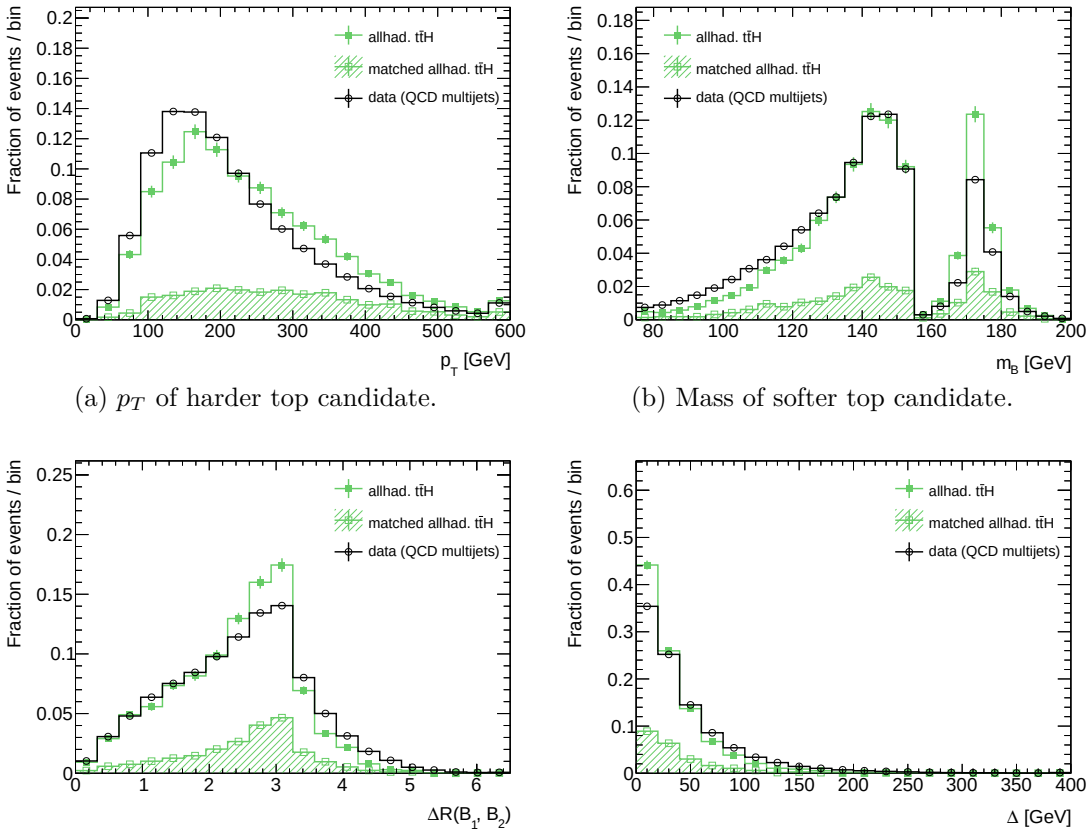

(a) p_T of harder top candidate.

(b) Mass of softer top candidate.

(c) ΔR between top candidates.

(d) Metric Δ of first top reconstruction step.

Figure 7.7.: Shape comparison of signal and background distributions. The data is taken from the *b-tag control region* and consists mainly of QCD multijets. The matching in simulated signal events is done between the Higgs candidate and the truth Higgs using the geometrical requirement $\Delta R < 0.3$. The distributions are shown after the preselection described in Chapter 7.2.2 and summarized in Table 7.1.

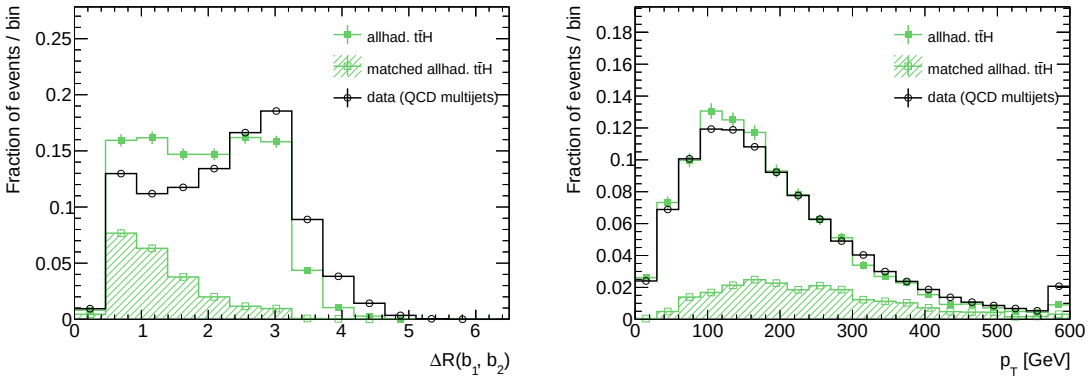

(a) ΔR of b-tagged jets of Higgs candidate.

(b) Higgs candidate p_T.

Figure 7.8.: Shape comparison of signal and background distributions. The data is taken from the *b-tag control region* and consists mainly of QCD multijets. The matching in simulated signal events is done between the Higgs candidate and the truth Higgs using the geometrical requirement $\Delta R < 0.3$. The distributions are shown after the preselection described in Chapter 7.2.2 and summarized in Table 7.1.

is true for the distribution of signal events which have a correctly matched Higgs candidate. As observed in previous chapters, the accuracy of the top quark reconstruction improves with higher transverse momentum of the top quarks as is shown in Figure 7.7(a). The metric of the first bucket reconstruction step Δ, which quantifies the mass difference between the top buckets and the true top masses, is presented in Figure 7.7(d). Both signal and background peak in the lowest bin of the distribution. The mass of the reconstructed Higgs candidate, the geometrical distance $\Delta R(b_1, b_2)$ between the b-tagged jets associated to the Higgs boson and the p_T of the reconstructed Higgs boson are shown in Figure 7.5 and 7.8. The $\Delta R(b_1, b_2)$ and the transverse momentum distribution highlight that a boost of the Higgs boson could reduce the combinatorics. Higgs boson related variables are known to be correlated. So any selection based on Higgs variables would also affect the invariant mass distribution. Therefore, the event classification is making use of combined variables as is explained in Chapter 7.8.

7.5. Signal and background modeling

After the event preselection, the background consists mainly of QCD multijets and a $\mathcal{O}(10\%)$ contribution from SM $t\bar{t}$ depending on the region considered. The $t\bar{t}H$ signal and the SM $t\bar{t}$ are modeled by MC simulation. In all simulated samples the properties of heavy-flavor hadron decays are modeled with `EvtGen` v1.2.0 [170]. The used top mass is $m_{\text{top}} = 172.5$ GeV and for the Higgs boson a mass of $m_{\text{Higgs}} = 125$ GeV is used during simulation. The overwhelming QCD multijet production is

Sample	SM $t\bar{t}$	$t\bar{t}H$
Abbreviation	Powheg+Pythia6	aMC@NLO + Pythia8
Uncertainty	Nominal	Nominal
ME gen.	Powheg-Box	aMC@NLO
	r2330.3	2.3.2
PS/UE gen.	Pythia	Pythia
	6.427	8.210
Ren. scale	$\sqrt{m_t^2 + p_{T,t}^2}$	$\frac{1}{2}H_T$
Fac. scale	$\sqrt{m_t^2 + p_{T,t}^2}$	$\frac{1}{2}H_T$
hdamp	m_t	–
ME PDF	CT10	NNPDF3.0NLO
PS/UE PDF	CTEQ6L1	–
PS Tune	P2012	A14
Matching	Powheg Matching	MC@NLO

Table 7.3.: Overview of used MC settings for different simulated samples. Table modified from Reference [122, 123]. The transverse momentum of the top quark $p_{T,t}$ is given in the $t\bar{t}$ center of mass frame.

determined from data in control regions as explained in Chapter 7.5.3.

A full Geant4 [140] simulation of the ATLAS detector [105] is performed on the simulated MC events. All selection criteria involving event, trigger and quality criteria are applied to both data and MC. Soft proton-proton collisions are simulated with Pythia and added to the hard scattering events to model the effect of pileup. Out-of-time and in-time pileup from multiple proton collisions can affect the event reconstruction. This pileup effect is corrected in simulation by reweighting the events such that the distribution of the average number of vertices matches data. The MC setups used are summarized in Table 7.3.

7.5.1. Signal Monte Carlo simulation

For the simulation of the $t\bar{t}H$ signal process, the `MadGraph5_aMC@NLO` [120] program version 2.3.2 is used together with the `NNPDF3.0NLO` [195] parton density functions. A Higgs boson mass of $m_{\text{Higgs}} = 125$ GeV is used and all possible Higgs decay channels are considered. The final state parton shower is modeled by the `Pythia` 8.210 [107] program together with the A14 underlying event tune [110]. The renormalization and factorization scale are both set to half the scalar sum of the transverse mass $\sqrt{p_T^2 + m^2}$ of all final state particles. Next-to-leading order calculations are used for the $t\bar{t}H$ cross-section [217–221] and the branching fractions are derived with the `HDECAY` [222] program. Spin correlations are preserved by using the `MadSpin` [181] program for the top quark decays. The $t\bar{t}H$ cross section used is 0.50701 pb. The corresponding cross section of the allhadronic mode is

0.23082 pb.

7.5.2. Top quark pair simulation

The default set-up relying on `Powheg+Pythia6` as described in Chapter 3.3.1 is used. The MC sample available for this analysis suffers from a small number of events after preselection. The reduced sample size is caused by the requirement of having at least four b-tagged jets. Due to the four b-tagged jet selection in the CR and SR the background will be likely dominated by $t\bar{t}+ \geq 1b$ contributions. Previous studies and a fiducial measurements with leptonic final states [216] have shown that there are large systematic uncertainties related to the modeling of such processes. The chosen sample is considered as sufficient for the sideband study given the high statistical uncertainty present. The selection optimization based on the multivariate technique uses a data-driven approach which does not suffer from a potential mis-modeling of the $t\bar{t}$ process.

7.5.3. QCD multijet estimation

Attempts to model the QCD multijet by MC also suffers from small sample sizes for the four b-tagged jet selection. In addition, it is expected to have very large systematic uncertainties due to the modeling. In principal, one could use multi b-quark samples but the flavor composition of the QCD background is not known and subject to the employed b-tagging algorithm. The capability of the b-tagging algorithm to reject light jets and charm jets and correlations between the jets have to be considered which can modify the known benchmark efficiencies and rejections. To accommodate these subtleties, the QCD multijet estimation is based on data. It is extracted from the almost signal free control region CR defined by the *loose* b-tagging WP. The control region ($\geq$ 8j, $\geq$ 4b-CR) contains around 10300 data events as listed in Table 7.2. This provides enough events to construct a background template as the $t\bar{t}$ contribution is only around 9%. The template is constructed by subtracting the $t\bar{t}$ MC contribution from the data in the CR to get the shape of the multijet distribution.

$$n^{\mathrm{QCD}}(x) = n^{\mathrm{Data}}(x) - n^{t\bar{t}\mathrm{MC}}(x) \tag{7.5.1}$$

Due to this construction, the $t\bar{t}$ uncertainties have an significant impact on the multijet template. As systematic uncertainties are not discussed in this proof of principal analysis the yield of the multijet template in the signal region is therefore simply estimated to be the difference of data minus $t\bar{t}$ MC. The $|\eta|$ of the leading b-tagged jet is restricted to $|\eta| < 1.6$ in order to achieve a better description in the signal region. This is motivated by the known differences between the b-tagging WPs from Chapter 6. This approach could of course be improved in the future by explicitly using transfer functions that take the differences between the b-tag regions into account.

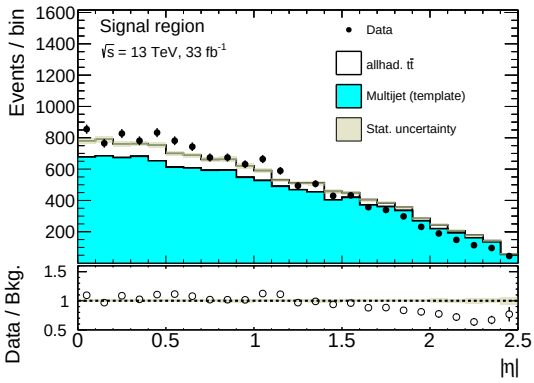

Figure 7.9.: $|\eta|$ distributions of the hardest b-tagged jet in the signal region. The distribution is shown before the cut on the $|\eta|$ of the hardest b-jet. The statistical (Stat.) uncertainty denotes the statistical uncertainty of the background model.

7.6. Control distributions

The background estimation procedure and the modeling of the bucket algorithm can be validated in a model to data comparison. Therefore, the background model is compared to data in the signal region for several kinematic variables and variables resulting from the bucket algorithm. The normalization of the multijet background is determined from the difference between data and simulated $t\bar{t}$ events in the signal region.

First, the multijet background estimation is validated using b-tagged jet kinematic distributions. These are relevant for the analysis as a large fraction of jets in the event is b-tagged. In particular, the top candidates are seeded by b-tagged jets. In addition, the Higgs candidate is constructed from two b-tagged jets. Hence, an adequate modeling of the b-tagged jet properties is crucial for the analysis. Distributions are shown in Figure 7.10 for the three leading b-tagged jets and in Figure 7.11 for the fourth hardest b-tagged jet and the b-tagged jet multiplicity. A mis-modeling is observed for large $|\eta| > 1.6$ of the b-tagged jets as shown in Figure 7.9. As this behavior emerges especially for the leading jet the corresponding phase space is vetoed as shown in Figure 7.10(a) resulting in adequate agreement for $|\eta^{\text{jet1}}| < 1.6$. As the b-tagged jets are likely to be correlated modifying the η of the leading jet is sufficient to also improve the pseudorapidity η distribution of the other b-tagged jets. The bulk of the $|\eta|$ and transverse momentum distributions is well described as shown for the softer b-tagged jets in Figure 7.10 and Figure 7.11.

Additional control plots based on combined variables and illustrating the top reconstruction which is relevant for the sideband method are shown in Figure 7.12 and 7.13. The distribution of the metric in the first bucket reconstruction step, see Figure 7.12(a), illustrates that the mass of the top candidates is well described. The four types of event categories in Figure 7.12(b) validate that the second reconstruc-

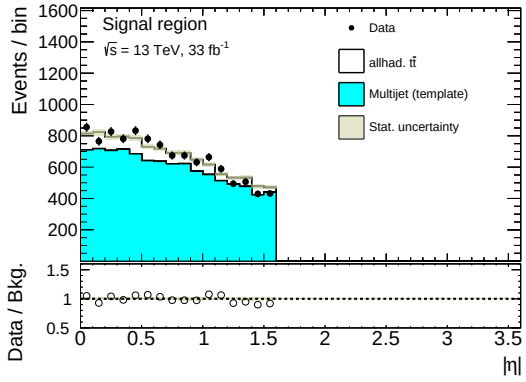

(a) $|\eta|$ of b-tagged jet 1.

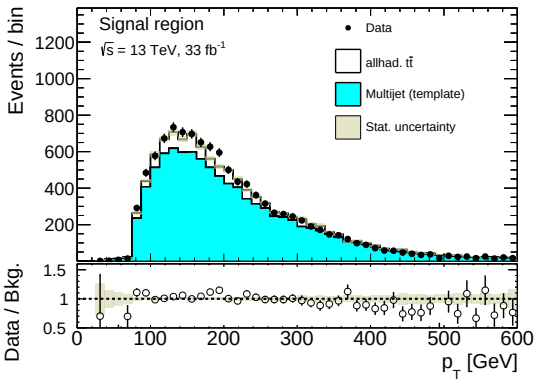

(b) p_T of b-tagged jet 1.

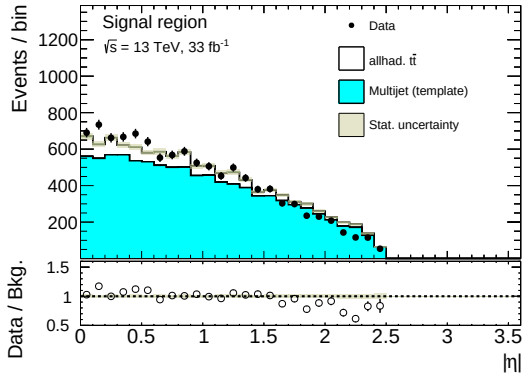

(c) $|\eta|$ of b-tagged jet 2.

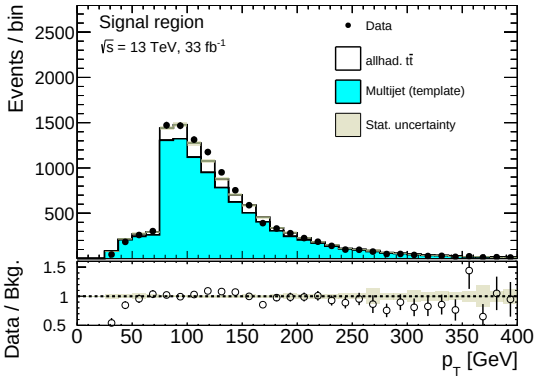

(d) p_T of b-tagged jet 2.

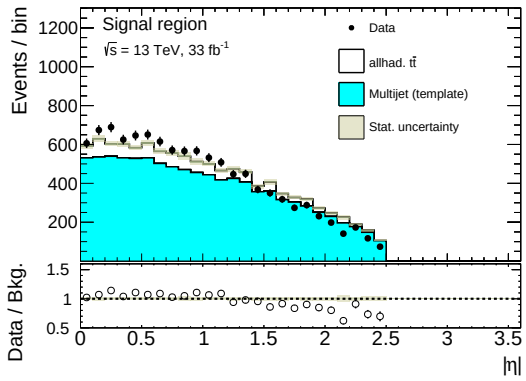

(e) $|\eta|$ of b-tagged jet 3.

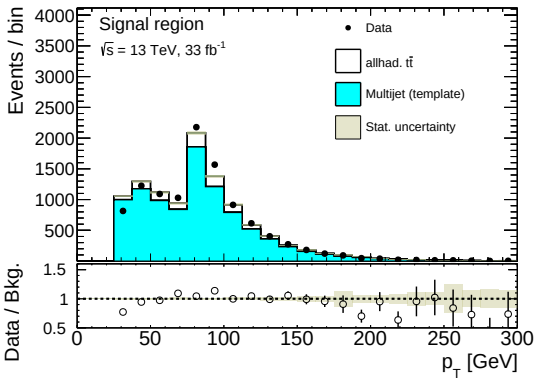

(f) p_T of b-tagged jet 3.

Figure 7.10.: Distributions of b-tagged jet variables in the signal region. The jets are numbered with decreasing transverse momentum. The statistical (Stat.) uncertainty denotes the statistical uncertainty of the background model. The multijet shapes are determined in the CR. The normalization of the multijet background is given by the difference between data and simulated $t\bar{t}$ events.

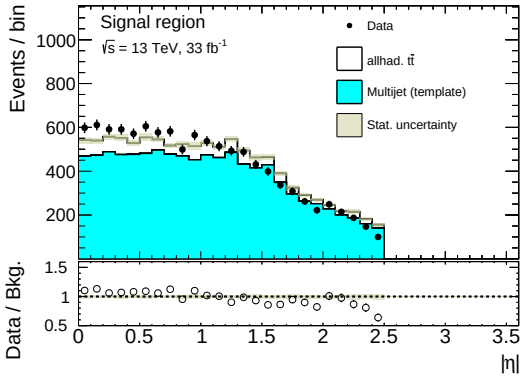

(a) $|\eta|$ of b-tagged jet 4.

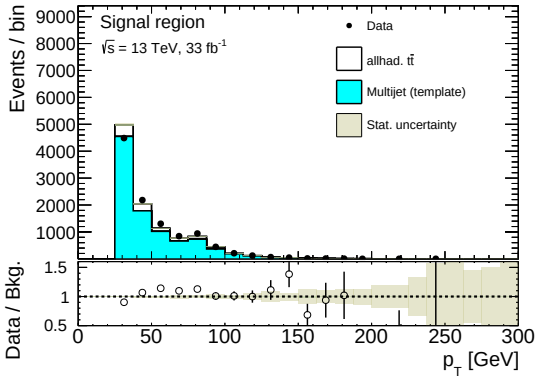

(b) p_T of b-tagged jet 4.

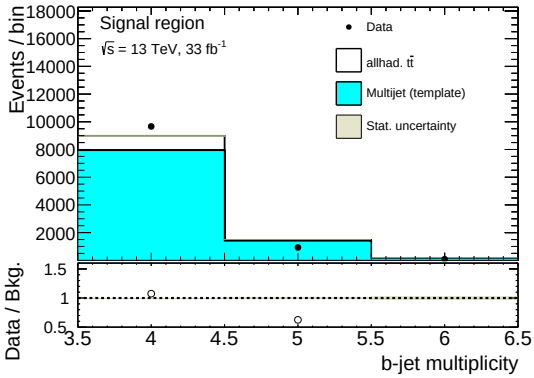

(c) b-tagged jet multiplicity.

Figure 7.11.: Distributions of b-tagged jet variables in the signal region. The jets are numbered with decreasing transverse momentum. The statistical (Stat.) uncertainty denotes the statistical uncertainty of the background model. The multijet shapes are determined in the CR. The normalization of the multijet background is given by the difference between data and simulated $t\bar{t}$ events.

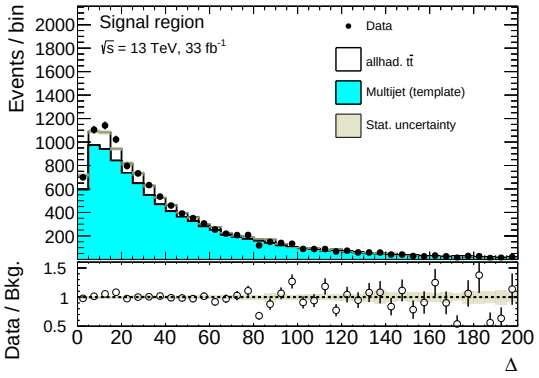

(a) Metric Δ of bucket algorithm.

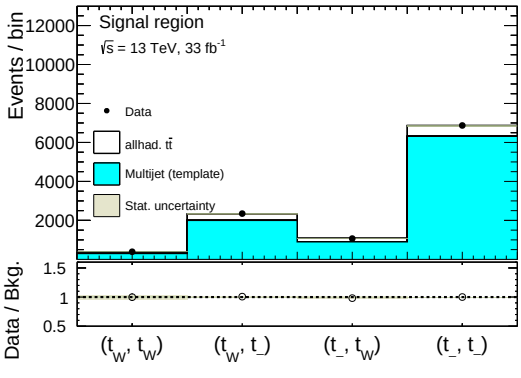

(b) Event category.

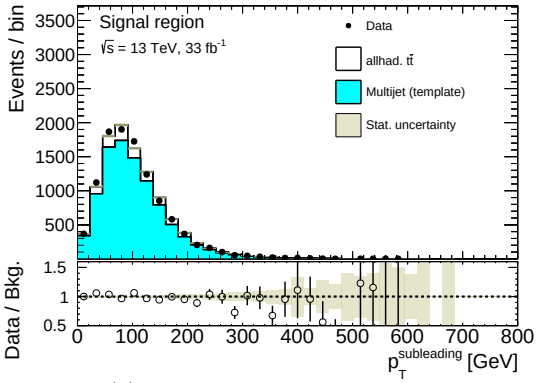

(c) p_T of softer top bucket.

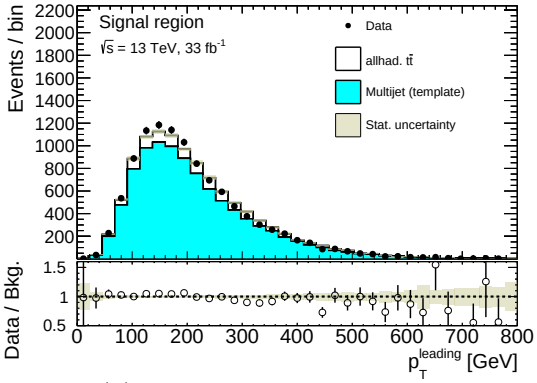

(d) p_T of harder top bucket.

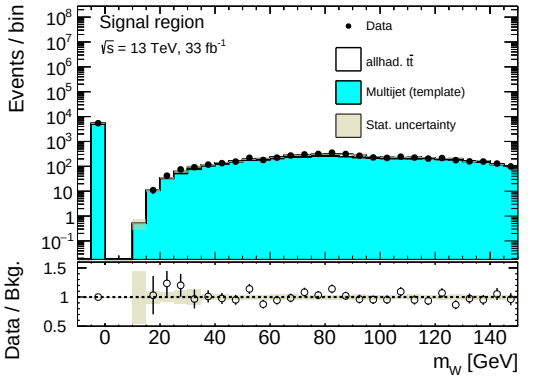

(e) Mass of W candidate in bucket 1. A mass of $m_{\mathrm{W}} = -1$ GeV is assigned to $\mathfrak{t}_-$ buckets.

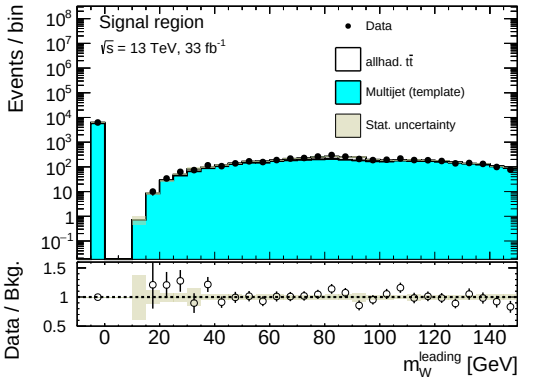

(f) Mass of W candidate in harder top bucket. A mass of $m_{\mathrm{W}} = -1$ GeV is assigned to $\mathfrak{t}_-$ buckets.

Figure 7.12.: Distributions of bucket algorithm related variables in the signal region. The statistical (Stat.) uncertainty denotes the statistical uncertainty of the background model. The multijet shapes are determined in the CR. The normalization of the multijet background is given by the difference between data and simulated $t\bar{t}$ events. In case of $\mathfrak{t}_-$ buckets, without a W candidate, the single bin below $m_{\mathrm{W}} < 0$ GeV is filled.

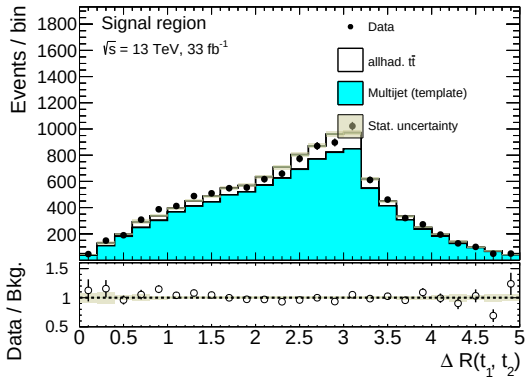

(a) ΔR between top buckets.

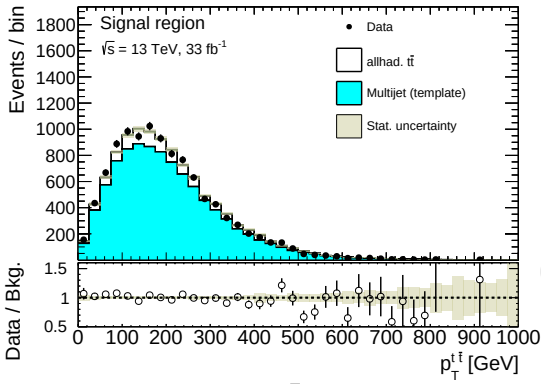

(b) p_T of the $t\bar{t}$ system.

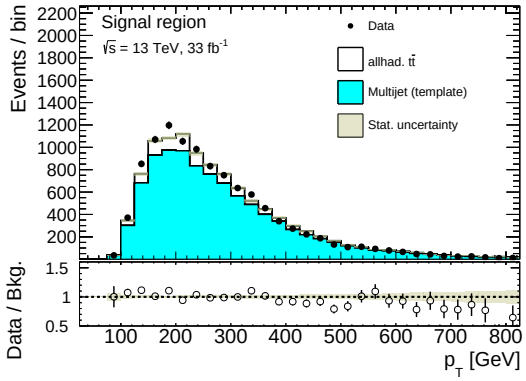

(c) p_T of the hardest jet.

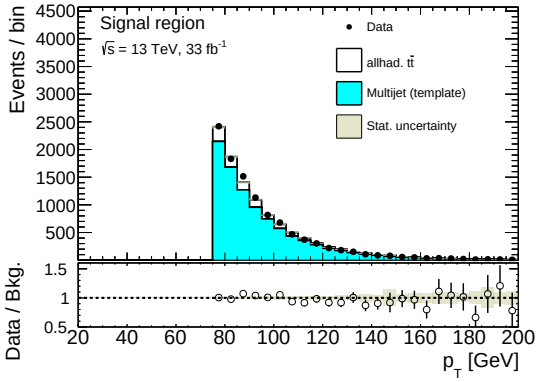

(d) p_T of the fifth hardest jet.

Figure 7.13.: Distributions of bucket algorithm related variables and variables describing the jets in the signal region. The statistical (Stat.) uncertainty denotes the statistical uncertainty of the background model. The multijet shapes are determined in the CR. The normalization of the multijet background is given by the difference between data and simulated $t\bar{t}$ events.

tion step is also correctly modeled by the $t\bar{t}$ MC and the QCD multijet template. Agreement is also observed in the transverse momentum of the top candidates and the mass of the W boson candidate. Due to the higher combinatorial background induced by the relatively high jet multiplicity, the distribution of the W candidate has a reduced separation for $t\bar{t}$ and the QCD template compared to previous studies and selections as shown in e.g. Chapter 5. The distribution of the ΔR between the top candidates peaks around $\Delta R = \pi$ as shown in Figure 7.13(a). This illustrates that back-to-back topologies are slightly favored by the selection. The transverse momentum of the $t\bar{t}$ system as shown in Figure 7.13(b) is of special interest as it quantifies the p_T scale against which the Higgs candidate has to recoil. The p_T distribution of the leading jet and fifth 5^{th} hardest jet in the event are adequately described see Figure 7.13(c) and Figure 7.13(d). As the trigger requires at least five jets at the high-level trigger this illustrates that also the trigger turn-on curve is reasonably modeled in MC.

The final analysis depends on combined objects. The selection and modeling of the combined variables used in the multivariate method is discussed in the corresponding Chapter 7.8.

7.7. Sideband method

In Reference [214] it was suggested to use parametrizations of the reconstructed Higgs mass m_{bb} for signal and background distributions. Such parametrizations can facilitate inferring both the background shape and the background normalization. In particular, this would be advantageous after the application of additional background suppression cuts due to the MVA classification which is conducted in Chapter 7.8. The feasibility of parameterizing the m_{bb} distribution after preselection with a combination of a Lognormal and a Gaussian function is studied in the following.

The background is expected to be largely caused by combinatorics. Therefore, it is possible to describe the background by a Lognormal distribution. The m_{bb} distribution for signal is described by a sum of a Gaussian distribution and a Lognormal distribution as the correct Higgs identification by the bucket algorithm can occasionally fail. The Lognormal and the Gauss parametrization as a function of the variable x, are defined by the following equations

$$\text{Lognormal}(x;\mu,\sigma,n,d) = \frac{n}{\sqrt{2\pi}\sigma\frac{x}{d}} \exp -\frac{(\log\frac{x}{d}-\mu)^2}{2\sigma^2} \tag{7.7.1}$$

$$\text{Gauss}(x;\mu,\sigma,n) = \frac{n}{\sqrt{2\pi}\sigma} \exp -\frac{(x-\mu)^2}{2\sigma^2} \ . \tag{7.7.2}$$

The parameters μ, σ, n, d describe the width, the mean and the normalization of the functions and are determined by a fit. For the data, which is almost signal-free after preselection, the Lognormal function is used in the fit. The $t\bar{t}$ distribution is also fitted by the Lognormal function. For the fit of the $t\bar{t}H$ signal the function $f^{\text{sig}}(x;\mu_l,\sigma_l,n_l,d,\mu_g,\sigma_g,n_g)$ is used. The function is defined by the following equation

$$f^{\text{sig}}(x;\mu_l,\sigma_l,n_l,d,\mu_g,\sigma_g,n_g) = \text{Lognormal}(x;\mu_l,\sigma_l,n_l,d) \tag{7.7.3}$$

$$+ \text{Gauss}(x;\mu_g,\sigma_g,n_g) \ . \tag{7.7.4}$$

The parameters μ_l, σ_l, n_l, d are the to be fitted parameters of the Lognormal and the μ_g, σ_g, n_g the corresponding parameters of the Gauss function. The shapes of signal and background distributions are investigated in the signal and in the control region separately. The fits in the control region are only provided as a cross-check. The functions are fitted to the corresponding m_{bb} distributions using a least-square fit. The results are summarized in Figure 7.14.

The distribution for data in the control region (signal region) is shown in Figure 7.14(a) (7.14(b)). In the signal region the window 80 GeV $< m_{bb} <$ 160 GeV around the Higgs mass is blinded in data. It is expected that some of the selection requirements like the trigger which induces relatively high transverse momentum thresholds on the jets can effect the m_{bb} distribution. Therefore, due to the kinematic selection also the background peaks around $m_{bb} = 100$ GeV close to the Higgs

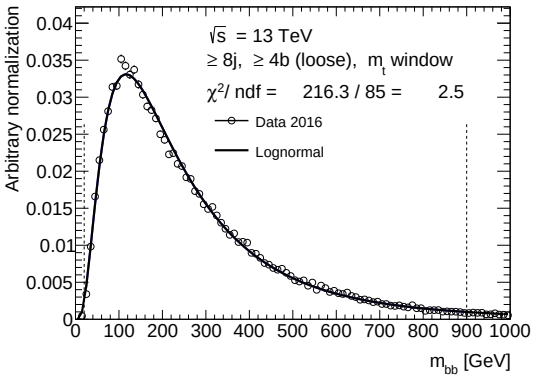

(a) Data (multijets) in the control region.

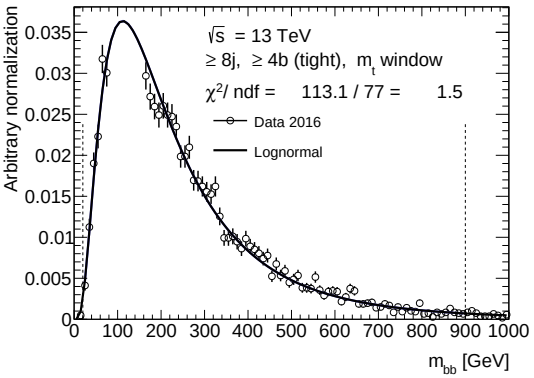

(b) Data (multijets) in the signal region. The mass range $80 < m_{bb} < 160$ GeV is blinded and excluded from the fit.

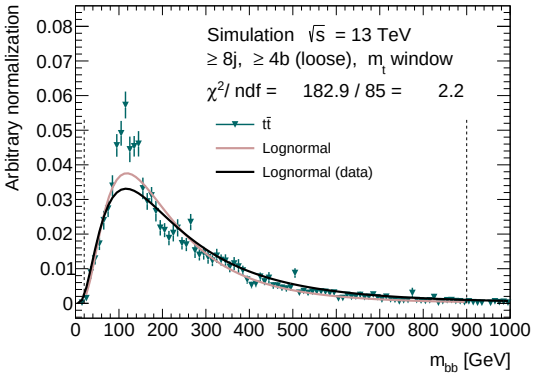

(c) Simulated $t\bar{t}$ events in the control region. The fitted data distribution from the CR is overlayed in black.

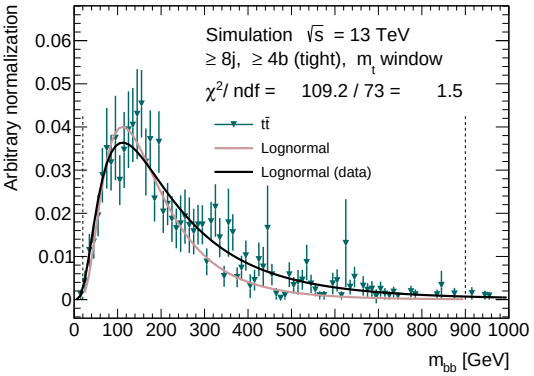

(d) Simulated $t\bar{t}$ events in the signal region. The fitted data distribution from the SR is overlayed in black.

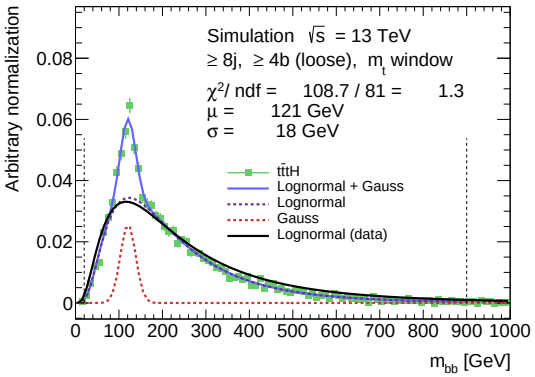

(e) Simulated $t\bar{t}H$ events in the control region. The fitted data distribution from the CR is overlayed in black.

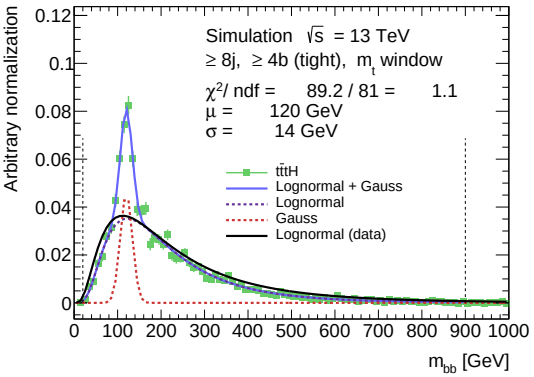

(f) Simulated $t\bar{t}H$ events in the signal region. The fitted data distribution from the SR is overlayed in black.

Figure 7.14.: Parametrization and fit of reconstructed m_{bb} distribution in the control region and the signal region for data (a, b), simulated $t\bar{t}$ events (c, d) and simulated $t\bar{t}H$ events (e, f) after preselection. The dotted vertical lines indicate the mass range considered in the fit.

mass. The sum of all backgrounds which is estimated by the data distribution is well described by a Lorgnormal for higher invariant masses $m_{bb} \gtrsim 200$ GeV and for small masses $m_{bb} \lesssim 80$ GeV in the control region with an overall χ^2/n.d.f. = 2.5, see Figure 7.14(a). In the signal region the distribution can be described by a Lorgnormal over the entire mass range considered with a lower χ^2/n.d.f. of 1.5 which indicates a better description by the Lognormal function.

The distribution for simulated $t\bar{t}$ events in the control region (signal region) is shown in Figure 7.14(c) (7.14(d)). The large statistical uncertainties that are present in the sample available, compromise the interpretation of the shape of the m_{bb} distribution for $t\bar{t}$. In the control region the m_{bb} distribution deviates from the Lorgnormal distribution with an overall χ^2/n.d.f. = 2.2, see Figure 7.14(c). In particular, around $m_{bb} = 100$ GeV the fitted function underestimates the simulated distribution. In the signal region the statistical uncertainties are even larger making a statement on the fit quality and the shape differences between the $t\bar{t}$ MC and the total background difficult as seen in Figure 7.14(d). The χ^2/n.d.f. = 1.5 is smaller and the difference around $m_{bb} = 100$ GeV is less pronounced. In the end, only the fit results in the signal region are relevant for a potential application of the sideband method.

The distribution for $t\bar{t}H$ in the control region (signal region) is shown in Figure 7.14(e) (7.14(f)). In the control region and in the signal region the signal MC can be well described by the parametrization $f^{\text{sig}}(x; \mu_l, \sigma_l, n_l, d, \mu_g, \sigma_g, n_g)$ with a χ^2/n.d.f. close to 1. The events with an incorrect reconstruction of the $t\bar{t}H$ system are supposed to be described by the Lognormal part, whereas the events with a correct reconstruction of the $t\bar{t}H$ system are expected to be described by the Gaussian part of the signal parametrization f^{sig}. Even in the signal region the majority of $t\bar{t}H$ events has an incorrectly reconstructed Higgs candidate (around 22% are successfully matched, see Chapter 7.3). The Lognormal part of the parametrization for $t\bar{t}H$ covers the complete mass range considered up to $m_{bb} = 1000$ GeV and also peaks around the Higgs mass. Hence, it is not possible to construct a fully signal free sideband based on m_{bb}. Nevertheless, a similar approach as the ABCD-Likelihood presented in Chapter 6.7 can be used to take the signal contamination in the sidebands into account. In the control region and signal region the mean value is around 5 GeV below the generated Higgs mass. From the width of the Gaussian the Higgs mass resolution can be derived. The width of the Gaussian decreases from $\sigma = 17.5 \pm 1.4$ GeV in the control region to $\sigma = 14.0 \pm 1.0$ GeV in the signal region. This difference is likely caused by the different b-tagging WPs which can influence the performance of the bucket algorithm. In addition, the ratio of the normalization of the Gauss over the Lorgnormal distribution increases by a factor 1.5. As the difference between control region and signal region is characterized by different b-tagging WPs this suggests that the Higgs reconstruction with the bucket algorithm improves with tighter b-tagging selections.

In all simulated samples, it can be observed that the shape of the Lorgnormal distribution in data slightly deviates from the Lorgnormal in simulated $t\bar{t}$ and simulated $t\bar{t}H$ events.

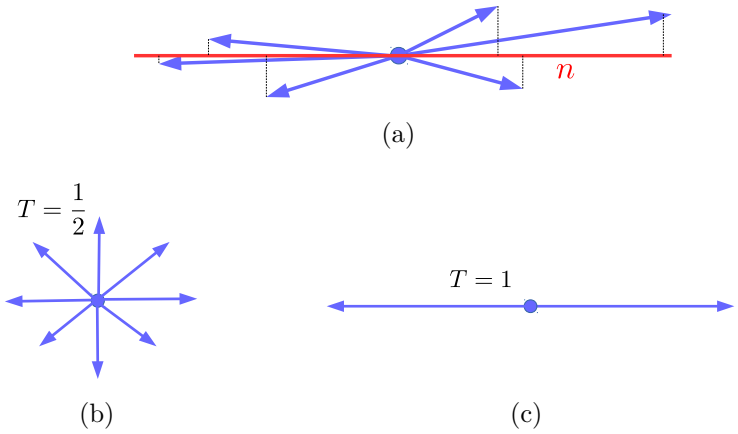

Figure 7.15.: Schematic illustration of the construction of the thrust variable (a), of an isotropic event (b) and of a two-jet like structure (c).

7.8. Multivariate discrimination

The main purpose of the multivariate analysis is the suppression of the large multijet background. It is included in the general analysis structure as presented in Figure 7.6. The top quark and Higgs boson reconstruction alone is not sufficient to achieve a good sensitivity as the expected signal contribution in the mass window $80\text{GeV} < m_{bb} < 160$ GeV is still relatively small after preselection. Hence, it would be necessary to combine the classification and reconstruction parts of the analysis to achieve better sensitivity.

The `TMVA` [223] framework is used to train multivariate classifiers for $t\bar{t}H$ signal and the background. The performance of a boosted decision tree BDT [224] and the linear Fisher discriminant as described in Reference [223] are tested and compared. The background sample for training is constructed from the data in the control region. Hence, the sample consists of the sum of all background components like e.g. $t\bar{t}$ or multijets. Training and testing uses simulated $t\bar{t}H$ events in the signal region for the signal. The sample is randomly split in a test and training sample of equal size.

The input variables include the minor, major, thrust, D, C, aplanarity, sphericity, centrality and variables based on scalar sums of jet properties such as HT, $HT5wo3$, $HT3$. As the quantities are likely to be correlated to the number of jets in the event, the jet multiplicity is also considered as an input variable to the multivariate analysis. The set of variables used in the multivariate analysis is summarized in the following. They are build from all the jets and b-tagged jets after preselected, see Chapter 7.2.2 for a detailed overview of the selection. The definition of the variables uses the notation of the particle four-momentum $p_i = (E_i, \boldsymbol{p}_i)$ for each particle i in an event with n particles. Thereby the definition follows the conventions given in Reference [106].

The thrust T [225, 226] is calculated by maximizing the following equation

$$T = \max_{|\boldsymbol{n}|=1} \frac{\sum_i |\boldsymbol{n} \cdot \boldsymbol{p}_i|}{\sum_i |\boldsymbol{p}_i|} \ . \tag{7.8.1}$$

The vector $\boldsymbol{n}$ for which the maximum is achieved defines the so-called thrust axis $\boldsymbol{a}_t$. The construction of the thrust variable is shown in Figure 7.15. Events which have a two-jet like structure are characterized by thrust values closer to $T = 1$ where for the extreme case the thrust axis is aligned along the jet axis. In contrast, more isotropic events tend to thrust values around $T = 0.5$. The implementation of the calculation and minimization is based on the code in Reference [227]. Starting from the thrust axis $\boldsymbol{a}_t$ the major M_a [228] can be constructed in the perpendicular plane defined by

$$M_a = \max_{|\boldsymbol{n}|=1, \boldsymbol{n}\cdot\boldsymbol{a_t}=0} \frac{\sum_i |\boldsymbol{n} \cdot \boldsymbol{p}_i|}{\sum_i |\boldsymbol{p}_i|} \ . \tag{7.8.2}$$

In a similar way the minor M_i is constructed by a third axis which is perpendicular to the thrust and major axis.

The sphericity tensor $S^{\alpha\beta}$ [229] is constructed from the $\alpha, \beta = x, y, z$, components

$$S^{\alpha\beta} = \frac{\sum_i |\boldsymbol{p_i}|^{r-2} p_i^\alpha p_i^\beta}{\sum_i |\boldsymbol{p_i}|^r} \ . \tag{7.8.3}$$

The parameter r is an adjustable regularization parameter which controls the p_T dependence of the sphericity tensor. Throughout this analysis the value $r = 2$ is chosen. Diagonalization of the sphericity tensor results in three eigenvectors λ_j which are ordered in size and have to satisfy

$$\lambda_1 \geq \lambda_2 \geq \lambda_3 \tag{7.8.4}$$

and have to satisfy

$$1 = \lambda_1 + \lambda_2 + \lambda_3 \ . \tag{7.8.5}$$

The eigenvectors are used to construct the quantities aplanarity A and sphericity S in the following way

$$S = \frac{3}{2}(\lambda_2 + \lambda_3) \tag{7.8.6}$$

$$A = \frac{3}{2}\lambda_3 \ . \tag{7.8.7}$$

A low sphericity value corresponds to two-jet like events whereas a high sphericity is achieved for more isotropic events. Similarly higher values of the aplanarity indicate more isotropic events. The aplanarity quantifies the transverse momentum perpen-

dicular to the event plane. Planar events have a smaller aplanarity value. Further combinations of eigenvectors can be considered. The C and D combinations [230] are defined by the following equation

$$C = 3(\lambda_1\lambda_2 + \lambda_1\lambda_3 + \lambda_2\lambda_3) \tag{7.8.8}$$
$$D = 27\lambda_1\lambda_2\lambda_3 \tag{7.8.9}$$

The parameter C is often associated to the three-jet structure and the D value to the four-jet structure of an event. They also serve as a prototype for a generalization in the context of jet-substructure variables as a set of energy correlation functions [231].

The centrality is extracted from the sum of the jet four-vectors in the event. The ratio of the transverse momentum over the mass is calculated

$$\text{centrality} = \frac{p_T(\sum p_{\text{jet}})}{\text{mass}(\sum p_{\text{jet}})} \ . \tag{7.8.10}$$

Similarly to the numerator of the centrality the HT can be calculated as the scalar sum of all selected small-R jets. As the events have a relatively large jet multiplicity ≥ 8 the HT is modified to contain only the sum of the three leading jets $HT3$ or the five leading jets excluding the three leading ones $HT5wo3$. All variables are constructed from combined objects. Only the $HT3$ and $HT5wo3$ are based on a reduced number of jets.

In order to reduce effects on the shape of the reconstructed m_{bb} distribution the variables are constructed from a combination of multiple objects. But the objects used are not restricted and all selected offline jets are considered. This includes the two b-tagged jets that constitute the Higgs candidate. The linear correlation coefficients of the Higgs mass m_{bb} and the input variables are shown in Figure 7.18. The correlation of the Higgs mass and the variables based on the scalar sums of jet transverse momenta are below 39%. For the remaining input variables the linear correlation coefficients with the Higgs mass are smaller and below 12%. Eventually the effect of the classification on m_{bb} is studied in Chapter 7.9.

The data to MC comparison plots for all 12 input variables are shown in Figure 7.16 and 7.17. While some small deviations in the tails of several distributions are observed, the bulk of them is adequately described. As the Fisher discriminant relies on the modeling of the correlations between the input variables it is checked that also the linear correlation coefficients agree between the control region and the signal region as shown in the Appendix A.1. The input variables for the background rely on the data in the control region. It is crucial for the performance of the multivariate discrimination that these variables are also well described in the signal region. Otherwise any difference in the distribution could result in a reduction of the performance.

All input variables have a relatively small separation as can be seen in Table 7.4.

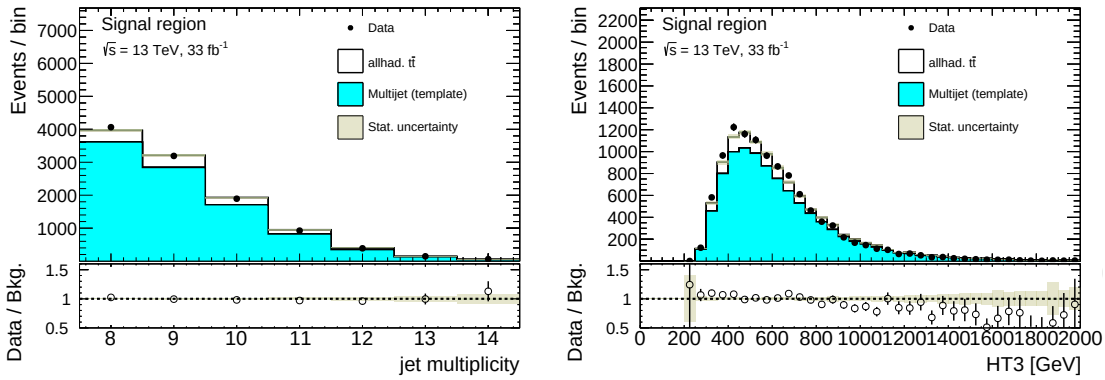

(a) Jet multiplicity

(b) $HT3$

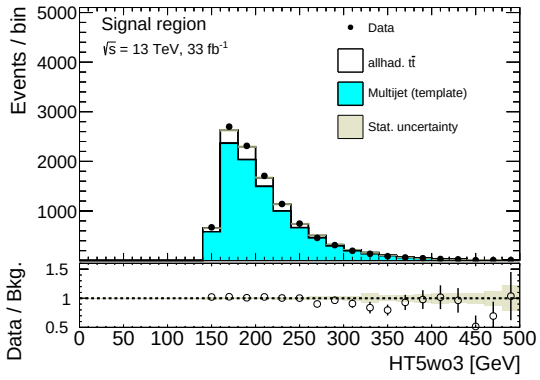

(c) $HT5wo3$

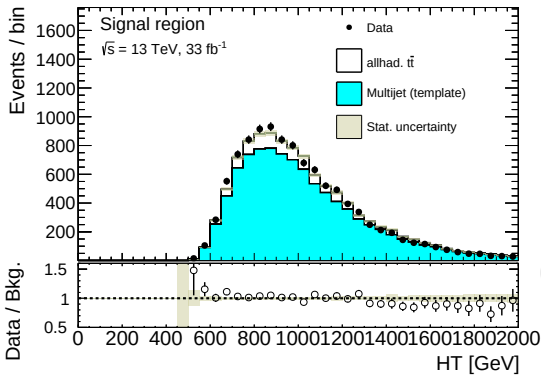

(d) HT

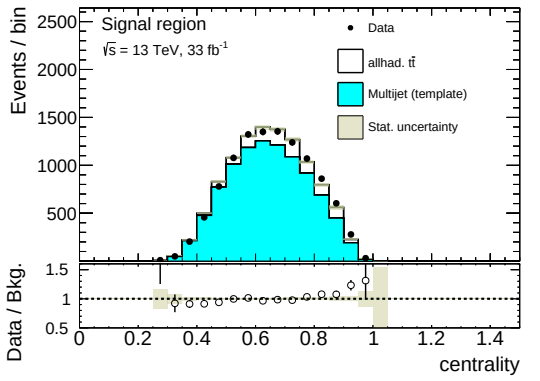

(e) Centrality

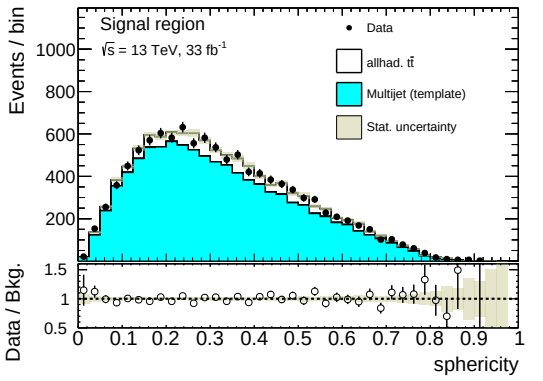

(f) Sphericity

Figure 7.16.: Distributions of variables used in the MVA discrimination. They are shown in the signal region. The statistical (Stat.) uncertainty denotes the statistical uncertainty of the background model. The multijet shapes are determined in the CR. The normalization of the multijet background is given by the difference between data and simulated $t\bar{t}$ events.

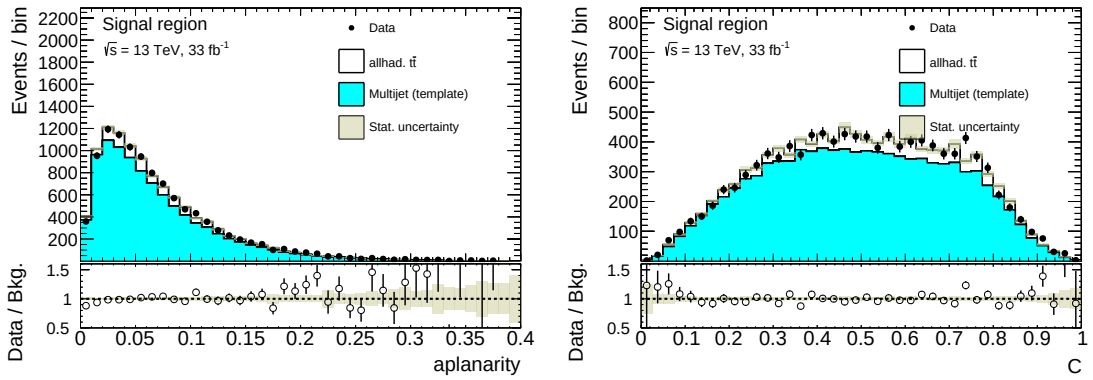

(a) Aplanarity

(b) Jet C

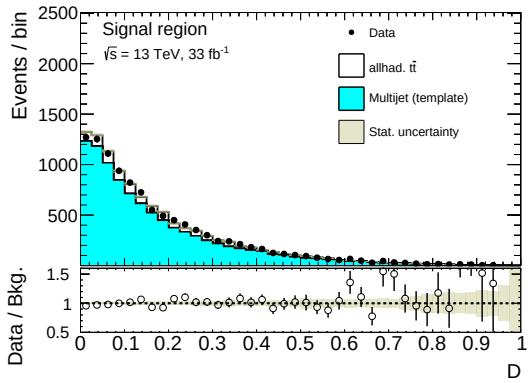

(c) Jet D

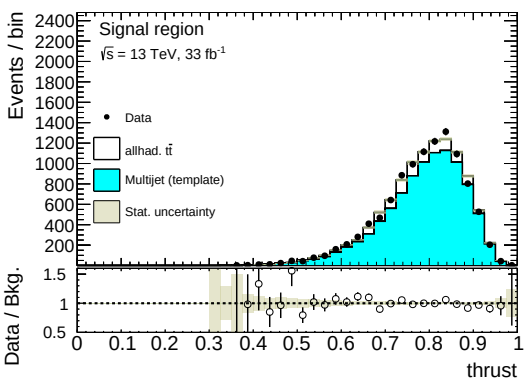

(d) Thrust

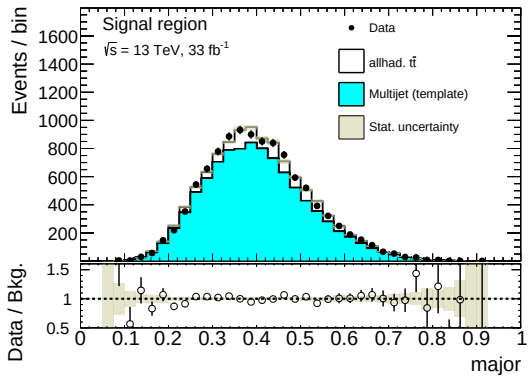

(e) Major

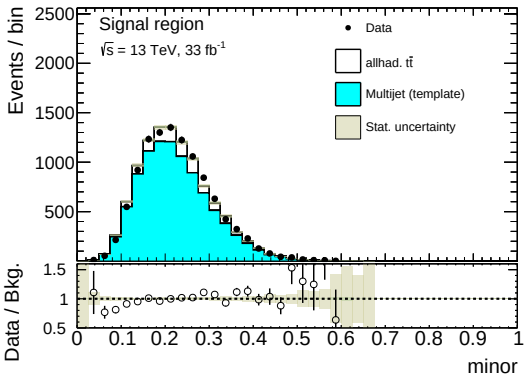

(f) Minor

Figure 7.17.: Distributions of variables used in the MVA discrimination. They are shown in the signal region. The statistical (Stat.) uncertainty denotes the statistical uncertainty of the background model. The multijet shapes are determined in the CR. The normalization of the multijet background is given by the difference between data and simulated $t\bar{t}$ events.

Variable	Separation
centrality	9.090×10^{-2}
minor	4.285×10^{-2}
D	4.053×10^{-2}
thrust	3.905×10^{-2}
aplanarity	3.894×10^{-2}
C	3.164×10^{-2}
sphericity	2.867×10^{-2}
major	2.552×10^{-2}
HT	1.875×10^{-2}
HT3	1.089×10^{-2}
HT5wo3	6.584×10^{-3}
jet multiplicity	6.506×10^{-3}

Table 7.4.: Ranking of input variables based on the separation.

Where the separation $\langle S^2 \rangle$ is defined in the following way

$$\langle S^2 \rangle = \frac{1}{2} \int \frac{(\hat{y}_S(y) - \hat{y}_B(y))^2}{\hat{y}_S(y) + \hat{y}_B(y)} \mathrm{d}y \ . \tag{7.8.11}$$

with the signal $\hat{y}_S$ and background $\hat{y}_B$ PDFs of the classifier y [223].

In addition, most of them show a relatively large linear correlation as summarized in Figure 7.18. The linear correlations of the majority of variables slightly differ for signal and background processes. The linear correlation between centrality and thrust is e.g. -58% (-45%) in the background (signal) sample. Generally, also the mean of the signal and background distribution differ for the input variables as shown in Figure 7.19 and 7.20. The Fisher discriminant is expected to handle setups with such properties of the input variables successfully [223]. Therefore, it is chosen as one of the benchmark classification methods. The Fisher discriminant provides a measure to rank the input variables based on the between-class separation and the within-class dispersion as described in Reference [223]. For the set of input variables the Fisher discrimination power is presented in Table 7.5. The BDT classification method is widely used in analyses focusing on $t\bar{t}H$ production at ATLAS as e.g. presented in References [212, 213]. Therefore, the BDT is considered as a second benchmark method. The BDT method is expected to work effectively even without a specific tuning of the setup [223]. The input variables can be ranked according to their importance in the BDT classification as described in Reference [223]. The corresponding ranking takes the usage of the variable in constructing tree nodes and the associated separation gain into account. The BDT variable importance for the input variables is shown in Table 7.6 The centrality, which is the variable with the largest separation, is first ranked in both classification methods. The ranking of the other variables slightly differs for the Fisher and the BDT method. The

Variable	Discrimination power
centrality	4.473×10^{-2}
D	1.895×10^{-2}
minor	1.854×10^{-2}
aplanarity	1.775×10^{-2}
C	1.639×10^{-2}
thrust	1.622×10^{-2}
sphericity	1.492×10^{-2}
major	9.223×10^{-3}
jet multiplicity	7.426×10^{-3}
HT3	1.833×10^{-3}
HT5wo3	5.714×10^{-4}
HT	1.542×10^{-4}

Table 7.5.: Ranking of input variables based on the Fisher method discrimination power as defined in Reference [223].

Variable	Variable Importance
centrality	1.237×10^{-1}
HT	1.072×10^{-1}
HT3	1.035×10^{-1}
jet multiplicity	8.233×10^{-2}
minor	7.928×10^{-2}
HT5wo3	7.805×10^{-2}
major	7.782×10^{-2}
C	7.319×10^{-2}
thrust	7.232×10^{-2}
sphericity	6.868×10^{-2}
aplanarity	6.789×10^{-2}
D	6.610×10^{-2}

Table 7.6.: Ranking of input variables based on the BDT variable importance as defined in Reference [223].

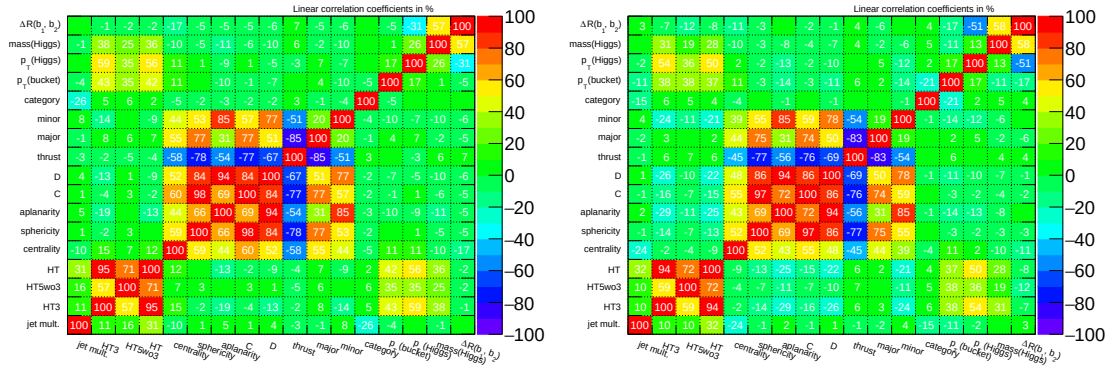

(a) Background (b) Signal

Figure 7.18.: Linear correlation coefficients of input variables and some additional spectator variables such as the Higgs candidate mass and the p_T of the top candidate.

variables based on the scalar p_T sum of jets are ranked higher for the BDT (2^{nd}, 3^{rd}, 6^{th} position) than for the Fisher method (10^{th}, 11^{th}, 12^{th} position).

The Receiver Operating Characteristic (ROC) curves quantify the performance of the classification. The ROC curve compares the signal efficiency with the background efficiency for specific operating points. For the two considered classifiers the corresponding signal and background efficiencies are shown in Figure 7.21. For both classifiers a slightly modified setup is also included. In the FisherVT the input variables are transformed to a different space but otherwise the Fisher discrimination part is unchanged. In a first transformation step the input variables are linearly scaled depending on the minimum and maximum value to lie in the range $[-1, 1]$. The second input transformation aims at achieving a more Gaussian shape of the input variables [223]. The BDT is extended by a gradient version denoted as BDTG. All classifiers and set ups achieve a comparable performance. Only at small signal efficiencies below 20% the ROC curves deviate but in that region also statistical uncertainties become relevant.

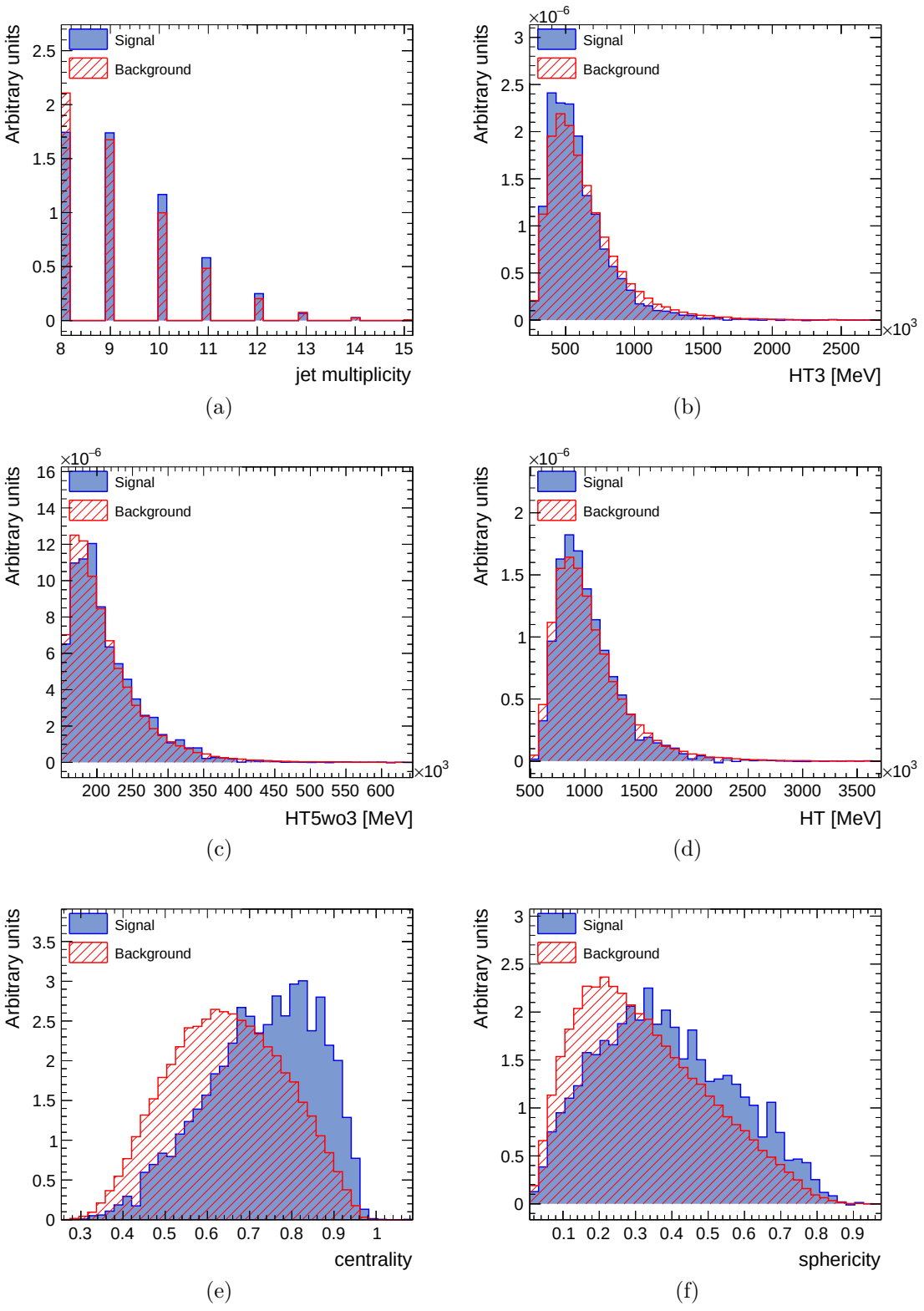

Figure 7.19.: Shape comparison between the $t\bar{t}H$ signal (blue) and background (red) distributions of several input variables.

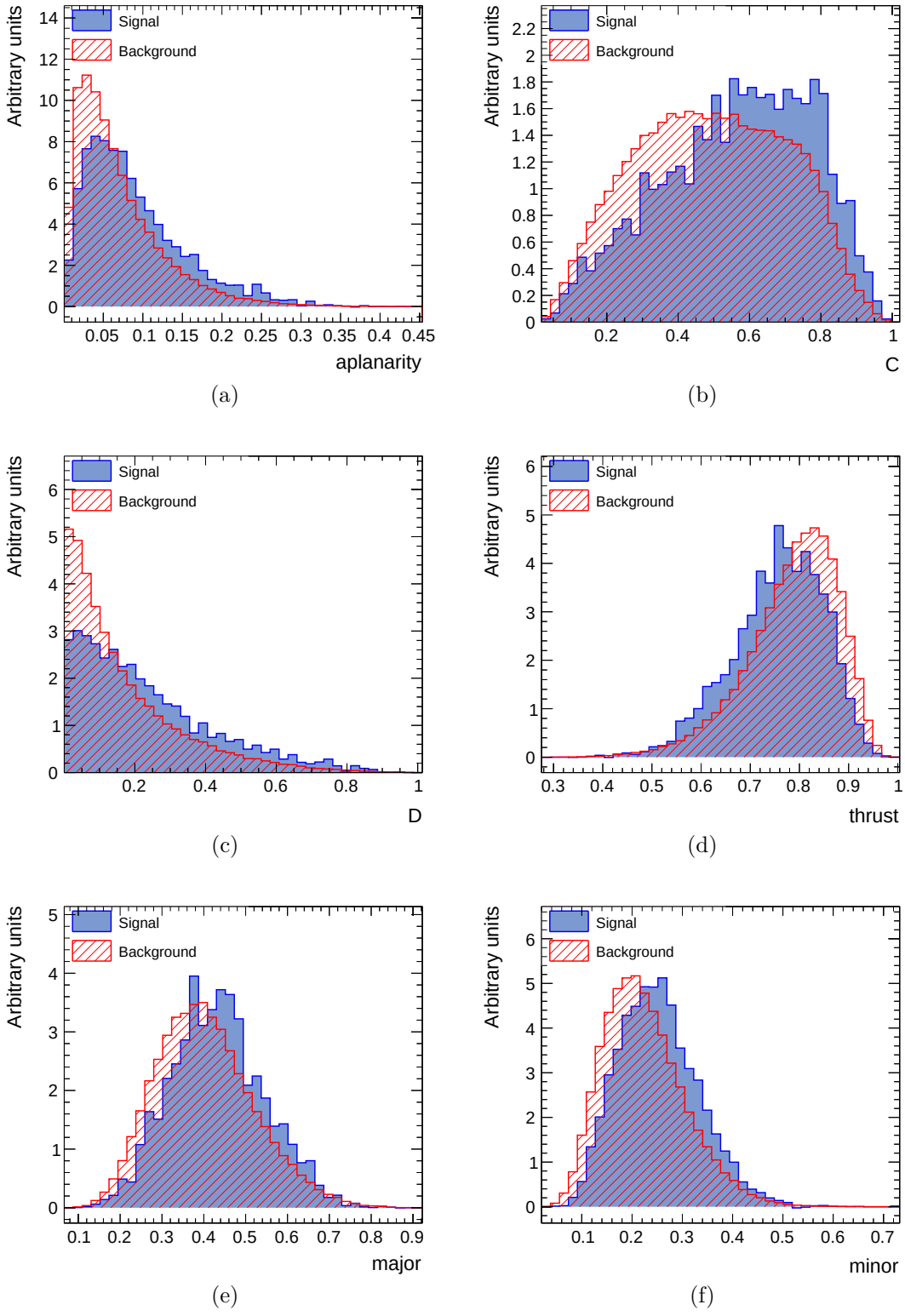

Figure 7.20.: Shape comparison between the $t\bar{t}H$ signal (blue) and background (red) distributions of several input variables.

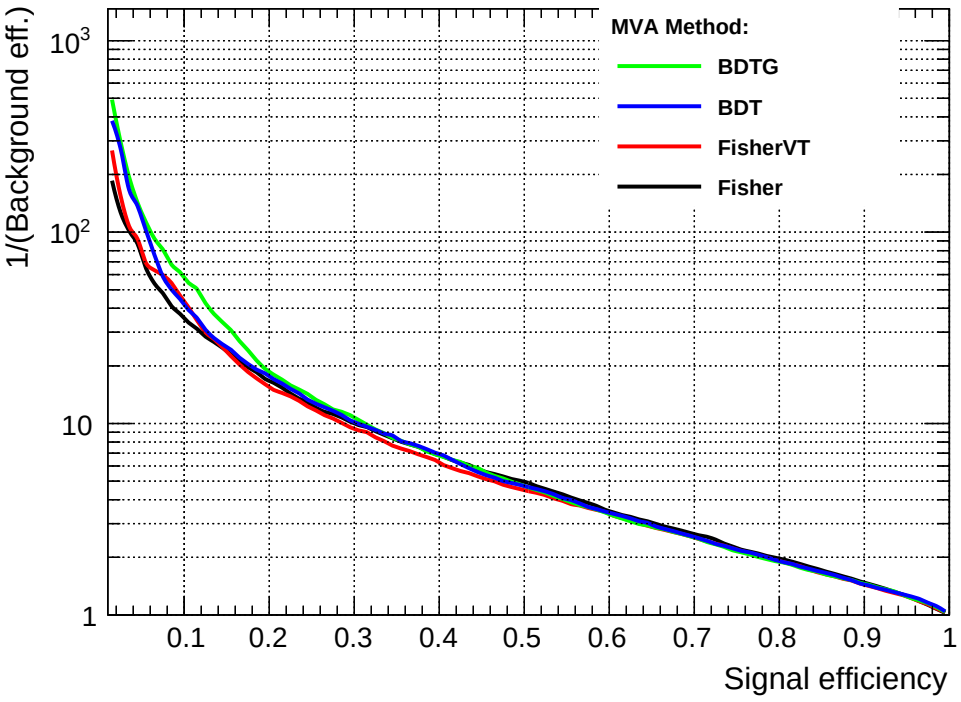

Figure 7.21.: ROC curves of several classifiers.

Class	Normalization	BDT shape
Data stat. only	0.780	0.953
Multijet + $t\bar{t}$ + $t\bar{t}H$ stat.	0.672	0.777
$t\bar{t}$ + $t\bar{t}H$ stat.	0.704	0.812
Multijet + $t\bar{t}H$ stat.	0.737	0.898
Multijet + $t\bar{t}$ stat.	0.672	0.777

Table 7.7.: Expected sensitivity in standard deviations for set-ups with different considered classes of uncertainties at $\sqrt{s} = 13$ TeV with $\int L\mathrm{d}t = 33.3$ fb^{-1} of pp data recorded in 2016.

7.9. Results

A data to model comparison is performed for the reconstructed Higgs mass and the distribution of the multivariate discriminant. For the Higgs mass the region 80 GeV $< m_{bb} <$ 160 GeV is blinded. For the Fisher and BDT weight the bins with an expected signal to background ration above $S/B > 0.02$ are blinded. The corresponding distributions are shown in Figure 7.22.

In particular, the reconstructed Higgs mass is presented in Figure 7.22(a) and including the signal hypothesis $\mu = 1$ in Figure 7.22(b). The low mass region $m_{bb} < 80$ GeV and the high mass region $m_{bb} > 160$ GeV are relatively well described taking into account that the uncertainty model only considers statistical uncertainties. The signal contribution in the mass window 80 GeV $< m_{bb} <$ 160 GeV is small after the preselection. The distribution of the Fisher weight is shown in Figure 7.22(c) and including the signal hypothesis $\mu = 1$ in Figure 7.22(d). The background model overestimates the lower values of the Fisher weight. Assuming the expected yields after the preselection as listed in Table 7.2 the optimal cut on the Fisher weight based on optimizing $S/\sqrt{S+B}$ is at -0.03 which results in $S/\sqrt{S+B} \approx 0.89$. The distribution of the BDT weight is shown in Figure 7.22(e) and including the signal hypothesis $\mu = 1$ in Figure 7.22(f). The background model describes the data reasonable well taking into account that the uncertainty model only considers statistical uncertainties. Assuming the expected yields after the preselection as listed in Table 7.2 the optimal cut on the BDt weight based on optimizing $S/\sqrt{S+B}$ is at -0.02 which results in $S/\sqrt{S+B} \approx 0.88$.

Even though the Fisher and BDT achieve a comparable performance in terms of the ROC curve, the data–MC comparison favors the BDT weight which is better described by the background prediction. Making a realistic estimate of the expected sensitivity requires an assessment of the systematic uncertainties on the MVA weights as well as on the sideband method which is not the subject of this proof of concept analysis. Performing a profile-likelihood fit as described in Chapter 2.5.2 with the Asimov dataset taking into account only the data statistical uncertainties and the expected yields results in an expected sensitivity of 0.78σ

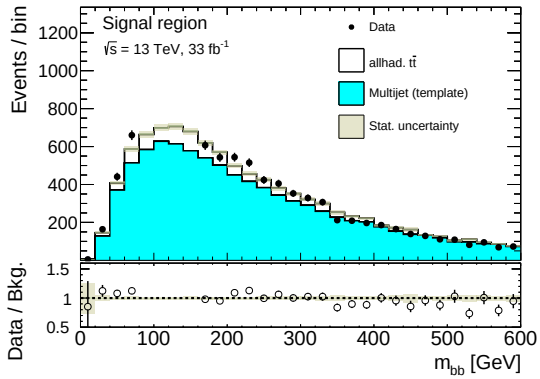

(a) Reconstructed m_{bb} for data and background.

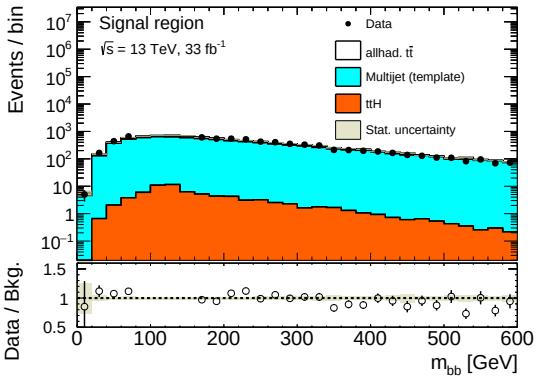

(b) Reconstructed m_{bb} for data, background and using the signal hypothesis $\mu = 1$.

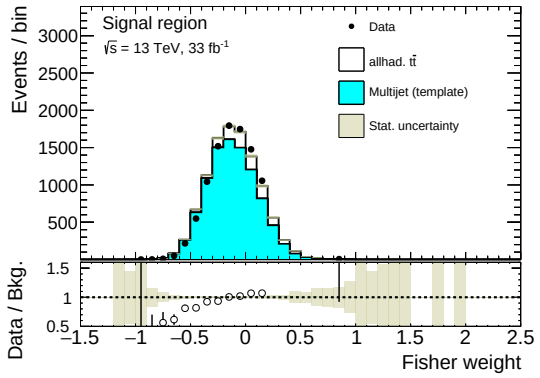

(c) Fisher weight for data and background.

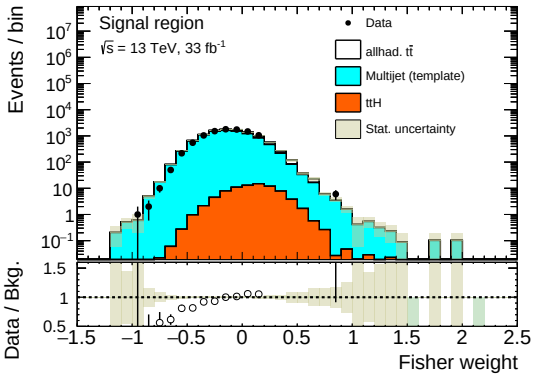

(d) Fisher weight for data, background and using the signal hypothesis $\mu = 1$.

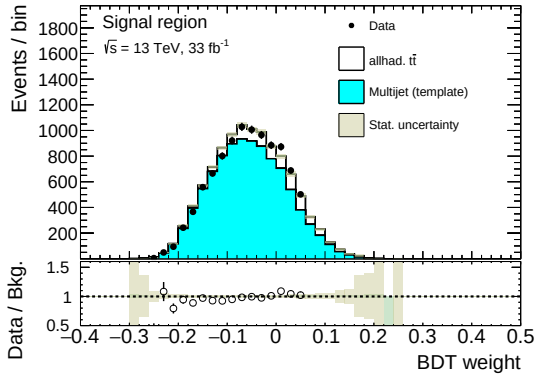

(e) BDT weight for data and background.

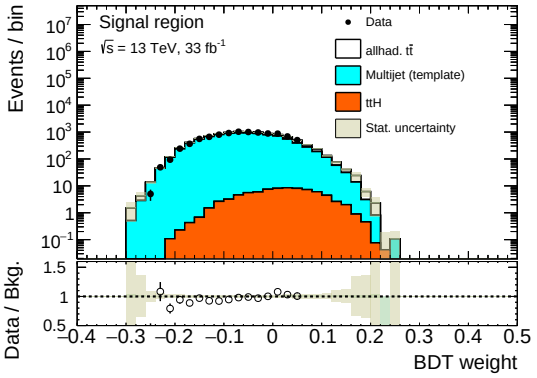

(f) BDT weight for data, background and using the signal hypothesis $\mu = 1$.

Figure 7.22.: Data to model comparison at pre-fit level. The statistical (Stat.) uncertainty denotes the statistical uncertainty of the background model. The multijet shapes are determined in the CR. The normalization of the multijet background is given by the difference between data and simulated $t\bar{t}$ events. The window 80 GeV $< m_{bb} <$ 160 GeV around the Higgs boson mass is blinded in data. For the MVA weights the bins with an expected signal to background ration above $S/B > 0.02$ are blinded

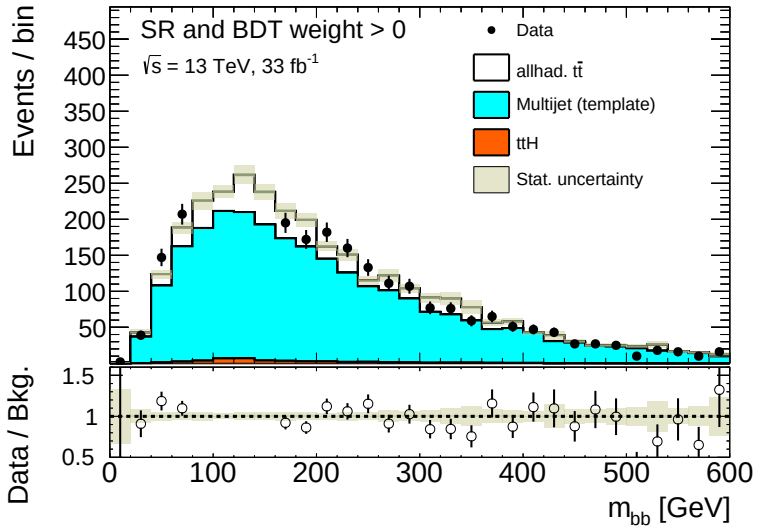

Figure 7.23.: Distribution of the reconstructed Higgs mass m_{bb} after selecting events with a BDT weight larger than 0. The statistical (Stat.) uncertainty denotes the statistical uncertainty of the background model. The multijet shapes are determined in the CR. The normalization of the multijet background is given by the difference between data and simulated $t\bar{t}$ events. The window 80 GeV $< m_{bb} <$ 160 GeV around the Higgs boson mass is blinded in data.

without using any MVA shape information. If the same fit procedure is used together with the BDT weight distribution as input an expected sensitivity of 0.95σ is achieved. This corresponds to an improvement of around 20% by the BDT information. The expected sensitivities for different classes of uncertainties considered is summarized in Table 7.7. The expected sensitivity for the setup including the statistical uncertainties on the multijet background, simulated $t\bar{t}$ and $t\bar{t}H$ events is re-calculated. The additional statistical uncertainties induce a reduction of the expected sensitivity of around 19% (14%) if the BDT shape information is included (excluded). The main contribution to the reduction is caused by the multijet background and $t\bar{t}$ statistical uncertainties.

Extrapolating the expected sensitivity, based on the model considering only the statistical uncertainties on the data derived from the yields (shape of the BDT weight), suggests an integrated luminosity of 1400 fb^{-1} (950 fb^{-1}) in order to achieve a 5σ significance in the allhadronic $t\bar{t}H$ channel alone. Nevertheless, if it is possible to control the systematic uncertainties with e.g. the sideband method the allhadronic $t\bar{t}H$ channel could play a useful role in a combination with other channels which have a better expected sensitivity. The distribution of the reconstructed Higgs mass m_{bb} after selecting events with a BDT weight larger than 0.0 is presented in Figure 7.23. This selection results in 3093 events in data and an expected $t\bar{t}H$ yield of 48.4 ± 0.9 (stat.). As explained before the Higgs quantities

are not explicitly used in the classification and the linear correlation between several Higgs variables like mass or p_T and the MVA variables is not very strong as supported by the correlations shown in Figure 7.18. Therefore, the selection on the BDT weight has only a slight effect on the shape of the m_{bb} distribution.

As shown in Chapter 7.2.2 the high trigger threshold reduces the signal efficiency by a factor 1/3 which compromises to some extend the advantage of the large branching fraction of the allhadronic $t\bar{t}$ final state. Possible improvements in the context of the trigger are addressed in Chapter 8.

7.10. Conclusion and outlook

This proof of principal analysis for the search for the standard model Higgs in association with top quarks in the fully hadronic decay mode shows that a suppression of the overwhelming QCD multijet background is possible based on event shape and kinematic quantities. The bucket algorithm can reconstruct the top quark pair and provides a Higgs candidate. The reconstructed mass of the Higgs candidate can be described by parametrizations for signal and background which could be exploited by a sideband-method in order to control the uncertainties. The expected sensitivity based on the purely statistical uncertainties indicates that this channel could serve as a useful extension in the form of a combination with other analysis aiming at measuring the top Yukawa coupling. The presented analysis especially emphasizes the treatment of the description and suppression of the QCD multijet background. After a simple preselection this background is dominating, and in addition generally hard to predict and simulate accurately. The requirement of at least four b-tagged jets is one of the main issues in that context as the QCD flavor composition will depend on the performance of the b-tagging algorithm in the experimental environment. Therefore, a fully data driven approach is chosen for the QCD modeling in the multivariate method.

One main open point which requires further studies is the treatment of the $t\bar{t}$ background by the simulation. The investigation of systematic uncertainties on the $t\bar{t}$ modeling in Chapter 6 and the large statistical uncertainties present suggest that the associated uncertainties could have a sizable effect on the overall sensitivity. As outlined in the resonance search a suitable set of side bands should help to control such uncertainties.

In principal, both steps of the analysis the event reconstruction and the event classification, could be further optimized. The finite matching efficiency between the offline small-R jets and the truth level partons limits the achievable quality of the event reconstruction. At low transverse momentum, tracks can help to improve the jet reconstruction which could eventually result in a higher matching efficiency. Any event reconstruction procedure would profit from input jets which describe the $t\bar{t}H$ decay topology better. The bucket algorithm itself could be further optimized for the $t\bar{t}H$ channel. In particular, the reconstruction of events with more than four b-tagged jets could be modified to take e.g. the topology where a jet which

originates from the W boson decay is b-tagged into account. Also the Higgs mass could be directly used in the reconstruction. This would likely reduce the signal combinatorics but at the cost of a modified m_{bb} shape putting the validity of the sideband procedure in question. Other reconstruction approaches like e.g. kinematic fitting, a multivariate reconstruction or the matrix method will also suffer from the finite matching efficiency between the small-R jets and the partons of the $t\bar{t}H$ system which is already present after general preselections.

The event classification relies on a background data set which consists not only of QCD multijets but also of SM $t\bar{t}$. Explicitly using $t\bar{t}$ MC predictions in the classification step could help to increase the separation between SM $t\bar{t}$ and the $t\bar{t}H$ signal.

Nevertheless, all optimizations depend on the constant performance of the trigger system. In the context of the HL-LHC, the increasing instantaneous luminosities result in increasing trigger thresholds which can lead to strong reductions of the $t\bar{t}H$ signal efficiency in the allhadronic decay mode. Therefore, trigger level studies aiming at improving the trigger performance are discussed in Chapter 8.

8. Bucket algorithm at trigger level

8.1. Introduction

The overwhelming contribution to jet production in proton-proton collisions at $\sqrt{s} = 13$ TeV at the LHC originates from QCD multijet processes which are generally several orders of magnitude larger than typical signal processes. Therefore, a reduction of the trigger rates is necessary to avoid saturation with uninteresting multijet events. Generally, this is achieved with the requirement of high transverse momentum thresholds on the jets or of high jet multiplicities at trigger level. As shown in the previous chapters many signal scenarios with fully hadronic final states are indeed characterized by a high transverse momentum and large jet multiplicities. But the trigger selection is inevitably reducing the acceptance for signals with a moderate transverse momentum of the top quarks. This is illustrated for a Z'_{TC2} signal model with a mass of 750 GeV in Figure 8.1. Simplified algorithms at trigger level lead to turn-on curves which require even higher E_T selections at offline jet level compared to trigger level in order to operate in the plateau of the trigger. This strongly degrades the achievable performance for the resonance search at low masses < 750 GeV as shown in Chapter 6 and significantly reduces the signal in the $t\bar{t}H$ analysis as described in Chapter 7.2.2. The negative effect of the high trigger thresholds on the signal selection is expected to increase with rising instantaneous luminosities as foreseen for future data taking runs. In principal, there are three ways to deal with this acceptance reduction. First, one can derive scale factors to loosen the offline selection into the regime where the trigger is not fully efficient as carried out in Chapter 6.5. Secondly, an improved calibration and treatment of online jets can result in steeper turn-on curves. For single jet triggers this is proven in Reference [19] in the context of updated calibrations and the addition of track information to give an improvement as shown in Figure 8.16(a). Furthermore, a more advanced event selection at trigger level that is specific to the signal model under study, based on e.g. the flavor tagging or top quark decay related quantities, can be a way to optimize the trigger. The possibility last mentioned is investigated in this chapter. Specifically, new trigger chains are constructed which run parts of the bucket algorithm on high-level trigger jets.

A dedicated dataset is used to measure the performance of new trigger chains in data. The design of this dataset is explained in Chapter 8.2. Chapter 8.3 describes the necessary modifications of the bucket algorithm to be run at trigger level. The effect of the modified bucket algorithm on the top quark reconstruction performance is studied at offline jet level using the Z'_{TC2} signal benchmark model

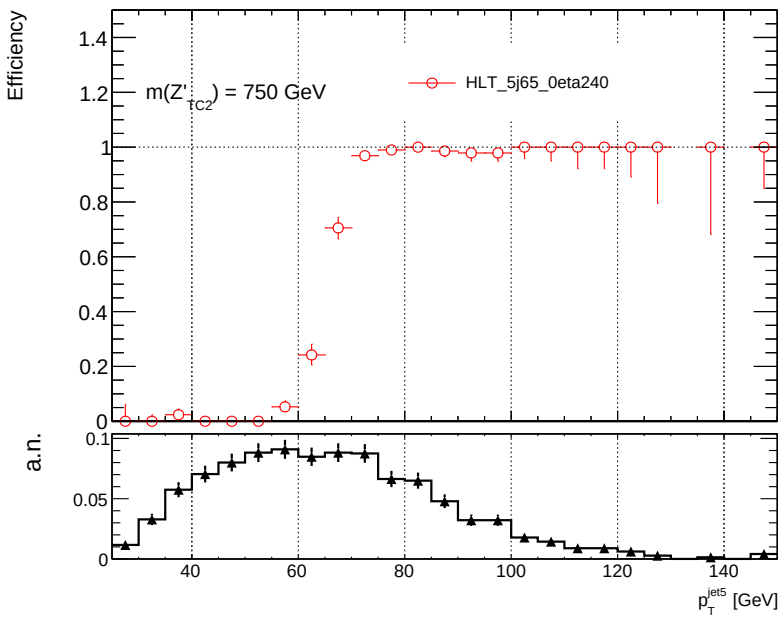

Figure 8.1.: Trigger turn-on curve and the distribution of the fifth hardest jet in simulated Z'_{TC2} signal events with $m_{Z'_{\mathrm{TC2}}} = 750$ GeV. The same selection as in Chapter 6.2.2 is applied except for the fifth hardest jet p_T requirement and the pseudorapidity η restrictions on the jets.

as introduced in Chapter 6.3.1. Different trigger approaches based on jets are presented and their performance is tested and summarized in Chapter 8.4. The reconstruction and the calibration of the jets at HLT trigger level is close to the offline procedure. The differences of the jets at trigger and offline level are also described in Chapter 8.4. An outlook on the prospects of the presented approach in future data taking conditions is given in Chapter 8.5.

8.2. Data and event selection

As outlined above the goal of this trigger study is to lower the high multijet trigger thresholds. Initially, this is tested with simulated trigger jets. As there could be mis-modeling of the trigger properties in simulation it is interesting to validate the performance in data. Therefore, a validation dataset which allows testing the reconstruction at lowered trigger thresholds is used. Instead of combining the new trigger chain with other already existing high-level trigger chains this analysis studies what complementary information it can add after the level-1 decision of the trigger system. So in order to circumvent any bias coming from supporting HLT triggers the event selection in data is completely based on the level-1 trigger decisions.

The simple way to estimate trigger rates would be to use a random trigger. This would also have the advantage of zero trigger bias. At the LHC such a trigger chain

would be dominated by low transverse momentum jet production. The fraction of interesting processes involving topologies like the ones present in $t\bar{t}$ production would be small. The dataset used relies on the so-called enhanced bias (EB) data run procedure that is described in full detail in Reference [232]. The idea of the enhanced bias dataset is to create a dataset with a relatively large contribution from high transverse momentum events and higher multiplicities to address the kinematic regime relevant for a high level trigger decision. This is achieved by using a diverse collection of level-1 trigger chains. In principal, a zero bias spectrum can be reconstructed by weights which are derived to correct for prescales. From this weights and additional information for the enhanced bias data taking set-up the HLT rate can be predicted. As motivated later the calculation of these EB weights is not necessary for this trigger study and a light-weighted estimation of the expected rate is used instead. The collection of the EB dataset is performed in parallel to the physics data taking. Hence, the same menu with respect to the level-1 prescales is used in the EB data taking.

The EB dataset is recorded at a center-of-mas energy of 13 TeV with the ATLAS detector. Eventually, a total of 1569643 events is used for the performance study in data. As a baseline selection the level-1 multijet trigger with at least four jets with $E_T > 15$ GeV is considered. It provides a selection of 54390 events as input to the rate study in Chapter 8.4.5. In the EB run considered in this analysis the average interactions per bunch crossing $\langle\mu\rangle = 36.0 \pm 1.6$ was relatively large compared to the full ATLAS 2016 data taking run. For future ATLAS data taking periods higher pileup conditions with up to $\langle\mu\rangle \approx 200$ at the HL-LHC are expected. The ability to reject pileup is limited online compared to offline reconstruction due to e.g. missing global track information. A significant change of $\langle\mu\rangle$ would require a reevaluation of the expected trigger performance. Future pileup suppression strategies and the interplay with the study presented are explained in Chapter 8.5.

A large variety of trigger chains is investigated in this chapter. This involves different online trigger selections at level-1 and at the high level trigger as well as emulated decisions based on online trigger objects. Therefore, a labeling scheme is introduced to categorize the different types of triggers. Multijet triggers are characterized by an integer number in front of the letter `j` denoting the jet multiplicity. The multiplicity is followed by a value which defines the E_T threshold in GeV. Level-1 trigger decisions are started by the character `L1` and high level trigger decisions are started by `HLT`. In contrast emulated trigger chains are labeled by `EMU`. The terminology of the emulated buckets triggers is described in Chapter 8.4. The multijet trigger used in the $t\bar{t}$ resonance search would e.g. be denoted by `HLT_5j65_0eta240` were in addition a restriction on the pseudorapidity of the HLT jets $|\eta| < 1.6$ is indicated by the suffix `0eta240`.

8.3. Adapting the bucket algorithm for trigger jets

The bucket algorithm has to be modified in order to work at the high-level trigger level. As is argued in Chapter 8.4.1 the online and offline jets are in reasonable agreement which allows testing the top reconstruction also at trigger level. On the other hand the b-tagging is known to show differences at trigger level due to reduced available information in form of tracks. In addition, the b-tagging itself is time consuming making a subsequent top reconstruction questionable. To deal with these limitations, the bucket algorithm is modified to run without b-tagging information as input seed. Besides that, the reconstruction procedure as described in Chapter 4 stays unaltered. For $t\bar{t}$ events no strong performance degradation is expected. But for the background events the fact that the b-tagging info is not used will likely increase the combinatorial background. The b-tagging during the reconstruction procedure effectively reduces the possibilities to assign jets to the top buckets. Furthermore, the number of jets considered to search for a W boson candidate inside a top bucket is increased if no b-tagging is used. Therefore, the background rejection is expected to become worse. This is validated in two ways. First, the applicability of the modified version is investigated on the Z'_{TC2} signal benchmark model using the event selection of the 2016 data setup as described in Chapter 6.2.2. This shows that the modified version could serve as a basis for a realistic analysis scenario once applied at trigger level without significant loss of signal acceptance. Even though the precise effects on the signal efficiency have to be studied separately in a future search application. The modified version can address a larger phase space than the default bucket algorithm and should also deal with lower jet multiplicities. Therefore in a second validation step the performance is cross-checked on a looser event selection.

The modified bucket algorithm differs from the default reconstruction only in the usage of the b-tagging information. The b-tagged jets are treated as any other selected jet in the event. The top buckets are no longer seeded by the bottom jets. The two setups are labeled "*with b-tag*" for the default reconstruction and "*without b-tag*" for the adapted $t\bar{t}$ reconstruction. The performance of the two setups is compared and validated using jets at offline level.

The signal mass resolutions corresponding to the event selection as presented in the $t\bar{t}$ resonance search are shown in Figure 8.2 for a Z'_{TC2} signal mass of 750 GeV characterized by a moderate transverse momentum of the top quarks and for 1250 GeV with higher transverse momentum of the top quarks. It reveals that the mass resolution for both p_T ranges is equally good for the two top quark reconstruction procedures. As they are both normalized to the default reconstruction technique the acceptance for the signals are also in agreement. Besides the reconstructed invariant mass the p_T of the top candidates is proven to be a useful variable to quantify the reconstruction performance. For the two Z'_{TC2} benchmark models the p_T of the softer top bucket is shown in Figure 8.3 where the minimal p_T requirement was omitted. For both mass points the adapted bucket algorithm yields slightly softer top quark candidates but the overall agreement is good and indicates a similar

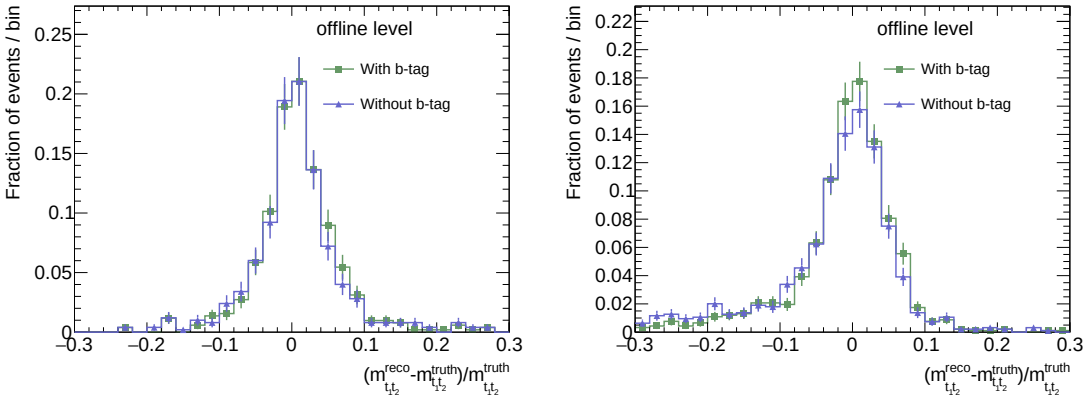

(a) $m_{Z'_{\mathrm{TC2}}} = 750$ GeV. (b) $m_{Z'_{\mathrm{TC2}}} = 1250$ GeV.

Figure 8.2.: Mass resolution in simulated events for the Z'_{TC2} signal model at different generated Z'_{TC2} masses. The distributions are normalized with respect to the default reconstruction technique using the b-tag information. The default selection of the $t\bar{t}$ resonance analysis as described in Chapter 6.2 is applied. The inputs are offline level objects.

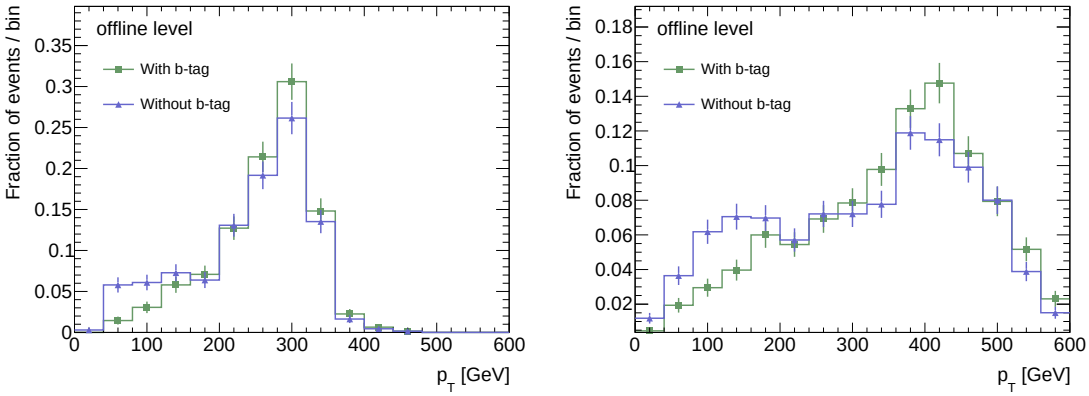

(a) $m_{Z'_{\mathrm{TC2}}} = 750$ GeV. (b) $m_{Z'_{\mathrm{TC2}}} = 1250$ GeV.

Figure 8.3.: Transverse momentum distribution of the softer top bucket in simulated events for the Z'_{TC2} signal model at different generated Z'_{TC2} masses. The distributions are normalized with respect to the default reconstruction technique using the b-tag information. The default selection of the $t\bar{t}$ resonance analysis as described in Chapter 6.2 is applied but omitting the p_T requirements on the top buckets. The inputs are offline level objects.

p_T dependence of the reconstruction efficiency. This comparable performance is a good starting point for the more general event preselection which is tested in the following[1].

The performance of the adapted bucket algorithm is further studied in simulated allhadronic SM $t\bar{t}$ events with jets at offline level. The corresponding simulation is described in Chapter 3.3.1. The quality of the reconstruction is quantified by a geometrical matching in the $\eta - \phi$ plane. The reconstructed top candidates are matched to the truth top quarks after radiation with $\Delta R(t_i^{\text{reco}}, t_j^{\text{truth}}) = \sqrt{(\eta_i - \eta_j)^2 + (\phi_i - \phi_j)^2}$. If both reconstructed top quarks satisfy the following equation the matching is considered successful

$$\Delta R(t_i^{\text{reco}}, t_j^{\text{truth}})) < 0.3 \ . \tag{8.3.1}$$

The bucket algorithm reconstructs top quarks from 2 or more jets. Hence, a preselection of at least four offline jets is applied in this performance study. The distributions of several top bucket quantities are shown in Figure 8.4. Also with the adapted bucket algorithm an accurate reconstruction is possible. The incorrectly reconstructed events are mostly at small p_T of the top buckets . Therefore, selecting top buckets with a minimal transverse momentum requirement is improving the quality of the reconstruction. In addition, the purely geometrical matched top candidates also achieve an adequate transverse momentum reconstruction as can be inferred from Figure 8.4(c) and Figure 8.4(d). The ΔR distribution of each top bucket in Figure 8.4(e) and Figure 8.4(f) reveals that the harder top candidate generally reconstructs the truth top quark better than the softer top candidate. The single top reconstruction efficiency is much larger than the pair reconstruction efficiency.

The distribution of the QCD multijet background is modeled using data. As no b-tagging is required the EB dataset is dominated by QCD multijet events after preselection. Without any further MC corrections the EB dataset is compared to the allhadronic SM $t\bar{t}$ simulation in Figure 8.5. The purpose of this comparison is to highlight shape and event category differences. The SM $t\bar{t}$ simulation and the EB dataset are both normalized to unity. The transverse momentum of the QCD template in Figure 8.5(a) is slightly softer than the SM $t\bar{t}$. However, the shape difference is not sufficient to achieve a significant separation. Nevertheless, knowing that the well reconstructed $t\bar{t}$ events are predominantly at higher transverse momentum opens possibilities to exploit this quantity during the trigger selection. The event categories based on the top quark and W boson mass windows are presented in Figure 8.5(b). In SM $t\bar{t}$ events it is more likely to select top quarks satisfying the mass conditions. In particular, the ($\mathfrak{t}_w$, $\mathfrak{t}_w$) category which takes the W boson mass into account provides the strongest QCD multijet suppression as expected from the study in Chapter 5.

[1]It should be mentioned that even though there are slight differences, the default bucket algorithm could still be applied on top of the modified version at offline level to achieve the advantages related to the direct usage of the b-tagging.

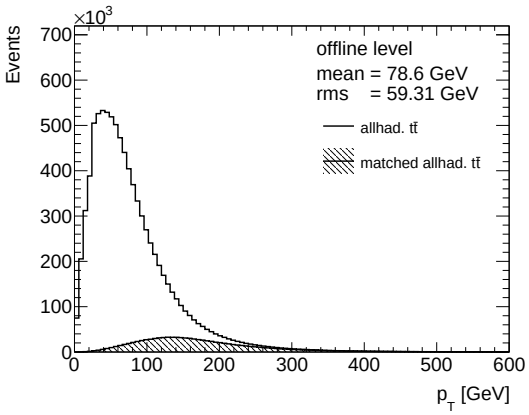

(a) p_T of softer top bucket.

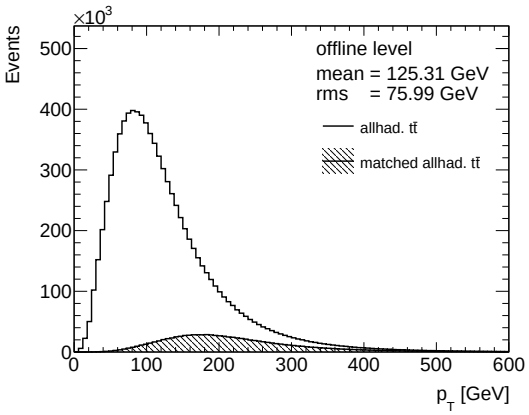

(b) p_T of harder top bucket

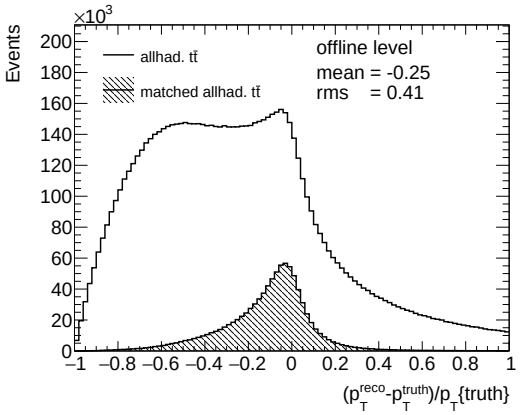

(c) p_T resolution of softer top bucket.

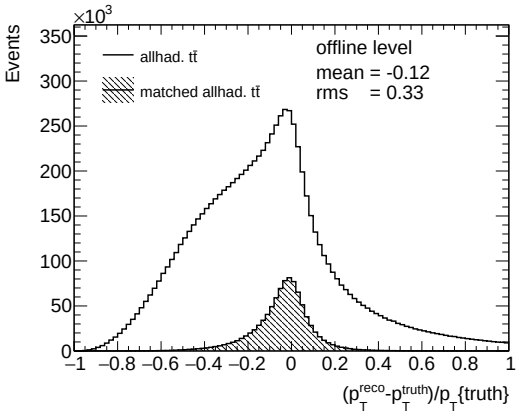

(d) p_T resolution of harder top bucket.

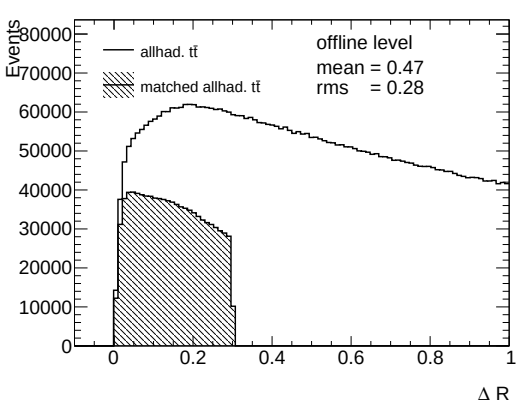

(e) ΔR of softer top bucket.

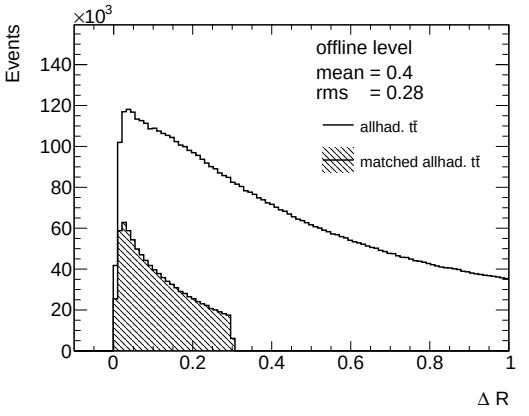

(f) ΔR of harder top bucket.

Figure 8.4.: Distributions of variables describing reconstructed top quark candidates in simulated allhadronic SM $t\bar{t}$ events. The adapted bucket algorithm is used. The events are preselected to contain at least four offline jets. The fraction of events in which the reconstructed top quark pair is matched to the truth top quarks after radiation with $\Delta R(t_i^{\mathrm{reco}}, t_j^{\mathrm{truth}})) < 0.3$ is indicated by the shaded area. The inputs are offline level objects.

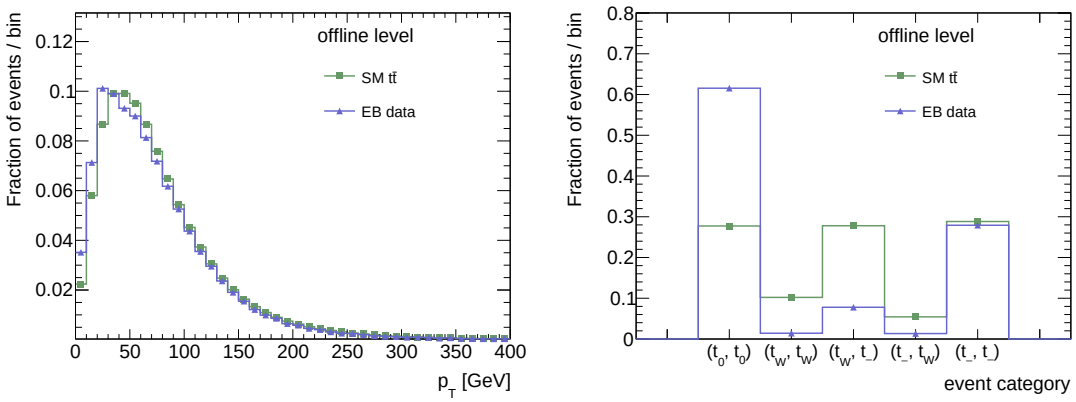

(a) p_T of softer top bucket.

(b) Event category.

Figure 8.5.: Shape comparison of distributions in simulated allhadronic SM $t\bar{t}$ events and in the EB dataset. The events are preselected to contain at least four offline jets. The dominating contribution in the EB data is given by QCD multijets. Therefore, the data serves as a QCD template. The adapted bucket algorithm is used. The inputs are offline level objects.

8.4. Performance

The motivation of studying top reconstruction at trigger level is the expected increase of acceptance for various signal models with low transverse momentum of the top quarks and an improved selection for $t\bar{t}$ decay topologies where the W boson from the top quark decay is more likely to be reconstructed. The top quark reconstruction based on high-level trigger jets follows the same algorithm and methods used for the offline top quark reconstruction. As for any other trigger chain the ability to achieve better acceptance of interesting events has to balance the potential rate increase. The performance of the jet and top quark reconstruction is evaluated in Chapter 8.4.1. The construction and labeling of the new trigger chains is described in Chapter 8.4.2. The performance of the emulated trigger chains in simulated events is evaluated in Chapter 8.4.3. The accuracy of the trigger emulation is validated on data in Chapter 8.4.4. Estimated rates with respect to a reference trigger for various set-ups are studied in Chapter 8.4.5. Finally, the timing and CPU consumption of the bucket algorithm is investigated and means to reduce these crucial parameters for triggering are discussed in Chapter 8.4.6.

8.4.1. Comparison of trigger and offline jets

As emphasized before, the main differences of the top reconstruction are likely caused by the differences in the input objects. As the top reconstruction is solely based on the Anti-k_T ($R = 0.4$) jets it should consequently be dependent on changes of the properties of the jets. Especially different calibrations and levels of accuracy

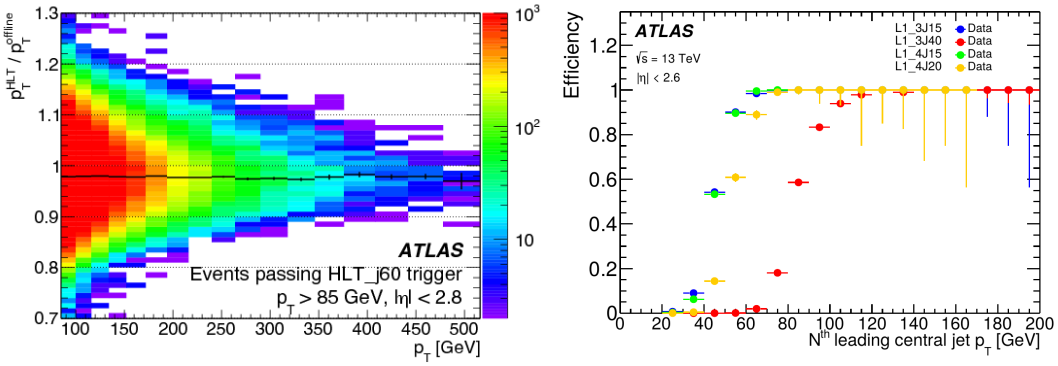

(a) Jet energy scale comparison between HLT jets and offline jets. The mean value of the distribution is shown by the black points.

(b) Efficiency of level-1 multijet trigger chains with respect to the n^{th} offline jet p_T.

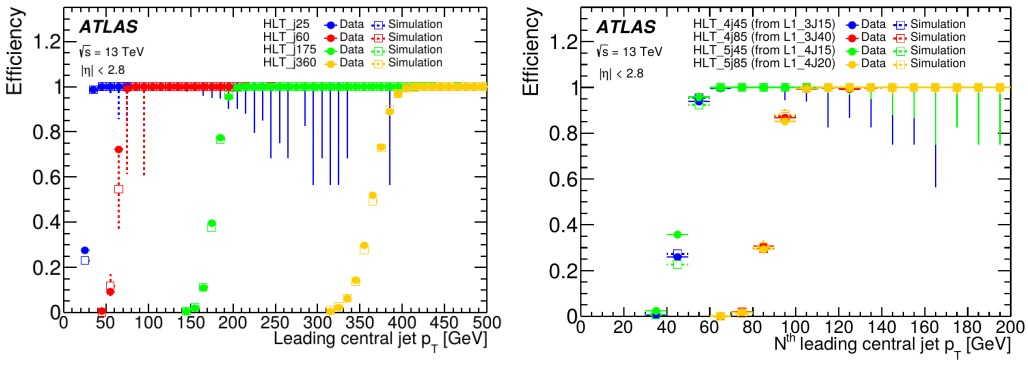

(c) Efficiency of HLT single-jet trigger chains with respect to the offline jet p_T.

(d) Efficiency of HLT multijet trigger chains with respect to the n^{th} offline jet p_T.

Figure 8.6.: Comparison of jet energy scale and efficiency for HLT and offline jets. Taken from Reference [100].

to suppress pileup effects on the jets can affect the jet collection in an event.

The reconstruction of HLT jets largely follows the offline procedure as described in Reference [233]. The full set of calorimeter cells calibrated at the EM scale is used to form topo-clusters. The topo-clusters are used as input to the Anti-k_T ($R = 0.4$) jet finding algorithm [36]. The resulting jets are calibrated with a pileup subtraction and a jet response correction. The ρ-area based pileup suppression uses the area of each jet and the energy density within $|\eta| < 2$. The p_T and η dependent response corrections are derived from the simulation using the offline configuration of the 2012 data taking period in the ATLAS experiment. In contrast, the offline jets rely on corrections based on a newer simulation configuration as described in Chapter 3.4.5. The performance of the trigger jets for single jet and multijet chains is discussed in full detail in Reference [100]. A comparison of the jet energy scale between HLT and offline jets is shown in Figure 8.6(a). A good agreement of the jet energy scale for online and offline jets is observed for jets with transverse momentum

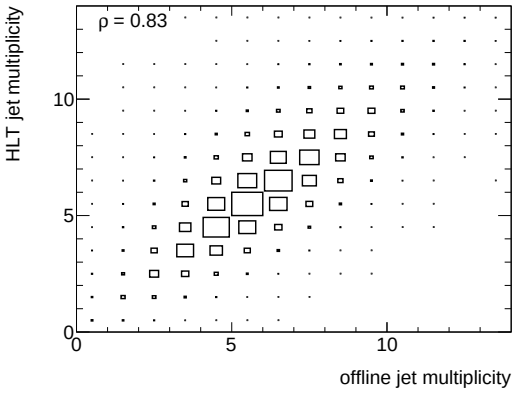

(a) Jet multiplicity.

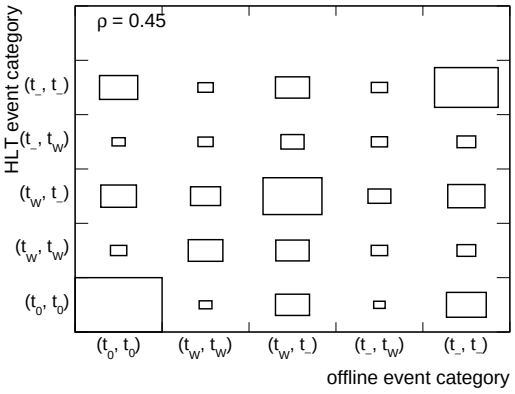

(b) Event categories.

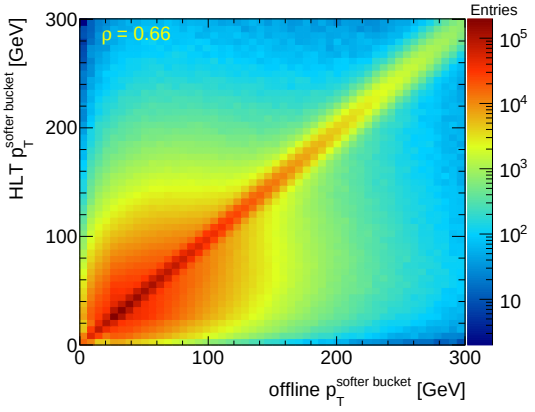

(c) p_T^{bucket} of softer top bucket.

Figure 8.7.: Comparison of online (HLT) and offline jets in simulated allhadronic $t\bar{t}$ events.

above 85 GeV. The 2% difference of the mean of the p_T ratio is a result of the different calibrations. Furthermore, the single jet trigger efficiencies are shown as a function of the offline jet transverse momentum in Figure 8.6(c). The corresponding efficiencies of level-1 multijet trigger chains are presented in Figure 8.6(b). These level-1 trigger chains can be used to seed the to be constructed HLT trigger chains. In addition, the efficiencies of existing HLT multijet trigger chains are shown in Figure 8.6(d).

The HLT jets in this analysis have to satisfy $p_T > 25$ GeV and $|\eta| < 2.5$ to be consistent with the offline selection. The jet multiplicities for online and offline jets are compared in Figure 8.7(a) in simulated SM $t\bar{t}$ events. On average the mean for online $n_{\text{jet}}^{\text{online}} = 5.4 \pm 1.6$ and offline $n_{\text{jet}}^{\text{offline}} = 5.3 \pm 1.6$ jet multiplicities agree. The distributions are strongly correlated but nevertheless tend to differ. The main background at lower top quark momenta is given by combinatorics. Higher jet multiplicities increase the probability to accidentally reconstruct a top quark pair candidate in a background event. It is expected that the jet multiplicity is strongly

Type	Trigger chain
standard top trigger	EMU_tb50 EMU_tb100 EMU_tb150 EMU_tb200
advanced top trigger	EMU_tb50_c1234_5j45_0eta250_L14J15 EMU_tb100_c1234_5j45_0eta250_L14J15 EMU_tb150_c1234_5j45_0eta250_L14J15 EMU_tb200_c1234_5j45_0eta250_L14J15

Table 8.1.: Definition and labeling of several emulated *standard top trigger* and *advanced top trigger* setups. The `tbxx` denotes the selection on the transverse momentum of the top buckets and the `c1234` indicates the mass window selections as described in Chapter 8.4.2.

related to the relative grouping in top event categories. The online and offline event categories are shown in Figure 8.7(b). The online and offline selection is correlated but the deviations for individual categories in this discrete spectrum are more pronounced. Even if a W candidate is not found during the online reconstruction the t_{-} top bucket can still be correct and give a good approximation of the top quark four momentum. The transverse momentum of the softer top bucket can be used to suppress the background and to improve the accuracy of the reconstruction. The corresponding correlation of the transverse momentum of the softer top bucket which is constructed from HLT or offline jets is shown in Figure 8.7(c). It is characterized by a strong correlation over the full considered transverse momentum range. This makes the transverse momentum of the softer top bucket a suitable variable to trigger on.

8.4.2. Construction and labeling of new trigger chains

Given the motivation mentioned above several new trigger chains are constructed and tested in the following chapters. Depending on the transverse momentum threshold present at HLT level the trigger chains are labeled by `EMU_tb`. Where `tb` stands for the bucket algorithm and it is followed by the value of the p_T threshold in GeV. The set of these triggers, based on the transverse momentum of the top buckets, is referred to as *standard top trigger*. In addition, a set of trigger chains with further top quark related selections is constructed and denoted by *advanced top trigger*. The *advanced top trigger* combines the *standard top trigger*, a multijet trigger chain and the event category information in one trigger chain. The top quark reconstruction becomes more precise if more jets originating from top quark decay products are present in the event. Therefore, one often requires a minimum jet multiplicity of five or more jets offline. This is mimicked also at HLT by letting

the *advanced top trigger* be seeded by a multijet trigger. The seed multijet trigger selects at least five HLT jets with $p_T > 45$ GeV and $|\eta| < 2.5$. It is abbreviated by `HLT_5j45_0eta250`. The threshold is low enough that improvements with the top trigger are still possible and no interference with the corresponding level-1 multijet trigger turn-on is expected. The extra background rejection and rate reduction is achieved by requiring two top candidates based on the mass window selections. The four top event categories are labeled in the following way 1: ($\mathtt{t}_w$, $\mathtt{t}_w$) 2: ($\mathtt{t}_w$, $\mathtt{t}_-$) 3: ($\mathtt{t}_-$, $\mathtt{t}_w$) 4: ($\mathtt{t}_-$, $\mathtt{t}_-$). Depending on the selected category `cx`, where `x` is a natural number representing the category, the following naming convention is applied `EMU_tbxx_cxx_5j45_0eta250_L14J15`. As the correlation between the online and offline event grouping is not perfect it could lead to an efficiency loss for the *advanced top trigger*. To keep this potential efficiency loss minimal only the scenario where all mass selections are passed `c1234` is studied. The fraction of interesting events not passing the online mass selection but having a W candidate in the offline reconstruction is relatively small as indicated in Figure 8.7(b). This is further investigated quantitatively in the next Chapter. Several *standard top trigger* and *advanced top trigger* chains are listed in Table 8.1. In addition, the new trigger chains can be combined with other HLT multijet trigger chains. The *advanced top trigger* is expected to achieve smaller rates as the *standard top trigger* as it uses additionally the mass information. The relative rates with respect to a reference trigger are explained in Chapter 8.4.5.

8.4.3. Trigger efficiency in simulated events

The quality of the online top reconstruction and trigger selection is studied in simulated allhadronic SM $t\bar{t}$ events. The statistical treatment for the calculation of trigger efficiencies is introduced in Chapter 6.5. In simulated events it is straight forward to calculate the trigger efficiency as also the events not passing the trigger selection are known. The efficiency is projected on a single offline variable which is considered to adequately represent the top quark performance. Previous studies motivate to choose the transverse momentum of the softer top quark candidate as a reference variable. The performance of the new trigger chains is compared to the 5-jet multijet trigger that is used in the analyses in Chapters 6 and 7. The 5-jet reference trigger is denoted by `HLT_5j65_0eta240`. The trigger rates relative to this 5-jet trigger are described in Chapter 8.4.5.

Ideally the trigger turn-on-curve reach a plateau meaning that the trigger can be operated under constant conditions. A trigger in a non-plateau regime is still usable but would require additional calibrations in a realistic analysis scenario. The *standard top trigger* chains with selection of $p_T > 100, 150, 200$ GeV are presented in Figure 8.8. The trigger turn-on-curve for the *standard top trigger* and the typical ATLAS 5-jet multijet trigger are compared in Figure 8.8(a) for the efficiency ϵ_T.

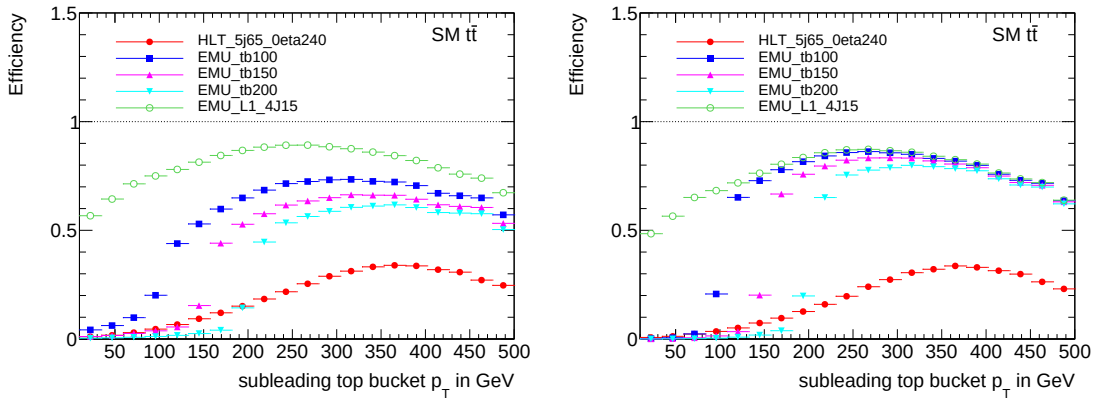

(a) p_T^{bucket} of softer top bucket.

(b) p_T^{bucket} of softer top bucket, trigger matched within $\Delta R < 0.4$.

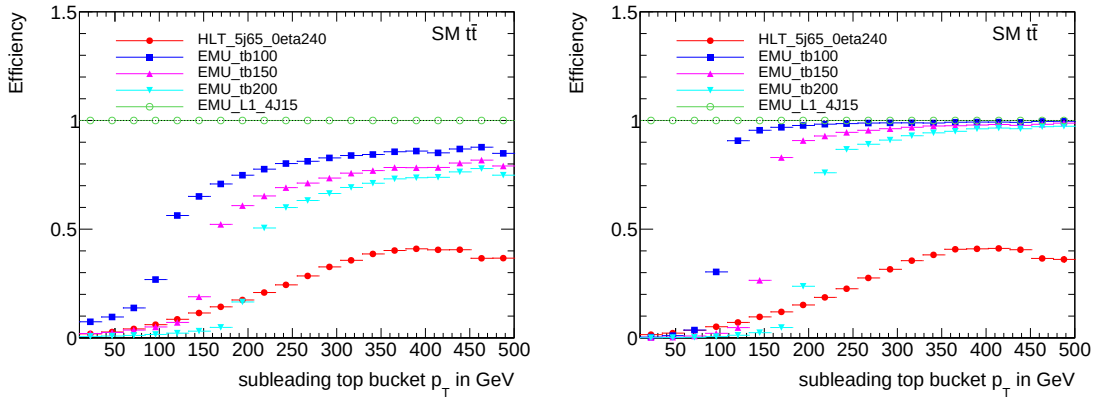

(c) p_T^{bucket} of softer top bucket with active level-1 reference trigger.

(d) p_T^{bucket} of softer top bucket with active level-1 reference trigger, trigger matched within $\Delta R < 0.4$.

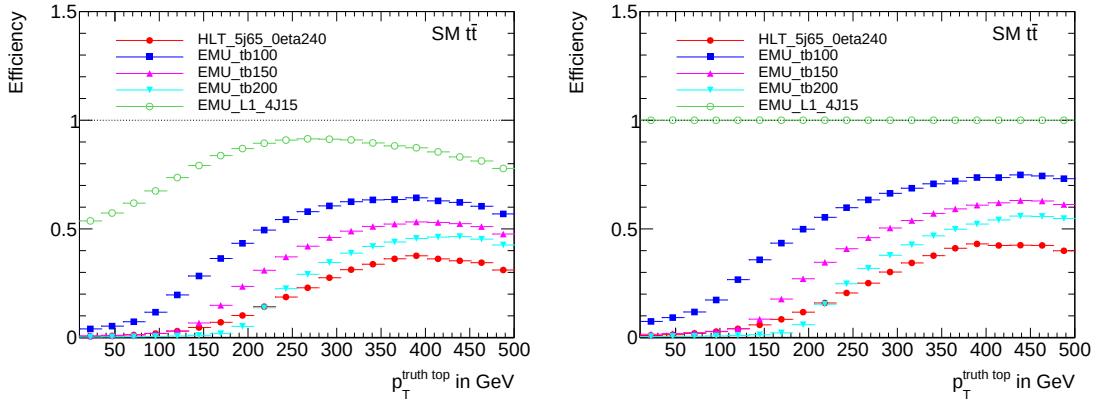

(e) $p_T^{\text{t, truth}}$ of softer truth top.

(f) $p_T^{\text{t, truth}}$ of softer truth top with active level-1 reference trigger.

Figure 8.8.: Turn-on curves evaluated in simulated allhadronic $t\bar{t}$ events. The `L14J15` is used as a level-1 reference trigger if indicated. The *standard top trigger* chains are shown shown together with a five jet multijet trigger for comparison.

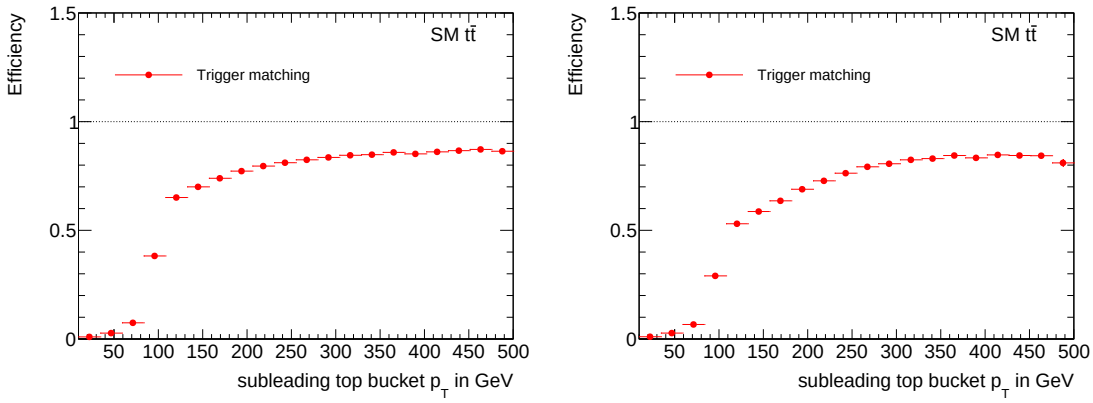

(a) *standard top trigger* (b) *advanced top trigger*

Figure 8.9.: Matching efficiency using $\Delta R(\text{bucket}_i^{\text{HLT}}, \text{bucket}_j^{\text{offline}}) < 0.4$. The top trigger must satisfy $p_T > 100$ GeV in simulated allhadronic $t\bar{t}$ events.

The efficiency is defined for each bin j in the offline variable as

$$\epsilon_T = \frac{N(\text{allhadronic } t\bar{t} \text{ process AND top trigger active})}{N(\text{allhadronic } t\bar{t} \text{ process })} \,. \tag{8.4.1}$$

Compared to the multijet trigger the efficiency increases for the $p_T = 100$ GeV top trigger over the full p_T range. For the $p_T = 150$ GeV ($p_T = 200$ GeV) top trigger the efficiency increases around $p_T \approx 140$ GeV ($p_T \approx 200$ GeV). But only the alternative $p_T = 200$ GeV trigger achieves a trigger rate comparable to the 5-jet reference trigger as shown in Table 8.2. The $p_T = 100$ GeV ($p_T = 150$ GeV) setup increases the rate by a factor of about 7.5 (2.7). All HLT trigger are not reaching a real plateau in the offline top candidate p_T as they rise and fall again above around 300 GeV. This could be related to inefficiencies occurring when the jets start to merge or are very close to each other. As can be seen this effect is also present at the level-1 trigger which seeds the HLT trigger. The efficiency of the level-1 trigger reaches the maximum around $p_T \approx 250$ GeV. At level-1 a much coarser jet reconstruction is applied which is likely to suffer from such high p_T effects [234]. To overcome a bias introduced by level-1 a second efficiency ϵ_T^{L1} is calculated where the level-1 multijet trigger is treated as a reference:

$$\epsilon_T^{\text{L1}} = \frac{N(\text{L1 trigger AND allhadronic } t\bar{t} \text{ AND top trigger })}{N(\text{L1 trigger AND allhadronic } t\bar{t})} \,. \tag{8.4.2}$$

The relevant turn-on-curves are shown in Figure 8.8(c). The ϵ_T^{L1} efficiencies for the *standard top trigger* are reaching a plateau depending on the specific trigger bucket p_T in this setup.

In addition, the offline events can be filtered in order to select events where the online top candidates are likely to be the same as offline. This is achieved

via a geometrical matching in the $\eta - \phi$ plane between the online and offline top candidates. The formula used to define the matching is

$$\Delta R(\mathrm{t}_i^{\mathrm{HLT}}, \mathrm{t}_j^{\mathrm{offline}}) = \sqrt{(\eta_{\mathrm{t}_i^{\mathrm{HLT}}} - \eta_{\mathrm{t}_j^{\mathrm{offline}}})^2 + (\phi_{\mathrm{t}_i^{\mathrm{HLT}}} - \phi_{\mathrm{t}_j^{\mathrm{offline}}})^2} < 0.4 \ . \tag{8.4.3}$$

The corresponding efficiencies using matched trigger objects are presented in Figure 8.8(b) and 8.8(d). For this selection the properties of the *standard top trigger* turn-on curves are further improved and a plateau at 100% efficiency can be reached. On the other hand, this improvement is connected to a loss in acceptance due to a finite matching efficiency $\epsilon_{\mathrm{match}}$. The efficiency is defined for each bin in the studied variable and depending on the preselection as

$$\epsilon_{\mathrm{match}} = \frac{N(\text{preselection AND } \Delta R(\mathrm{t}_i^{\mathrm{HLT}}, \mathrm{t}_j^{\mathrm{offline}}) < 0.4}{N(\text{preselection})} \ . \tag{8.4.4}$$

The matching efficiency is shown as a function of the p_T^{bucket} for the *standard top trigger* with $p_T = 100$ GeV in Figure 8.9(a). The efficiency improves with increasing transverse momentum but stays below 100% reaching up to $\approx 85\%$ above $p_T^{\mathrm{bucket}} > 200$ GeV.

As a cross-check which is relevant for offline analysis the turn-on curves are shown as a function of the softer true top quark p_T in Figure 8.8(e) and 8.8(f). At high true top p_T the efficiency improvement relative to the multijet trigger is smaller compared to the gain at a corresponding top bucket p_T. The shape and plateau properties of the *standard top trigger* as a function of the softer truth top quark are comparable to the corresponding properties as a function of the softer top bucket p_T.

A similar set of studies is performed for the *advanced top trigger* and shown in Figure 8.10. The *advanced top trigger* chains `EMU_tbxx_c1234_5j45_0eta250_L14J15` with selections on the softer top bucket p_T of $p_T > 50, 100, 200$ GeV (`tb50`, `tb100`, `tb200`) are presented. For simplicity only the efficiency ϵ_T^{L1} with activated level-1 trigger is studied. The *advanced top trigger* with $p_T > 200$ GeV does not improve the efficiency relative to the HLT multijet trigger. The *advanced top trigger* chains with the lower p_T threshold result in an efficiency improvement over the full offline p_T^{bucket} and $p_T^{\text{truth top}}$ range but no plateau is reached. The efficiency decreases around $p_T^{\mathrm{bucket}} \approx 350$ GeV. The *advanced top trigger* chains studied are expected to have a comparable or even smaller rate as the 5-jet reference trigger. The corresponding relative rates are summarized in Table 8.3. The difference in efficiency between the *advanced top trigger* chains is reduced if the geometrical matching is used but still no plateau is reached, see Figure 8.10(b). This suggests that the additional online–offline deviations introduced due to the top event grouping are present over the full top p_T range and even larger at higher transverse momentum where the efficiency decreases. This can be understood from the fact that a merging of jets which influences the top event grouping as not all decay products can be resolved is more likely to happen at higher p_T. The efficiency as a function of the true top

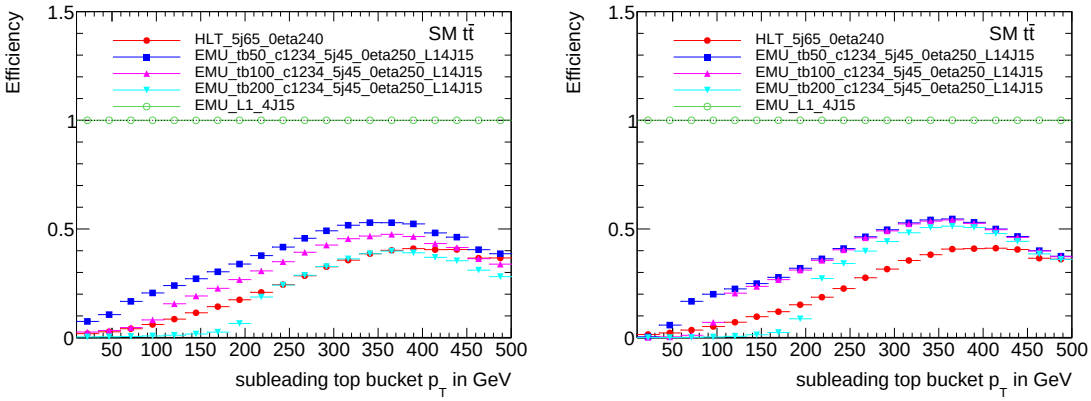

(a) p_T^{bucket} of softer top bucket.

(b) p_T^{bucket} of softer top bucket, trigger matched within $\Delta R < 0.4$.

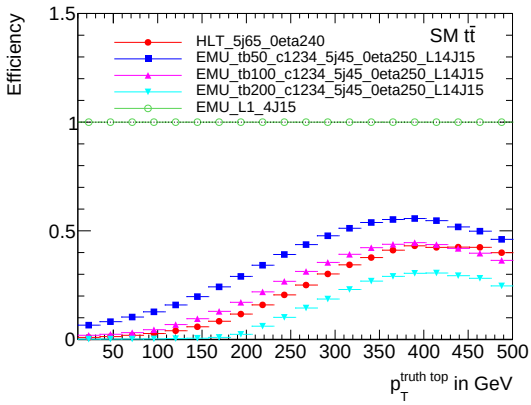

(c) $p_T^{\text{t, truth}}$ of softer truth top.

Figure 8.10.: Turn-on curves evaluated in simulated allhadronic $t\bar{t}$ events. The `L14J15` is used as a level-1 reference trigger. The *advanced top trigger* chains are shown shown together with a five jet multijet trigger for comparison.

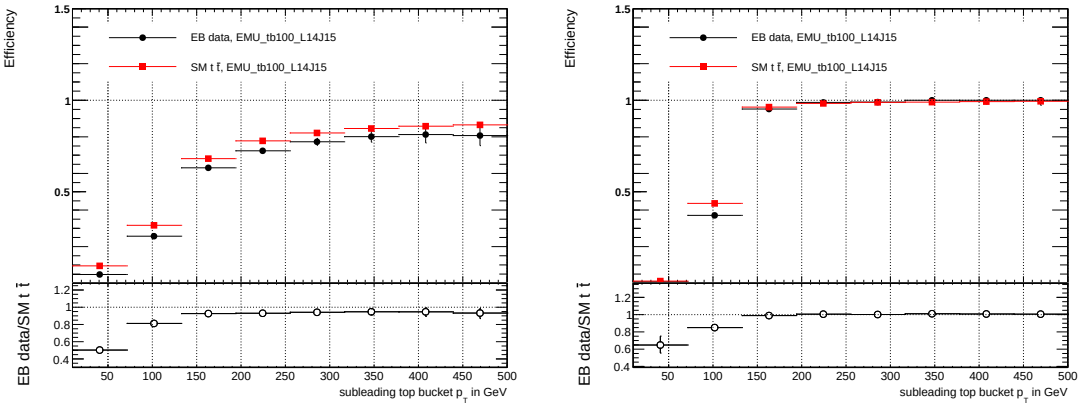

(a) p_T^{bucket} of softer top bucket. (b) p_T^{bucket} of softer top bucket, trigger matched within $\Delta R < 0.4$.

Figure 8.11.: Efficiency of the *standard top trigger* in EB data and simulated all-hadronic $t\bar{t}$ events using the `L14J15` as level-1 reference trigger.

p_T, presented in Figure 8.10(c), shows a small efficiency gain with respect to the HLT multijet trigger for the $p_T^{\text{bucket}} > 50, 100$ GeV setups for the bulk of the true top p_T range. Nevertheless, future analysis dependent offline selections on e.g. the top event categories can again result in an increased efficiency gain. The matching efficiency for the *advanced top trigger* with $p_T = 100$ GeV is shown in Figure 8.9(b). Compared to the *standard top trigger* it is less steep and reaches the plateau later. Also the maximal efficiency is slightly lower.

The emulation of trigger decisions in MC events is limited by the accuracy of the detector description. Deviations from the real performance in data can arise from insufficient modeling of the detector. In addition, background processes present in ATLAS and not simulated in MC can bias the trigger efficiency and alter the uncertainty.

8.4.4. Trigger efficiency using enhanced bias data

The EB mechanism allows studying the trigger efficiency in a data-driven way. Even though, the procedure outlined in the following is suitable to calculate object level efficiencies the event level efficiency can still depend on the topology under consideration.

The bucket algorithm reconstructs the two top quarks simultaneously based on a moderately large multiplicity of Anti-k_T ($R = 0.4$) jets. Due to the fact that low transverse momentum top quarks are targeted the jets are not necessarily collimated and can especially for large jet multiplicities fill up a large area of the detector. Therefore, the method applied in this study to estimate the trigger efficiency is the *bootstrap method* as described in e.g. Reference [184, 235] and Chapter 6.5.

The trigger efficiency in SM allhadronic $t\bar{t}$ MC $pp \to t_h t_h$ and in EB data is shown in Figure 8.11(a). It is based on the selection of four trigger towers with $E_T > 15$

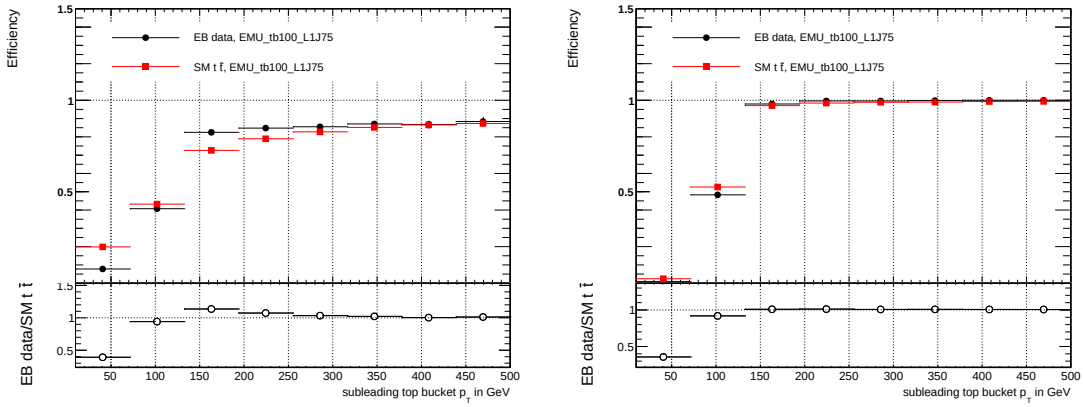

(a) p_T^{bucket} of softer top bucket. (b) p_T^{bucket} of softer top bucket, trigger matched within $\Delta R < 0.4$.

Figure 8.12.: Efficiency of the *standard top trigger* in EB data and simulated all-hadronic $t\bar{t}$ events using the `L1J75` as level-1 reference trigger.

GeV at level-1 (`L14J15`) as reference trigger in the *bootstrap method*. It is shown as a function of the transverse momentum of the subleading (softer) top bucket which is reconstructed from offline jets. The efficiency measured in data is slightly below the MC efficiency over the full p_T range. Below $p_T < 140$ GeV larger deviations are present with a MC efficiency twice as large as the data efficiency for the lowest p_T bin. In this low p_T regime the differences could be caused by an incorrect emulation of the level-1 trigger objects.

In a cross check study the efficiencies are investigated for matched trigger objects. Thereby, the online and offline top candidates are geometrically matched in the $\eta-\phi$ plane. This comes at the cost of a reduced overall efficiency due to the not fully efficient matching as shown in Figure 8.9. The ΔR value to consider the matching successful is chosen as

$$\Delta R(\mathrm{t}_i^{\mathrm{HLT}}, \mathrm{t}_j^{\mathrm{offline}}) < 0.4 \ . \tag{8.4.5}$$

Even though this accuracy measurement is purely geometrical and does not directly affect the p_T the data–MC efficiency agrees better over the whole p_T range after selecting only matched events, see Figure 8.11(b). This suggests that the data–MC efficiency differences are mainly caused by events where the top quark reconstruction fails. Insufficient information available at the high-level trigger stage can result in such imperfect top quark reconstruction. A more sophisticated jet collection at HLT could then possibly also improve the data–MC agreement. On the other hand, in the current setup such a matching procedure would bring disadvantaged due to the reduced acceptance introduced by the matching efficiency of $\approx$ 85% in the plateau.

The topology dependence of the above mentioned trigger efficiencies is studied as a cross check. For this purpose a single jet trigger is used to select events at

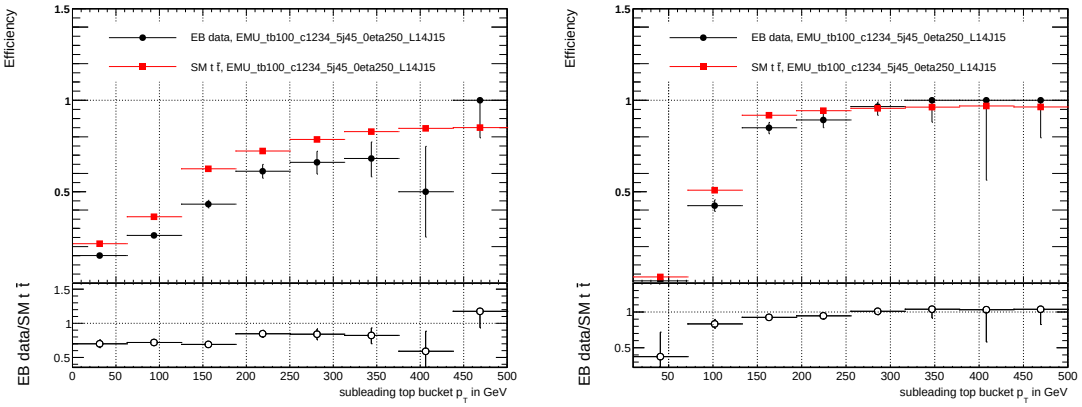

(a) p_T^{bucket} of softer top bucket. (b) p_T^{bucket} of softer top bucket, trigger matched within $\Delta R < 0.4$.

Figure 8.13.: Efficiency of the *advanced top trigger* in EB data and simulated all-hadronic $t\bar{t}$ events using the `L14J15` as level-1 reference trigger. A cut of $p_T > 55$ GeV is applied on the fifth hardest reconstructed offline jet.

level-1. A level-1 jet which satisfies a transverse energy threshold of $E_T > 75$ GeV is required (`L1J75`). This selection solely serves as a cross-check to the standard selection with four trigger towers with $E_T > 15$ GeV at level-1 (`L14J15`). The efficiency for the topology scenario based on the single jet trigger (`L1J75`) is shown in Figure 8.12. Small deviations are present which decrease with increasing p_T of the top candidates. Matching the online and offline top buckets within $\Delta R < 0.4$ results in an improved agreement consistent with the observation made with the level-1 multijet trigger. This supports that the result of the efficiency measured in data is relatively stable and has a small topology dependence.

The *advanced top trigger* combining the p_T information with the mass reconstruction of the top quarks and the constituents of the top quark decay is studied in data too. The effects originating from incorrect emulation of the HLT multijet trigger are reduced by requiring $p_T > 55$ GeV for the fifth hardest reconstructed offline jet. The data efficiency as shown in Figure 8.13(a) is systematically below the MC efficiency. The geometrical matching between online and offline top buckets within $\Delta R < 0.4$ results in a better agreement, see Figure 8.13(b). The background rejection for this trigger is higher. This is achieved by making further use of $t\bar{t}$ specific selection. Therefore, it is expected that SM $t\bar{t}$ MC–data differences are more pronounced. The main differences should correspond to the requirement of top event categories corresponding to a set of selections on the top quark candidate mass.

In addition, the efficiency dependence on the offline selection on the event categories can be studied. But such selections significantly increase the statistical uncertainties which already start to dominate the comparison. Therefore, the enhanced bias mechanism is not the best testing ground for a deeper study of the data–MC agreement. In a future iteration a support trigger similar to the HLT

Type	Trigger	Ratio
Reference	HLT_5j65_0eta240	1.0
Alternative	EMU_tb50	21.64(62)
	EMU_tb100	7.48(22)
	EMU_tb150	2.68(9)
	EMU_tb200	1.13(4)
In addition	EMU_tb50 AND HLT_5j65_0eta240	0.86(4)
	EMU_tb100 AND HLT_5j65_0eta240	0.54(3)
	EMU_tb150 AND HLT_5j65_0eta240	0.27(2)
	EMU_tb200 AND HLT_5j65_0eta240	0.12(1)

Table 8.2.: Estimate of the trigger rates. The Ratio of the rate of several trigger chains to the rate of the unprescaled five jet (5j) multijet trigger is listed for the *standard top trigger*. The emulated (EMU) trigger chains based on the bucket algorithm are indicated by tb followed by the minimal transverse momentum of the top buckets in GeV .

multijet trigger with a prescale could be used to measure the efficiencies in data. As this is very analysis dependent, the efficiency measurement based on support triggers is not further pursued in this feasibility study.

8.4.5. Estimation of the trigger rates

Every improvement in acceptance for $t\bar{t}$ events has to be considered in the context of an eventual simultaneous increase of the trigger rates. The HLT multijet trigger with five jets and $p_T > 65$ GeV and $|\eta| < 2.4$ was unprescaled at level-1 and HLT during the full 2016 ATLAS data taking period with instantaneous luminosities up to $1.4 \times 10^{34}\text{cm}^{-1}\text{s}^{-1}$. For a peak luminosity of $1.2 \times 10^{34}\text{cm}^{-1}\text{s}^{-1}$ it provides a level-1 rate of 2200 Hz and a HLT rate of 11.1 Hz. This HLT multijet trigger chain is anticipated to remain unprescaled even for higher peak luminosities up to $1.7 \times 10^{34}\text{cm}^{-1}\text{s}^{-1}$. As it shares the unprescaled level-1 trigger with the top trigger studied and as it is available in the EB dataset the expected trigger rates can be estimated relative to it. The level-1 rate cannot be increased by the new top trigger. To calculate the rate all events are preselected to have an active level-1 multijet trigger with at least four trigger towers with $E_T > 15$ GeV. The estimated rate is than quantified by the ratio of events selected by the top trigger to the events selected by the HLT multijet reference trigger. The expected rates for the *standard top trigger* with respect to the unprescaled multijet trigger are summarized in Table 8.2. The rate of the alternative *standard top trigger* chains is higher than the rate of the HLT reference trigger. For the *standard top trigger* with $p_T > 200$ GeV the rate would be almost identical to the HLT multijet trigger rate. A rate reduction can still be achieved by combining the reference trigger with the *standard*

Trigger	Ratio
HLT_5j65_0eta240	1.0
EMU_tb50_c1234_5j45_0eta250_L14J15	2.91(9)
EMU_tb100_c1234_5j45_0eta250_L14J15	1.22(5)
EMU_tb150_c1234_5j45_0eta250_L14J15	0.44(2)
EMU_tb200_c1234_5j45_0eta250_L14J15	0.17(1)
EMU_5j45_0eta250_L14J15 AND EMU_12j25_0eta250_L14J15	0.03(0)
EMU_5j45_0eta250_L14J15 AND EMU_11j25_0eta250_L14J15	0.08(1)
EMU_5j45_0eta250_L14J15 AND EMU_10j25_0eta250_L14J15	0.24(2)
EMU_12j25_0eta250_L14J15	0.03(1)
EMU_11j25_0eta250_L14J15	0.12(1)
EMU_10j25_0eta250_L14J15	0.40(2)

Table 8.3.: Estimate of the trigger rates. The Ratio of the rate of several trigger chains to the rate of the unprescaled five jet (5j) multijet trigger is listed for the *advanced top trigger*. In addition, the rate ratios for several emulated high multiplicity multijet trigger chains are shown. The emulated (EMU) trigger chains based on the bucket algorithm are indicated by tb followed by the minimal transverse momentum of the top buckets in GeV. In addition, the event categories are indicated by c1234 corresponding to (t_w, t_w), (t_w, t_-), (t_-, t_w) and (t_-, t_-) as described in Chapter 8.4.2.

top trigger. The corresponding $p_T > 100$ GeV setup would reduce the rate by 50%.

A significant rate reduction is provided by the *advanced top trigger* as shown in Table 8.3. An *advanced top trigger* with $p_T > 100$ GeV gives a rate of a similar size as the HLT multijet trigger. Any further increase in the p_T threshold reduces the rate e.g. to a fraction of 0.17 ± 0.01 at $p_T > 200$ GeV.

8.4.6. Processing time

The CPU consumption is crucial for any HLT trigger chain. In this study the processing time is evaluated on a separate CPU and not under real data taking conditions to give a basic estimate. The CPU time is estimated via a timer functionality introduced in the analysis code. The top reconstruction has to run after the construction of the jet collection input. The CPU times estimated in this chapter have to be added to this.

The corresponding results are presented in Figure 8.14. The timing performance is investigated separately for a low jet multiplicity environment in the EB dataset

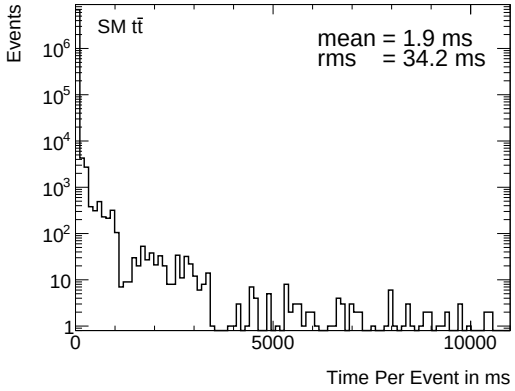

(a) Time per Event in simulated $t\bar{t}$ events.

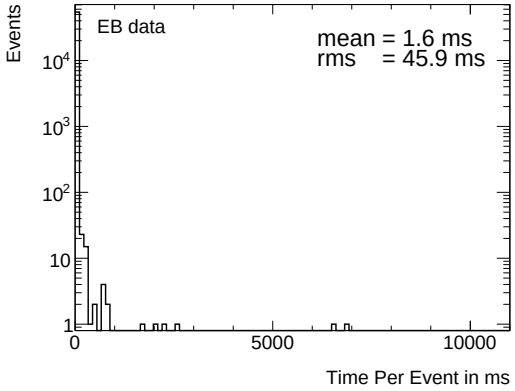

(b) Time per Event in EB data.

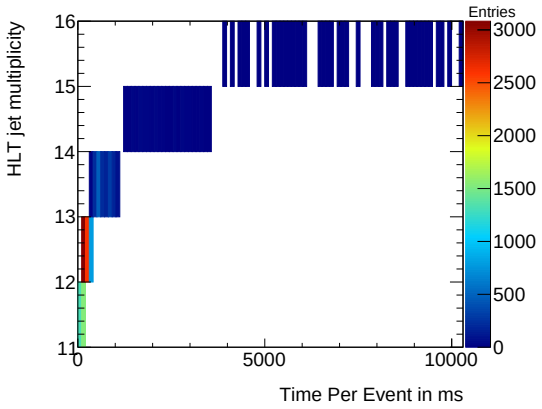

(c) Time per Event against HLT jet multiplicity in simulated $t\bar{t}$ events. Only events with a processing time longer than 100 ms are shown.

Figure 8.14.: CPU Time for top bucket grouping per event evaluated in allhadronic $t\bar{t}$ events and enhanced bias data.

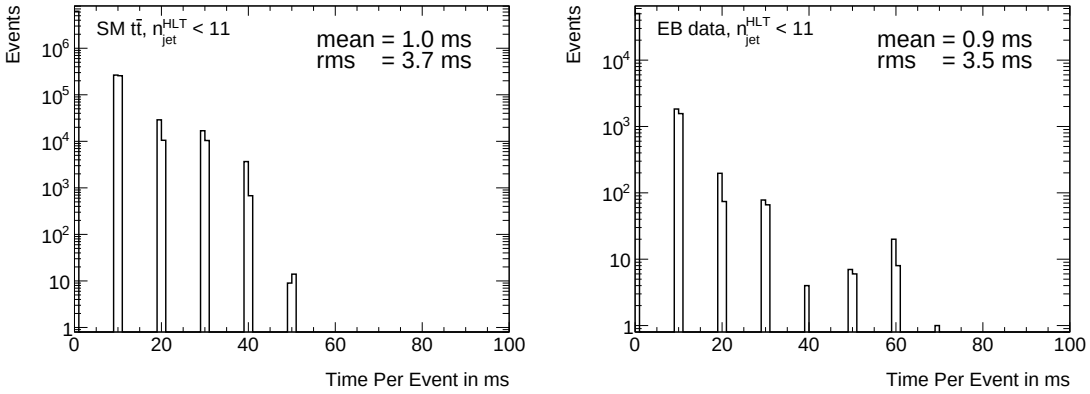

(a) Time per Event in simulated $t\bar{t}$.

(b) Time per Event in EB dataset.

Figure 8.15.: CPU Time for top bucket grouping per event evaluated in allhadronic $t\bar{t}$ events and enhanced bias data. In addition only events with $n_{\text{jet}}^{\text{HLT}} < 11$ are accepted for the reconstruction.

and for a high jet multiplicity environment in the SM $t\bar{t}$ MC sample. The mean CPU time increases from 1.6 ms in the EB dataset to 1.9 ms in simulated $t\bar{t}$ events. The bucket algorithm depends on the possible combinations of jets. Therefore, the processing time is a discrete function of jet multiplicity. A complication arises from the fact that the reconstruction is performed in two coupled steps. This results in a nonlinear dependence of the reconstruction time on the jet multiplicity. Higher jet multiplicities tend to increase the processing time as observed for the SM $t\bar{t}$ events compared to the EB dataset. Most relevant in the timing distribution are the tails as they can delay the data taking system. The processing times larger than 100 ms are caused by events with more than 10 jets as shown Figure 8.14(c).

The jet multiplicity distribution is steeply falling in background events. Hence, it is possible to accept events with a high jet multiplicity without significantly increasing the trigger rates as supported by the relative multijet rates in Table 8.3. So the time expensive top reconstruction is not necessary for these events and the tails are cut off. The timing performance is shown for the specific selection where only events with less than 11 jets are taken into account in Figure 8.15. The mean CPU time is reduced to 0.9 ms in EB data and 1.0 ms in simulated $t\bar{t}$ events respectively. The maximal CPU time stays well below 200 ms which characterizes the average HLT decision time [100]. Future improvements on the underlying code structure of the bucket algorithm can further reduce the CPU time.

8.5. Outlook on future improvements

As discussed in Chapter 8.4.1 the online and offline jets are differing by the calibration procedure used. Applying the same cuts this can result in inefficiencies in the context of the top quark reconstruction. Adjusting the online calibration to offline

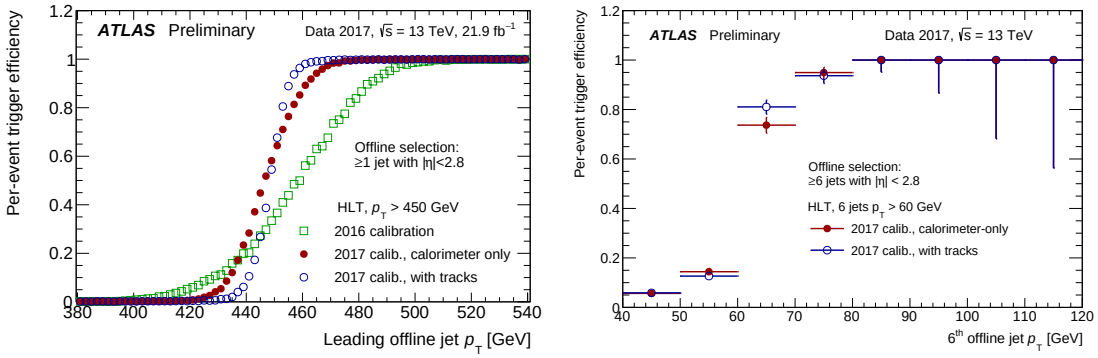

(a) Efficiencies for an unprescaled single-jet trigger, from [19].

(b) Efficiencies for an unprescaled 6-jet trigger, from [237].

Figure 8.16.: Efficiencies for unprescaled ATLAS high level triggers. Three different types of calibrations are applied on the jets. Taken from Reference [19, 237].

should improve the agreement of the top quark transverse momentum distribution as well as the grouping in event categories based on the mass window selection. Using 2016 and 2017 data taking several calibration updates are tested on the HLT level as described in References [18, 19]. This involves the introduction of jet global sequential corrections (GSC) [154] and several in-situ corrections making use of a data-driven determination of the energy scale and the resolution of jets [236].

The GSC is based on the longitudinal shower shape and track information associated to a jet. Tracks are available at HLT from dedicated region of interest tracking executed in the context of the flavor tagging trigger chains as explained in Reference [100]. As the tracks are only available for jets above a certain p_T threshold the updated online calibrations are tested with and without the track component. The HLT calibration configurations are compared in Figure 8.16 for a single jet and a multijet trigger chain. In both trigger chains the resolution is improved resulting in a steeper turn-on curve.

Offline, a suppression of pure pileup jets with $p_T < 60$ GeV and $|\eta| < 2.4$ is achieved by the Jet Vertex Tagger (JVT) requirement [158] which exploits information from associating tracks to jets. The JVT relies on global track information. Therefore it cannot directly be used online. In the future this could be solved by the FastTracker (FTK) trigger system [208] which performs a global track reconstruction at the beginning of the HLT. In addition, the FTK would allow the usage of the tracking information for lower jet transverse momentum thresholds too.

8.6. Summary

Performing a reconstruction based on the bucket algorithm at trigger level could help to maintain acceptable trigger rates for multijet trigger chains. Such multijet

trigger chains are essential for many analysis characterized by an allhadronic $t\bar{t}$ final state and a moderate transverse momentum of the involved jets. Therefore, the bucket algorithm is tested at the high-level trigger level. By construction the method is relatively agnostic to the topology of the $t\bar{t}$ decay and the availability of the products of the $t\bar{t}$ decay in terms of jets. Also extra hadronic activity, originating from e.g. initial state radiation, in an event is considered. The top quark pair is reconstructed in a two step procedure leading to a discrete set of top event categories based on mass window selections. As a consequence it is flexible and also relatively fast. These properties make the bucket algorithm well suited to be tested at trigger level. The differences between the information available online and offline requires to adapt the bucket algorithm. The modified version is independent of the b-tagging identification. However, the relevant performance on benchmark signal models is compatible with the default version.

In particular, the transverse momentum of the softer top bucket provides a promising variable for the construction of trigger chains. Corresponding trigger chains are referred to as *standard top trigger*. In addition, the *advanced top trigger* chains rely on the event categorization of the bucket algorithm. Inconsistencies in online and offline jets are observed. The trigger efficiencies are studied in simulated events. The *standard top trigger* can help to enhance the selection of top quark pairs compared to the multijet trigger that is used in e.g. the $t\bar{t}$ resonance analysis. Depending on the transverse momentum selection of the top buckets at HLT level, the *advanced top trigger* can improve the $t\bar{t}$ selection too. The latter is also expected to improve the selection of $t\bar{t}$ events in which a full reconstruction of the $t\bar{t}$ system is feasible. A comparison of the efficiencies in data and simulation confirms that the efficiencies are well modeled for high enough transverse momenta of the top buckets e.g. above around 100 GeV for the *standard top trigger* with $p_T^{\text{bucket}} > 100$ GeV at trigger level. The *standard top trigger* is largely independent on assumptions with respect to the topology of the $t\bar{t}$ decay. Generally, this trigger chain can also be used in an analysis relying on other $t\bar{t}$ reconstruction methods at offline level than the bucket algorithm.

Depending on the configuration, the rates of the emulated trigger chains alone can compete with the reference multijet trigger chain. The emulated and the multijet trigger chains can also be combined in order to reduce the overall trigger rates. The relative rate for a top bucket trigger with transverse momentum larger than 200 GeV at trigger level which is combined with the reference multijet trigger is reduced to a fraction of 0.12. The study of the CPU consumption and the intrinsic rate reduction show that an application of the newly emulated trigger chains in ATLAS is feasible.

9. Conclusion

In this thesis the reconstruction of top quark pairs based on small radius, i.e. Anti-k_T ($R = 0.4$), jets is investigated using proton-proton collision data at a center of mass energy of 13 TeV recorded in 2015 and 2016 by the ATLAS experiment at the LHC. The studies focus on the $t\bar{t}$ decay channel that is characterized by a fully hadronic decay of the top quark system. This channel has to deal with the overwhelming background of QCD multijet production. The construction of small-R jets in an experimental environment such as in the ATLAS experiment requires a selection on the minimal transverse momentum of these jets. Therefore, the $t\bar{t}$ decay topology can often only be partially reconstructed. In such scenarios the bucket algorithm [16, 214] provides an efficient approach to reconstruct the $t\bar{t}$ pairs. The bucket algorithm targets the transverse momentum range from around 100 GeV to 400 GeV of the top quarks. The performance of the bucket algorithm is validated in ATLAS specific simulations and data recorded at a center of mass energy of 13 TeV in 2015 and 2016 at ATLAS. It allows the reconstruction of the four momenta of the top quarks in the fully hadronic decay mode and the suppression of the QCD multijet background. The bucket algorithm is investigated and applied in three analyses.

A search for new heavy particles decaying into top quark pairs in the fully hadronic decay mode is performed using a dataset with an integrated luminosity of 36.1 fb^{-1} recorded in pp collisions at $\sqrt{s} = 13$ TeV in 2015 and 2016 by ATLAS. The event selection is based on an unprescaled multijet trigger requiring five jets. Moderately boosted top quark pair candidates with transverse momenta above 200 GeV are identified and reconstructed by the bucket algorithm. The analysis is optimized depending on the expected sensitivity and targets the mass range of the $t\bar{t}$ system from 500 GeV to around 1250 GeV. No excess or deficit from the Standard Model prediction is observed. Upper limits on the production cross section times branching ratio are set at 95% confidence level for the topcolor assisted technicolor model Z'_{TC2}, the mediators Z'_{med} in simplified dark matter models, Kaluza-Klein excitations of the gluon g_{KK} in the Randall–Sundrum model and Kaluza-Klein excitations of the graviton G_{KK} in the *bulk* Randall–Sundrum model of warped extra dimensions. The first search for resonant $t\bar{t}$ production in the allhadronic decay channel at $\sqrt{s} = 13$ TeV at low invariant masses is presented in this thesis. The analysis establishes a double sideband likelihood method for the estimation of the QCD multijet background and the hypothesis test. The corresponding search in the lepton–plus–jets $t\bar{t}$ decay mode at $\sqrt{s} = 13$ TeV at ATLAS achieves a higher sensitivity in that mass range [59]. At low mass of the Z'_{TC2} of 500 GeV the observed upper limits of the analysis in the lepton–plus–jets channel are significantly

better by about 97%. In the mass range from 750 GeV to 1250 GeV they are better by around 40% to 60% and for a G_{KK} of 750 GeV the difference is only 13%. Nevertheless, the two channels are fully orthogonal and a future combination can improve the limits. The results of the fully hadronic $t\bar{t}$ resonance search which is presented in this thesis are currently prepared for publication. In this context an additional top reconstruction procedure is used to increase the sensitivity over a wider range of masses. The search based on the bucket algorithm complements the other approach which focuses on higher masses of the $t\bar{t}$ system. The optimization of the analysis presented for the multijet trigger and the excellent usage of the small-R jets by the bucket algorithm results in a better performance in the low mass range.

In the second analysis the associated production of a Higgs Boson with a top quark pair in the fully hadronic final state is investigated in simulation and 32.8 fb^{-1} of pp collision data. The data was recorded in 2016 at $\sqrt{s} = 13$ TeV by ATLAS. The event selection uses an unprescaled multijet trigger that requires five jets. The analysis focuses on the subsequent decay of the Higgs boson to a pair of bottom quarks. Despite the high multiplicities of jets and b-tagged jets the bucket algorithm can reconstruct the $t\bar{t}$ system and provide a candidate for the Higgs boson as proposed in Reference [214]. The relatively low transverse momentum of the top quarks and the large QCD multijet background causes a large combinatorial background. In this proof of concept analysis it is shown that the bucket algorithm can extract the signal of the $t\bar{t}H$ production. The background suppression based on the bucket algorithm and variables constructed from the jets is studied in a multivariate analysis. Using the shape of the multivariate discriminant improves the expected sensitivity. Nevertheless, an observation of $t\bar{t}H$ in this fully hadronic channel alone is not feasible with the dataset studied. Such a 5σ observation would require at least 950 fb^{-1} of data. In Reference [213] it was shown using a dataset collected at $\sqrt{s} = 8$ TeV that the sensitivity of the allhadronic channel is generally smaller than the other $t\bar{t}H$ decay channels also if the systematic uncertainties are included. However, a combination of the allhadronic $t\bar{t}H$ decay mode with other orthogonal channels can help to improve the measurement of $t\bar{t}H$. The high b-tagged jet multiplicity allows for the usage of b-tagging at trigger level [17, 18, 100, 206, 207] in order to optimize the analysis.

Furthermore, in a trigger optimization study the bucket algorithm motivates the construction of new trigger chains based on jets that are reconstructed at trigger level. The performance of the new trigger chains is evaluated in simulation and in an enhanced bias dataset that has an average number of interactions per bunch crossing of around 36. The new trigger chains can improve the selection efficiency of events corresponding to a topology of the $t\bar{t}$ decay in the transverse momentum regime that is targeted by the bucket algorithm. The simulation describes the trigger efficiencies measured in data well for moderately boosted top quark candidates. In addition, an offline prediction of the anticipated rate and CPU usage is derived indicating that a future application in the ATLAS trigger system is feasible. Such an application can profit from updated calibrations of jets and the availability of

tracking information at trigger level [19, 100, 208]. The new trigger chains can help to improve trigger strategies based on multijets for events with a $t\bar{t}$ topology or to maintain the selection capabilities for such topologies in future data taking periods characterized by higher luminosities.

Developments in the reconstruction procedure and calibration of jets or in the b-tagging techniques are likely to translate to a better performance of the bucket algorithm. Especially at higher luminosities of the LHC, the performance of the trigger is crucial for the usage of the search channel presented. Combining the results of the study at trigger level and the analyses described above can contribute to improvements of the selection of $t\bar{t}$ pairs in the fully hadronic decay mode at low transverse momenta of the top quarks.

Acknowledgments

First of all, I would like to thank my supervisor Prof. Dr. André Schöning for his continuous motivating guidance and for introducing the interesting topic of top quark physics to me which eventually resulted in this thesis. I would also like to express my sincere gratitude to Prof. Dr. Tilman Plehn for acting as second referee. I am grateful to Prof. Dr. Björn Malte Schäfer and Prof. Dr. Hans-Christian Schultz-Coulon for completing my examination committee.

Further, I am thankful to Dr. Christoph Anders for his very capable and ever-patient support during the course of this thesis. I would like to thank Dr. Danilo Ferreira de Lima for his constant support full of expertise. A special thanks goes to Arthur Bolz and Dr. Misha Lisovyi. It was a great time sharing the office with them for a long period during my thesis.

I benefited greatly from the wonderful working atmosphere provided by the former and current members of the ATLAS group in Heidelberg, especially Dr. Maddalena Giulini, Tamasi Kar, Dr. Tatsiana Klimkovich, Anjali Krishnan, Dr. Rohin Narayan, Christof Sauer, Priv.-Doz. Dr. Sebastian Schätzel, Dr. David Sosa and Dr. Jike Wang. Finally, I'd like to cordially thank my family and friends for their support.

A. Multivariate analysis in the search for the SM Higgs boson in association with top quarks

A.1. Correlations between input variables

The linear correlation coefficients of data in the CR and the SR as well as the corresponding ratio is shown in Figure A.1.

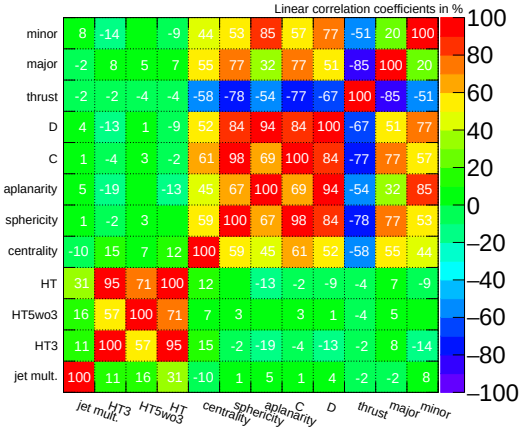

(a) Data CR

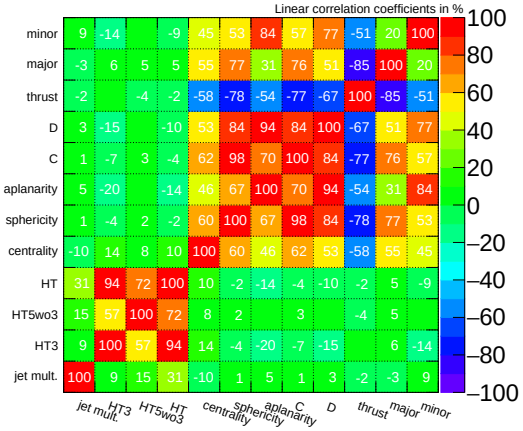

(b) Data SR

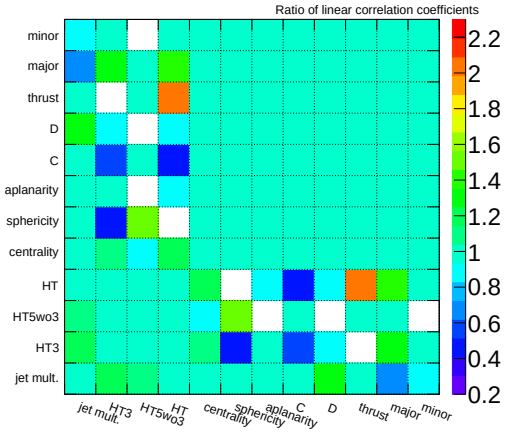

(c) Ratio CR/SR

Figure A.1.: Input variables linear correlation coefficients. The linear correlations between the input variables are calculated in the CR and the SR using data. Afterwards the ratio CR/SR is calculated. If the correlation is close to zero in both regions the ratio is not shown (white boxes) to facilitate the visualization.

Bibliography

[1] Sheldon L. Glashow. "Partial-symmetries of weak interactions". In: *Nuclear Physics* 22.4 (1961), pp. 579 –588. ISSN: 0029-5582. DOI: https://doi.org/10.1016/0029-5582(61)90469-2. URL: http://www.sciencedirect.com/science/article/pii/0029558261904692.

[2] Steven Weinberg. "A Model of Leptons". In: *Phys. Rev. Lett.* 19 (21 Nov. 1967), pp. 1264–1266. DOI: 10.1103/PhysRevLett.19.1264. URL: https://link.aps.org/doi/10.1103/PhysRevLett.19.1264.

[3] Abdus Salam. "Weak and Electromagnetic Interactions". In: *Elementary particle theory. Relativistic groups and analyticity.* Proceedings of the Eighth Nobel Symposium. (Aspenäsgarden, Lerum, May 19–25, 1968). Ed. by Nils Svartholm. Stockholm: Almquist & Wiksell, 1968, pp. 367–377.

[4] G. 't Hooft and M. Veltman. "Regularization and renormalization of gauge fields". In: *Nuclear Physics B* 44.1 (1972), pp. 189 –213. ISSN: 0550-3213. DOI: https://doi.org/10.1016/0550-3213(72)90279-9. URL: http://www.sciencedirect.com/science/article/pii/0550321372902799.

[5] Peter W. Higgs. "Broken symmetries, massless particles and gauge fields". In: *Phys. Lett.* 12 (1964), pp. 132–133. DOI: 10.1016/0031-9163(64)91136-9.

[6] Peter W. Higgs. "Broken Symmetries and the Masses of Gauge Bosons". In: *Phys. Rev. Lett.* 13 (1964). [,160(1964)], pp. 508–509. DOI: 10.1103/PhysRevLett.13.508.

[7] F. Englert and R. Brout. "Broken Symmetry and the Mass of Gauge Vector Mesons". In: *Phys. Rev. Lett.* 13 (1964). [,157(1964)], pp. 321–323. DOI: 10.1103/PhysRevLett.13.321.

[8] Georges Aad et al. "Observation of a new particle in the search for the Standard Model Higgs boson with the ATLAS detector at the LHC". In: *Phys.Lett.* B716 (2012), pp. 1–29. DOI: 10.1016/j.physletb.2012.08.020. arXiv: 1207.7214 [hep-ex].

[9] Serguei Chatrchyan et al. "Observation of a new boson at a mass of 125 GeV with the CMS experiment at the LHC". In: *Phys.Lett.* B716 (2012), pp. 30–61. DOI: 10.1016/j.physletb.2012.08.021. arXiv: 1207.7235 [hep-ex].

[10] Johannes Erdmann et al. “A likelihood-based reconstruction algorithm for top-quark pairs and the KLFitter framework”. In: *Nucl. Instrum. Meth.* A748 (2014), pp. 18–25. DOI: 10.1016/j.nima.2014.02.029. arXiv: 1312.5595 [hep-ex].

[11] Michael H. Seymour. “Searches for new particles using cone and cluster jet algorithms: A Comparative study”. In: *Z.Phys.* C62 (1994), pp. 127–138. DOI: 10.1007/BF01559532.

[12] Tilman Plehn and Michael Spannowsky. “Top Tagging”. In: *J.Phys.* G39 (2012), p. 083001. DOI: 10.1088/0954-3899/39/8/083001. arXiv: 1112.4441 [hep-ph].

[13] A. Abdesselam, E. Bergeaas Kuutmann, U. Bitenc, G. Brooijmans, J. Butterworth, et al. “Boosted objects: A Probe of beyond the Standard Model physics”. In: *Eur.Phys.J.* C71 (2011), p. 1661. DOI: 10.1140/epjc/s10052-011-1661-y. arXiv: 1012.5412 [hep-ph].

[14] A. Altheimer, S. Arora, L. Asquith, G. Brooijmans, J. Butterworth, et al. “Jet Substructure at the Tevatron and LHC: New results, new tools, new benchmarks”. In: *J.Phys.* G39 (2012), p. 063001. DOI: 10.1088/0954-3899/39/6/063001. arXiv: 1201.0008 [hep-ph].

[15] Sebastian Schätzel. “Boosted Top Quarks and Jet Structure”. In: *Eur. Phys. J.* C75.9 (2015), p. 415. DOI: 10.1140/epjc/s10052-015-3636-x. arXiv: 1403.5176 [hep-ex].

[16] Matthew R. Buckley, Tilman Plehn, and Michihisa Takeuchi. “Buckets of Tops”. In: *JHEP* 1308 (2013), p. 086. DOI: 10.1007/JHEP08(2013)086. arXiv: 1302.6238 [hep-ph].

[17] *2015 start-up trigger menu and initial performance assessment of the ATLAS trigger using Run-2 data*. Tech. rep. ATL-DAQ-PUB-2016-001. Geneva: CERN, Mar. 2016. URL: https://cds.cern.ch/record/2136007.

[18] *Trigger Menu in 2016*. Tech. rep. ATL-DAQ-PUB-2017-001. Geneva: CERN, Jan. 2017. URL: https://cds.cern.ch/record/2242069.

[19] *Trigger Menu in 2017*. Tech. rep. ATL-DAQ-PUB-2018-002. Geneva: CERN, June 2018. URL: http://cds.cern.ch/record/2625986.

[20] ATLAS Collaboration. *Technical Design Report for the Phase-II Upgrade of the ATLAS TDAQ System*. Tech. rep. CERN-LHCC-2017-020. ATLAS-TDR-029. Geneva: CERN, Sept. 2017. URL: https://cds.cern.ch/record/2285584.

[21] ATLAS Collaboration. *Public Luminosity Results*. June 2018. URL: https://twiki.cern.ch/twiki/bin/view/AtlasPublic/LuminosityPublicResults (visited on 09/06/2018).

[22] Tilman Plehn. “Lectures on LHC Physics”. In: *Lect. Notes Phys.* 844 (2012), pp. 1–193. DOI: 10.1007/978-3-642-24040-9. arXiv: 0910.4182 [hep-ph].

[23] C. Englert et al. “Precision Measurements of Higgs Couplings: Implications for New Physics Scales”. In: *J. Phys.* G41 (2014), p. 113001. DOI: 10.1088/0954-3899/41/11/113001. arXiv: 1403.7191 [hep-ph].

[24] C. Patrignani et al. “Review of Particle Physics”. In: *Chin. Phys.* C40.10 (2016), p. 100001. DOI: 10.1088/1674-1137/40/10/100001.

[25] Guido Altarelli and G. Parisi. “Asymptotic Freedom in Parton Language”. In: *Nucl. Phys.* B126 (1977), pp. 298–318. DOI: 10.1016/0550-3213(77)90384-4.

[26] V. N. Gribov and L. N. Lipatov. “Deep inelastic e p scattering in perturbation theory”. In: *Sov. J. Nucl. Phys.* 15 (1972). [Yad. Fiz.15,781(1972)], pp. 438–450.

[27] Yuri L. Dokshitzer. “Calculation of the Structure Functions for Deep Inelastic Scattering and e+ e- Annihilation by Perturbation Theory in Quantum Chromodynamics.” In: *Sov. Phys. JETP* 46 (1977). [Zh. Eksp. Teor. Fiz.73,1216(1977)], pp. 641–653.

[28] F. D. Aaron et al. “Combined Measurement and QCD Analysis of the Inclusive e+- p Scattering Cross Sections at HERA”. In: *JHEP* 01 (2010), p. 109. DOI: 10.1007/JHEP01(2010)109. arXiv: 0911.0884 [hep-ex].

[29] sherpa.hepforge.org. *Monte Carlo event generators*. Aug. 2018. URL: http://sherpa.hepforge.org/event.png (visited on 08/27/2018).

[30] Gavin P. Salam. “Elements of QCD for hadron colliders”. In: *High-energy physics. Proceedings, 17th European School, ESHEP 2009, Bautzen, Germany, June 14-27, 2009*. 2010. arXiv: 1011.5131 [hep-ph]. URL: https://inspirehep.net/record/880643/files/arXiv:1011.5131.pdf.

[31] R. Keith Ellis, W. James Stirling, and B. R. Webber. “QCD and collider physics”. In: *Camb. Monogr. Part. Phys. Nucl. Phys. Cosmol.* 8 (1996), pp. 1–435.

[32] Bo Andersson, G. Gustafson, G. Ingelman, and T. Sjostrand. “Parton Fragmentation and String Dynamics”. In: *Phys. Rept.* 97 (1983), pp. 31–145. DOI: 10.1016/0370-1573(83)90080-7.

[33] Jan-Christopher Winter, Frank Krauss, and Gerhard Soff. “A Modified cluster hadronization model”. In: *Eur. Phys. J.* C36 (2004), pp. 381–395. DOI: 10.1140/epjc/s2004-01960-8. arXiv: hep-ph/0311085 [hep-ph].

[34] Gerald C. Blazey et al. “Run II jet physics”. In: *QCD and weak boson physics in Run II. Proceedings, Batavia, USA, March 4-6, June 3-4, November 4-6, 1999*. 2000, pp. 47–77. arXiv: hep-ex/0005012 [hep-ex]. URL: http://lss.fnal.gov/cgi-bin/find_paper.pl?conf-00-092.

[35] Gavin P. Salam. “Towards Jetography”. In: *Eur. Phys. J.* C67 (2010), pp. 637–686. DOI: 10.1140/epjc/s10052-010-1314-6. arXiv: 0906.1833 [hep-ph].

[36] Matteo Cacciari, Gavin P. Salam, and Gregory Soyez. "The Anti-k(t) jet clustering algorithm". In: *JHEP* 04 (2008), p. 063. DOI: 10.1088/1126-6708/2008/04/063. arXiv: 0802.1189 [hep-ph].

[37] Matteo Cacciari, Gavin P. Salam, and Gregory Soyez. "The Catchment Area of Jets". In: *JHEP* 0804 (2008), p. 005. DOI: 10.1088/1126-6708/2008/04/005. arXiv: 0802.1188 [hep-ph].

[38] Matteo Cacciari, Gavin P. Salam, and Gregory Soyez. "FastJet User Manual". In: *Eur.Phys.J.* C72 (2012), p. 1896. DOI: 10.1140/epjc/s10052-012-1896-2. arXiv: 1111.6097 [hep-ph].

[39] Matteo Cacciari and Gavin P. Salam. "Dispelling the N^3 myth for the k_t jet-finder". In: *Phys.Lett.* B641 (2006), pp. 57–61. DOI: 10.1016/j.physletb.2006.08.037. arXiv: hep-ph/0512210 [hep-ph].

[40] *Pile-up subtraction and suppression for jets in ATLAS*. Tech. rep. ATLAS-CONF-2013-083. Geneva: CERN, Aug. 2013. URL: http://cds.cern.ch/record/1570994.

[41] ATLAS collaboration. *Jet 2012 Monte Carlo Event Displays*. Aug. 2018. URL: https://twiki.cern.ch/twiki/bin/view/AtlasPublic/JetEtmissApprovedBOOST2014EventDisplays (visited on 08/27/2018).

[42] Fabian Kohn. "Measurement of the charge asymmetry in top quark pair production in *pp* collision data at $\sqrt{s} = 7\,\text{TeV}$ using the ATLAS detector". PhD thesis. U. Gottingen (main), 2012. arXiv: 1204.0952 [hep-ex]. URL: https://inspirehep.net/record/1103034/files/arXiv:1204.0952.pdf.

[43] ATLAS Collaboration. *Summary plots from the ATLAS Top physics group*. Aug. 2018. URL: https://atlas.web.cern.ch/Atlas/GROUPS/PHYSICS/CombinedSummaryPlots/TOP/ (visited on 08/15/2018).

[44] Werner Bernreuther. "Top quark physics at the LHC". In: *J. Phys.* G35 (2008), p. 083001. DOI: 10.1088/0954-3899/35/8/083001. arXiv: 0805.1333 [hep-ph].

[45] Frank-Peter Schilling. "Top Quark Physics at the LHC: A Review of the First Two Years". In: *Int.J.Mod.Phys.* A27 (2012), p. 1230016. DOI: 10.1142/S0217751X12300165. arXiv: 1206.4484 [hep-ex].

[46] *First combination of Tevatron and LHC measurements of the top-quark mass*. Tech. rep. ATLAS-CONF-2014-008. ATLAS-CONF-2014-008. CDF-NOTE-11071. CMS-PAS-TOP-13-014. D0-NOTE-6416. Work within the Tevatron Electroweak (TEV-EW-WG) and the Top Physics LHC (TOP-LHC-WG) working groups. Geneva: CERN, Mar. 2014. URL: https://cds.cern.ch/record/1669819.

[47] ATLAS Collaboration. *Summary plots from the ATLAS Standard Model physics group*. Aug. 2018. URL: https://atlas.web.cern.ch/Atlas/GROUPS/PHYSICS/CombinedSummaryPlots/SM/ (visited on 08/15/2018).

[48] *Measurement of inclusive-jet cross-sections in proton-proton collisions at $\sqrt{s}$ = 13 TeV centre-of-mass energy with the ATLAS detector*. Tech. rep. ATLAS-CONF-2016-092. Geneva: CERN, Aug. 2016. URL: http://cds.cern.ch/record/2209210.

[49] Martin Schmaltz and David Tucker-Smith. "Little Higgs review". In: *Ann. Rev. Nucl. Part. Sci.* 55 (2005), pp. 229–270. DOI: 10.1146/annurev.nucl.55.090704.151502. arXiv: hep-ph/0502182 [hep-ph].

[50] Stephen P. Martin. *A Supersymmetry primer*. [Adv. Ser. Direct. High Energy Phys.18,1(1998)]. 1997. arXiv: hep-ph/9709356 [hep-ph].

[51] R. D. Peccei. "The Strong CP problem and axions". In: *Lect. Notes Phys.* 741 (2008). [,3(2006)], pp. 3–17. DOI: 10.1007/978-3-540-73518-2_1. arXiv: hep-ph/0607268 [hep-ph].

[52] P. A. R. Ade et al. "Planck 2015 results. XIII. Cosmological parameters". In: *Astron. Astrophys.* 594 (2016), A13. DOI: 10.1051/0004-6361/201525830. arXiv: 1502.01589 [astro-ph.CO].

[53] Christopher T. Hill and Elizabeth H. Simmons. "Strong dynamics and electroweak symmetry breaking". In: *Phys. Rept.* 381 (2003). [Erratum: Phys. Rept.390,553(2004)], pp. 235–402. DOI: 10.1016/S0370-1573(03)00140-6. arXiv: hep-ph/0203079 [hep-ph].

[54] Christopher T. Hill. "Topcolor: Top quark condensation in a gauge extension of the standard model". In: *Phys. Lett.* B266 (1991), pp. 419–424. DOI: 10.1016/0370-2693(91)91061-Y.

[55] Christopher T. Hill. "Topcolor assisted technicolor". In: *Phys. Lett.* B345 (1995), pp. 483–489. DOI: 10.1016/0370-2693(94)01660-5. arXiv: hep-ph/9411426 [hep-ph].

[56] Robert M. Harris, Christopher T. Hill, and Stephen J. Parke. *Cross-Section for Topcolor Z'_t Decaying to $t\bar{t}$*. 1999. arXiv: hep-ph/9911288 [hep-ph].

[57] Steven Weinberg. "Implications of Dynamical Symmetry Breaking". In: *Phys. Rev.* D13 (1976). [Addendum: Phys. Rev.D19,1277(1979)], pp. 974–996. DOI: 10.1103/PhysRevD.19.1277,10.1103/PhysRevD.13.974.

[58] Leonard Susskind. "Dynamics of Spontaneous Symmetry Breaking in the Weinberg-Salam Theory". In: *Phys. Rev.* D20 (1979), pp. 2619–2625. DOI: 10.1103/PhysRevD.20.2619.

[59] M. Aaboud et al. "Search for heavy particles decaying into top-quark pairs using lepton-plus-jets events in proton–proton collisions at $\sqrt{s}$ = 13 TeV with the ATLAS detector". In: *Eur. Phys. J.* C78.7 (2018), p. 565. DOI: 10.1140/epjc/s10052-018-5995-6. arXiv: 1804.10823 [hep-ex].

[60] Robert M. Harris and Supriya Jain. "Cross Sections for Leptophobic Topcolor Z' Decaying to Top-Antitop". In: *Eur. Phys. J.* C72 (2012), p. 2072. DOI: 10.1140/epjc/s10052-012-2072-4. arXiv: 1112.4928 [hep-ph].

[61] Paul Langacker. "The Physics of Heavy Z' Gauge Bosons". In: *Rev. Mod. Phys.* 81 (2009), pp. 1199–1228. DOI: 10.1103/RevModPhys.81.1199. arXiv: 0801.1345 [hep-ph].

[62] Lisa Randall and Raman Sundrum. "A Large mass hierarchy from a small extra dimension". In: *Phys. Rev. Lett.* 83 (1999), pp. 3370–3373. DOI: 10.1103/PhysRevLett.83.3370. arXiv: hep-ph/9905221 [hep-ph].

[63] Lisa Randall and Raman Sundrum. "An Alternative to compactification". In: *Phys. Rev. Lett.* 83 (1999), pp. 4690–4693. DOI: 10.1103/PhysRevLett.83.4690. arXiv: hep-th/9906064 [hep-th].

[64] David E. Morrissey, Tilman Plehn, and Tim M. P. Tait. "Physics searches at the LHC". In: *Phys. Rept.* 515 (2012), pp. 1–113. DOI: 10.1016/j.physrep.2012.02.007. arXiv: 0912.3259 [hep-ph].

[65] Theodor Kaluza. "Zum Unitätsproblem der Physik". In: *Sitzungsber. Preuss. Akad. Wiss. Berlin (Math. Phys.)* 1921 (1921), pp. 966–972. arXiv: 1803.08616 [physics.hist-ph].

[66] Oskar Klein. "Quantum Theory and Five-Dimensional Theory of Relativity. (In German and English)". In: *Z. Phys.* 37 (1926). [,76(1926)], pp. 895–906. DOI: 10.1007/BF01397481.

[67] Ben Lillie, Lisa Randall, and Lian-Tao Wang. "The Bulk RS KK-gluon at the LHC". In: *JHEP* 09 (2007), p. 074. DOI: 10.1088/1126-6708/2007/09/074. arXiv: hep-ph/0701166 [hep-ph].

[68] S. Ask, J. H. Collins, J. R. Forshaw, K. Joshi, and A. D. Pilkington. "Identifying the colour of TeV-scale resonances". In: *JHEP* 01 (2012), p. 018. DOI: 10.1007/JHEP01(2012)018. arXiv: 1108.2396 [hep-ph].

[69] Kaustubh Agashe, Hooman Davoudiasl, Gilad Perez, and Amarjit Soni. "Warped Gravitons at the LHC and Beyond". In: *Phys. Rev.* D76 (2007), p. 036006. DOI: 10.1103/PhysRevD.76.036006. arXiv: hep-ph/0701186 [hep-ph].

[70] A. Liam Fitzpatrick, Jared Kaplan, Lisa Randall, and Lian-Tao Wang. "Searching for the Kaluza-Klein Graviton in Bulk RS Models". In: *JHEP* 09 (2007), p. 013. DOI: 10.1088/1126-6708/2007/09/013. arXiv: hep-ph/0701150 [hep-ph].

[71] Daniel Abercrombie et al. *Dark Matter Benchmark Models for Early LHC Run-2 Searches: Report of the ATLAS/CMS Dark Matter Forum*. Ed. by Antonio Boveia, Caterina Doglioni, Steven Lowette, Sarah Malik, and Stephen Mrenna. 2015. arXiv: 1507.00966 [hep-ex].

[72] Andreas Albert et al. *Recommendations of the LHC Dark Matter Working Group: Comparing LHC searches for heavy mediators of dark matter production in visible and invisible decay channels. Recommendations of the LHC Dark Matter Working Group: Comparing LHC searches for heavy mediators of dark matter production in visible and invisible decay channels.* Tech. rep. CERN-LPCC-2017-01. 19 pages, 4 figures; v2: author list and LaTeX problem fixed. Mar. 2017. arXiv: 1703.05703 [hep-ex]. URL: https://cds.cern.ch/record/2256144.

[73] Georgios Choudalakis. "On hypothesis testing, trials factor, hypertests and the BumpHunter". In: *Proceedings, PHYSTAT 2011 Workshop on Statistical Issues Related to Discovery Claims in Search Experiments and Unfolding, CERN,Geneva, Switzerland 17-20 January 2011.* 2011. arXiv: 1101.0390 [physics.data-an].

[74] Eilam Gross and Ofer Vitells. "Trial factors for the look elsewhere effect in high energy physics". In: *Eur. Phys. J.* C70 (2010), pp. 525–530. DOI: 10.1140/epjc/s10052-010-1470-8. arXiv: 1005.1891 [physics.data-an].

[75] Kyle Cranmer. "Practical Statistics for the LHC". In: *Proceedings, 2011 European School of High-Energy Physics (ESHEP 2011): Cheile Gradistei, Romania, September 7-20, 2011.* [,247(2015)]. 2015, pp. 267–308. DOI: 10.5170/CERN-2015-001.247,10.5170/CERN-2014-003.267. arXiv: 1503.07622 [physics.data-an]. URL: https://inspirehep.net/record/1356277/files/arXiv:1503.07622.pdf.

[76] Glen Cowan, Kyle Cranmer, Eilam Gross, and Ofer Vitells. "Asymptotic formulae for likelihood-based tests of new physics". In: *Eur. Phys. J.* C71 (2011). [Erratum: Eur. Phys. J.C73,2501(2013)], p. 1554. DOI: 10.1140/epjc/s10052-011-1554-0,10.1140/epjc/s10052-013-2501-z. arXiv: 1007.1727 [physics.data-an].

[77] Alexander L. Read. "Modified frequentist analysis of search results (The CL(s) method)". In: *Workshop on confidence limits, CERN, Geneva, Switzerland, 17-18 Jan 2000: Proceedings.* 2000, pp. 81–101. URL: http://weblib.cern.ch/abstract?CERN-OPEN-2000-205.

[78] Alexander L. Read. "Presentation of search results: The CL(s) technique". In: *J. Phys.* G28 (2002). [,11(2002)], pp. 2693–2704. DOI: 10.1088/0954-3899/28/10/313.

[79] Lyndon R Evans and Philip Bryant. "LHC Machine". In: *JINST* 3 (2008). This report is an abridged version of the LHC Design Report (CERN-2004-003), S08001. 164 p. DOI: 10.1088/1748-0221/3/08/S08001. URL: https://cds.cern.ch/record/1129806.

[80] G. Aad et al. "The ATLAS Experiment at the CERN Large Hadron Collider". In: *JINST* 3 (2008), S08003. DOI: 10.1088/1748-0221/3/08/S08003.

[81] Oliver Sim Brüning et al. *LHC Design Report*. CERN Yellow Reports: Monographs. Geneva: CERN, 2004. URL: https://cds.cern.ch/record/782076.

[82] Philippe Mouche. "Overall view of the LHC. Vue d'ensemble du LHC". In: (June 2014). General Photo. URL: https://cds.cern.ch/record/1708847.

[83] W. W. Armstrong et al. *ATLAS: technical proposal for a general-purpose pp experiment at the Large Hadron Collider at CERN*. LHC Tech. Proposal. Geneva: CERN, 1994. URL: https://cds.cern.ch/record/290968.

[84] *CMS, the Compact Muon Solenoid: Technical proposal*. LHC Tech. Proposal. Geneva: CERN, 1994. URL: https://cds.cern.ch/record/290969.

[85] S. Amato et al. *LHCb technical proposal*. Tech. Proposal. Geneva: CERN, 1998. URL: http://cds.cern.ch/record/622031.

[86] *ALICE: Technical proposal for a Large Ion collider Experiment at the CERN LHC*. LHC Tech. Proposal. Geneva: CERN, 1995. URL: https://cds.cern.ch/record/293391.

[87] Peter Braun-Munzinger and Johanna Stachel. "The quest for the quark-gluon plasma". In: *Nature* 448 (2007), pp. 302–309. DOI: 10.1038/nature06080.

[88] Fabienne Marcastel. *CERN's Accelerator Complex. La chaîne des accélérateurs du CERN*. General Photo. Oct. 2013. URL: https://cds.cern.ch/record/1621583 (visited on 09/06/2018).

[89] Mike Lamont. *LHC accelerator performance*. Aug. 2016. URL: https://indico.cern.ch/event/432527/contributions/2255495/attachments/1321399/1981784/LHC-performance-ICHEP16.pdf (visited on 09/06/2018).

[90] Joao Pequenao and Paul Schaffner. *An computer generated image representing how ATLAS detects particles*. Jan. 2013. URL: https://cds.cern.ch/record/1505342.

[91] M. Aaboud et al. "Performance of the ATLAS Track Reconstruction Algorithms in Dense Environments in LHC Run 2". In: *Eur. Phys. J.* C77.10 (2017), p. 673. DOI: 10.1140/epjc/s10052-017-5225-7. arXiv: 1704.07983 [hep-ex].

[92] M Capeans et al. *ATLAS Insertable B-Layer Technical Design Report*. Tech. rep. CERN-LHCC-2010-013. ATLAS-TDR-19. Sept. 2010. URL: https://cds.cern.ch/record/1291633.

[93] Alessandro La Rosa. "The ATLAS Insertable B-Layer: from construction to operation". In: *JINST* 11.12 (2016), p. C12036. DOI: 10.1088/1748-0221/11/12/C12036. arXiv: 1610.01994 [physics.ins-det].

[94] *IBL Efficiency and Single Point Resolution in Collision Events*. Tech. rep. ATL-INDET-PUB-2016-001. Geneva: CERN, Aug. 2016. URL: https://cds.cern.ch/record/2203893.

[95] Lily Asquith et al. *Jet Substructure at the Large Hadron Collider : Experimental Review*. 2018. arXiv: 1803.06991 [hep-ex].

[96] A. Airapetian et al. "ATLAS: Detector and physics performance technical design report. Volume 1". In: Technical Design Report ATLAS (1999). URL: https://cds.cern.ch/record/391176.

[97] Morad Aaboud et al. "Charged-particle distributions at low transverse momentum in $\sqrt{s} = 13$ TeV *pp* interactions measured with the ATLAS detector at the LHC". In: *Eur. Phys. J.* C76.9 (2016), p. 502. DOI: 10.1140/epjc/s10052-016-4335-y. arXiv: 1606.01133 [hep-ex].

[98] *Track Reconstruction Performance of the ATLAS Inner Detector at* $\sqrt{s} =$ *13 TeV*. Tech. rep. ATL-PHYS-PUB-2015-018. Geneva: CERN, July 2015. URL: https://cds.cern.ch/record/2037683.

[99] W Lampl et al. *Calorimeter Clustering Algorithms: Description and Performance*. Tech. rep. ATL-LARG-PUB-2008-002. ATL-COM-LARG-2008-003. Geneva: CERN, Apr. 2008. URL: http://cds.cern.ch/record/1099735.

[100] Morad Aaboud et al. "Performance of the ATLAS Trigger System in 2015". In: *Eur. Phys. J.* C77.5 (2017), p. 317. DOI: 10.1140/epjc/s10052-017-4852-3. arXiv: 1611.09661 [hep-ex].

[101] R. Achenbach et al. "The ATLAS level-1 calorimeter trigger". In: *JINST* 3 (2008), P03001. DOI: 10.1088/1748-0221/3/03/P03001.

[102] Georges Aad et al. "Performance of the ATLAS Trigger System in 2010". In: *Eur. Phys. J.* C72 (2012), p. 1849. DOI: 10.1140/epjc/s10052-011-1849-1. arXiv: 1110.1530 [hep-ex].

[103] Peter Jenni, Marzio Nessi, Markus Nordberg, and Kenway Smith. *ATLAS high-level trigger, data-acquisition and controls: Technical Design Report*. Technical Design Report ATLAS. Geneva: CERN, 2003. URL: https://cds.cern.ch/record/616089.

[104] Andy Buckley et al. "General-purpose event generators for LHC physics". In: *Phys. Rept.* 504 (2011), pp. 145–233. DOI: 10.1016/j.physrep.2011.03.005. arXiv: 1101.2599 [hep-ph].

[105] G. Aad et al. "The ATLAS Simulation Infrastructure". In: *Eur. Phys. J.* C70 (2010), pp. 823–874. DOI: 10.1140/epjc/s10052-010-1429-9. arXiv: 1005.4568 [physics.ins-det].

[106] Torbjorn Sjostrand, Stephen Mrenna, and Peter Z. Skands. "PYTHIA 6.4 Physics and Manual". In: *JHEP* 05 (2006), p. 026. DOI: 10.1088/1126-6708/2006/05/026. arXiv: hep-ph/0603175 [hep-ph].

[107] Torbjorn Sjostrand, Stephen Mrenna, and Peter Z. Skands. "A Brief Introduction to PYTHIA 8.1". In: *Comput. Phys. Commun.* 178 (2008), pp. 852–867. DOI: 10.1016/j.cpc.2008.01.036. arXiv: 0710.3820 [hep-ph].

[108] *ATLAS tunes of PYTHIA 6 and Pythia 8 for MC11*. Tech. rep. ATL-PHYS-PUB-2011-009. Geneva: CERN, July 2011. URL: http://cds.cern.ch/record/1363300.

[109] *Summary of ATLAS Pythia 8 tunes*. Tech. rep. ATL-PHYS-PUB-2012-003. Geneva: CERN, Aug. 2012. URL: https://cds.cern.ch/record/1474107.

[110] *ATLAS Run 1 Pythia8 tunes*. Tech. rep. ATL-PHYS-PUB-2014-021. Geneva: CERN, Nov. 2014. URL: https://cds.cern.ch/record/1966419.

[111] Peter Zeiler Skands. "Tuning Monte Carlo Generators: The Perugia Tunes". In: *Phys. Rev.* D82 (2010), p. 074018. DOI: 10.1103/PhysRevD.82.074018. arXiv: 1005.3457 [hep-ph].

[112] G. Corcella et al. "HERWIG 6: An Event generator for hadron emission reactions with interfering gluons (including supersymmetric processes)". In: *JHEP* 01 (2001), p. 010. DOI: 10.1088/1126-6708/2001/01/010. arXiv: hep-ph/0011363.

[113] M. Bahr et al. "Herwig++ Physics and Manual". In: *Eur. Phys. J. C* 58 (2008), p. 639. DOI: 10.1140/epjc/s10052-008-0798-9. arXiv: 0803.0883 [hep-ph].

[114] Johannes Bellm et al. "Herwig 7.0/Herwig++ 3.0 release note". In: *Eur. Phys. J. C* 76.4 (2016), p. 196. DOI: 10.1140/epjc/s10052-016-4018-8. arXiv: 1512.01178 [hep-ph].

[115] J.M. Butterworth, Jeffrey R. Forshaw, and M.H. Seymour. "Multiparton interactions in photoproduction at HERA". In: *Z. Phys. C* 72 (1996), p. 637. DOI: 10.1007/s002880050286. arXiv: hep-ph/9601371.

[116] Paolo Nason. "A New method for combining NLO QCD with shower Monte Carlo algorithms". In: *JHEP* 11 (2004), p. 040. DOI: 10.1088/1126-6708/2004/11/040. arXiv: hep-ph/0409146 [hep-ph].

[117] Stefano Frixione, Paolo Nason, and Carlo Oleari. "Matching NLO QCD computations with Parton Shower simulations: the POWHEG method". In: *JHEP* 11 (2007), p. 070. DOI: 10.1088/1126-6708/2007/11/070. arXiv: 0709.2092 [hep-ph].

[118] Simone Alioli, Paolo Nason, Carlo Oleari, and Emanuele Re. "A general framework for implementing NLO calculations in shower Monte Carlo programs: the POWHEG BOX". In: *JHEP* 06 (2010), p. 043. DOI: 10.1007/JHEP06(2010)043. arXiv: 1002.2581 [hep-ph].

[119] Johan Alwall, Michel Herquet, Fabio Maltoni, Olivier Mattelaer, and Tim Stelzer. "MadGraph 5 : Going Beyond". In: *JHEP* 06 (2011), p. 128. DOI: 10.1007/JHEP06(2011)128. arXiv: 1106.0522 [hep-ph].

[120] J. Alwall et al. "The automated computation of tree-level and next-to-leading order differential cross sections, and their matching to parton shower simulations". In: *JHEP* 07 (2014), p. 079. DOI: 10.1007/JHEP07(2014)079. arXiv: 1405.0301 [hep-ph].

[121] Stefano Frixione and Bryan R. Webber. "Matching NLO QCD computations and parton shower simulations". In: *JHEP* 06 (2002), p. 029. arXiv: hep-ph/0204244.

[122] *Search for the Standard Model Higgs boson produced in association with top quarks and decaying into $b\bar{b}$ in pp collisions at $\sqrt{s}$ = 13 TeV with the ATLAS detector*. Tech. rep. ATLAS-CONF-2016-080. Geneva: CERN, Aug. 2016. URL: http://cds.cern.ch/record/2206255.

[123] *Simulation of top quark production for the ATLAS experiment at sqrt(s) = 13 TeV*. Tech. rep. ATL-PHYS-PUB-2016-004. Geneva: CERN, Jan. 2016. URL: https://cds.cern.ch/record/2120417.

[124] Stefano Frixione, Paolo Nason, and Giovanni Ridolfi. "A Positive-weight next-to-leading-order Monte Carlo for heavy flavour hadroproduction". In: *JHEP* 09 (2007), p. 126. DOI: 10.1088/1126-6708/2007/09/126. arXiv: 0707.3088 [hep-ph].

[125] Hung-Liang Lai et al. "New parton distributions for collider physics". In: *Phys. Rev.* D82 (2010), p. 074024. DOI: 10.1103/PhysRevD.82.074024. arXiv: 1007.2241 [hep-ph].

[126] J. Pumplin et al. "New generation of parton distributions with uncertainties from global QCD analysis". In: *JHEP* 07 (2002), p. 012. DOI: 10.1088/1126-6708/2002/07/012. arXiv: hep-ph/0201195 [hep-ph].

[127] M. Beneke, P. Falgari, S. Klein, and C. Schwinn. "Hadronic top-quark pair production with NNLL threshold resummation". In: *Nucl. Phys.* B855 (2012), pp. 695–741. DOI: 10.1016/j.nuclphysb.2011.10.021. arXiv: 1109.1536 [hep-ph].

[128] Matteo Cacciari, Michal Czakon, Michelangelo Mangano, Alexander Mitov, and Paolo Nason. "Top-pair production at hadron colliders with next-to-next-to-leading logarithmic soft-gluon resummation". In: *Phys. Lett.* B710 (2012), pp. 612–622. DOI: 10.1016/j.physletb.2012.03.013. arXiv: 1111.5869 [hep-ph].

[129] Peter Bärnreuther, Michal Czakon, and Alexander Mitov. "Percent Level Precision Physics at the Tevatron: First Genuine NNLO QCD Corrections to $q\bar{q} \to t\bar{t} + X$". In: *Phys. Rev. Lett.* 109 (2012), p. 132001. DOI: 10.1103/PhysRevLett.109.132001. arXiv: 1204.5201 [hep-ph].

[130] Michal Czakon and Alexander Mitov. "NNLO corrections to top-pair production at hadron colliders: the all-fermionic scattering channels". In: *JHEP* 12 (2012), p. 054. DOI: 10.1007/JHEP12(2012)054. arXiv: 1207.0236 [hep-ph].

[131] Michal Czakon and Alexander Mitov. "NNLO corrections to top pair production at hadron colliders: the quark-gluon reaction". In: *JHEP* 01 (2013), p. 080. DOI: 10.1007/JHEP01(2013)080. arXiv: 1210.6832 [hep-ph].

[132] Michał Czakon, Paul Fiedler, and Alexander Mitov. "Total Top-Quark Pair-Production Cross Section at Hadron Colliders Through $O(\frac{4}{S})$". In: *Phys. Rev. Lett.* 110 (2013), p. 252004. DOI: 10.1103/PhysRevLett.110.252004. arXiv: 1303.6254 [hep-ph].

[133] Michal Czakon and Alexander Mitov. "Top++: A Program for the Calculation of the Top-Pair Cross-Section at Hadron Colliders". In: *Comput. Phys. Commun.* 185 (2014), p. 2930. DOI: 10.1016/j.cpc.2014.06.021. arXiv: 1112.5675 [hep-ph].

[134] Michiel Botje et al. *The PDF4LHC Working Group Interim Recommendations*. 2011. arXiv: 1101.0538 [hep-ph].

[135] A. D. Martin, W. J. Stirling, R. S. Thorne, and G. Watt. "Parton distributions for the LHC". In: *Eur. Phys. J.* C63 (2009), pp. 189–285. DOI: 10.1140/epjc/s10052-009-1072-5. arXiv: 0901.0002 [hep-ph].

[136] A. D. Martin, W. J. Stirling, R. S. Thorne, and G. Watt. "Uncertainties on alpha(S) in global PDF analyses and implications for predicted hadronic cross sections". In: *Eur. Phys. J.* C64 (2009), pp. 653–680. DOI: 10.1140/epjc/s10052-009-1164-2. arXiv: 0905.3531 [hep-ph].

[137] Jun Gao et al. "CT10 next-to-next-to-leading order global analysis of QCD". In: *Phys. Rev.* D89.3 (2014), p. 033009. DOI: 10.1103/PhysRevD.89.033009. arXiv: 1302.6246 [hep-ph].

[138] Richard D. Ball et al. "Parton distributions with LHC data". In: *Nucl. Phys.* B867 (2013), pp. 244–289. DOI: 10.1016/j.nuclphysb.2012.10.003. arXiv: 1207.1303 [hep-ph].

[139] *NNLO+NNLL top-quark-pair cross sections*. Sept. 2015. URL: https://twiki.cern.ch/twiki/bin/view/LHCPhysics/TtbarNNLO (visited on 09/04/2018).

[140] S. Agostinelli et al. "GEANT4: A Simulation toolkit". In: *Nucl. Instrum. Meth.* A506 (2003), pp. 250–303. DOI: 10.1016/S0168-9002(03)01368-8.

[141] *Early Inner Detector Tracking Performance in the 2015 data at $\sqrt{s}$ = 13 TeV*. Tech. rep. ATL-PHYS-PUB-2015-051. Geneva: CERN, Dec. 2015. URL: https://cds.cern.ch/record/2110140.

[142] T Cornelissen et al. *Concepts, Design and Implementation of the ATLAS New Tracking (NEWT)*. Tech. rep. ATL-SOFT-PUB-2007-007. ATL-COM-SOFT-2007-002. Geneva: CERN, Mar. 2007. URL: https://cds.cern.ch/record/1020106.

[143] *Performance of the ATLAS Inner Detector Track and Vertex Reconstruction in the High Pile-Up LHC Environment*. Tech. rep. ATLAS-CONF-2012-042. Geneva: CERN, Mar. 2012. URL: https://cds.cern.ch/record/1435196.

[144] G. Piacquadio, Kirill Prokofiev, and A. Wildauer. "Primary vertex reconstruction in the ATLAS experiment at LHC". In: *J. Phys. Conf. Ser.* 119 (2008), p. 032033. DOI: 10.1088/1742-6596/119/3/032033.

[145] Morad Aaboud et al. "Reconstruction of primary vertices at the ATLAS experiment in Run 1 proton–proton collisions at the LHC". In: *Eur. Phys. J.* C77.5 (2017), p. 332. DOI: 10.1140/epjc/s10052-017-4887-5. arXiv: 1611.10235 [physics.ins-det].

[146] Georges Aad et al. "Measurement of the muon reconstruction performance of the ATLAS detector using 2011 and 2012 LHC proton–proton collision data". In: *Eur. Phys. J.* C74.11 (2014), p. 3130. DOI: 10.1140/epjc/s10052-014-3130-x. arXiv: 1407.3935 [hep-ex].

[147] Georges Aad et al. "Muon reconstruction performance of the ATLAS detector in proton–proton collision data at $\sqrt{s}$ =13 TeV". In: *Eur. Phys. J.* C76.5 (2016), p. 292. DOI: 10.1140/epjc/s10052-016-4120-y. arXiv: 1603.05598 [hep-ex].

[148] Georges Aad et al. "Topological cell clustering in the ATLAS calorimeters and its performance in LHC Run 1". In: *Eur. Phys. J.* C77 (2017), p. 490. DOI: 10.1140/epjc/s10052-017-5004-5. arXiv: 1603.02934 [hep-ex].

[149] Morad Aaboud et al. "Electron efficiency measurements with the ATLAS detector using 2012 LHC proton–proton collision data". In: *Eur. Phys. J.* C77.3 (2017), p. 195. DOI: 10.1140/epjc/s10052-017-4756-2. arXiv: 1612.01456 [hep-ex].

[150] Morad Aaboud et al. "Measurement of the photon identification efficiencies with the ATLAS detector using LHC Run-1 data". In: *Eur. Phys. J.* C76.12 (2016), p. 666. DOI: 10.1140/epjc/s10052-016-4507-9. arXiv: 1606.01813 [hep-ex].

[151] *Electron efficiency measurements with the ATLAS detector using the 2015 LHC proton-proton collision data*. Tech. rep. ATLAS-CONF-2016-024. Geneva: CERN, June 2016. URL: http://cds.cern.ch/record/2157687.

[152] M. Aaboud et al. "Measurement of inclusive jet and dijet cross-sections in proton-proton collisions at $\sqrt{s}$ = 13 TeV with the ATLAS detector". In: *JHEP* 05 (2018), p. 195. DOI: 10.1007/JHEP05(2018)195. arXiv: 1711.02692 [hep-ex].

[153] M. Aaboud et al. "Jet energy scale measurements and their systematic uncertainties in proton-proton collisions at $\sqrt{s}$ = 13 TeV with the ATLAS detector". In: *Phys. Rev.* D96.7 (2017), p. 072002. DOI: 10.1103/PhysRevD.96.072002. arXiv: 1703.09665 [hep-ex].

[154] *Jet global sequential corrections with the ATLAS detector in proton-proton collisions at sqrt(s) = 8 TeV*. Tech. rep. ATLAS-CONF-2015-002. Geneva: CERN, Mar. 2015. URL: https://cds.cern.ch/record/2001682.

[155] Georges Aad et al. "Jet energy measurement with the ATLAS detector in proton-proton collisions at $\sqrt{s} = 7$ TeV". In: *Eur. Phys. J.* C73.3 (2013), p. 2304. DOI: 10.1140/epjc/s10052-013-2304-2. arXiv: 1112.6426 [hep-ex].

[156] *Selection of jets produced in 13TeV proton-proton collisions with the ATLAS detector*. Tech. rep. ATLAS-CONF-2015-029. Geneva: CERN, July 2015. URL: http://cds.cern.ch/record/2037702.

[157] *Tagging and suppression of pileup jets with the ATLAS detector*. Tech. rep. ATLAS-CONF-2014-018. Geneva: CERN, May 2014. URL: http://cds.cern.ch/record/1700870.

[158] Georges Aad et al. "Performance of pile-up mitigation techniques for jets in pp collisions at $\sqrt{s} = 8$ TeV using the ATLAS detector". In: *Eur. Phys. J.* C76.11 (2016), p. 581. DOI: 10.1140/epjc/s10052-016-4395-z. arXiv: 1510.03823 [hep-ex].

[159] Georges Aad et al. "Performance of b-Jet Identification in the ATLAS Experiment". In: *JINST* 11.04 (2016), P04008. DOI: 10.1088/1748-0221/11/04/P04008. arXiv: 1512.01094 [hep-ex].

[160] *Optimisation of the ATLAS b-tagging performance for the 2016 LHC Run*. Tech. rep. ATL-PHYS-PUB-2016-012. Geneva: CERN, June 2016. URL: https://cds.cern.ch/record/2160731.

[161] *Expected performance of the ATLAS b-tagging algorithms in Run-2*. Tech. rep. ATL-PHYS-PUB-2015-022. Geneva: CERN, July 2015. URL: https://cds.cern.ch/record/2037697.

[162] Morad Aaboud et al. "Measurements of b-jet tagging efficiency with the ATLAS detector using $t\bar{t}$ events at $\sqrt{s} = 13$ TeV". In: *JHEP* 08 (2018), p. 089. DOI: 10.1007/JHEP08(2018)089. arXiv: 1805.01845 [hep-ex].

[163] Georges Aad et al. "Performance of Missing Transverse Momentum Reconstruction in Proton-Proton Collisions at 7 TeV with ATLAS". In: *Eur. Phys. J.* C72 (2012), p. 1844. DOI: 10.1140/epjc/s10052-011-1844-6. arXiv: 1108.5602 [hep-ex].

[164] Morad Aaboud et al. *Performance of missing transverse momentum reconstruction with the ATLAS detector using proton-proton collisions at $\sqrt{s} = 13$ TeV*. Tech. rep. 2018. arXiv: 1802.08168 [hep-ex].

[165] Tilman Plehn, Michael Spannowsky, Michihisa Takeuchi, and Dirk Zerwas. "Stop Reconstruction with Tagged Tops". In: *JHEP* 1010 (2010), p. 078. DOI: 10.1007/JHEP10(2010)078. arXiv: 1006.2833 [hep-ph].

[166] M. Aaboud et al. "Measurements of top-quark pair differential cross-sections in the lepton+jets channel in pp collisions at $\sqrt{s} = 13$ TeV using the ATLAS detector". In: *JHEP* 11 (2017), p. 191. DOI: 10.1007/JHEP11(2017)191. arXiv: 1708.00727 [hep-ex].

[167] Morad Aaboud et al. "Measurement of jet activity produced in top-quark events with an electron, a muon and two b-tagged jets in the final state in pp collisions at $\sqrt{s} = 13$ TeV with the ATLAS detector". In: *Eur. Phys. J.* C77.4 (2017), p. 220. DOI: 10.1140/epjc/s10052-017-4766-0. arXiv: 1610.09978 [hep-ex].

[168] Mathis Kolb. "Top quark reconstruction using the "Buckets of tops" method in the ATLAS experiment". MA thesis. Physikalisches Institut, Heidelberg University, 2014. URL: http://www.physi.uni-heidelberg.de//Publications/Masterarbeit_Mathis_Kolb.pdf.

[169] Tilman Plehn and Michihisa Takeuchi. "W+Jets at CDF: Evidence for Top Quarks". In: *J. Phys.* G38 (2011), p. 095006. DOI: 10.1088/0954-3899/38/9/095006. arXiv: 1104.4087 [hep-ph].

[170] David J. Lange. "The EvtGen particle decay simulation package". In: *Nuclear Instruments and Methods in Physics Research Section A: Accelerators, Spectrometers, Detectors and Associated Equipment* 462.1 (2001). BEAUTY2000, Proceedings of the 7th Int. Conf. on B-Physics at Hadron Machines, pp. 152 –155. ISSN: 0168-9002. DOI: http://dx.doi.org/10.1016/S0168-9002(01)00089-4. URL: http://www.sciencedirect.com/science/article/pii/S0168900201000894.

[171] Georges Aad et al. "A search for $t\bar{t}$ resonances using lepton-plus-jets events in proton-proton collisions at $\sqrt{s} = 8$ TeV with the ATLAS detector". In: *JHEP* 08 (2015), p. 148. DOI: 10.1007/JHEP08(2015)148. arXiv: 1505.07018 [hep-ex].

[172] Vardan Khachatryan et al. "Search for resonant $t\bar{t}$ production in proton-proton collisions at $\sqrt{s} = 8$ TeV". In: *Phys. Rev.* D93.1 (2016), p. 012001. DOI: 10.1103/PhysRevD.93.012001. arXiv: 1506.03062 [hep-ex].

[173] T. Aaltonen et al. "Search for Resonant Top-Antitop Production in the Lepton Plus Jets Decay Mode Using the Full CDF Data Set". In: *Phys. Rev. Lett.* 110.12 (2013), p. 121802. DOI: 10.1103/PhysRevLett.110.121802. arXiv: 1211.5363 [hep-ex].

[174] V.M. Abazov et al. "Search for $t\bar{t}$ resonances in the lepton plus jets final state in $p\bar{p}$ collisions at $\sqrt{s} = 1.96$ TeV". In: *Phys. Lett.* B668 (2008), pp. 98–104. DOI: 10.1016/j.physletb.2008.08.027. arXiv: 0804.3664 [hep-ex].

[175] Georges Aad et al. "Search for resonances decaying into top-quark pairs using fully hadronic decays in pp collisions with ATLAS at $\sqrt{s} = 7$ TeV". In: *JHEP* 01 (2013), p. 116. DOI: 10.1007/JHEP01(2013)116. arXiv: 1211.2202 [hep-ex].

[176] *Jet Calibration and Systematic Uncertainties for Jets Reconstructed in the ATLAS Detector at $\sqrt{s} = 13$ TeV*. Tech. rep. ATL-PHYS-PUB-2015-015. Geneva: CERN, July 2015. URL: http://cds.cern.ch/record/2037613.

[177] *Monte Carlo Calibration and Combination of In-situ Measurements of Jet Energy Scale, Jet Energy Resolution and Jet Mass in ATLAS*. Tech. rep. ATLAS-CONF-2015-037. Geneva: CERN, Aug. 2015. URL: http://cds.cern.ch/record/2044941.

[178] Georges Aad et al. "Electron reconstruction and identification efficiency measurements with the ATLAS detector using the 2011 LHC proton-proton collision data". In: *Eur. Phys. J.* C74.7 (2014), p. 2941. DOI: 10.1140/epjc/s10052-014-2941-0. arXiv: 1404.2240 [hep-ex].

[179] Jun Gao, Chong Sheng Li, Bo Hua Li, C. P. Yuan, and Hua Xing Zhu. "Next-to-leading order QCD corrections to the heavy resonance production and decay into top quark pair at the LHC". In: *Phys. Rev.* D82 (2010), p. 014020. DOI: 10.1103/PhysRevD.82.014020. arXiv: 1004.0876 [hep-ph].

[180] Fabrizio Caola, Kirill Melnikov, and Markus Schulze. "Complete next-to-leading order QCD description of resonant Z' production and decay into $t\bar{t}$ final states". In: *Phys. Rev.* D87.3 (2013), p. 034015. DOI: 10.1103/PhysRevD.87.034015. arXiv: 1211.6387 [hep-ph].

[181] Pierre Artoisenet, Rikkert Frederix, Olivier Mattelaer, and Robbert Rietkerk. "Automatic spin-entangled decays of heavy resonances in Monte Carlo simulations". In: *JHEP* 03 (2013), p. 015. DOI: 10.1007/JHEP03(2013)015. arXiv: 1212.3460 [hep-ph].

[182] J. H. Kühn, A. Scharf, and P. Uwer. "Weak Interactions in Top-Quark Pair Production at Hadron Colliders: An Update". In: *Phys. Rev.* D91.1 (2015), p. 014020. DOI: 10.1103/PhysRevD.91.014020. arXiv: 1305.5773 [hep-ph].

[183] W Lukas. *Fast Simulation for ATLAS: Atlfast-II and ISF*. Tech. rep. ATL-SOFT-PROC-2012-065. Geneva: CERN, June 2012. URL: https://cds.cern.ch/record/1458503.

[184] Olaf Behnke, Kevin Kröninger, Grégory Schott, and Thomas Schörner-Sadenius. *Data analysis in high energy physics: a practical guide to statistical methods*. Weinheim: Wiley-VCH, 2013. URL: https://cds.cern.ch/record/1517556.

[185] Georges Aad et al. "A search for prompt lepton-jets in pp collisions at $\sqrt{s} =$ 8 TeV with the ATLAS detector". In: *JHEP* 02 (2016), p. 062. DOI: 10.1007/JHEP02(2016)062. arXiv: 1511.05542 [hep-ex].

[186] Kyle Cranmer, George Lewis, Lorenzo Moneta, Akira Shibata, and Wouter Verkerke. *HistFactory: A tool for creating statistical models for use with RooFit and RooStats*. Tech. rep. CERN-OPEN-2012-016. New York: New York U., Jan. 2012. URL: https://cds.cern.ch/record/1456844.

[187] Roger Barlow and Christine Beeston. "Fitting using finite Monte Carlo samples". In: *Computer Physics Communications* 77.2 (1993), pp. 219 –228. ISSN: 0010-4655. DOI: https://doi.org/10.1016/0010-4655(93)90005-W. URL: http://www.sciencedirect.com/science/article/pii/001046559390005W.

[188] Morad Aaboud et al. "Luminosity determination in pp collisions at $\sqrt{s} = 8$ TeV using the ATLAS detector at the LHC". In: *Eur. Phys. J.* C76.12 (2016), p. 653. DOI: 10.1140/epjc/s10052-016-4466-1. arXiv: 1608.03953 [hep-ex].

[189] M. Aaboud et al. "Measurement of the Inelastic Proton-Proton Cross Section at $\sqrt{s} = 13$ TeV with the ATLAS Detector at the LHC". In: *Phys. Rev. Lett.* 117.18 (2016), p. 182002. DOI: 10.1103/PhysRevLett.117.182002. arXiv: 1606.02625 [hep-ex].

[190] Georges Aad et al. "Jet energy resolution in proton-proton collisions at $\sqrt{s} = 7$ TeV recorded in 2010 with the ATLAS detector". In: *Eur. Phys. J.* C73.3 (2013), p. 2306. DOI: 10.1140/epjc/s10052-013-2306-0. arXiv: 1210.6210 [hep-ex].

[191] *Improvements in $t\bar{t}$ modelling using NLO+PS Monte Carlo generators for Run2*. Tech. rep. ATL-PHYS-PUB-2018-009. Geneva: CERN, July 2018. URL: http://cds.cern.ch/record/2630327.

[192] Jon Butterworth et al. "PDF4LHC recommendations for LHC Run II". In: *J. Phys.* G43 (2016), p. 023001. DOI: 10.1088/0954-3899/43/2/023001. arXiv: 1510.03865 [hep-ph].

[193] Sayipjamal Dulat et al. "New parton distribution functions from a global analysis of quantum chromodynamics". In: *Phys. Rev.* D93.3 (2016), p. 033006. DOI: 10.1103/PhysRevD.93.033006. arXiv: 1506.07443 [hep-ph].

[194] L. A. Harland-Lang, A. D. Martin, P. Motylinski, and R. S. Thorne. "Parton distributions in the LHC era: MMHT 2014 PDFs". In: *Eur. Phys. J.* C75.5 (2015), p. 204. DOI: 10.1140/epjc/s10052-015-3397-6. arXiv: 1412.3989 [hep-ph].

[195] Richard D. Ball et al. "Parton distributions for the LHC Run II". In: *JHEP* 04 (2015), p. 040. DOI: 10.1007/JHEP04(2015)040. arXiv: 1410.8849 [hep-ph].

[196] G. Watt and R. S. Thorne. "Study of Monte Carlo approach to experimental uncertainty propagation with MSTW 2008 PDFs". In: *JHEP* 08 (2012), p. 052. DOI: 10.1007/JHEP08(2012)052. arXiv: 1205.4024 [hep-ph].

[197] Jun Gao and Pavel Nadolsky. "A meta-analysis of parton distribution functions". In: *JHEP* 07 (2014), p. 035. DOI: 10.1007/JHEP07(2014)035. arXiv: 1401.0013 [hep-ph].

[198] Stefano Carrazza, Stefano Forte, Zahari Kassabov, Jose Ignacio Latorre, and Juan Rojo. "An Unbiased Hessian Representation for Monte Carlo PDFs". In: *Eur. Phys. J.* C75.8 (2015), p. 369. DOI: 10.1140/epjc/s10052-015-3590-7. arXiv: 1505.06736 [hep-ph].

[199] Stefano Carrazza, José I. Latorre, Juan Rojo, and Graeme Watt. "A compression algorithm for the combination of PDF sets". In: *Eur. Phys. J.* C75 (2015), p. 474. DOI: 10.1140/epjc/s10052-015-3703-3. arXiv: 1504.06469 [hep-ph].

[200] Michal Czakon, David Heymes, and Alexander Mitov. "Dynamical scales for multi-TeV top-pair production at the LHC". In: *JHEP* 04 (2017), p. 071. DOI: 10.1007/JHEP04(2017)071. arXiv: 1606.03350 [hep-ph].

[201] Thomas Junk. "Confidence level computation for combining searches with small statistics". In: *Nuclear Instruments and Methods in Physics Research Section A: Accelerators, Spectrometers, Detectors and Associated Equipment* 434.2 (1999), pp. 435 –443. ISSN: 0168-9002. DOI: https://doi.org/10.1016/S0168-9002(99)00498-2. URL: http://www.sciencedirect.com/science/article/pii/S0168900299004982.

[202] S. S. Wilks. "The Large-Sample Distribution of the Likelihood Ratio for Testing Composite Hypotheses". In: *Annals Math. Statist.* 9.1 (1938), pp. 60–62. DOI: 10.1214/aoms/1177732360.

[203] Abraham Wald. "Tests of Statistical Hypotheses Concerning Several Parameters When the Number of Observations is Large". In: *Transactions of the American Mathematical Society* 54.3 (1943), pp. 426–482.

[204] Aaron Armbruster and Jianming Qian. "Discovery of a Higgs Boson with the ATLAS Detector". Presented 02 May 2013. PhD thesis. May 2013. URL: https://cds.cern.ch/record/1553771.

[205] *Search for resonant* tt *production in proton-proton collisions at* $\sqrt{s} = 13$ TeV. Tech. rep. CMS-PAS-B2G-17-017. Geneva: CERN, 2018. URL: https://cds.cern.ch/record/2621631.

[206] Laurie McClymont, John Alison, and Andreas Korn. *Measurement of the ATLAS b-jet trigger efficiency in 2016 data*. Tech. rep. ATL-COM-DAQ-2017-009. Geneva: CERN, Feb. 2017. URL: https://cds.cern.ch/record/2244862.

[207] ATLAS collaboration. *Public b-Jet Trigger Plots for Collision Data*. Jan. 2018. URL: https://twiki.cern.ch/twiki/bin/view/AtlasPublic/BJetTriggerPublicResults (visited on 01/22/2018).

[208] M Shochet et al. *Fast TracKer (FTK) Technical Design Report*. Tech. rep. CERN-LHCC-2013-007. ATLAS-TDR-021. ATLAS Fast Tracker Technical Design Report. June 2013. URL: https://cds.cern.ch/record/1552953.

[209] Georges Aad et al. "Measurements of the Higgs boson production and decay rates and constraints on its couplings from a combined ATLAS and CMS analysis of the LHC pp collision data at $\sqrt{s} = 7$ and 8 TeV". In: *JHEP* 08 (2016), p. 045. DOI: 10.1007/JHEP08(2016)045. arXiv: 1606.02266 [hep-ex].

[210] Morad Aaboud et al. *Observation of $H \to b\bar{b}$ decays and VH production with the ATLAS detector*. submitted to Phys. Lett. B. 2018. arXiv: 1808.08238 [hep-ex].

[211] M. Aaboud et al. "Observation of Higgs boson production in association with a top quark pair at the LHC with the ATLAS detector". In: *Phys. Lett.* B784 (2018), pp. 173–191. DOI: 10.1016/j.physletb.2018.07.035. arXiv: 1806.00425 [hep-ex].

[212] Morad Aaboud et al. "Search for the standard model Higgs boson produced in association with top quarks and decaying into a $b\bar{b}$ pair in pp collisions at $\sqrt{s} = 13$ TeV with the ATLAS detector". In: *Phys. Rev.* D97.7 (2018), p. 072016. DOI: 10.1103/PhysRevD.97.072016. arXiv: 1712.08895 [hep-ex].

[213] Georges Aad et al. "Search for the Standard Model Higgs boson decaying into $b\bar{b}$ produced in association with top quarks decaying hadronically in pp collisions at $\sqrt{s} = 8$ TeV with the ATLAS detector". In: *JHEP* 05 (2016), p. 160. DOI: 10.1007/JHEP05(2016)160. arXiv: 1604.03812 [hep-ex].

[214] Matthew R. Buckley, Tilman Plehn, Torben Schell, and Michihisa Takeuchi. "Buckets of Higgs and Tops". In: *JHEP* 02 (2014), p. 130. DOI: 10.1007/JHEP02(2014)130. arXiv: 1310.6034 [hep-ph].

[215] *Search for the Standard Model Higgs boson produced in association with top quarks and decaying into a $\boldsymbol{b\bar{b}}$ pair in $\boldsymbol{pp}$ collisions at $\boldsymbol{\sqrt{s}}$ =13 TeV with the ATLAS detector*. Tech. rep. ATLAS-CONF-2017-076. Geneva: CERN, Nov. 2017. URL: http://cds.cern.ch/record/2291393.

[216] Georges Aad et al. "Measurements of fiducial cross-sections for $t\bar{t}$ production with one or two additional b-jets in pp collisions at $\sqrt{s}$ =8 TeV using the ATLAS detector". In: *Eur. Phys. J.* C76.1 (2016), p. 11. DOI: 10.1140/epjc/s10052-015-3852-4. arXiv: 1508.06868 [hep-ex].

[217] Risto Raitio and Walter W. Wada. "Higgs-boson production at large transverse momentum in quantum chromodynamics". In: *Phys. Rev. D* 19 (3 Feb. 1979), pp. 941–944. DOI: 10.1103/PhysRevD.19.941. URL: https://link.aps.org/doi/10.1103/PhysRevD.19.941.

[218] W. Beenakker et al. "NLO QCD corrections to t anti-t H production in hadron collisions". In: *Nucl. Phys.* B653 (2003), pp. 151–203. DOI: 10.1016/S0550-3213(03)00044-0. arXiv: hep-ph/0211352 [hep-ph].

[219] S. Dawson, C. Jackson, L. H. Orr, L. Reina, and D. Wackeroth. "Associated Higgs production with top quarks at the large hadron collider: NLO QCD corrections". In: *Phys. Rev.* D68 (2003), p. 034022. DOI: 10.1103/PhysRevD.68.034022. arXiv: hep-ph/0305087 [hep-ph].

[220] Yu Zhang, Wen-Gan Ma, Ren-You Zhang, Chong Chen, and Lei Guo. "QCD NLO and EW NLO corrections to $t\bar{t}H$ production with top quark decays at hadron collider". In: *Phys. Lett.* B738 (2014), pp. 1–5. DOI: 10.1016/j.physletb.2014.09.022. arXiv: 1407.1110 [hep-ph].

[221] S. Frixione, V. Hirschi, D. Pagani, H. S. Shao, and M. Zaro. "Electroweak and QCD corrections to top-pair hadroproduction in association with heavy bosons". In: *JHEP* 06 (2015), p. 184. DOI: 10.1007/JHEP06(2015)184. arXiv: 1504.03446 [hep-ph].

[222] A. Djouadi, J. Kalinowski, and M. Spira. "HDECAY: A Program for Higgs boson decays in the standard model and its supersymmetric extension". In: *Comput. Phys. Commun.* 108 (1998), pp. 56–74. DOI: 10.1016/S0010-4655(97)00123-9. arXiv: hep-ph/9704448 [hep-ph].

[223] Andreas Hocker et al. "TMVA - Toolkit for Multivariate Data Analysis". In: (2007). arXiv: physics/0703039 [physics.data-an].

[224] H.-J. Yang, B. P. Roe, and J. Zhu. "Studies of boosted decision trees for MiniBooNE particle identification". In: *Nuclear Instruments and Methods in Physics Research A* 555 (Dec. 2005), pp. 370–385. DOI: 10.1016/j.nima.2005.09.022. eprint: physics/0508045.

[225] S. Brandt, Ch. Peyrou, R. Sosnowski, and A. Wroblewski. "The principal axis of jets — an attempt to analyse high-energy collisions as two-body processes". In: *Physics Letters* 12.1 (1964), pp. 57 –61. ISSN: 0031-9163. DOI: https://doi.org/10.1016/0031-9163(64)91176-X. URL: http://www.sciencedirect.com/science/article/pii/003191636491176X.

[226] Edward Farhi. "Quantum Chromodynamics Test for Jets". In: *Phys. Rev. Lett.* 39 (25 Dec. 1977), pp. 1587–1588. DOI: 10.1103/PhysRevLett.39.1587. URL: https://link.aps.org/doi/10.1103/PhysRevLett.39.1587.

[227] M. Iwasaki. *Event shape analyzers based on the JETSET thrust and event shape routines*. Aug. 2000. URL: ftp://ftp.slac.stanford.edu/groups/lcd/Physics_tools/ (visited on 09/06/2017).

[228] D. P. Barber et al. "Discovery of Three-Jet Events and a Test of Quantum Chromodynamics at PETRA". In: *Phys. Rev. Lett.* 43 (12 Sept. 1979), pp. 830–833. DOI: 10.1103/PhysRevLett.43.830. URL: https://link.aps.org/doi/10.1103/PhysRevLett.43.830.

[229] James D. Bjorken and Stanley J. Brodsky. "Statistical Model for Electron-Positron Annihilation into Hadrons". In: *Phys. Rev. D* 1 (5 Mar. 1970), pp. 1416–1420. DOI: 10.1103/PhysRevD.1.1416. URL: https://link.aps.org/doi/10.1103/PhysRevD.1.1416.

[230] R.K. Ellis, D.A. Ross, and A.E. Terrano. "The perturbative calculation of jet structure in e+e− annihilation". In: *Nuclear Physics B* 178.3 (1981), pp. 421 –456. ISSN: 0550-3213. DOI: https://doi.org/10.1016/0550-3213(81)90165-6. URL: http://www.sciencedirect.com/science/article/pii/0550321381901656.

[231] Andrew J. Larkoski, Gavin P. Salam, and Jesse Thaler. "Energy Correlation Functions for Jet Substructure". In: *JHEP* 06 (2013), p. 108. DOI: 10.1007/JHEP06(2013)108. arXiv: 1305.0007 [hep-ph].

[232] *Trigger monitoring and rate predictions using Enhanced Bias data from the ATLAS Detector at the LHC*. Tech. rep. ATL-DAQ-PUB-2016-002. Geneva: CERN, Oct. 2016. URL: https://cds.cern.ch/record/2223498.

[233] Georges Aad et al. "Jet energy measurement and its systematic uncertainty in proton-proton collisions at $\sqrt{s} = 7$ TeV with the ATLAS detector". In: *Eur. Phys. J.* C75 (2015), p. 17. DOI: 10.1140/epjc/s10052-014-3190-y. arXiv: 1406.0076 [hep-ex].

[234] R Achenbach et al. "The ATLAS Level-1 Calorimeter Trigger". In: *Journal of Instrumentation* 3.03 (2008), P03001. URL: http://stacks.iop.org/1748-0221/3/i=03/a=P03001.

[235] *Performance of the ATLAS Electron and Photon Trigger in p-p Collisions at sqrts = 7 TeV in 2011*. Tech. rep. ATLAS-CONF-2012-048. Geneva: CERN, May 2012. URL: https://cds.cern.ch/record/1450089.

[236] ATLAS collaboration. *Data-driven determination of the energy scale and resolution of jets reconstructed in the ATLAS calorimeters using dijet and multijet events at $\sqrt{s} = 8$ TeV*. Tech. rep. ATLAS-CONF-2015-017. Geneva: CERN, Apr. 2015. URL: https://cds.cern.ch/record/2008678.

[237] ATLAS Collaboration. *Jet Trigger Public Plots*. Oct. 2017. URL: https://twiki.cern.ch/twiki/bin/view/AtlasPublic/JetTriggerPublicResults#Jet_Trigger_Efficiency_Plots_Cal.